

**INVESTIGATE THE VARISTOR PROPERTIES OF THE
COMPOSITES OF TRANSITION METAL OXIDES,
POLYMER, SILVER AND REDUCED GRAPHENE OXIDE
NANOPOWDERS**

Thesis Submitted for the Award of the Degree of

DOCTOR OF PHILOSOPHY

in

Physics

By

Mehar Jyoti Panesar

(11719563)

Supervised By

Dr. Ajeet Kumar Srivastava

11459

Department of Physics (Professor)

Lovely Professional University



LOVELY PROFESSIONAL UNIVERSITY

PUNJAB

2023

CERTIFICATE

This is to certify that the work reported in the Ph. D. thesis entitled “**Investigate the Varistor Properties of the composites of Transition Metal Oxides, Polymer, Silver and Reduced Graphene Oxide Nanopowders**” submitted in fulfillment of the requirement for the reward of degree of **Doctor of Philosophy (Ph.D.)** in the Department of Physics / School of Chemical Engineering and Physical Sciences, is a research work carried out by Mehar Jyoti Panesar, 11719563, is bonafide record of his/her original work carried out under my supervision and that no part of thesis has been submitted for any other degree, diploma or equivalent course.



Name of supervisor: Dr. Ajeet Kumar Srivastava

Designation: Professor

Department of Physics

School of Chemical Engineering and Physical Sciences

Lovely Professional University,

Punjab, India

Abstract

Department of Physics
School of Chemical Engineering and Physical Engineering
Lovely Professional University,
Punjab, India

Ph.D. Physics

INVESTIGATE THE VARISTOR PROPERTIES OF THE COMPOSITES OF TRANSITION METAL OXIDES, POLYMER, SILVER AND REDUCED GRAPHENE OXIDE NANOPOWDERS

by MEHAR JYOTI PANESAR

Nano – crystalline systems in today’s world has the preference in its manufacturing desirability in every facet of the working domains. The inclination towards the employment of nano – materials and nano – technology has made the synthesis processes and characterisations of such nano – scaled system a necessity. Nonetheless, there are still various categories of materials that are yet to be studied up to its potency. Varistors are known to operate on varying resistance values and exhibit non – linear characteristics. ZnO is the only semi – conducting metal - oxide that has been exclusively studied on, therefore, this research work focused on investigating the working capabilities of other metal – oxides of likewise categories as; CuO, CdO and TiO₂ (anatase). This work also entails the electric conduction behaviour for carbon dominated materials like; PANI and rGO with the addition of a metallic nanopowders i.e., Ag. The studies were done using a host material in which the dopant was added in varying weight ratios with the preparation of following four composite sample mixtures:

- CuO + Ag (0:1, 1:1, 1:2 and 0:1)
- PANI + CdO (0:1, 1:1, 1:2 and 0:1)
- TiO₂ (anatase) + Ag (0:1, 1:1, 3:1 and 0:1)

- rGO + Ag (0:1, 1:1, 3:1 and 0:1)

Sol – Gel auto combustion method was used to synthesis the CuO and CdO nano – powders whereas, Ultrasonic assisted sol gel method was employed on to obtain nano – particle samples for TiO₂ (anatase form). Oxidative Polymerisation method was used for acquire PANI sample powders. Top – Down method with sodium borohydride as reducing agent was used for Ag nano – powders. Modified Hummer’s Method was applied to fabricate rGO nanoparticles and in this case hydrazine hydrate was used as reducing agent in method.

Thermo – Gravimetric Analysis (TGA), X – Ray Diffraction (XRD), Fourier Transform Infra – Red Spectroscopy (FTIR), Raman Spectroscopy, Field Emission Scanning Electron Microscopy (FESEM), Energy Dispersive X – Ray (EDX), Particle Size Analysis (PSA) and Current – Voltage plots and measurements were employed on to investigate and study the thermal behaviour, structural nature, molecular inhabitation, surface studies including the topographical morphology, elemental ratio and distribution pattern, particle size and varistor nature of the synthesised nano – powders.

Sol – Gel auto combustion method was employed on to fabricate CuO nano particles whereas, Top – Down method was used to obtain silver nano – powders. TGA characterisation revealed 600 °C as calcination temperature which was according to the theoretical studies as well. XRD and FTIR gave the necessity structural peaks which led to the confirmation of the desired sample nano – crystalline powders. Raman spectroscopy showed C_{2h}⁶ C2/c and O_h⁵Fm3m as space groups for CuO and Ag nano – structures. An elevation in the values for non – linear coefficient (α) was obtained for the composite mixtures, which meant the increase in the Ohm’s Law region. The current (I_N) and voltage (V_N) values for varistor studies were also found to be shown higher for the proceeding sample systems.

A steady growth in the values was observed for all the sample cases for current – voltage plot. An irregularity was obtained in the slope due to the amorphous nature of PANI but it was found to be insignificant and did not interfere with the operational aspects of sample sets. The changes were computed to fall within the smaller scale of differences which implied its applicational prospects in lower voltage varistor industries. XRD revealed cubic arrangement of crystals in monteponite phase (O_h⁵Fm3m) for CdO nano – powders whereas, Polyaniline exhibited

amorphous nature in C_s plane. The information regarding surface morphology and elemental ratios for constituents were studied using FESEM and EDX tools.

In this research work, composite mixtures of TiO_2 (anatase) and silver were investigated. The content of silver was increased gradually to observe its effect on varistor properties of TiO_2 nanopowders. Wet chemistry method and ultra – sonic assisted sol – gel method was used to obtain the Ag and TiO_2 nano powders respectively. Structural properties have been investigated using X-ray diffraction (XRD), Fourier transform infrared (FTIR) spectroscopy, Raman spectroscopy and Field emission scanning electron microscopy (FESEM). Thermal properties have been studied using thermogravimetric analysis (TGA) and revealed $450^\circ C$ for the calcination of the powders. FTIR and Raman analysis exhibited the structural peak values and FESEM gave details regarding the surface morphology. Current versus voltage graphs were obtained to examine the extent of applicational prospects and it was observed that TiO_2 sample mixtures gave small increase in current voltage values when used with single conductive material.

In this frame of work, behaviour of rGO individually and when mixed with Ag – nanopowders was for composition: RA1 [rGO, 1:0], RA2 [rGO + Ag, 3:1], RA3 [rGO + Ag, 1:1], RA4 [Ag, 0:1]. Modified hummers method and burst method were used to synthesise the reduced graphene oxide and silver nanopowders. The structural aspects were investigated through XRD, FTIR and Raman Analysis. Further, the purity of Ag – nanopowders was confirmed through Rietveld refinement. FESEM and EDX gave the surface and elemental details. Its capability for varistor applicational areas was studied via current versus voltage graph; rGO composite sample mixtures, despite showing smaller voltage changes, exhibited an increase in the values.

This thesis has been divided into five chapters i.e., introduction, literature review, method of synthesis, characterisation tools and formulae and results and discussions. In Introduction, the materials that have studied in the research paper have been discussed in details. The innate nature, structural arrangements, applicational prospects and electrical, thermal, magnetic properties of such materials have been reviewed. The applicational aspect of the work, purpose, scope and research gap has also been written under this chapter. In Literature Review, a brief summary for the papers have been given that were studied concerning the chemicals and synthesis processes that were employed on during the work. In Methods of Synthesis, various

fabrication processes that were adopted to obtain the nano – powders have been discussed. The working principle behind each experimental tool that has been studied and the formulae that were used for computing size and non – linear coefficient values were given with brief details under characterisation techniques and formulae. In Results and Discussions, the results obtained and analysed for each sample composition for all the objectives have been discussed.

Acknowledgements

Foremost, I set forth my indebted gratitude towards the almighty numen for bestowing me with the courage to proceed with the research work despite the challenges. In helping me to evolve as a human being along the journey and teaching me that “Knowledge has a beginning, but no end” and to be a forever seeker.

My earnest appreciation and respect for my supervisor Dr. Ajeet Kumar Srivastava for his patience, willingness, guidance and support during the entirety of my research labor. For his intangible support by providing me with honest constructive feedbacks and sharing his expertise knowledge regarding the matters.

I would also like to extend my gratitude towards Dean Dr. Kailash Chandra Juglan and Dr. Mukesh Kumar for their advices and moral encouragement. Furthermore, many thanks to the lab head Dr. Rajesh Kumar, lab assistants Parminder Singh, Nitin Kumar, Ramesh Kumar, Manoj Kumar and to the faculty of Physics department and Central Instrumentation Facility laboratory for their cordial liaison. An appreciative gesture for Dr. Pragati Kumar from Central University of Jammu and the faculty of Materials Research Centre, Malaviya National Institute of Technology, Jaipur as well.

I am beholden for all collaborative opportunities with the fellow researchers and the absolute pleasure of working with my friends. A special thanks to Dr. Tchouank Tekou Carol Trudel, Dr. Jibrin Mohammad for all their aid and assistance in proof – reading, editing sessions and to Anjori Sharma for commiseration. I sincerely acknowledge my regards for all the research scholars and cohort members for the support and well – wishes.

Lastly, words cannot express my gratitude and affection for my parents and brother for their immeasurable encouragement and plenteous support; emotionally, morally and financially. Their belief in me was the reason to continue with the work and be inspired throughout the course. I am forever obliged to them, for this work would have been unfeasible without their reassurance and confidence in me. May the supreme almighty shower them with limitless contentment and bless them with happy and healthy life.

Mehar Jyoti Panesar (*Research Scholar*)

Table of Contents

List of Figures.....	xii
List of Tables	xvii
1 INTRODUCTION	1
1.1 Copper Oxide (CuO)	5
1.2 Cadmium Oxide (CdO)	7
1.3 Titanium Dioxide (TiO ₂).....	9
1.4 Polyaniline (PANI).....	12
1.5 Silver (Ag).....	14
1.6 Reduced Graphene Oxide (rGO).....	16
1.7 Varistor.....	18
1.8 Chemicals and Reagents used	21
1.9 Materials under present investigation	22
1.10 Research Gap.....	23
1.11 Objectives of the present work.....	25
1.12 Purpose of the present work.....	25
1.13 Future Scope of the present work.....	26
2 LITERATURE REVIEW	28
3 METHOD OF SYNTHESIS	43
3.1 Sol – Gel Method	44
3.1.1 Sol – Gel Auto Combustion Method	45
3.1.2 Ultra-sonic assisted Sol – Gel Method.....	47
3.2 Oxidative Polymerisation Method	48
3.3 Top – Down Method	50
3.4 Modified Hummer’s Method	52
4 CHARACTERISATION TECHNIQUES AND FORMULAE	58
4.1 Thermal Analysis	58
4.1.1 Thermo – Gravimetric Analysis (TGA).....	58

4.2	Structural Analysis	60
4.2.1	X – Ray Diffraction (XRD)	60
4.2.2	Fourier Transform Infra – red Spectroscopy (FTIR)	63
4.3	Molecular Analysis	65
4.3.1	Raman Spectroscopy.....	65
4.4	Surface Analysis.....	67
4.4.1	Field Emission Scanning Electron Microscopy (FESEM)	67
4.4.2	Energy Dispersive X – Ray (EDX).....	68
4.4.3	Particle Size Analysis (PSA)	70
4.5	Varistor.....	70
5	RESULTS AND DISCUSSIONS.....	72
5.1	CuO mixed with Ag	72
5.1.1	TGA Studies.....	72
5.1.2	XRD Pattern.....	74
5.1.3	FTIR Analysis	79
5.1.4	Raman Spectroscopy.....	84
5.1.5	FESEM Analysis.....	87
5.1.6	EDX and Mapping Studies	89
5.1.7	PSA Analysis	91
5.1.8	Varistor Studies.....	92
5.2	PANI mixed with CdO.....	98
5.2.1	TGA Studies.....	98
5.2.2	XRD Pattern.....	100
5.2.3	FTIR Analysis	104
5.2.4	Raman Spectroscopy.....	109
5.2.5	FESEM Analysis.....	113
5.2.6	EDX and Mapping Studies	114
5.2.7	PSA Analysis	117
5.2.8	Varistor Studies.....	118
5.3	TiO₂ (anatase) mixed with Ag	124
5.3.1	TGA Studies.....	124

5.3.2	XRD Pattern.....	126
5.3.3	FTIR Analysis.....	131
5.3.4	Raman Spectroscopy.....	136
5.3.5	FESEM Analysis.....	139
5.3.6	PSA Pattern.....	141
5.3.7	Varistor Studies.....	141
5.4	rGO mixed with Ag.....	147
5.4.1	XRD Pattern.....	147
5.4.2	FTIR Analysis.....	153
5.4.3	Raman Spectroscopy.....	156
5.4.4	Surface Analysis.....	160
5.4.5	Varistor Studies.....	163
SUMMARY.....		167
BIBLIOGRAPHY.....		170

List of Figures

Figure 1.1 Figurative representation for the applicational aspects of the nano – technology [2].	1
Figure 1.2 Figurative representation for the nano – structured materials, their usage and fabrication routes [7].	3
Figure 1.3 Figurative representation for the applicational arenas of the nano – structured materials [10].	4
Figure 1.4 Figurative representation for the classifications of nano – particles [12].	5
Figure 1.5 Figurative representation for the Cuprous Oxide, Cu ₂ O and Copper Oxide, CuO [14].	6
Figure 1.6 Figurative representation for the various synthesis routes and applicational prospects of Copper Oxide, CuO [15].	6
Figure 1.7 Figurative representation for the Cadmium Oxide, CdO.	7
Figure 1.8 Figurative representation for the numerous fabrication processes for CdO nano – powders [22].	8
Figure 1.9 Figurative representation for the employment facilities of CdO nano – powders in medical field [22].	8
Figure 1.10 Figurative representation for crystalline structures of 3 phases of TiO ₂ : Rutile, Brookite and Anatase [31]	10
Figure 1.11 Figurative representation for the differences between each of the three crystalline structures phases.	10
Figure 1.12 Figurative representation for the varying utilizations of TiO ₂ nano – powders in several fields [34].	11
Figure 1.13 Figurative representation for the transformation of aniline monomer in polyaniline polymer in the presence of HCl and ammonium Persulphate, (NH ₄) ₂ S ₂ O ₈ [37].	12
Figure 1.14 Figurative representation for the conversion of polymer into the conductive form through the process of protonation [43].	13
Figure 1.15 Figurative representation for the applications domains of polyaniline [46][47].	13
Figure 1.16 Figurative representation for the classifications of metallic nano – powders [51].	14
Figure 1.17 Figurative representation for the uses of silver nano – structured powders [56].	15

Figure 1.18 Figurative representation for the sp ² – hybridised carbon derivatives: (a) Graphene, (b) Graphene Oxide and (c) Reduced Graphene Oxide [58].	16
Figure 1.19 Figurative representation for utilisations domains of Graphene Oxide and Reduced Graphene Oxide [63].	17
Figure 1.20 Figurative representation for (a) Voltage-Resistance Curve and (b) Voltage-Current Curve.	19
Figure 1.21 Figurative representation for uses of varistors as surge protector in different types of circuits and formats.	21
Figure 3.1 Figurative representation for the various routes of synthesis on nano – powders [108].	43
Figure 3.2 Illustration of the Sol-Gel Method and its various synthesis routes.	44
Figure 3.3 The step – by – step schematic illustration of sol – gel auto combustion method [109].	45
Figure 3.4 Diagrammatic representation of Sol – Gel Auto – Combustion method of synthesis for CuO nanopowders.	46
Figure 3.5 Diagrammatic representation of Sol – Gel Auto – Combustion method of synthesis for CdO nanopowders.	46
Figure 3.6 Figurative description of the placement of the solution in the ultrasonic water bath.	47
Figure 3.7 Diagrammatic representation of Ultra – Sonic assisted Sol – Gel method of synthesis for TiO ₂ (anatase) nanopowders.	48
Figure 3.8 Figurative description of the placement of the PANI solution with temperature at 0 °C [110].	49
Figure 3.9 Diagrammatic representation of Oxidative Polymerisation method of synthesis for PANI nanopowders.	49
Figure 3.10 Figurative representation of the Top – Down and Bottom – Up methods of synthesis [111].	50
Figure 3.11 Figurative description of the cluster formation and breakdown of the solution.	51
Figure 3.12 Diagrammatic representation of Top - Down method of synthesis for Ag – nanopowders.	52
Figure 3.13 Tabular representation of improvisations done in Hummer’s Method by time [115].	54
Figure 3.14 Figurative representation of conversion of Graphene into Graphene Oxide and final transformation into Reduced Graphene Oxide [118].	55

Figure 3.15 Diagrammatic representation of Modified Hummer’s method of synthesis for rGO – nanopowders.	57
Figure 4.1 Figurative representation of the apparatus for thermo – gravimetric analysis.	59
Figure 4.2 Figurative representation of the working for x – ray diffraction analysis [119]. ..	61
Figure 4.3 Figurative representation of the Bragg’s Law [119].	62
Figure 4.4 Figurative representation of the working for Fourier transform infrared spectroscopy analysis.....	64
Figure 4.5 Figurative representation of the working for Raman and Rayleigh scattering.....	66
Figure 4.6 Figurative representation of the working for Raman spectroscopy analysis.....	66
Figure 4.7 Figurative representation of the working for Field Emission Scanning Electron Microscopy analysis.....	68
Figure 4.8 Figurative representation of the working for Energy Dispersive X - Ray analysis.	69
Figure 5.1 TGA Analysis of CA1 [CuO, 1:0] and CA4 [Ag, 0:1].....	73
Figure 5.2 XRD Analysis of CA1 [CuO, 1:0], CA2 [CuO + Ag, 1:1], CA3 [CuO + Ag, 1:2] and CA4 [Ag, 0:1].....	76
Figure 5.3 XRD-Refinement plot of CA1 [CuO, 1:0], CA2 [CuO + Ag, 1:1], CA3 [CuO + Ag, 1:2] and CA4 [Ag, 0:1].	79
Figure 5.4 FTIR Analysis of CA1 [CuO, 1:0], CA2 [CuO + Ag, 1:1], CA3 [CuO + Ag, 1:2] and CA4 [Ag, 0:1].....	82
Figure 5.5 Raman Analysis of CA1 [CuO, 1:0], CA2 [CuO + Ag, 1:1], CA3 [CuO + Ag, 1:2] and CA4 [Ag, 0:1].....	86
Figure 5.6 FESEM Analysis of CA1 [CuO, 1:0], CA2 [CuO + Ag, 1:1], CA3 [CuO + Ag, 1:2] and CA4 [Ag, 0:1].....	88
Figure 5.7 EDX Analysis of CA1 [CuO, 1:0], CA2 [CuO + Ag, 1:1], CA3 [CuO + Ag, 1:2] and CA4 [Ag, 0:1].....	89
Figure 5.8 Elemental Mapping for CA1 [CuO, 1:0], CA2 [CuO + Ag, 1:1], CA3 [CuO + Ag, 1:2] and CA4 [Ag, 0:1].	91
Figure 5.9 Particle Size Distribution Analysis of CA1 [CuO, 1:0] and CA4 [Ag, 0:1].	92
Figure 5.10 Current – Voltage Plot Analysis for CA1 [CuO, 1:0], CA2 [CuO + Ag, 1:1], CA3 [CuO + Ag, 1:2] and CA4 [Ag, 0:1].	93
Figure 5.11 Graphical plot for α – value against the CuO content of CA1 [CuO, 1:0], CA2 [CuO + Ag, 1:1], CA3 [CuO + Ag, 1:2] and CA4 [Ag, 0:1].	97
Figure 5.12 TGA Analysis of PC1 [PANI, 1:0] and PC4 [CdO, 0:1].....	99

Figure 5.13 XRD Analysis of PC1 [PANI, 1:0], PC2 [PANI + CdO, 1:1], PC3 [PANI + CdO, 1:2] and PC4 [CdO, 0:1].	102
Figure 5.14 FTIR Analysis of PC1 [PANI, 1:0], PC2 [PANI + CdO, 1:1], PC3 [PANI + CdO, 1:2] and PC4 [CdO, 0:1].	107
Figure 5.15 Raman Analysis of PC1 [PANI, 1:0], PC2 [PANI + CdO, 1:1], PC3 [PANI + CdO, 1:2] and PC4 [CdO, 0:1].	112
Figure 5.16 FESEM Analysis of PC1 [PANI, 1:0], PC2 [PANI + CdO, 1:1], PC3 [PANI + CdO, 1:2] and PC4 [CdO, 0:1].	114
Figure 5.17 EDX Analysis of PC1 [PANI, 1:0], PC2 [PANI + CdO, 1:1], PC3 [PANI + CdO, 1:2] and PC4 [CdO, 0:1].	115
Figure 5.18 EDX - Mapping Analysis of PC1 [PANI, 1:0], PC2 [PANI + CdO, 1:1], PC3 [PANI + CdO, 1:2] and PC4 [CdO, 0:1].	117
Figure 5.19 Particle Size Distribution Analysis of PC4 [CdO, 0:1].	118
Figure 5.20 Current – Voltage Plot Analysis of PC1 [PANI, 1:0], PC2 [PANI + CdO, 1:1], PC3 [PANI + CdO, 1:2] and PC4 [CdO, 0:1].	119
Figure 5.21 Graphical view of current values against the PANI content for PC1 [PANI, 1:0], PC2 [PANI + CdO, 1:1], PC3 [PANI + CdO, 1:2] and PC4 [CdO, 0:1].	122
Figure 5.22 TGA Analysis of (a) TA1 [TiO ₂ , 1:0] and (b) TA4 [Ag, 0:1].	125
Figure 5.23 XRD Analysis of TA1 [TiO ₂ , 1:0], TA2 [TiO ₂ + Ag, 3:1], TA3 [TiO ₂ + Ag, 1:1] and TA4 [Ag, 0:1].	127
Figure 5.24 XRD Refinement Analysis of (a) TA1 [TiO ₂ , 1:0], (b) TA2 [TiO ₂ + Ag, 3:1], (c) TA3 [TiO ₂ + Ag, 1:1] and (d) TA4 [Ag, 0:1].	130
Figure 5.25 FTIR Analysis of TA1 [TiO ₂ , 1:0], TA2 [TiO ₂ + Ag, 3:1], TA3 [TiO ₂ + Ag, 1:1] and TA4 [Ag, 0:1].	135
Figure 5.26 Raman Analysis of TA1 [TiO ₂ , 1:0], TA2 [TiO ₂ + Ag, 3:1], TA3 [TiO ₂ + Ag, 1:1] and TA4 [Ag, 0:1].	138
Figure 5.27 Raman fitting of TA1 [TiO ₂ , 1:0], TA2 [TiO ₂ + Ag, 3:1], TA3 [TiO ₂ + Ag, 1:1] and TA4 [Ag, 0:1].	139
Figure 5.28 FESEM Images of (a) TA1 [TiO ₂ , 1:0], (b) TA2 [TiO ₂ + Ag, 3:1], (c) TA3 [TiO ₂ + Ag, 1:1], (d) TA4 [Ag, 0:1].	140
Figure 5.29 Particle Size Distribution images for (a) TA1 [TiO ₂ , 1:0] and (b) TA4 [Ag, 0:1].	141
Figure 5.30 Current – Voltage Plot Analysis of TA1 [TiO ₂ , 1:0], TA2 [TiO ₂ + Ag, 3:1], TA3 [TiO ₂ + Ag, 1:1] and TA4 [Ag, 0:1].	143

Figure 5.31 Graphical view of current values against the TiO ₂ (anatase) content for TA1 [TiO ₂ , 1:0], TA2 [TiO ₂ + Ag, 3:1], TA3 [TiO ₂ + Ag, 1:1] and TA4 [Ag, 0:1].	146
Figure 5.32 XRD Analysis of GO, RA1 [rGO, 1:0], RA2 [rGO + Ag, 3:1], RA3 [rGO + Ag, 1:1], RA4 [Ag, 0:1].	148
Figure 5.33 XRD Refinement Analysis of RA4 [Ag, 0:1], RA3 [rGO + Ag, 1:1] and RA2 [rGO + Ag, 3:1].	151
Figure 5.34 FTIR Analysis of GO, RA1 [rGO, 1:0], RA2 [rGO + Ag, 3:1], RA3 [rGO + Ag, 1:1], RA4 [Ag, 0:1].	154
Figure 5.35 Raman Analysis of GO, RA1 [rGO, 1:0], RA2 [rGO + Ag, 3:1], RA3 [rGO + Ag, 1:1], RA4 [Ag, 0:1].	158
Figure 5.36 (a) FESEM Analysis and (b) EDX Analysis of GO.	161
Figure 5.37 FESEM Analysis of (a) RA1 [rGO, 1:0], (b) RA2 [rGO + Ag, 3:1], (c) RA3 [rGO + Ag, 1:1], (d) RA4 [Ag, 0:1] and (e) Particle Size Distribution of RA4 [Ag, 0:1].	162
Figure 5.38 Current / Voltage Analysis of RA1 [rGO, 1:0], RA2 [rGO + Ag, 3:1], RA3 [rGO + Ag, 1:1], RA4 [Ag, 0:1].	164
Figure 5.39 Graphical plot for α – value against the rGO content of RA1 [rGO, 1:0], RA2 [rGO + Ag, 3:1], RA3 [rGO + Ag, 1:1], RA4 [Ag, 0:1].	166

List of Tables

Table 4:1: Tabular representation for the sample materials and drying and calcination temperatures.....	59
Table 4:2: Tabular representation for the Crystal Structure, Lattice Parameters and Formulae, Space Group, JCPDS for the sample materials of the present work.....	63
Table 5:1: Values for the XRD peaks and (hkl) index planes of CA1 [CuO, 1:0], CA2 [CuO + Ag, 1:1], CA3 [CuO + Ag, 1:2] and CA4 [Ag, 0:1].	77
Table 5:2: Lattice parameters (a, b, c), Crystallite Size (D), FWHM (β^*), Bragg's angle (2θ) and Volume (V) for CA1 [CuO, 1:0], CA2 [CuO + Ag, 1:1], CA3 [CuO + Ag, 1:2] and CA4 [Ag, 0:1]......	78
Table 5:3: FTIR peaks and the corresponding bonds associations for CA1 [CuO, 1:0], CA2 [CuO + Ag, 1:1], CA3 [CuO + Ag, 1:2] and CA4 [Ag, 0:1].	82
Table 5:4: Raman Spectra peaks and the adjacent bonds for CA1 [CuO, 1:0], CA2 [CuO + Ag, 1:1], CA3 [CuO + Ag, 1:2] and CA4 [Ag, 0:1]......	86
Table 5:5: Tabular form for the values of non – linear coefficient ' α ', voltage across the device ' V_N (V/mm)' and current across the device ' I_N (mA/cm ²)' for CA1 [CuO, 1:0], CA2 [CuO + Ag, 1:1], CA3 [CuO + Ag, 1:2] and CA4 [Ag, 0:1].	96
Table 5:6: XRD peak values for PC1 [PANI, 1:0], PC2 [PANI + CdO, 1:1], PC3 [PANI + CdO, 1:2] and PC4 [CdO, 0:1]......	102
Table 5:7: Lattice parameters (a, b, c), crystallite size (D), FWHM (β^*), Bragg's angle (2θ) and volume (V) of PC2 [PANI + CdO, 1:1], PC3 [PANI + CdO, 1:2] and PC4 [CdO, 0:1].	104
Table 5:8: FTIR peaks and the associated bonds for PC1 [PANI, 1:0], PC2 [PANI + CdO, 1:1], PC3 [PANI + CdO, 1:2] and PC4 [CdO, 0:1]......	107
Table 5:9: Raman peak values and the bonds for PC1 [PANI, 1:0], PC2 [PANI + CdO, 1:1], PC3 [PANI + CdO, 1:2] and PC4 [CdO, 0:1]......	112
Table 5:10: V_N (V/mm) = Varistor Voltage and I_N (mA/cm ²) = Varistor current for PC1 [PANI, 1:0], PC2 [PANI + CdO, 1:1], PC3 [PANI + CdO, 1:2] and PC4 [CdO, 0:1].	121
Table 5:11: XRD bonds and values for TA1 [TiO ₂ , 1:0], TA2 [TiO ₂ + Ag, 3:1], TA3 [TiO ₂ + Ag, 1:1] and TA4 [Ag, 0:1].	128
Table 5:12: Lattice parameters (a, b, c), crystallite size (D), FWHM (β^*), Bragg's Angle (2θ) and volume (V) of TA1 [TiO ₂ , 1:0], TA2 [TiO ₂ + Ag, 3:1], TA3 [TiO ₂ + Ag, 1:1] and TA4 [Ag, 0:1]......	129

Table 5:13: Conditions for refinement, reliability factor (<i>Rp</i> , <i>Rwp</i> , <i>Rexp</i>), chi-square (χ^2) and good of fit (GoF) of prepared samples	130
Table 5:14: FTIR bonds and the peak values for TA1 [TiO ₂ , 1:0], TA2 [TiO ₂ + Ag, 3:1], TA3 [TiO ₂ + Ag, 1:1] and TA4 [Ag, 0:1].	133
Table 5:15: Raman peak names and the values for TA1 [TiO ₂ , 1:0], TA2 [TiO ₂ + Ag, 3:1], TA3 [TiO ₂ + Ag, 1:1] and TA4 [Ag, 0:1].....	137
Table 5:16: V _N (V/mm) = Varistor Voltage and I _N (mA/cm ²) = Varistor current for TA1 [TiO ₂ , 1:0], TA2 [TiO ₂ + Ag, 3:1], TA3 [TiO ₂ + Ag, 1:1] and TA4 [Ag, 0:1].	145
Table 5:17: XRD bonds and values for RA1 [rGO, 1:0], RA2 [rGO + Ag, 3:1], RA3 [rGO + Ag, 1:1] and RA4 [Ag, 0:1]	149
Table 5:18: Lattice parameters (a, b, c), crystallite size (D), FWHM (β^*), Braggs angle (2θ) and volume (V) of RA2 [rGO + Ag, 3:1], RA3 [rGO + Ag, 1:1] and RA4 [Ag, 0:1].	150
Table 5:19: Conditions for refinement, reliability factor (<i>Rp</i> , <i>Rwp</i> , <i>Rexp</i>), refined half-width parameters (U, V, W) chi-square (χ^2) and good of fit (GoF) of prepared samples.....	152
Table 5:20: FTIR Bonds and the Peak values for the bonds obtained for the GO sample powders.	153
Table 5:21: FTIR bonds and peaks values for the samples RA1 [rGO, 1:0], RA2 [rGO + Ag, 3:1], RA3 [rGO + Ag, 1:1], RA4 [Ag, 0:1].	155
Table 5:22: Raman bonds and values for GO sample powders.	157
Table 5:23: Raman bonds and values for RA1 [rGO, 1:0], RA2 [rGO + Ag, 3:1], RA3 [rGO + Ag, 1:1] and RA4 [Ag, 0:1].	159
Table 5:24: Tabular form for the values of non – linear coefficient ‘ α ’, voltage across the device ‘V _N (V/mm)’ and current across the device ‘I _N (mA/cm ²)’ for RA1 [rGO, 1:0], RA2 [rGO + Ag, 3:1], RA3 [rGO + Ag, 1:1] and RA4 [Ag, 0:1].	165

Dedicated to My Mom and Dad ...

Chapter 1

1 INTRODUCTION

In this globalized sphere, the advancements in the machineries have made the tranquil lifestyle to have a pre – eminent involvement in our day – to – day chores. Be it in any domain; work, home, industrial sectors or medical prospects etc, the device construction for that purpose and material synthetisation are the pertinent aspects. The discipline of Nano – technology comes under such classified category of technology. Nanotechnology, is the province of research and development that concerns with the blueprint of making, classifications and characterisations of the materials, varying from microscopic, atomic or molecular and macroscopic degrees. They entail the synthetisation engineering and manoeuvring of the nano-scaled materials [1] **(Figure 1.1).**



Figure 1.1 Figurative representation for the applicational aspects of the nano – technology [2].

Incessant evolution in the sector of nano – scaled materials and their technology has unfastened the doors for the opportunities for the furtherance in the field of material science; from the commencement of newer materials, newer combinations of materials and the constant requirement in the upgradation of the technologies to keep up with the need, to uncovering the newer domains and applicational areas for such said materials. Nano – particles by definition, having the size scale from 1nm – 100 nm have precisely amassed the attention in the field of synthesis of materials and their employment in the device fabrication [3]. Why these nano – structured particles are appraised? These nanopowders as they are known, have unequivocal uniqueness attached to it, which are dominantly due to their structural conduct [4]. Nanoparticles unlike their peer bulk materials, have very distinct physio – chemical traits, they have the competence to interfere with the intermural arrangements of the material’s networks involved and to enhance their potency for various chemical, physical, biological or magnetic needs. They have the leverage of having availability of atoms near if not at, the surface, for wide – ranging exposure to surface areas, which helps them with better interaction and thus acts as a catalyst for phenomenon [5]. Furthermore, these nano – powders also allocate the availability of options as per the necessity. They are cost – effective and easy to synthesis. Their structures can be effortlessly controlled and are easy to work with, when aligned with other materials. They have very distinct surface to volume ratio, which further helps in the advancement of various reactions. They have specific phase – dependent, electrical, catalytic, optical and magnetic traits and possess fine values of sensitivity time and response time in case of sensors [6] (**Figure 1.2**).

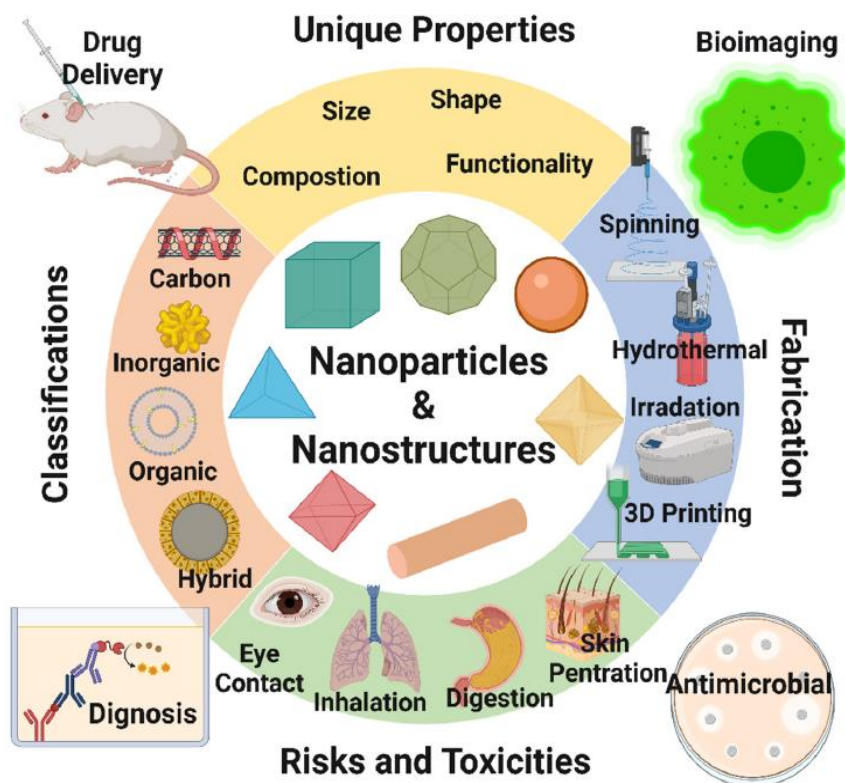


Figure 1.2 Figurative representation for the nano – structured materials, their usage and fabrication routes [7].

Their expanse of accessibility covers a broader spectrum; nanopowders have its existence very well established for the device fabrications in innumerable well – recognised industrial provinces such as; environmental sectors, medical devices, IT, nano reactors, nano sensors, commercial areas, raw materials for pigments and coatings, for the constructions of semiconductors, varistors, thermostats etc. They have extended the usage of their properties in miscellaneous provinces as well in self – care products and skin / makeup products; lipsticks, sunscreens and body lotions [8][9] (**Figure 1.3**).

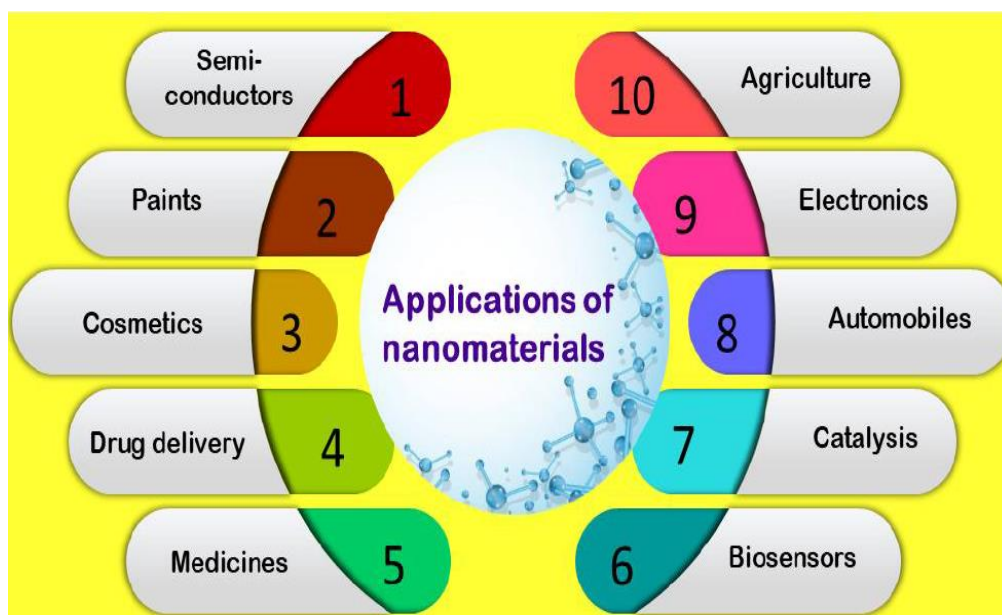


Figure 1.3 Figurative representation for the applicational arenas of the nano – structured materials [10].

From the immeasurable diversity of nano – powders (**Figure 1.4**) to select from, semi – conducting or metal oxide nanoparticles are the commending choices. They are used in various opto – electrical, magnetic fields; sensors, energy storage devices, thermostats, capacitors, piezo – electric devices, fuel cells and much more. They are favoured over because, they have cost – friendly synthesis processes, their size and structures can be controlled by outer forces and can be obtained in room temperature, they are readily available and are fashioned in almost every aspect of life, from industries to commercial networks [11]. Transparent or Transition metal – oxides is another form of denomination for them and they are further sub – categorised as transparent conductive oxides and transparent semi – conducting oxides. The present work is concerned with three such semi – conducting metal oxides: Copper Oxide (CuO), Cadmium Oxide (CdO) and the Anatase form of Titanium Dioxide (TiO₂).

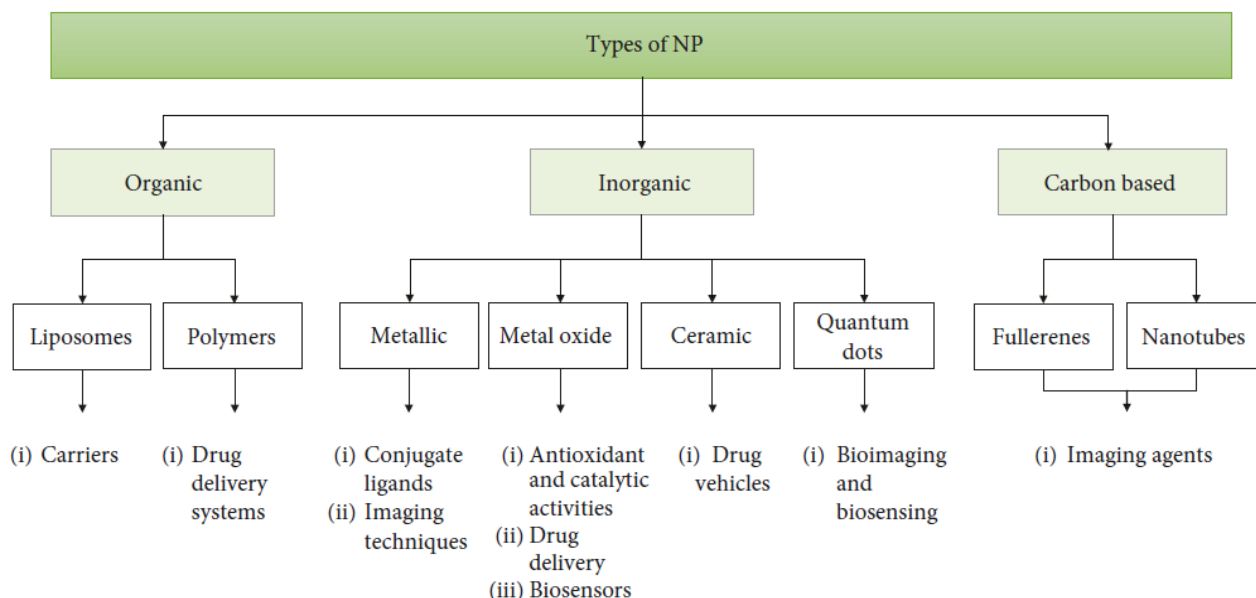


Figure 1.4 Figurative representation for the classifications of nano – particles [12].

1.1 Copper Oxide (CuO)

Copper wholesome has been the subject of an extensive study; be its nature-structure-properties or the oxides. Copper and oxygen interact with each other and give two structures: Cupric Oxide (CuO) and Cuprous Oxide (Cu₂O). *CuO* is an intrinsically p-type semiconductor because of the Cu vacancies. It has monoclinic crystal structure and have black color. It is occurring as tenorite rocks in nature. Its bandgap is 1.2-1.9 eV and has work function of 5.3eV. The copper atom is coordinated by 4 oxygen atoms in an approximately square planar configuration. *Cu₂O* is also a p-type semiconductor with cubic crystal structure having energy gap of 2.1 eV. And occurring as red mineral known as cuprite, which is less stable than CuO. It is used for water photo decomposition or photo degradation of organic pollutants [13] **(Figure 1.5).**

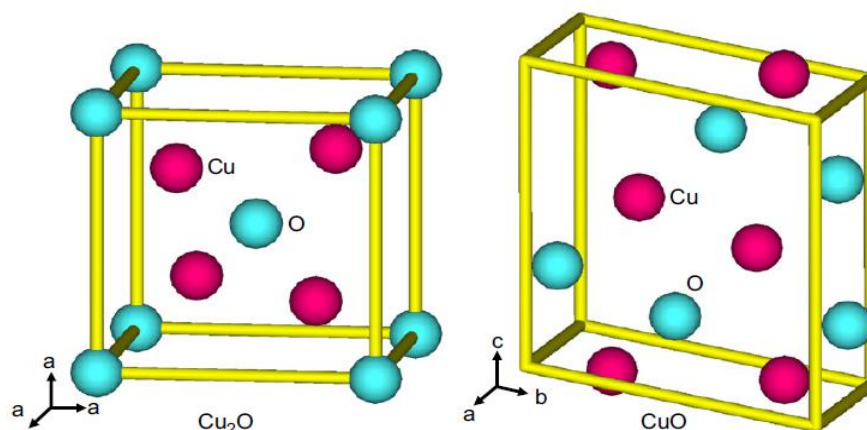


Figure 1.5 Figurative representation for the Cuprous Oxide, Cu_2O and Copper Oxide, CuO [14].

CuO is endowed with some pronounced features; it has stronger electrochemical facet, higher values for the specific areas, exceeding stability in the solutions, refined potential for redox reactions, it has distinct magnetic, optical and electrical characteristics. CuO has its applicational employment in diverse disciplines; electro – chemistry branch, filters, sensors, raw materials for paints and coatings where they are utilized as anti – fouling barriers, catalysts in reactions, energy storage devices, super capacitors, magnetic storage mediums and medical and commercial sectors as well [15] (**Figure 1.6**).

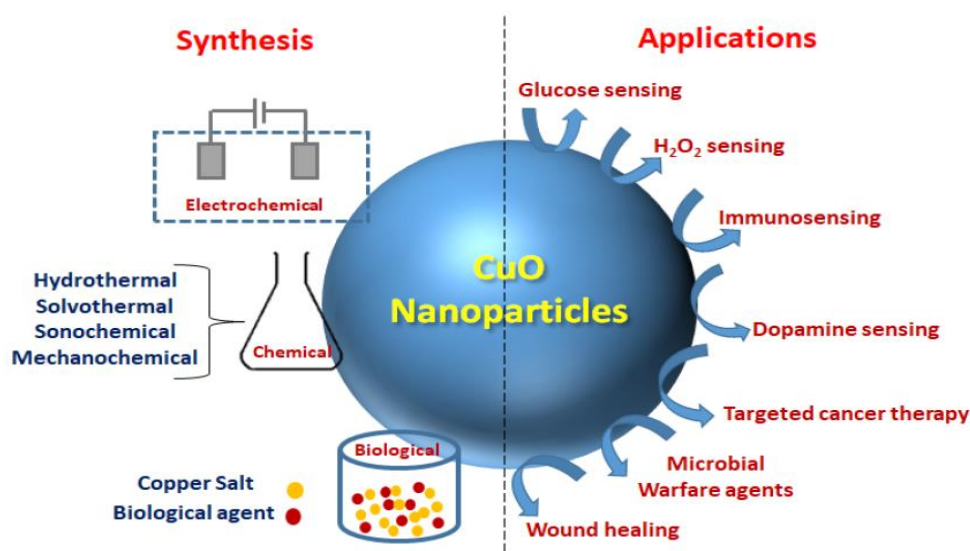


Figure 1.6 Figurative representation for the various synthesis routes and applicational prospects of Copper Oxide, CuO [15].

1.2 Cadmium Oxide (CdO)

Transparent conducting oxides such as; indium–tin oxide (ITO), cadmium oxide (CdO), zinc oxide (ZnO), tin oxide (SnO₂) have been colossally researched on because of the excessive implementations in semiconductor optoelectronic device technology [16][17].

Cadmium oxide is the n-type II – VI metal oxide semiconductor having direct band gap: 2.5eV and an indirect bandgap: 1.98eV. It exhibits lower resistivity towards electrical conduction i.e., $10^{-2} \Omega \text{ cm}$ to $10^{-4} \Omega \text{ cm}$ because of the defect caused by the formation of oxygen vacancies and cadmium interstitials [18]. It has density value of 8150 kg/m^3 which is quite high, and efficient refractive index of 2.75 [19]. It's an inorganic compound with conducting and transparent properties that solidifies itself with the cubic rock – salt lattice having face – centred cubic or FCC crystal structure alike sodium chloride that contains an octahedral cation with anion in the middle (**Figure 1.7**). It accommodates stronger carrier transporters, exceeding capability for electrical conduction, higher values of transparency within the visible region on the electro – magnetic scale [20].

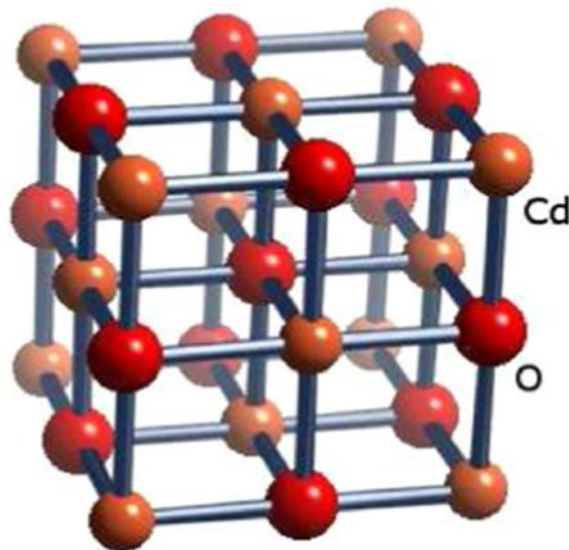


Figure 1.7 Figurative representation for the Cadmium Oxide, CdO.

There are numerous routes to synthesis CdO nano – powders such as; chemical spray – pyrolysis, micro – emulsion, sol – gel, pulsed laser deposition, solvo – thermal and hydro – thermal, electro – chemical deposition, successive ionic layer adsorption and reaction (SILAR),

DC magnetron reactive sputtering, chemical bath deposition (CBD) and chemical vapor deposition (CVD) [21] (Figure 1.8).

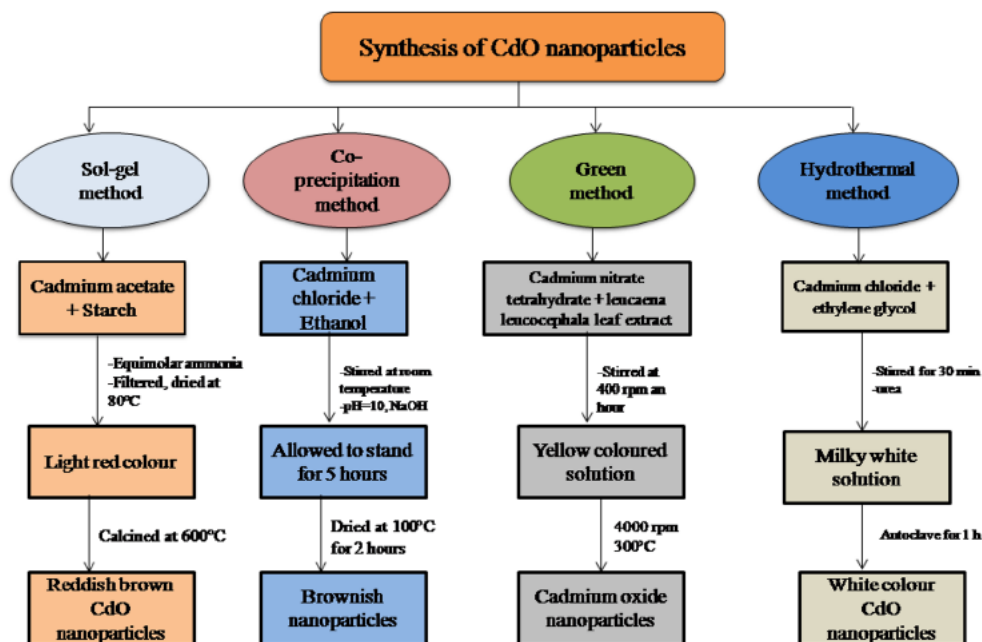


Figure 1.8 Figurative representation for the numerous fabrication processes for CdO nano – powders [22].

CdO is widely utilized in medical, commercial industries but more specifically in the electrical and electronical sectors; in fabrication of semiconductors, used as raw materials in dyes, paints and coating pigments, for the photo – catalytic degradation for the unsafe organic components, solar cells, gas sensors, opto – electronic devices etc [23] (Figure 1.9).

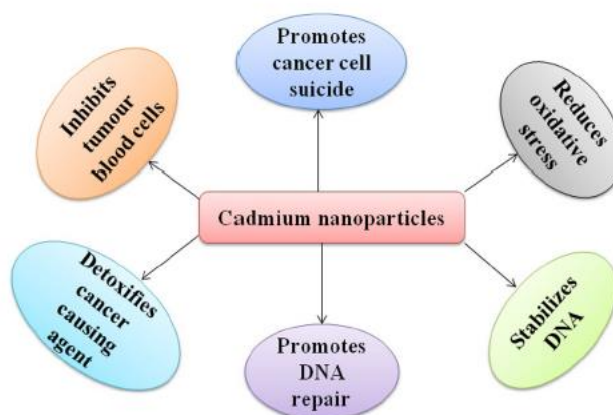


Figure 1.9 Figurative representation for the employment facilities of CdO nano – powders in medical field [22].

1.3 Titanium Dioxide (TiO₂)

Titanium dioxide, TiO₂ has made its presence well celebrated, for experimental and theoretical purview. It's a multifaceted material owing some of the remarkable physical, chemical, magnetic and thermal assets; high photo – preformation efficiency, commendable electron re – combination speed, chemical inertness, high melting point, thermal stability etc. Its employment ranges from capacitors, raw materials for paint pigments, varistors, thermostats, has durability in harsher, rougher environments [24][25]. TiO₂ takes form in three constitutional polymorphisms: (I). Rutile (Metastable Phase having Tetragonal Crystal Structure and Space Group = P4₂ / mnm), (II). Anatase (Thermodynamically Metastable Phase with Slender Tetragonal Crystal Structure and Space Group = I4₁ / amd) and (III). Brookite (Thermodynamically Metastable Phase having Orthorhombic Crystal Structure of Space Group = Pbca). Anatase form of TiO₂ exists at lower temperatures and starts to transmute to the Rutile structure at the temperature 600°C approximately [26][27] (**Figure 1.10**). Both Rutile and Anatase TiO₂ relish their integration in working provinces of the lifestyle; Rutile TiO₂ is mainly applied in the fields requiring higher reflectivity, white paint pigments and opacifiers, its thin films are used in capacitors for having noticeable dielectric constant. Anatase TiO₂ is used for fabrication of nano – structured devices, photo – catalysts etc. Whereas Brookite TiO₂ does not has its utilization in the commercial sectors [28]. Anatase TiO₂ has a broad band – gap around 3.23 eV and also arrays magnificent optical transmittance values both visible and near IR – regions [29][30]. The differences between all three forms of titanium dioxide are represented by (**Figure 1.11**).

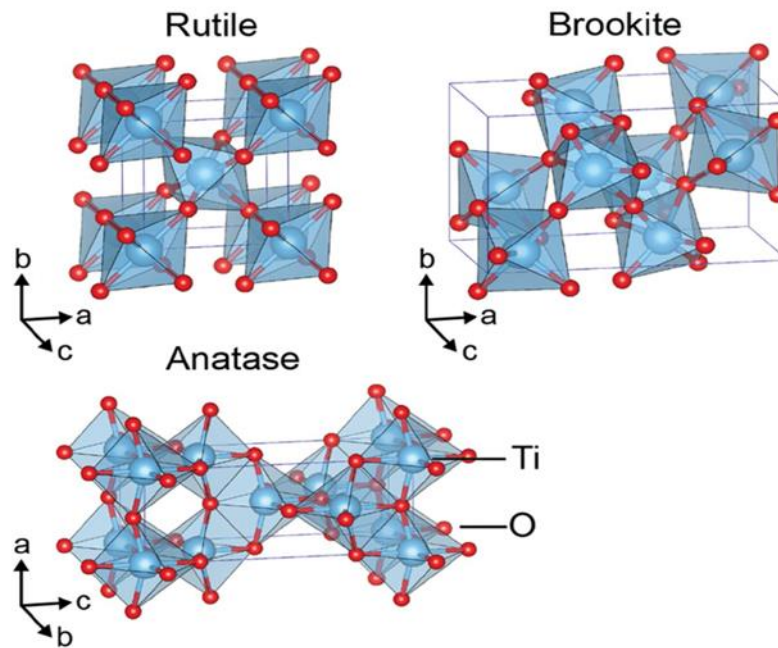


Figure 1.10 Figurative representation for crystalline structures of 3 phases of TiO₂: Rutile, Brookite and Anatase [31]

<i>Rutile TiO₂ Structure</i>	<i>Anatase TiO₂ Structure</i>	<i>Brookite TiO₂ Structure</i>
Tetragonal structure.	Slender tetragonal prisms.	Flat orthorhombic plates.
Has the most uses because of its nature. It has high refractive index, high chemical stability, high specific gravity. It has high melting point of 1825 °C.	Transforms to rutile structure at the beginning of 500 °C (irreversible process).	Has the greatest distortion among all the structures.
Stable phase at ambient temperatures and pressures at <i>microscopic sizes</i> .	Stable phase at <i>nanoscopic sizes</i> .	<i>Least stable</i> and least common structure
Optical band gap ~3.0 eV.	Optical band gap ~3.4 eV.	Optical band gap ~3.3 eV.

Figure 1.11 Figurative representation for the differences between each of the three crystalline structures phases.

TiO₂ nano – powders have made themselves available in disparate ways; environmental cleaning – protection, solar cells for the generation of electric energy and also hydrogen energy, sensors, medical facilities, paper, printing ink, and day – to – day necessities as food colouring agents, sunscreen lotions and other cosmetic products, they are heavily used in paints and coatings industries in the form of white pigments for better stronger thermal stability. They are also employed on in numerous others industrial branches; they are appraised for gas sensing abilities, used in earth sciences, electrical sciences, medical sciences where they are considered for biocompatibility for bone implants and much more [32][33] (**Figure 1.12**).



Figure 1.12 Figurative representation for the varying utilizations of TiO₂ nano – powders in several fields [34].

There are copious procedures for the production of nano – scaled TiO₂; Thin film and spin coating, electrochemical, chemical vapour decomposition (CVD), chemical solvent decomposition (CSD), electrodeposition, thermal treatments (Solvo – Thermal, Ethanol – Thermal, Hydro – Thermal), pulsed – laser deposition and various other sol – gel Methods [35][36].

1.4 Polyaniline (PANI)

As the varistor devices are cementing their presence in day-to-day activities, various other materials are being explored for the fabrication of a better sensing equipment. One of the domains in the world of the materials that are been excessively studied on are Polymers and amid them comes the name Polyaniline, PANI which is the conducting form of the polymers. Polyaniline are formed by the repetition of aniline monomers. These are the non – complex aromatic amines having formula $C_6H_5NH_2$ (**Figure 1.13**).

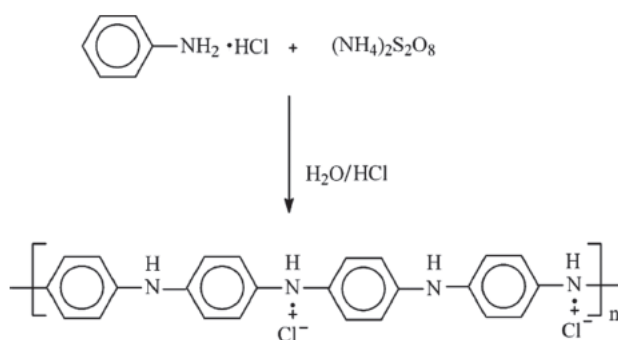


Figure 1.13 Figurative representation for the transformation of aniline monomer in polyaniline polymer in the presence of HCl and ammonium Persulfate, $(\text{NH}_4)_2\text{S}_2\text{O}_8$ [37].

PANI benefits from its inert nature as it possesses stronger chemical and environmental solidity over longer periods of time, simpler and cost – efficient routes for its fabrications, capability to form affinities with metal – oxides and ceramics, it allocates the availability to be worked with at room temperatures, its distinctive electrical and opto-electrical properties, inexpensive monomer, higher sensitivity values, reversible process, fast response time etc. all leading up to its potential for a better material [38][39][40][41]. This conducting polymer (**Figure 1.14**) are also used in sensors because they can be functionalized at room temperatures whilst inorganic sensors function only at certain elevated temperatures. It also exhibits stronger reactivity regarding humidity and gases as they have porous nature. They are light weighted chemical with flexibility [42].

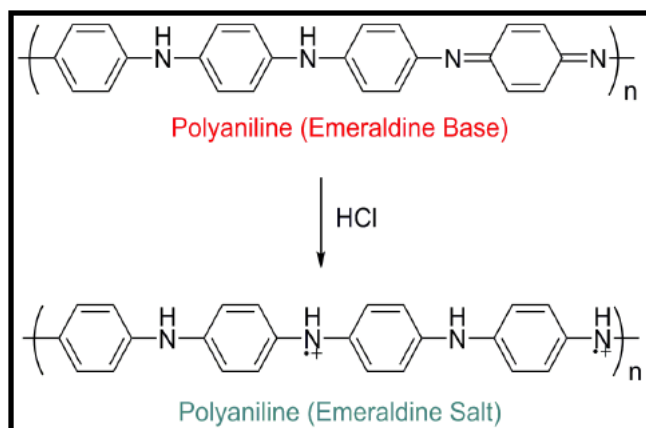


Figure 1.14 Figurative representation for the conversion of polymer into the conductive form through the process of protonation [43].

It has its usages in various potential industries, for example: commercial sectors, electrical – electronical units, secondary batteries, photovoltaic devices, micro-electronic devices memory device, biological sensors, gas sensors etc (**Figure 1.15**). Various synthetization methods are used to obtain PANI: electro – chemical and oxidative polymerization reactions, chemical and electrochemical deposition, spin coating etc [44][45].

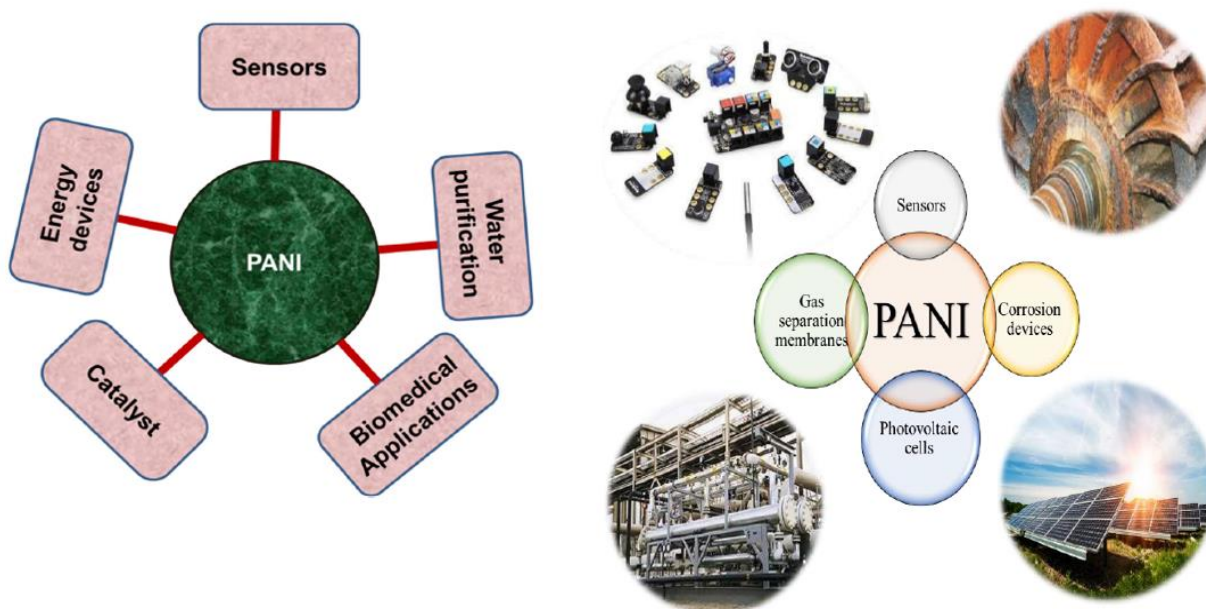


Figure 1.15 Figurative representation for the applications domains of polyaniline [46][47].

1.5 Silver (Ag)

Metal – oxide semiconductors or polymers, even though they possess abundance of distinctive properties under its name, lags behind to match the momentum and needs demanded in the continuously developing sectors of research, when used individually and hence the mixing and doping of materials comes into play. Incorporation of foreign materials, has proved to elevate the working mechanism of the host materials. Crystal phase and surface area are the vitals, when manipulating the physical attributes of the semiconducting material. Defined crystal structure influences the rate of reactions, re – combination rate, facilitating with compelling oxidizing and reducing powers whereas the surface areas provide with the betterment of the reactions and interactions of the molecules and faster adsorption rates [48][49]. Metallic nano – powders, due to their notable structure alignment and characteristics, have been successful dopants. They inherently have atypical physico – chemical nature and because of the definite shape – size and distribution of the molecules, they are made use in build – ups of nano – ranged devices [5][50] (**Figure 1.16**).

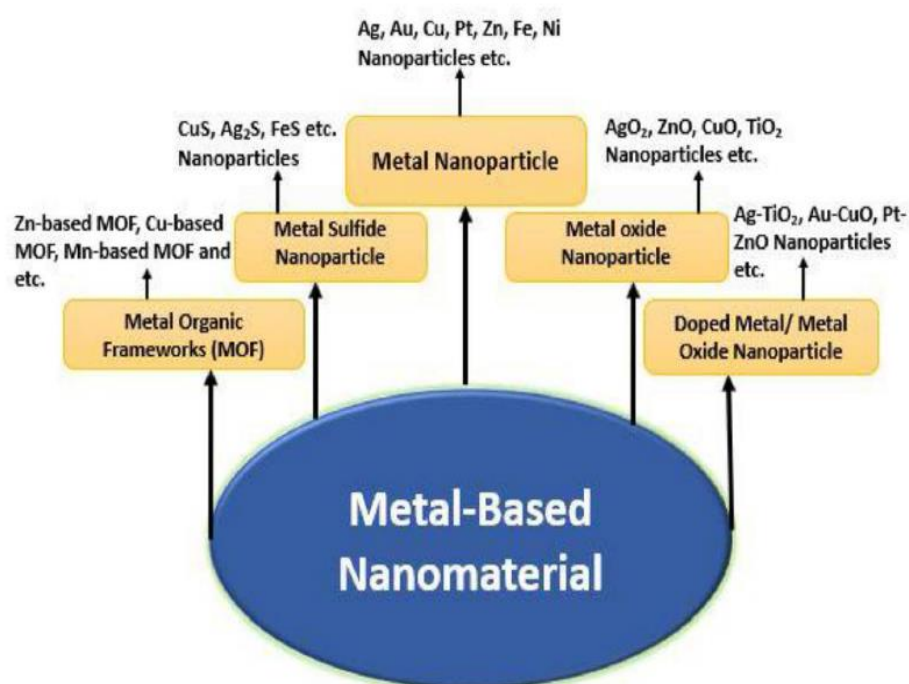


Figure 1.16 Figurative representation for the classifications of metallic nano – powders [51].

Silver nano – powders have very prominent electrically conductive nature and defined arrangement of atoms. They are cost – effective, have easy synthesis and the fabrication process can be controlled through external terms and needs room temperature. They comprise of unique traits; atypical chemical, biological and physical characteristics, high thermal and electrical conductivity, surface – enhanced Raman scattering, non – linear optical nature, chemical solidity. These properties are by the reason of its crystal network, morphology and dimensions of the Ag – nano – particles. These nano – powders are fully taken advantage of, they are pre – dominantly utilized in every discipline possible; commercial arenas, industrial sectors, used as edible decorative measures in food sectors, in medical firms they uphold a strong foot, coatings for medical equipments, biomedical devices, anti – cancer agents, anti – bacterial facets, pharmaceutical, they are as well employed in keyboards, textiles and electrical circuits (**Figure 1.17**). There is a dire necessity to prepare the nano – particles via uncomplicated and constructive methods so as to have as well command over their shape and sizes. Ag – nano – powders can be obtained by the means of many mechanical and chemical procedures, such as; electro – chemical method, photo – chemical reaction, micro – wave assisted reaction, chemical reduction, Burst method [52][53][54][55].

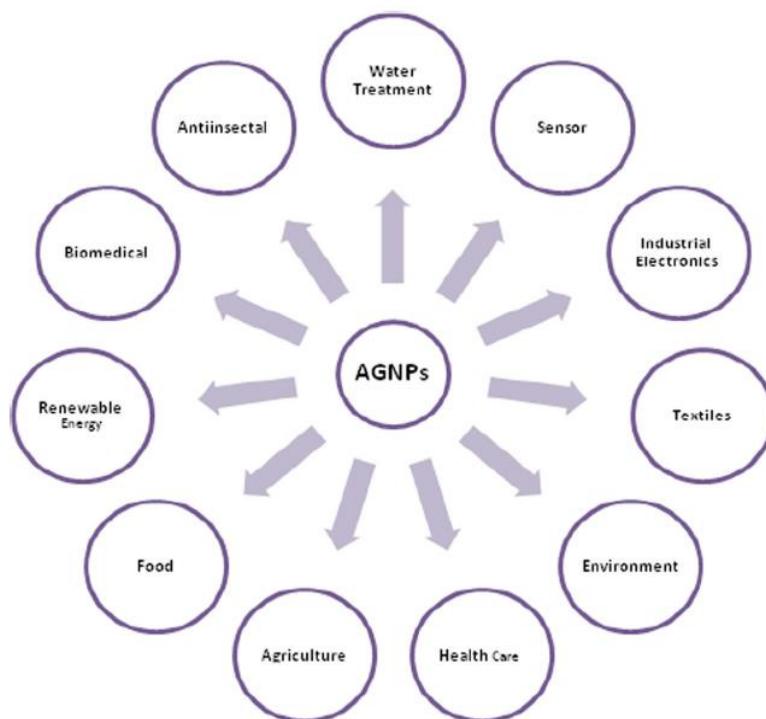


Figure 1.17 Figurative representation for the uses of silver nano – structured powders [56].

1.6 Reduced Graphene Oxide (rGO)

The selection of the materials for the fabrication of devices, has an undeviating impression on its applicational purposes. And with the pace of developments, search for the newer kinds of materials also rises. Carbon dominated networks are a no – shy factor and graphene and its derivatives are the prime example of it. Graphene is a two – dimensional system that has enjoyed recognition in the arena of material and appliance build-up. Graphite oxide (GO) or Graphitic Oxide in simple words can be explained as a set of functionalized graphene sheets that has constituents of carbon, oxygen (– containing functional groups; epoxy (– COC), hydroxyl (–OH), and carboxyl groups (– COOH)) and hydrogen atoms on its surface [57]. Graphene has a two-dimensional honeycomb monolayer structure comprising of sp^2 – bonded carbon atoms. This material can be used as a precursor for graphene itself. Graphene and its derivatives (GO, rGO) brags of the fact that it is the only 2 – D material that is been studied vigorously for its applications in broader range of industrial sectors. It has high electron mobility at room temperature, large surface to volume ratio, high specific area (**Figure 1.18**).

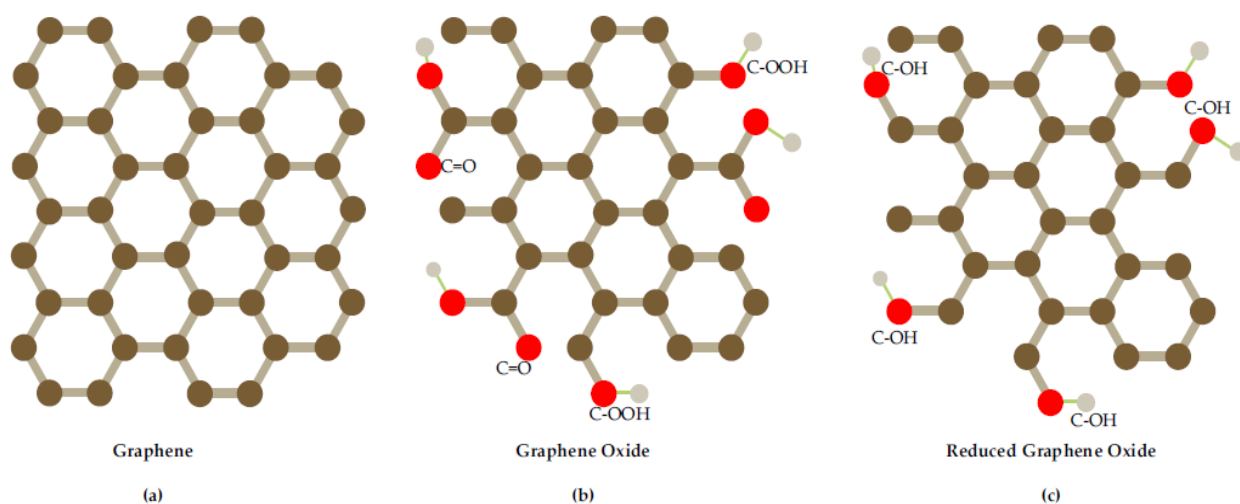


Figure 1.18 Figurative representation for the sp^2 – hybridised carbon derivatives: (a) Graphene, (b) Graphene Oxide and (c) Reduced Graphene Oxide [58].

Graphene and its derivatives (GO, rGO) has garnered colossal recognition in fields of biological/ chemical sensors, electronics/ opto-electronics, humidity detection etc. because of its unique physical, mechanical, electrical, thermal conductivity nature, high conductivity. Reduced graphene oxide (rGO) is one of the graphene derivatives. It is classified as an

interesting one of its kind of material. rGO has oxygen-containing functional groups such as -COOH and -OH on the surface [59][60].

Graphene can be obtained from graphite using by chemical vapor deposition (CVD), mechanical or chemical method whilst Graphene oxide is obtained by hummers method and further oxidation of the obtained product leads to reduced graphene oxide [61]. Graphene oxide (GO) and Reduced Graphene Oxide (rGO) illustrates exceptional performances as: ultrahigh sensitivity, ultrafast response time, light weight, easy fabrication, ultrahigh sensitivity, low hysteresis, fast response/recovery time, excellent repeatability and good long-term stability. Few of its application examples are: electronics, bio-medical, energy storage, super-capacitor [62] (Figure 1.19).

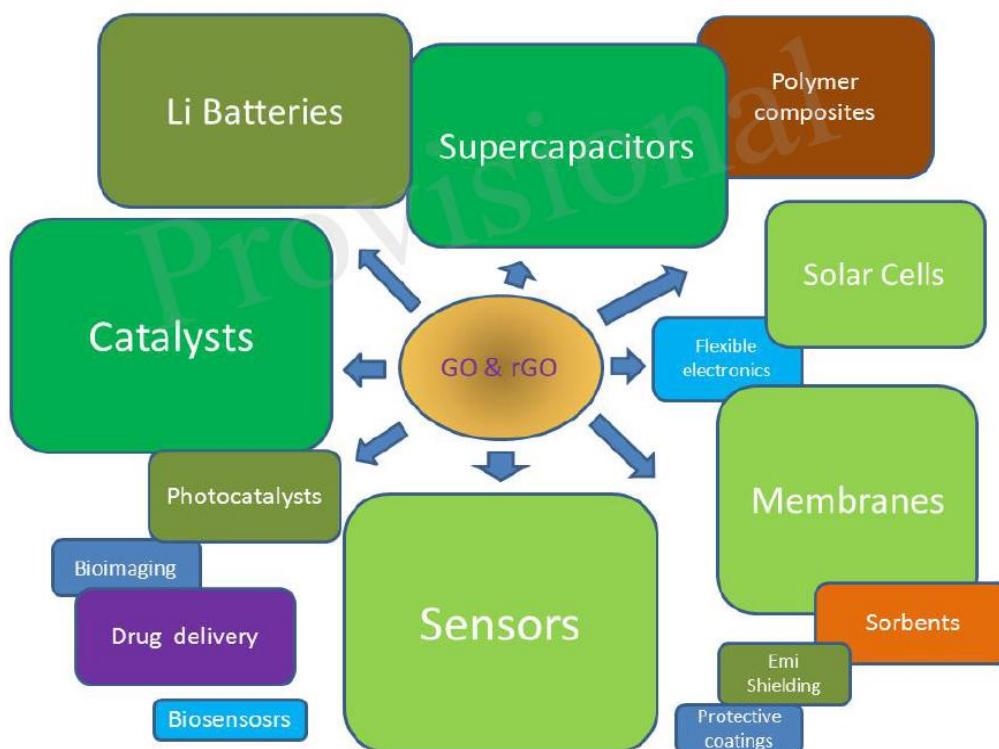


Figure 1.19 Figurative representation for utilisations domains of Graphene Oxide and Reduced Graphene Oxide [63].

1.7 Varistor

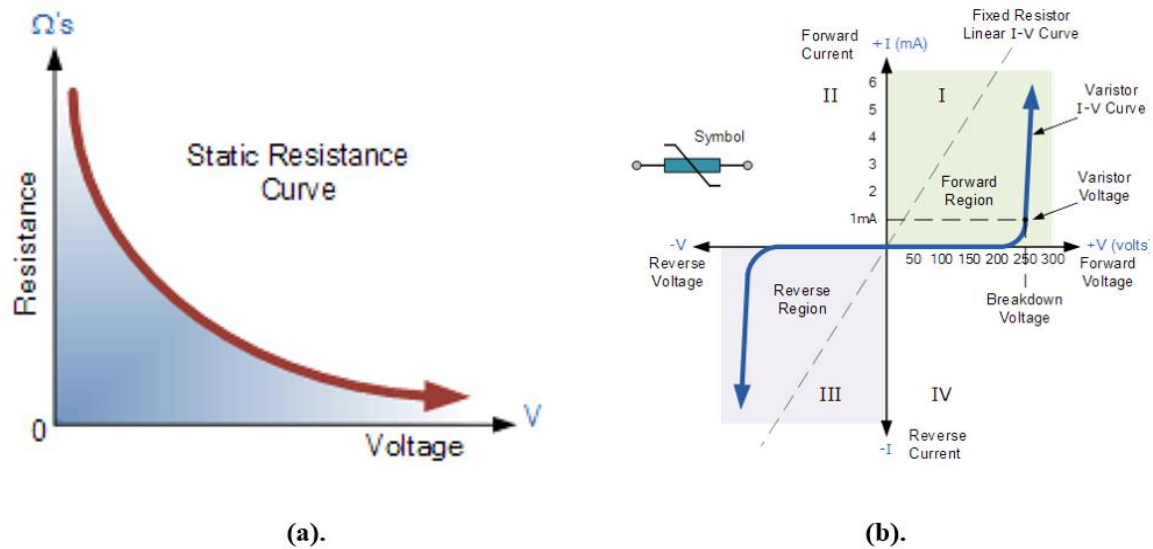
The integration of the nano – dimensional materials has seen a sustainable progress throughout the years, novel materials and incorporation of different kinds are demanded for, as the industrial machinery sees an advancement in the terms of technology. The applicational domains for these materials have broadened now as well, from space and aviation, optics, solar – industries, automotive engineering, thermo – electric equipments, to medical sectors and even cosmetic and skin – care products. In electronics, nano – materials also share an appreciable fascination. They are utilized in the construction of lasers, batteries, fuel – cells, chips, lighting and displays etc. One such important constituent of / in and electrical circuit is varistor.

Varistors are the electrical appliances that regulates a curb on the transient voltage whilst its operation. They are used as protective measurements in the electrical circuits, as they shut down the system when a specific value is surpassed, hence saving the whole unit from short – circuiting or catching fires. And because of this factor they are recognize with their other tags; surge suppressers, non – linear resistor / voltage sensor, voltage regulators / arrestors. They are competent to function over a larger – scale of voltage values. And therefore, their capabilities and functionality can be modulated in terms of size and voltage value as per the demand of the tool i.e., they can be used from higher voltage systems to modest voltage valued set – ups as well. They are effectively exercised in many industrial and domestic gadgets and devices; mobile phones, cameras, LED's, TV's, computers, notebooks, laptops, doorbells, smart house gadgets etc. They can work on both DC and AC and are capable of absorbing and supressing both the positive and negative transient values. Varistor mechanism and structure necessitates inclusion of foreign materials to elevate its working conditions. They have poly – crystalline micro structure which is a crucial need for the existence of the Varistor – Effect [64][65].

- Structures and Working Mechanisms.

Varistor is an electro – ceramic device that is the blend of the words VARI-able resi-STOR. It is dependent on the voltage and exhibits non – linear behaviour with respect to the resistance values. The resistance decreases with the increase in the voltage and in case of excessive voltage increase, the resistance shows a steep decline. It consists of an ohmic and non – ohmic region depending on its behavioural aspects under certain conditions. In the pre – breakdown

area it follows the ohm's law whereas in the breakdown area, the resistance sees a dramatic drop. Now due to this kind of deformation, it is associated with the properties indicated because of the grain boundaries present. And thus, making them suitable as the protective measurements against the extreme voltage surges [66] (**Figure 1.20**).



When the voltage across the varistor exceeds the varistor threshold value, its effective resistance decreases strongly with an increasing voltage.

I-V curves of a varistor is not a straight line as very small changes of voltage cause a significant change in the value of the current.

Figure 1.20 Figurative representation for (a) Voltage-Resistance Curve and (b) Voltage-Current Curve.

Varistors, unlike their peers Zener – diode operating on single junctions, are actually multi – junctional devices. Their working prospects mainly depend on the factors; grain boundaries and Schottky barriers. Their electrical nature is governed through interface state of the grain boundaries existing within them. The varistor incorporates of the inter – granular non – conductive grains and the conductive grain layers. Now, as mentioned there are linear and non – linear approach of the varistor and the non – linear behaviour depends on the potential barrier formed at the grain boundaries. Schottky barrier, the potential barrier is created because the electrons present at the grain boundaries are confined. Simply put, consecutive Zener diodes are formed at the grain boundaries due to the attenuated inter – granular layers between the molecular grains. Because to this structure build up, the potential barrier obstructs the charge carriers and thus decreasing the movements of such carriers [65]. The junction formed because of the Schottky barrier is Schottky junction, which is explained as the junction created at the

immediate contact between the semi – conductor and metal. This kind of structural behaviour sees its uses in the likes of; rectifiers, integrated circuits, microwave mixers, MESFEST etc [67].

- Requirements for a varistor.

A varistor is considered a functional liability when it compromises of the following factors:

- (I) Stronger energy absorption capacity.
- (II) Availability at lower prices.
- (III) Higher threshold voltage to withstand all kinds of stresses; environmental and manual or within the system.
- (IV) The prospects of mass production at the industrial scale.
- (V) Has slow aging process.
- (VI) Positive approach towards the thermal, electrical, mechanical and chemical stress [68].

- Applicational areas.

Varistor has applications as a protector of the electrical/ electronical appliances as: Telephone and communication line protection, Radio communication equipment transient suppression, Cable TV system surge protectors, Power supply protection, Microprocessor protection, Low voltage board level protection, Car electronics protection, Industrial high energy AC protection etc. They are employed on in electrical circuits as to safe guard the electrical circuits and as protective measures against sudden surges in the AC and DC motors, as they are highly sensitive towards the voltage changes (**Figure 1.21**).

Their applicational view of point is not limited to any specific spectrum rather, they have broad spectrum;

- (I) Low voltage varistors – fire protection system, house systems, garage alarms.
- (II) High voltage varistors – This is used in the circuits for the protection purposes. As it shuts down the circuit system, when a certain value of voltage is acquired and saves the system from short circuiting.

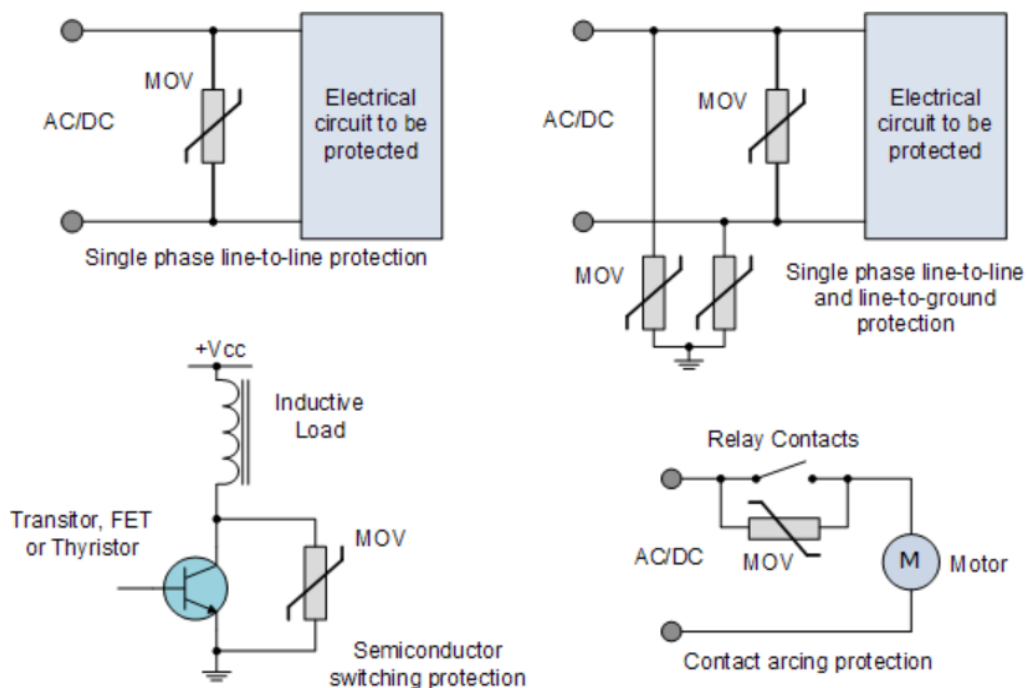


Figure 1.21 Figurative representation for uses of varistors as surge protector in different types of circuits and formats.

1.8 Chemicals and Reagents used

Copper Oxide, CuO : Copper (II) Nitrate Trihydrate ($Cu(NO_3)_2 \cdot 3H_2O$) (AR/ACS grade 99.5%, Central Drug House (P) Ltd.), Polyvinyl Alcohol (PVA, $(C_2H_4O)_n$) (AR grade, Loba Chemie Pvt. Ltd.), distilled water.

Cadmium Oxide, CdO : Cadmium Nitrate Tetrahydrate ($Cd(NO_3)_2 \cdot 4H_2O$), (AR grade 99%, MOLYCHEM), Absolute Ethanol (C_2H_5OH) (AR grade 99.9%, Suzhou Yacoo Laboratories), Polyvinyl Alcohol (PVA, $(C_2H_4O)_n$) (AR grade, Loba Chemie Pvt. Ltd.), distilled water.

Titanium Dioxide, TiO_2 (Anatase): Titanium Tetra-isopropoxide (TTIP, $C_{12}H_{28}O_4Ti$) (AR grade, Spectrochem Pvt. Ltd. Mumbai, India), Iso – Propyl Alcohol ($(CH_3)_2CHOH$) (AR grade 99.5%, MOLYCHEM), Hydrochloric Acid (HCl) (AR grade, Loba Chemie Pvt. Ltd.), distilled water.

Polyaniline, PANI: Aniline ($C_6H_5NH_2$) (AR grade 99.5%, MOLYCHEM), Ammonium Persulphate ($(NH_4)_2S_2O_8$) (AR grade 98%, Central Drug House (P) Ltd.), Hydrochloric Acid (HCl) (AR grade, Loba Chemie Pvt. Ltd.), distilled water.

Silver Nanoparticles, Ag-nanopowders: Sodium Borohydride ($NaBH_4$) (AR grade 98.00-102%, HIMEDIA), Silver Nitrate ($AgNO_3$) (AR grade 99.9%, MOLYCHEM), Ice bath.

Reduced Graphene Oxide, rGO: Graphite powder (AR grade $< 20 \mu m$, SIGMA – ALDRICH), Hydrogen Peroxide (H_2O_2) (AR grade 30% W/V solution, MOLYCHEM), Sulphuric Acid (H_2SO_4) (AR grade 98%, Loba Chemie Pvt. Ltd.), Hydrochloric Acid (HCl) (AR grade, Loba Chemie Pvt. Ltd.), Potassium Permanganate ($KMnO_4$) (AR/ACS grade 99.5-100.5%, Central Drug House (P) Ltd.), Hydrazine Hydrate ($NH_2NH_2H_2O$) (AR grade 80%, MOLYCHEM), Ammonia Solution (NH_3) (AR/ACS grade, Central Drug House (P) Ltd.), distilled water.

1.9 Materials under present investigation

The research work done on the topic of varistor is copious but limits itself to only ZnO with addition of ferrites therefore, the present work focuses on newer categories of materials for their structural and varistor characteristics. The present work studies the methodical analysis of the structural and the electrical properties of the individual as well as the composites of the semiconducting metal oxides (CuO, CdO, TiO_2 – anatase), polymer (PANI), metallic nanopowders (Ag) and graphene derivative (rGO) through varying compositions. The materials for the present investigation are:

(i) Objective 1 – CuO + Ag

Sample Code	Composition	Elemental Ratio
CA1	CuO	1 : 0
CA2	CuO + Ag	1 : 1
CA3	CuO + Ag	1 : 2
CA4	Ag	0 : 1

(ii) Objective 2 – PANI + CdO

Sample Code	Composition	Elemental Ratio
PC1	PANI	1 : 0
PC2	PANI + CdO	1 : 1
PC3	PANI + CdO	1 : 2
PC4	CdO	0 : 1

(iii) Objective 3 – TiO₂ + Ag

Sample Code	Composition	Elemental Ratio
TA1	TiO ₂	1 : 0
TA2	TiO ₂ + Ag	3 : 1
TA3	TiO ₂ + Ag	1 : 1
TA4	Ag	0 : 1

(iv) Objective 4 – rGO + Ag

Sample Code	Composition	Elemental Ratio
RA1	rGO	1 : 0
RA2	rGO + Ag	3 : 1
RA3	rGO + Ag	1 : 1
RA4	Ag	0 : 1

1.10 Research Gap

The foremost applicational purpose of varistors is to protect the circuit from short – circuiting and catching fires. These devices undergo incessant flow of voltage which furthermore leads to the leakage current, initially in smaller values. But as the time goes, the varistor commences to show decline in its working system as thus results in gradual and increased amounts of leakage currents. This results into the thermal degradation of device and as a consequence shortens the working life of the device. Therefore, newer materials are now needed to be researched on to solve such occurring problems [69].

In the past, research has been extensively and solely focused on ZnO with the addition of ferrites. The raw materials for such are expensive and need extremely high temperatures for

the sintering and calcination purposes as well. These materials are not much of good electrical conductors thus leading to lesser life time of the devices. Some chemicals are expensive to acquire and also the synthesis processes for obtaining such materials are as well time consuming. Moreover, there is very less independent research done in the field of varistors using other semi-conducting materials, polymer and graphene derivatives without the usage of ZnO. Furthermore, the area of varistors that has been studied majorly has dealt with only higher values of voltage and current. The areas where varistors were used at larger scale concerning the electrical circuits where higher amounts of currents and voltages flow, for example; industries where the varistors are used as surge-suppressers for the whole building. However, the sectors with usage of low voltage varistors have not been studied thoroughly. This category of varistors is employed in smaller scale circuits such as; smart house devices, smart switches, sensors etc, where the flow of current and voltages are comparably less where varistors act as voltage arrestor for a certain appliance, sensor or switch rather in contrast to high scales industrial circuits. In simpler words, as opposed to the varistors that are used in industries where the burden of whole building falls upon on the varistors where the electrical circuits amass larger volumes of current-voltage values, the present work deals with varistors that are used in the circuits of appliances or sensors where smaller values of current – voltages occur. Work on small scaled industrial sectors of varistors has not been done intensively.

The present work focuses on studying newer domain of materials that demonstrates stronger thermal withstanding capability, good electrical conductivity values to withhold recognisable amounts of voltage and current before the system gets shut down. The system is studied on metallic nanopowders, semi – conducting metal oxides with conducting polymer and graphene derivative. The raw materials are cheap, affordable and available moreover, the synthesis processes also include easy fabricating procedures with lower temperatures required for the calcinations. These materials have been studied to be better electrical conductors and are presently widely used for anti – bacterial properties which will help with elongated functionality periods of the appliances. These afore – mentioned materials have higher melting temperatures i.e., stronger thermal stability, are prepared via non – complex synthesis routes and have robust strength which lengthens the working life period of the device. These qualities make them candidates as raw materials in the fabrication of varistor devices.

1.11 Objectives of the present work

The aims of the present work are to investigate the varistor properties of the semiconducting metal oxides, polyaniline, silver and reduced graphene oxide independently and in amalgam with one another. The studies are done to investigate the capacity of nano – composite materials with regards to how much amounts of voltage and current they can withstand before reaching the saturation point for the sample matrix.

The objectives of the present research work include the studying of the following:

- (i) Varistor properties [current-voltage graph] of Copper (II) Oxide (CuO) and Silver (Ag) Nanopowders nano-composites.
- (ii) Varistor properties [current-voltage graph] of Polyaniline (PANI) and Cadmium Oxide (CdO) nanocomposites.
- (iii) Varistor properties [current-voltage graph] of Titanium Dioxide (TiO₂-anatase form) and Silver (Ag) nanocomposites.
- (iv) Varistor properties [current-voltage graph] of Reduced Graphene Oxide (rGO) and Silver (Ag) nanocomposites.

1.12 Purpose of the present work

With the background mentioned above, the purpose of the present work incorporates:

- (i) The values for current and voltage that the system can hold before shutting down or exhibiting saturation has been tried to increase.
- (ii) The efforts have been done to recognise and expand the categories of materials considered for the studies of varistor properties.
- (iii) Copper oxide and Cadmium oxide have been synthesised using sol – gel auto combustion method, anatase form of Titanium dioxide has been obtained through ultra – sonic assisted sol – gel technique. Top – down method has been employed on for silver nanopowders and polyaniline has been acquired with oxidative polymerisation method. Reduced graphene oxide has been procured using modified hummer’s method.

- (iv) The structural studies have been through X – Ray Diffraction (XRD) and Fourier Transform Infra – Red Spectroscopy (FTIR). The Raman Spectrum has done for the molecular analysis. Field Emission Scanning Electron Microscopy (FESEM), Energy Dispersive X – Ray (EDX) and Particle Size Analysis (PSA) has been investigated for surface and elemental details. The varistor studies has been conducted through current versus voltage plot.

1.13 Future Scope of the present work

The integration of the nano – dimensional materials has seen a sustainable progress throughout the years, novel materials and incorporation of different kinds are demanded for, as the industrial machinery sees an advancement in the terms of technology. The applicational domains for these materials have broadened now as well, from space and aviation, optics, solar – industries, automotive engineering, thermo – electric equipments, to medical sectors and even cosmetic and skin – care products. In electronics, nano – materials also share an appreciable fascination. They are utilized in the construction of lasers, batteries, fuel – cells, chips, lighting and displays etc. One such important constituent of/in and electrical circuit is varistor.

Varistors are the electrical appliances that regulates a curb on the transient voltage whilst its operation. They are used as protective measurements in the electrical circuits, as they shut down the system when a specific value is surpassed, hence saving the whole unit from short – circuiting or catching fires. And because of this factor they are recognize with their other tags; surge suppressers, non – linear resistor/voltage sensor, voltage regulators/arrestors.

They are competent to function over a larger – scale of voltage values. And therefore, their capabilities and functionality can be modulated in terms of size and voltage value as per the demand of the tool i.e., they can be used from higher voltage systems to modest voltage valued set – ups as well. They are effectively exercised in many industrial and domestic gadgets and devices; mobile phones, cameras, LED's, TV's, computers, notebooks, laptops, doorbells, smart house gadgets etc. They can work on both DC and AC and are capable of absorbing and suppressing both the positive and negative transient values. Varistor mechanism and structure necessitates inclusion of foreign materials to elevate its working conditions. They have poly –

Chapter 1. *Introduction*

crystalline micro structure which is a crucial need for the existence of the Varistor – Effect [65][64].

Chapter 2

2 LITERATURE REVIEW

Singhal *et al.* [2012] studied the DC electrical resistivity response, the structural characterisations and synthesis process for ZnO nanopowders; pure and doped with Cu in varying percentiles i.e., 5, 10, 15, 20, 25 and 30 at% Cu. The incline of the Cu nanopowders decreased the values for both the resistivity and activation energy. The activation energy gave values from ~ 0.67 eV for pure ZnO to ~ 0.41 eV for ZnO doped with 30 at% Cu content. The co – precipitation method was employed on to acquire the aforementioned nanopowders. A broad absorption band for Zn – O bond stretching was obtained at ~ 490 cm^{-1} which was confirmed through FTIR. Though the CuO peaks in 10 at% Cu solution were insignificantly apparent nonetheless, Powder XRD exhibited the peaks for ZnO and the structured doping of Cu up to 10 at% Cu sample composites. In the proceeding sample composites, the Cu peaks adjacent to CuO was confirmed with formation of separate secondary phases of CuO. A Quasi – spherical structural was observed using TEM analysis [70].

Cho *et al.* [2004] synthesised polyaniline (PANI) nanoparticles by disseminating them in the aqueous solution which were arranged with the utilization of polyvinyl alcohol (PVA) and poly (styrene sulphonic acid) (PSSA) which were further used as polymer stabilizers. The PVA based sample composite films were made with PANI – PSSA (PANI – PSSA/PVA) and PANI – HCl (PANI – HCl/PVA) for varying compositions of PANI. These were further procured by employing castor method to study the electrical conductivities of the said samples. The sample composite of PANI – PSSA (PANI – PSSA/PVA) exhibited an increase in the electrical conductivity beyond the threshold value as compared to PANI – HCl (PANI – HCl/PVA) composite because the percolation threshold value for conductivity was obtained around 10 wt.% of PANI for PANI – PSSA (PANI – PSSA/PVA) solution. UV – visible spectrometer also showed an increased value for the doping level for PANI – PSSA (PANI – PSSA/PVA) sample. The spherical structure was obtained for PANI prepared by both the solutions, with PANI – PSSA (PANI – PSSA/PVA) giving nanopowders of size 50 nm along with uniform

distribution whereas a diameter of 150 nm was observed for the PANI – HCl (PANI – HCl/PVA) sample [71].

Karthik *et al.* [2010] used sol – gel method to synthesis anatase form of TiO₂ nanoparticles and used Ni – doping to study the structural impact, optical properties and electrical response of the said nanopowders. The tetragonal structure was obtained through powder XRD which corresponds to the anatase TiO₂. A crystallite size of 14 nm was acquired through TEM. The dielectric loss, $\tan \delta$ and dielectric constant, ϵ' revealed a prominent frequency dependency in the frequency scale of 42 Hz to 5 MHz at room temperature. This behaviour was observed for the composite samples with varying levels of doping. At lower frequency scale, higher values for dielectric constant were obtained because of the production of the interfacial polarization which furthermore, were the resultant of the accumulation of mobile charge transporters at grain boundary. The frequency dependence of dielectric losses for the primal relaxation operations disclosed an asymmetrical structure. The AC – conductivity analysis showed the decline in the conductivity values with the increase of the Ni – dopant level for the composite samples [72].

Ma *et al.* [2008] studied the enhancement of electrical conductivity of carbon nanotubes, CNTs with the addition of silver nanopowders, Ag – NPs. The CNTs were put into operation through ball mining method in the company of ammonium bicarbonate, which were further followed by the reduction process of silver ions in N, N – dimethylformamide and as a result silver decorated CNT's, Ag@CNTs were fabricated. Next, electrically conductive composites of polymer were produced by applying the Ag@CNTs obtained as the conducting filler in the epoxy resin. The mechanical, electrical and thermal characteristics of pure and functionalised CNTs were studied with comparisons to the aforementioned composites. The results showed that at pH ~ 6, the highly dispersed Ag nanoparticles could feasibly decorate the CNT's. The electrical conductivity of the 0.10 wt.% of Ag@CNTs sample composites were observed to be greater than the four order of magnitude, which were higher as compared to the pure and functionalised CNT consisting of the same content [73].

Alshehri *et al.* [2012] showed an amplification in the values of electrical conductivity up to frequency scale of 220 GHz, for the silver nanopowders (*n*Ag) that were obtained through screen – printing at lower temperatures. It was observed that the electrical losses in the co –

planar waveguide structures procured through *n*Ag has lower values at 350°C temperature and frequency > 80 GHz, in comparison to the counterpart thick film Ag – Nano sized conductors synthesised at 850°C. This upgraded electrical production was the resultant of the superior packing of the Ag – NPs, which furthermore lessened the roughness of the surface amounting by the factor of 3. The work discussed the applicational forefront of the silver nanopowders in the arena of temperature sensitive substrates with sub – THz metamaterials at higher frequency spectrum [50].

Vidyasagar *et al.* [2011] used one – step mechano – mechanical procedure called solid state reaction synthesis process in the attendance of poly – ethylene glycol 400 for the preparation of the semi – conducting nanopowders, individually and when doped with copper; ZnO, CuO, CdO, Cu – ZnO, Cu – CdO. In this method, they proceeded with physical size reduction of the sample materials through grinding them in desired nanoscale scale via both conventional and chemical ways. This paper aimed to study the effect of temperature on the optical properties of the aforementioned samples. The applicational prospects considered were; photovoltaic cells and higher absorbance values in case of solar energy. The Cu – ZnO composite gave 3.28 eV as the value for band gap whereas, Cu – CdO gave the value in the range of 2.80–2.21 eV. The prepared samples were studied for their structural confirmation using XRD, FTIR and FESEM – EDAX and UV – vis absorption spectra was done to study the optical properties. The XRD results obtained showed that the values of the band gap energy values showed a decline as the annealing temperatures of the samples were increased, which led to the enhanced crystallinity of the sample powders. This observation was attributed to the fact that the doping of Cu made the lattice constants change its values to a specific extent [74].

Pourbeyram *et al.* [2019] prepared the fabricated a non-enzymatic glucose sensor for the detection of glucose that was a pencil-based graphite electrode (PGE) which was further enhanced using a composite of modified by copper oxide nanoparticles decorated with reduced graphene oxide (CuO (NP) / rGO – PGE). Improved Hummer’s Method was used for the synthesis of GO powders and the rGO – PEG was prepared by putting the PEG in the GO suspension and further reducing it for obtaining the rGO – PEG sample. The XRD results showed that GO was electrochemically reduced and gave confirmation regarding the formation of CuO on the surface of PEG. A nano – porous structure was confirmed through SEM analysis and TEM showed the homogeneous formation of CuO on rGO that exhibited semi – spherical

shape following the diameter scale range of 3 – 5 nm. The samples exhibited that immobilized CuO nanopowders displayed a stronger stability in the alkaline solutions with higher electro – catalytic values towards the glucose oxidation. The values were obtained using amperometry in the detection limit of 0.091 (± 0.003) μM and 4760 (± 3.2) $\mu\text{AmM}^{-1} \text{cm}^{-2}$ for concentration sensitivity. The showed their candidacy in the applicational sectors where the concentration of glucose determination needs to be done in the human blood [75].

Baturay *et al.* [2017] investigated the n – type conduction for the pristine and Cobalt, Co metal doped CuO thin films. The sample were prepared using spin – coating technique and the procured thin films were studied for their structural and electrical framework through Van der Pauw Hall measurement system. XRD exhibited the impact on the structure of CuO thin films because of the varying concentration ratios. The transmutation of the conductivity by 3% of cobalt doped content was obtained. UV – Spectroscopy in the wavelength scale of 300 – 1100 nm was used for analysing the effects of doping the metal on the optical band gap width and the values for optical band gaps were obtained around 1.43 eV, 1.44 eV, 1.44 eV and 1.42 eV for un – doped and 2 %, 4%, 6% Co doped – CuO thin films respectively [76].

Dang *et al.* [2011] used chemical reduction technique to synthesis colloidal samples for nano – sized Copper using water and ethylene glycol, EG. The difference in the impact of using the aforementioned solvents and surfactants on copper was investigated through XRD, UV – spectroscopy and TEM. The results for surface plasmon resonance were taken immediately after the synthesis process and it was obtained around 551 nm and 579 nm for colloidal copper in EG and water respectively. Also, the stability factor for the colloidal copper in ethylene glycol was observed to be longer as compared to water. The sample solution in water changed its colour from lighter – red to black and after time period of 22 days, precipitation took place which was associated with the oxidation process of copper in copper (I) oxide and it was further confirmed using optical absorption measurements. Whereas, the sample solution in EG had red colour attributed to it and it displayed a stability even after 2 months. In this work, polyvinyl pyrrolidone was used to control size and to also act as a polymeric capping agent. This prevents the nuclei from the production of polar groups agglomeration, because the copper nanoparticles get effectively absorbed on the surface forming coordination bonds. The capability of ascorbic acids to find available radicals and reactive oxygen molecules helps with its anti – oxidant properties for the colloidal copper samples [77].

Thema et al. [2015] used certain specific tools to understand the nature of the molecular bonding and structural nature of the CdO nanopowders. X – Ray Diffraction (XRD) was used to obtain the structural build – up and as well the lattice parameters of the nanopowders. The vibrational properties were studied using Attenuated Total Reflection - Fourier Transform Infrared spectroscopy (ATR-FTIR). The molecular level analysis was done via Raman Spectroscopy and the surface and elemental ration analysis was done using High Resolution Scanning Electron Microscopy (HRSEM), X – Rays Fluorescence (XRF) and Energy Dispersive X – Ray Spectroscopy (EDS). This paper opted on preparing the CdO nanopowders via a non – toxic and green route using plant extract namely; *Agathosma betulina* which was to be used as an effective agent for bio – reduction and bio – oxidation processes [78].

Ranjithkumar et al. [2016] studied the synthesis process and the structural characterizations for CdO and Fe – doped CdO nanopowders. The sample powders were obtained through the process of chemical co – precipitation method. The structural behaviour was studied through various characterization tools; the XRD analysis confirmed the crystal phase of the sample powders which was observed to be face centred cubic structure (FCC). The vibration pattern was obtained using Fourier Transform Infra – red spectroscopy. The topographical morphology was done via Field Emission Scanning Electron Microscopy and the elemental ratio as well the constituting elements was obtained using Energy Dispersive X – Ray analysis. UV – Visible analysis was done to attain the absorption spectra [79].

Askarinejad et al. [2009] prepared the nano – sized samples for cadmium (II) carbonate, CdCO₃ and cadmium (II) hydroxide, Cd (OH)₂ using hydrothermal and sonochemical routes of synthesis processes at the air and inert temperature atmospheres for varying conditions. Whereas, cadmium (II) oxide, CdO was obtained by thermally treating CdCO₃ and Cd (OH)₂ at a temperature of 400 °C. The structural investigations were done through scanning electron microscopy, SEM and powered x – ray diffraction, XRD techniques. The results from XRD revealed that the CO₂ was the reason behind the CdCO₃ production [80].

Saha et al. [2008] used radio frequency magnetron sputtering route to synthesis a highly conductive and transparent titanium doped – CdO thin films. A defined set of environments with substrate temperature of 473 K and 0.1 mbar of pressure in Ar atmosphere was used to set down the thin films on the silicon and the glass substrates using varying Ti – percentages. The

said sample films were studied on for electrical and optical characteristics and XRD, AFM, XPS and UV – vis – NIR spectroscopy were used to obtain results regarding the crystallographic structures. A rock – salt structure was observed for the sample composite thin films. A structured incline was obtained in the values for the optical band gap and electrical conductivity with the increase in the Ti – content [81].

Navale *et al.* [2007] studied the varistor values for the Tantalum doped Titanium dioxide, Ta – doped TiO₂. The current versus voltage studies were conducted on the composite mixture with addition of 0.05–0.5 at. % Of tantalum pentoxide. The non – linear coefficient was obtained in the range scale of 25 – 30 with breakdown field strength, E_B approx. around 4000 V / cm. Schottky equation was used to compute the grain boundary barrier values which was formed on the surface of the acceptor due to absorption of oxygen whilst the sintering and cooling of the sample. The work was done on the pellets of the sample material and structural studies were done via XRD and varistor analysis was done using the current – voltage plot and certain formulae [82].

Oh *et al.* [2004] procured the pure form of titanium dioxide in two of its forms; rutile and anatase using the procedure of in – flight oxidation of titanium nitride powder in RF thermal plasma reactor. The obtained sample powders gave 93 % pure TiO₂ anatase nanopowders with higher oxygen content. Hydrogen was added in the oxygen deficient TiO₂ rutile phase to obtain purest form of rutile with average diameter of particle size of 50 nm. The formation of structures and presence of said phases were confirmed through optical microscopy, Raman spectroscopy, XRD and FESEM [83].

Zhang *et al.* [2008] modelled a newer kind of humidity measuring sensor. The work used anodic oxidation reaction procedure to procure TiO₂ nano – sized powders and calcinated them at 5 temperatures; 300 °C, 400 °C, 500 °C and 600 °C. The study was done to understand the effect of different temperatures w.r.t humidity sensing capability. The sample nanopowders that underwent the thermal treatment at 600 °C exhibited high sensitivity having approximately two order change in the values of the resistance. The results for recovery time were obtained to be < 190 sec and a shorter time period was also observed for response time. The obtained sample powders were characterised using XRD and FESEM tools [84].

Yadav et al. [2008] prepared the composite samples consisting of ZnO – TiO₂ nano – composites to investigate the humidity sensing and sensing properties of the said composites. The structural characterizations were studied at varying temperature scales using XRD and SEM tools. The best results were obtained at room temperature set at 19 °C. The minimal size for the nanoparticles was 50 nm and the highest values for sensitivity obtained was 18 MΩ / %RH at the set ambient temperature. The radii of the pores, known as Kelvin Radii was also calculated and the average value measured at 8.35 Å [85].

Thampi et al. [2015] worked on improving the anti – bacterial nature of the fabrics by introducing immobilized CuO and PANI nanopowders as one of the raw materials to be used whilst the synthesis process of the fabrics. The chemical precipitation method was used to obtain CuO nanopowders. The CuO and PANI matrix was settled down onto two types of fabrics; woven fabrics (WF) which were prepared by weaving and are cellulose rich and the other one was non – woven fabrics (NWF) which are also the regenerated fabrics that are porous – flat sheets, obtained from the chemical, mechanical, heat – solvent processes. These have their uses in textile and medical industries respectively. PANI – matrix was used to slow down the Cu – ion release on to the fabrics and then were coated on the sample fabrics for further analysis. The results obtained underwent characterization tools as; XRD, FESEM – EDAX, Raman Spectroscopy and TEM for the understanding of the structural domain of the samples obtained and as well to observe the values for the types of bonds obtained. The monoclinic structure with size = 50 nm was observed for the CuO nanopowders and agar diffusion plate method was used to study the anti – bacterial activity of CuO coated sample [86].

Zeng et al. [2010] synthesised a conducting polyaniline nano – fibres-based humidity sensor and its response time to change in the humidity. A shift in the oxidation state of polymer and an abnormal amount of water absorption was confirmed by IR – analysis. The behaviour obtained was found to be very distinguishable as compared to the conventional sensing materials. the sensors response when subjected to lower humidity environments i.e., < 50 % RH, a decline in the electrical resistance was observed w.r.t. increasing humidity values. Whereas at > 50 % RH, there was an increase in the electrical resistance with regards to humidity. This “reversed behaviour” was attributed to the polymer swelling due to the distortion of the nano – fibres [87].

Vijayan *et al.* [2008] fabricated a humidity sensor using optical fibre of Co – Polyaniline clad. The recovery time was obtained to be 1 min for 95 – 20 % RH and the high – speed response time of 8 secs for 20 – 95 % RH was acquired for the fibre optical wavelength in the range scale of 20 – 100 % RH. The response results obtained by the sensor was observed to completely reversible, reproducible and repeatable. The length and thickness of the clad was also reformed by eliminating the primal cladding of the commercially acquired plastic optical fibre for much finer execution. Co – immersed Polyaniline which was deposited as clad had thickness and length of 10.38 μm and 10 mm respectively. FTIR, SEM and XRD were employed on for the studying the structural and surface morphology [39].

Trchová *et al.* [2014] studied oligoaniline and polyaniline thin films for Raman Spectroscopy. These thin films were transferred via in – situ route on the non – conductive silicon supports whilst the chemical oxidation for aniline was taking place using ammonium persulfate in numerous liquid mediums. Polyaniline films exhibited globular structure when the polymerization was proceeded in a stronger sulphuric acid solution whereas, polyaniline nanotubes were obtained when the polymerization was done in a weaker medium; succinic acid, acetic acid and water – solutions. When the oxidation polymerization of aniline was carried following alkaline conditions, aniline oligomers were obtained having micro – spherical morphology. FTIR analysis showed that oligomers acquired at the initial stage of the oxidation process exhibited similarity nonetheless of the acidity levels of media, but the molecular morphology was unexplainable. The effect of the smooth gold support for Raman spectroscopy was done for the said sample thin films [88].

Zong *et al.* [2013] used a rational route to synthesis the novel composite mixture of rGO / Fe_3O_4 / Ag to study the microwave absorption capacity of the aforementioned sample. GO was obtained using Hummer's Method whereas rGO and rGO / Fe_3O_4 composite was prepared by the in – situ process in which Ag was gradually added to enhance the absorption reaction of the composite. The synthesised sample gave – 58.1 dB of maximum reflection loss at 9.0 GHz constituting of thickness of 2.6 mm. The absorption bandwidth was obtained around 13.4 GHz. Higher values for the microwave absorption capacity were acquired for the studied sample composite mixture [89].

Govarathanan et al. [2014] took the green synthesis route for the production of silver nanopowders using the traditional Indian farming formulating agent Panchakavya. Silver nitrate solution of 1mM was prepared and mixed with the formulating agent Panchakavya. The obtained dispersion was then studied on by using surface plasmon absorbance at 430 nm. Structural (XRD and FTIR) and morphological (FESEM – EDX and TEM) characterizations were also done to study to confirm the presence and formation of silver nanopowders. The process of reduction and capping of Ag nanopowders because of the proteins present in Panchakavya was confirmed through FTIR. Furthermore, the anti – bacterial study of the said synthesised Ag samples were also researched and it was found that acquired Ag sample powders showed the capability of declining the growth rate of bacteria as; *Acinetobacter* sp., *Aeromonas* sp., and *Citrobacter* sp. The used method of synthesis was observed to be non – toxic, organic and eco – friendly [90].

Power et al. [2010] fabricated Ag – Polymer nanopowders composite humidity sensor. Silver was obtained using chemical reduction method where an aqueous colloidal dispersion was assembled. UV – vis spectroscopy, XRD, dynamic light scattering and TEM were studied for material characterisations. The average diameter for the nanopowders was obtained around 20 – 22 nm. To study the humidity sensing capability of the said sample, Ag – Polymer composite was layered on to the platinum digital electrodes as sensing coats. At 1 V, the produced current was observed to in direct proportionality w.r.t the humidity levels. The values obtained exhibited selective, quick and reversible responses which were proportional to humidity levels in the humidity scale range of 10 – 60 % RH. The working of the sensor response was also done and observed to be in accordance with the theory for the second order Langmuir adsorption framework [91].

Narasimha et al. [2013] investigated the eco – friendly synthesis procedure for silver nanopowders using *Actinomycetes*, the structural characterisations and the anti – bacterial properties for medical field were also studied. The silver nanopowders were procured through extracellular synthesis procedure which included the usage of *Actinomycetes* that were separated from the mangrove soil and they exhibited an average size around 5 – 50 nm. The structural analysis was done using FTIR and UV – visible spectroscopy and the morphology was studied using TEM. Exceptional sets of results were observed for the anti – bacterial facet

for the said sample powders when used for both the multi – drug resistance negative and positive bacterial strains [92].

Guo *et al.* [2016] fabricated a computer – aided humidity sensor having fast response and higher levels of humidity sensitivity using graphene oxide. This COSMOL framework was an interdigital capacitive humidity sensor and the theory for diffusion methods of water molecules and the impact on the capacitance values were also provided. The capacitance values have been obtained for varying relative humidity stimulations and its effects on the structural variables have also been studied. These values show the capability to be used as reference work to design an electrode in order to elevated the humidity sensing abilities of the sensor. The dynamic process simulation was used to study the response time of the module and the results acquired exhibited an upgraded behaviour, which further makes it a candidate for the gas capacitive sensors as well [93].

Li *et al.* [2009] used reduction synthesis route on graphite oxide and H_2PtCl_6 to acquire the graphene nano structured sheets which were layered with platinum, Pt. These graphene sheets were studied for the electrochemical behaviour. The results showed an elevated catalytic characteristic regarding the methanol oxidation process. The positive results of the electrochemical studies showed the potency of Pt / graphene nano – composites to be used as catalysts transporters for electro catalysis and fuel cells [94].

Sohail *et al.* [2017] used different types of Hummer’s method; Modified Hummer’s Method and Improved Hummer’s Method to obtain the graphene oxide nanopowders and further used these sample powders to understand the difference between the values obtained for capacitors. The results showed that GO – powders exhibited approximately same physico – chemical nature. Structural studies were done using XRD and FTIR, both of them confirming the production of the GO – nanopowders by providing details regarding semi – crystallite phase of the sample. The crystallite size was obtained in the range scale of 27 – 28 nm. Impedance or Dielectric studies provided with reasoning of them being active at lower values of frequency which was found because of the interfacial polarization and furthermore, showing relaxed behaviour whilst being present at high frequency. The dielectric tangent loss was obtained to be 0.03 – 0.39 and 3.1 – 3.9 eV was observed to be range scale for the optical band gap energy [95].

Ahmad *et al.* [2016] studied reduced graphene oxide for its relative humidity sensing properties which were based on a tapered single mode microfiber loop resonator, MLR of diameter 4.04 μm . The refractive index of the MLR – microfiber was improved through environmental humidity and the emission wavelength exhibited a change in its values w.r.t the RH – levels. The consideration for rGO was done on the basis of the inert nature of the material to have higher sensing capability with exceeding reduction in the recovery times and response times and as well having higher water permeability. The tapered fibres were analysed with and without the inclusion of rGO content. The fibres having rGO content gave a shift w.r.t increasing relative humidity. The sensitivity values for rGO – tapered fibres were obtained to be 0.0537 nm / % RH in the 30 – 50 % RH relative humidity scale as compared to 0.0316 nm / % RH, which was observed for the fibres without rGO content [96].

Park *et al.* [2018] studied rGO / MoS₂ sample composite for room temperature humidity sensing because of the oxygen rich functional groups of rGO and dangling bonds present at the edge sites in MoS₂. The hydrothermal route of synthesis was used to obtain two – dimensional rGO/MoS₂ hybrid (MS – GOs) nano – composites. rGO and MoS₂ were used in varying molar ratios and further drop – casted on a SiO₂ substrate having a Pt – interdigitated electrode. This optimised sensor device displayed exceeding behaviour with regards to sensitive nature, selectivity and recovery and response time and as well as showed satisfactory linearity. This behaviour of the sensor was attributed to the p – n junction existing in the middle of rGO and MoS₂. The study showed the excellent performance rate and response time for 2D – 2D heterojunction and thus concluded its uses as chemo resistive humidity sensors [59].

Mohan *et al.* [2015] studied the structural characterisations of reduced graphene oxide procured using different reducing agents and the impact on its behaviour with regards to electrical conduction because of the aforementioned agents. The reducing agents used in synthesis process were; Hydroiodic acid (HI), Hydrazine Hydrate (N₂H₄) and Hydrobromic acid (HBr). XPS, Raman spectroscopy and XRD were employed on to understand the structural nature and behaviour of rGO and to compare the results so as to orderly upgrade its electrical conduction. The electrical conduction value was obtained to be 103.3 S cm⁻¹ for the rGO reduced using HI acid, which was observed to be best results in comparisons to the results

obtained for the same using HBr acid and N_2H_4 . The rGO obtained using HI acid also gave better flexibility [97].

Bidadi et al. [2013] studied the usage range of the gallium arsenide–polyaniline–polyethylene (GaAs – PANI – PE) composite varistors. The applicational domain was found between 46 V up to 54 V over voltages and furthermore, the values for bandgap, the breakdown voltage and the non – linearity attached to it exhibited an increase with the raise in the temperature it was being sintered but the hysteresis showed a decline in the values. The studies were conducted on the sample pellets that were hot pressed at pressure of 60 MPa and were sintered at varying temperatures [98].

Cristovan et al. [2011] prepared the organic polymers varistors using different categories of polymer materials; a conducting polymer i.e., PANI (polyaniline), a dielectric polymer and copolymer of acrylonitrile – butadiene – styrene composite. The results exhibited low – voltage varistor values consisting of approx. 10 V as breakdown voltage and 5.0 as non – linear coefficient. These materials showed stronger stability during the time duration of repeated voltage – current cycles. The studied composites were observed to be flexible with their nature, had inexpensive raw materials and the synthesis procedures were easy as well [99].

Lu et al. [2009] studied the electrical stability and varistor properties of ZnO thin films which were deposited by Gas Discharge Activated Reaction Evaporation (GDARE) technique. The micro-structural properties were examined by X-ray diffraction (XRD) and Atomic Force Microscope (AFM) and electrical nature was investigated by studying the I-V Graph. The ZnO thin films were annealed at 250 °C for 2 h and their varistor graph showed a strong nonlinear varistor-type I-V characteristics. Under the influence of a certain DC bias at the respective of temperature of 150 °C, the thin films proclaimed a good electrical stability. The structural characterization technique showed the polycrystalline structure of the films [100].

Gaponov et al. [2010] studied the $SnO_2 - Co_3O_4 - Nb_2O_5 - Cr_2O_3$ composite ceramic varistor with the gradual addition of CuO for its electrical properties as well as their current – voltage response and temperature dependency attributes. It was found that the non – linearity showed an increase in the values in the range of 0 – 0.5 mol % CuO from 54 to 75 and further gave decrease in range of 2 – 8 mol % CuO with the values 3 – 7 range. The nature of non – linearity

was observed to be diminishing with increase in the amount of CuO added and the thickness dependence on the aforementioned trait has also been studied [101].

Fernandes *et al.* [2009] formed a morphologically homogenetic material which showed large particle size and purity. These characteristics were studied and confirmed through Scanning electron microscopy (SEM), X-ray diffraction (XRD), Fourier transform infrared spectroscopy (FT-IR), thermo – gravimetric (TGA) and differential scanning calorimetry (DSC). ZnO, CuO and a mixed composite $\text{Cu}_{0.05}\text{Zn}_{0.95}\text{O}$ were synthesised with the sol-gel method using poly (vinyl alcohol) [PVA] aqueous solutions and the respective metal nitrate precursors. The average nano-crystallite size for ZnO and $\text{Cu}_{0.05}\text{Zn}_{0.95}\text{O}$ was found to be 25-30 nm and 40nm for CuO which was calculated using the Scherrer's equation [102].

Cui *et al.* [2020] studied ZnO-Bi₂O₃ based ceramics varistors which were sintered at low values of temperatures i.e., 900°C for only 2 hours and these were fabricated using conventional solid-state method. The research was done for non-linear coefficient and electrical breakdown voltage values. The studies were conducted using doped composite ZnO-Bi₂O₃-Co₂O₃-MnO₂ [ZBCM] for Bi-Sb-O phase. The results for the experiment concluded that ZBCM-Bi-Sb-O phase was capable of undergoing sintering at higher densities (above 0.98) and at the same time exhibiting non-linear coefficient (α) value = 53.0 which the result of an improved barrier height value = 1.85 eV. Moreover, smaller values of leakage current density were obtained due to the increased grain resistance and dielectric loss being its lowest at lower frequency values [103].

Muremi *et al.* [2021] analysed the degradation effect on electrical properties of ZnO low-voltage varistors that were under the influence of voltage switching surges. It was studied that functioning capability of ZnO varistors were determined from its physical-electrical properties and the type of stress that were applied. The conclusions were derived by comparing low-varistors that same kind of electrical properties and sizes but were obtained from different manufactures A and B. These varistors then underwent Ac switching surges. Pearson correlation equation was used to study the degree of the relationship between the clamping and reference voltages. The mean percentile change for reference voltage value was obtained above 10 – 11% for manufacture A and in 9.19 – 10.11% range for manufacture B respectively. An

increase in calculated clamping voltage ratio was obtained with decrease in capacitance under the applied surges [104].

Shaifudin *et al.* [2019] fabricated a low voltage varistor with composites of ZnO and BaTiO₃ through solid state reaction synthesis process. Various characterisation such as; XRD (X-Ray diffraction), EDS (Energy Dispersive X-Ray Analysis Spectroscopy), SEM (Scanning Electron Microscopy) were studied to understand the effects of BaTiO₃ on ZnO varistor microstructure. Current density and electric field plot were analysed to investigate the electrical properties of above-mentioned sample composite varistors. The results exhibited that nonlinear coefficient value was obtained within range of 1.8 – 4.8 with barrier height values falling in range from 0.70 – 0.88 eV. Varistor voltage of values from 4.7 – 14.1 V/mm with voltage grain boundary values from 0.03 – 0.05 V were obtained with the usage of BaTiO₃ additive produced. 348 $\mu\text{A}/\text{cm}^2$ was acquired as lowest leakage current density value. The studies also concluded that as a result of increasing BaTiO₃ content, barrier height values showed a decrease because of presence of O – vacancies in grain boundaries [105].

Staikos *et al.* [2020] researched the frequency response for low voltage metal oxide varistors that were used as circuit protectors in industrial sectors of telecommunication systems. The study of current voltage plot was done w.r.t. several excitation frequency values. A crossover point was obtained where effect of frequency on varistor resistance exhibited a reversal behaviour. It was observed that varistor resistance values that were obtained less than crossover current values showed a linear decrease with frequency. The objective of research work was aimed to study the development of metal – oxide varistors keeping in consideration the effect of frequency on the electrical properties of devices and its overall functionality [106].

Syaizwadi *et al.* [2021] worked with nonlinear coefficient property of cobalt oxide Co₃O₄ and barium titanate BaTiO₃ composites that were used as additives in varying for the ceramic ZnO varistor structure. The analysis was done through the investigation of plot for current density and voltage density characteristics. Nonlinear coefficient gave an increased value of = 4.3 when 12 wt.% BaTiO₃ sample was studied but on the other hand, the varistor voltage value underwent a decrease in value from 8.9V/mm to 7.0 V/mm when Co₃O₄ content was increased from 0.5 wt.% to 1.5 wt.% respectively. Moreover, barrier height values exhibited an increase in the values 0.88 to 0.98 eV for 0.0 to 1.0 wt.% for Co₃O₄ concentration. 7.2 was observed to be

Chapter 2. *Literature Review*

highest value acquired nonlinear coefficient for 0.5 wt.% Co₃O₄ concentration which was considered to be the performance value for the ceramic varistors. however, as the cobalt content was increased the nonlinear value exhibited decreasing plot. This was because of reduction in barrier height due to the variations in electronic states at the grain boundaries as it led to formation of spinel phase [107].

Chapter 3

3 METHOD OF SYNTHESIS

There are numerous methods for the synthesis of nano – structured materials (**Figure 3.1**). In the present work, the powdered form of the nano – structured materials are used. The desired transparent metal oxides; Copper Oxide (CuO), Cadmium oxide (CdO) and Titanium Dioxide (TiO₂ – anatase) are synthesized using Sol-gel method, with the usage of nitrates of the materials. The conductive form of polymer; Polyaniline (PANI) is obtained through the employment of Oxidative Polymerization Process. The Top – Bottom approach of the wet chemistry method is used for the production of silver nanopowders. Modified Hummer’s Method is being used for the production of Graphene Oxide (GO) and the conducting form of graphene derivative i.e., Reduced graphene oxide (rGO) is procured by the reduction process of GO using hydrazine hydrate.

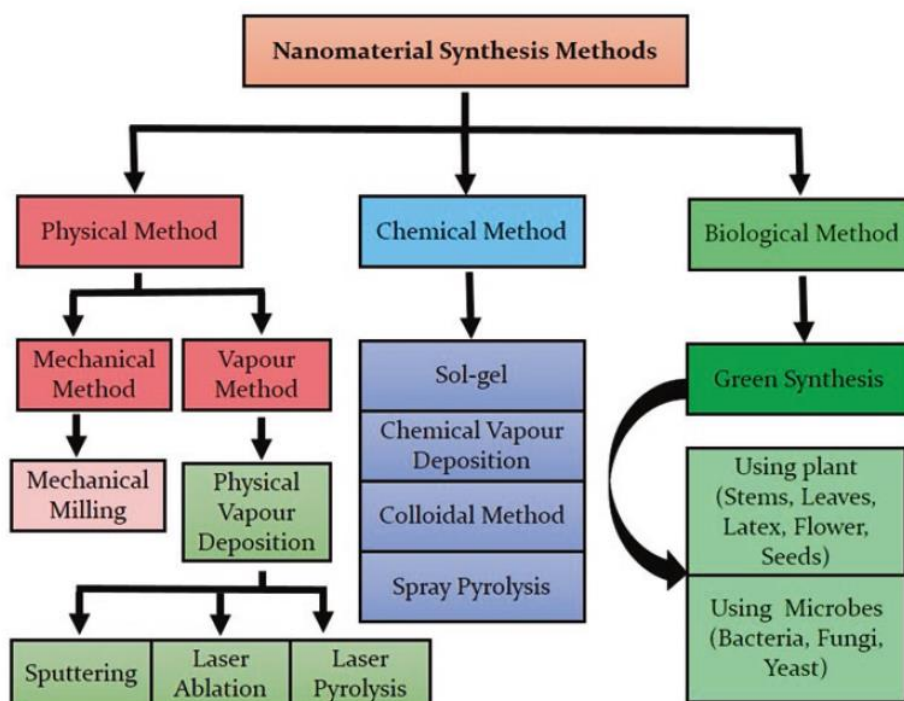


Figure 3.1 Figurative representation for the various routes of synthesis on nano – powders [108].

3.1 Sol – Gel Method

The Sol-Gel Method is a wet chemical method that is been substantially utilized in obtaining the desired materials. This method is more favoured over other categories of material synthesis; co-precipitation method, hydrothermal method, solid state method available and the credit goes to its unique and yet easy advantages as: performed at low temperature, easy to control and perform, complex appliance/ instruments are not required hence making this method low cost effective and simple process and can have better hold of the desired particle size and porosity, highly homogeneity and can also be used for the synthetization of the thin films. The raw materials that are commonly metal nitrates or alkoxides are dissolved in a liquid medium as: ethylene glycol, water or a suitable acid to compose a colloidal suspension known as ‘SOL’ which is further accompanied by the aging and subsequent heating of the sol to obtain then called ‘GEL’. A colloid that is suspended in a liquid is called a sol whereas a suspension that keeps its shape is called a gel, thence the name *SOL-GEL* [109] (**Figure 3.2**).

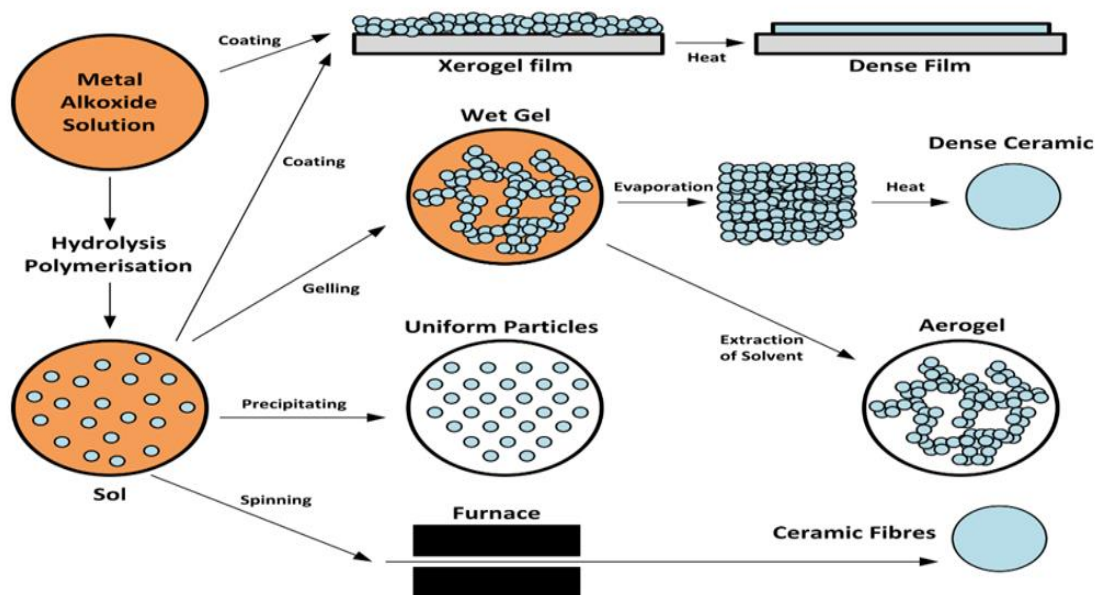


Figure 3.2 Illustration of the Sol-Gel Method and its various synthesis routes.

3.1.1 Sol – Gel Auto Combustion Method

The GEL which is procured by the employment of the above-mentioned procedure is then further facilitated by heating / drying of the gel at higher temperatures which is a self – ignition process that happens due to catalyst added in solution i.e., polyvinyl alcohol (PVA) or citric acid. This self – ignition step is called ‘auto – combustion’ which evaporates the liquid channel and converts the gel into a ‘Precursor’. This precursor furthermore undergoes the thermal treatment; annealing, sintering or calcination at respective temperatures as per the requirement (**Figure 3.3**). After this step, the resultant nanopowders are the desired outcome that are further used for the purposes of structural characterizations and to check its applicational prospects. This method is being used to synthesize CuO nanopowders (**Figure 3.4**) and CdO nanopowders (**Figure 3.5**).

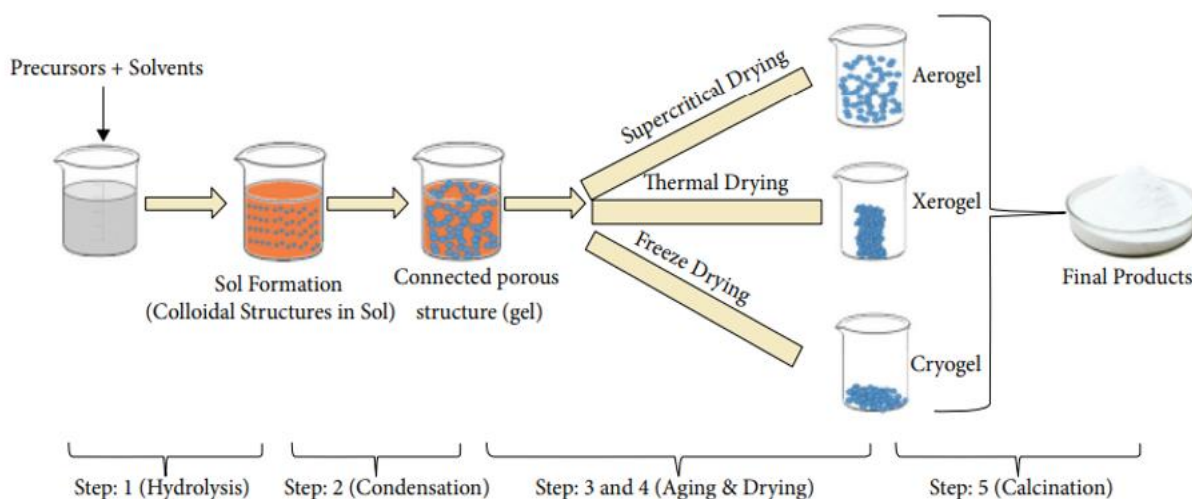


Figure 3.3 The step – by – step schematic illustration of sol – gel auto combustion method [109].

- Synthesis process of Copper Oxide, CuO.

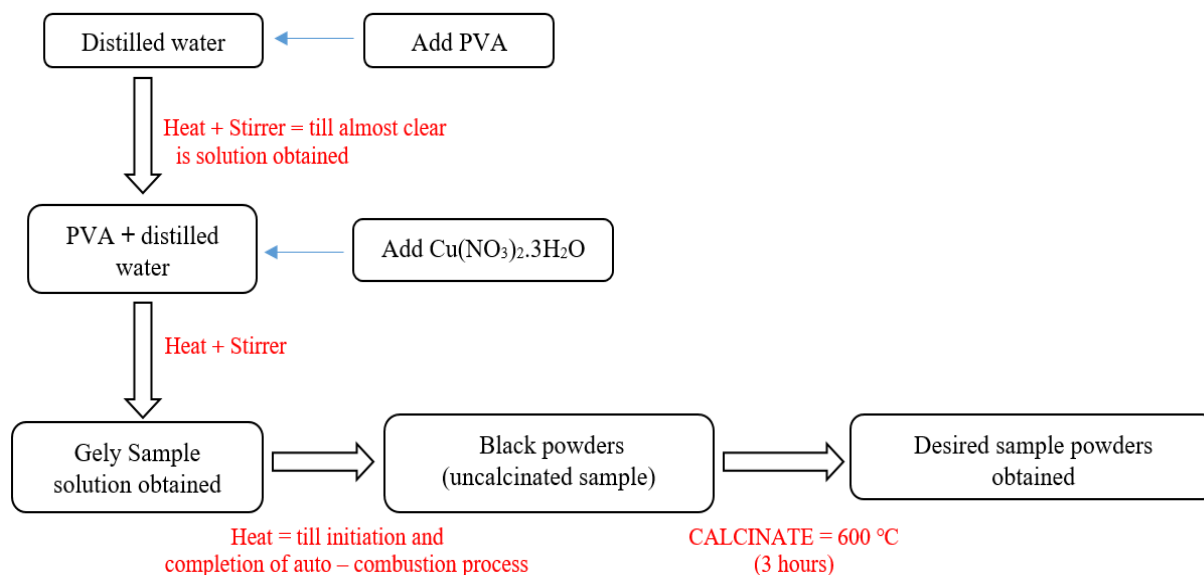


Figure 3.4 Diagrammatic representation of Sol – Gel Auto – Combustion method of synthesis for CuO nanopowders.

- Synthesis process of Cadmium Oxide, CdO.

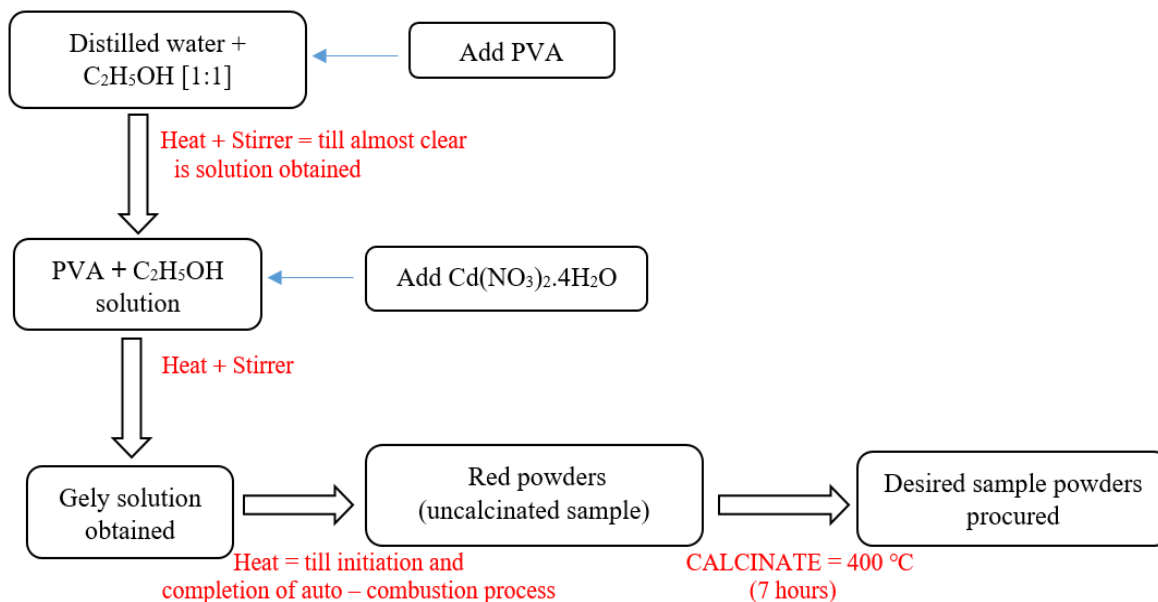
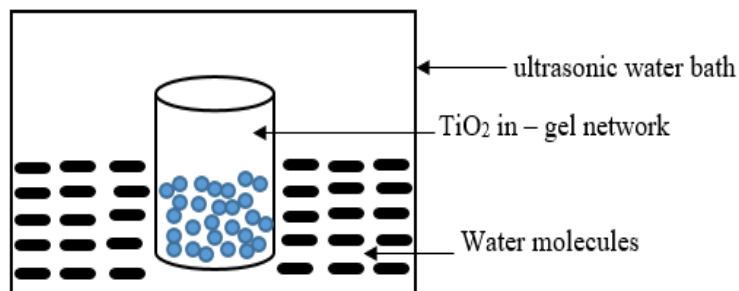


Figure 3.5 Diagrammatic representation of Sol – Gel Auto – Combustion method of synthesis for CdO nanopowders.

3.1.2 Ultra-sonic assisted Sol – Gel Method

In this step the obtained sol from the sol – gel method step does not undergo auto – combustion step as the chemicals involved are extremely volatile and can lead to explosion or fire. Rather, the sol undergoes the ultrasonic treatment to make the particles of the solution homogeneous (**Figure 3.6**) and henceforth, heated till the water content gets evaporated and gel is left behind. This gel is then dried at lower temperatures in order to break the remaining water bonds and to obtain a solid form of the sample. The sample is obtained with flak – like structure and it is further calcinated at desired temperatures to get the desired sample nanopowders. TiO₂ – anatase nanopowders (**Figure 3.7**) are obtained using the ultrasonic assisted sol – gel procedure.



TiO₂ solution becomes homogeneous after sonication because ultrasonic vibrations breakdowns the gely network and makes layers of the solution homogeneous.

Figure 3.6 Figurative description of the placement of the solution in the ultrasonic water bath.

- Synthesis process of Titanium Dioxide, TiO₂ - anatase.

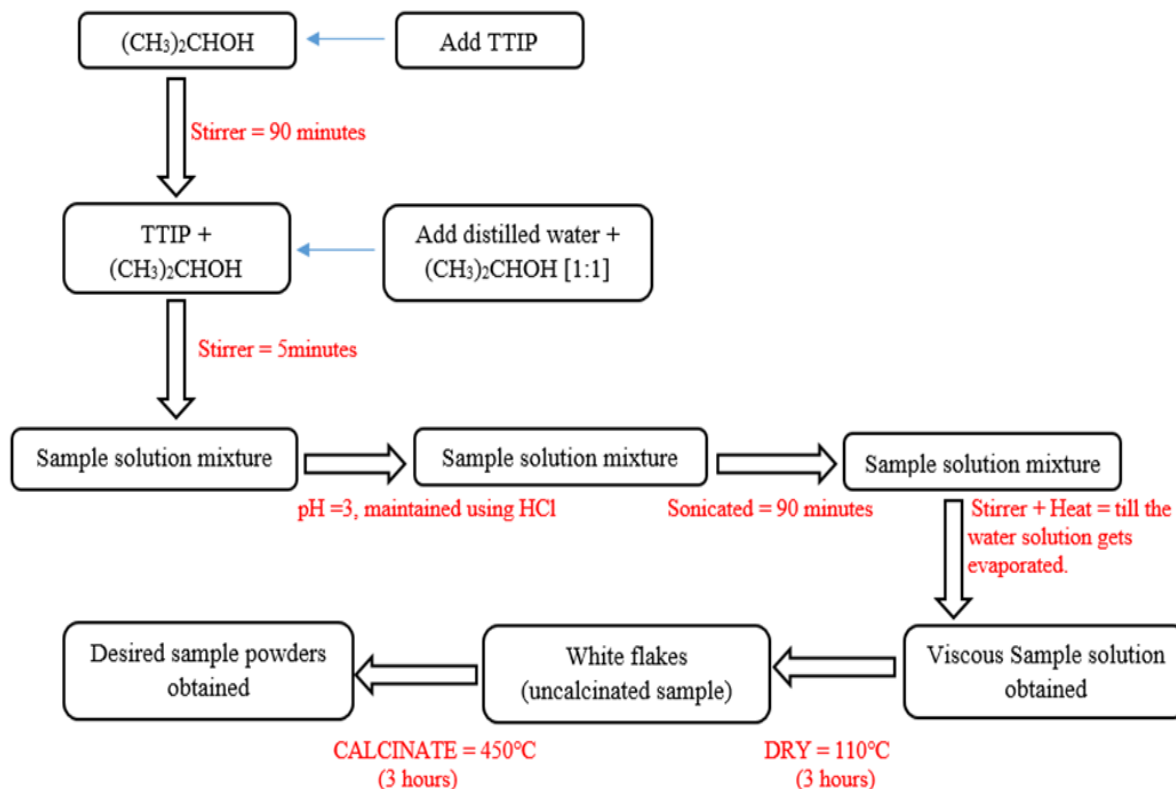


Figure 3.7 Diagrammatic representation of Ultra – Sonic assisted Sol – Gel method of synthesis for TiO₂ (anatase) nanopowders.

3.2 Oxidative Polymerisation Method

The conducting form of polymers i.e., Polyaniline (PANI) was synthesized on by the usage of chemical oxidative polymerization method. In this process, a catalyst protonic acid; HCl is used as a dopant whereas ammonium Persulphate solution (APS) is used as an oxidizing agent. The whole procedure takes place in the water bath with placement of large amounts of ice because the synthesis of PANI takes around 0 °C (**Figure 3.8**) and also the presence of large amounts of monomer and HCl acid makes the process extremely exothermic. The heat produced can result in combining of the aniline monomer hastily and therefore to slow down the reaction and to have quality polyaniline sample, the temperature is dropped down below 0 °C (**Figure 3.9**).

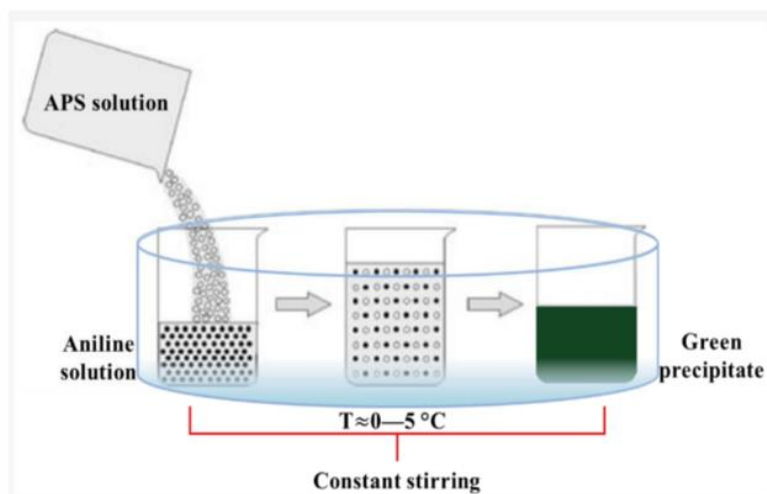


Figure 3.8 Figurative description of the placement of the PANI solution with temperature at $0 \text{ }^\circ\text{C}$ [110].

- Synthesis process of Polyaniline, PANI.

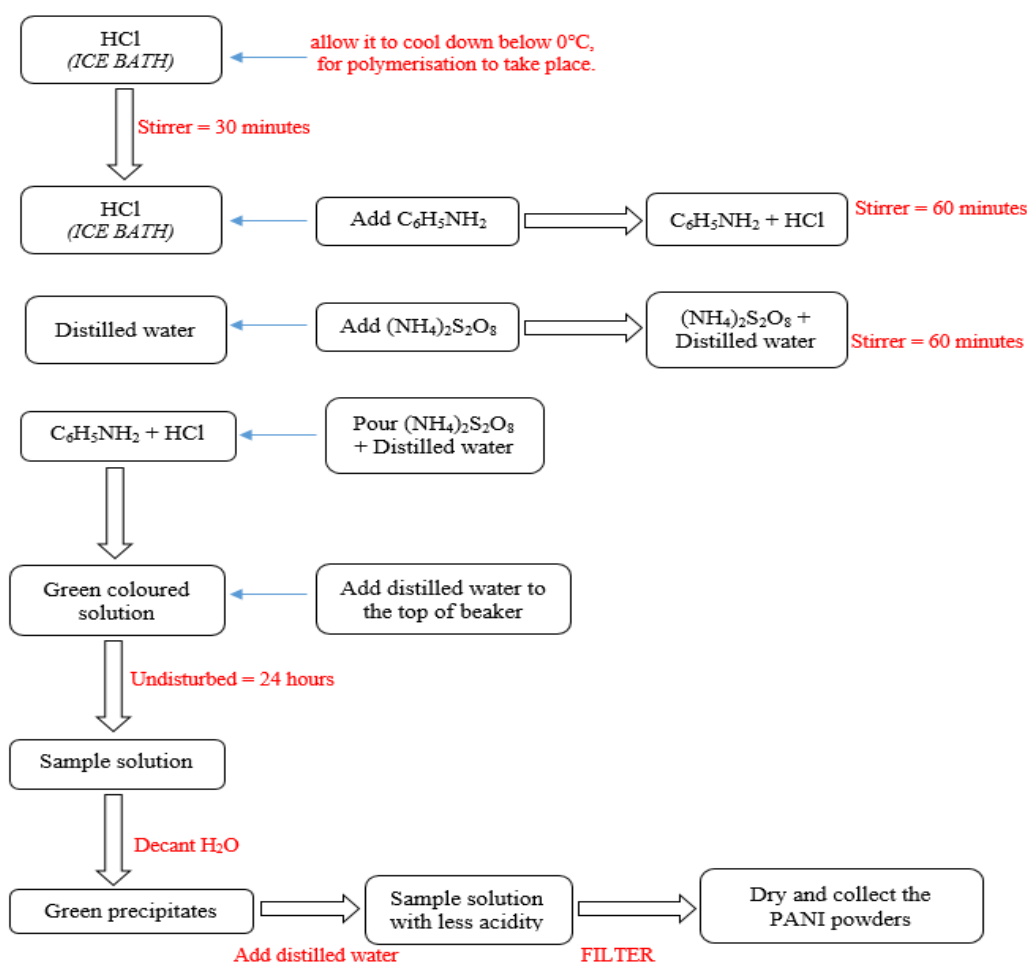


Figure 3.9 Diagrammatic representation of Oxidative Polymerisation method of synthesis for PANI nanopowders.

3.3 Top – Down Method

Wet chemistry method was used to obtain the silver nanopowders. There are numerous techniques involved in the above-mentioned method and they are widely assorted in two categories: top – down and bottom – up method (**Figure 3.10**).

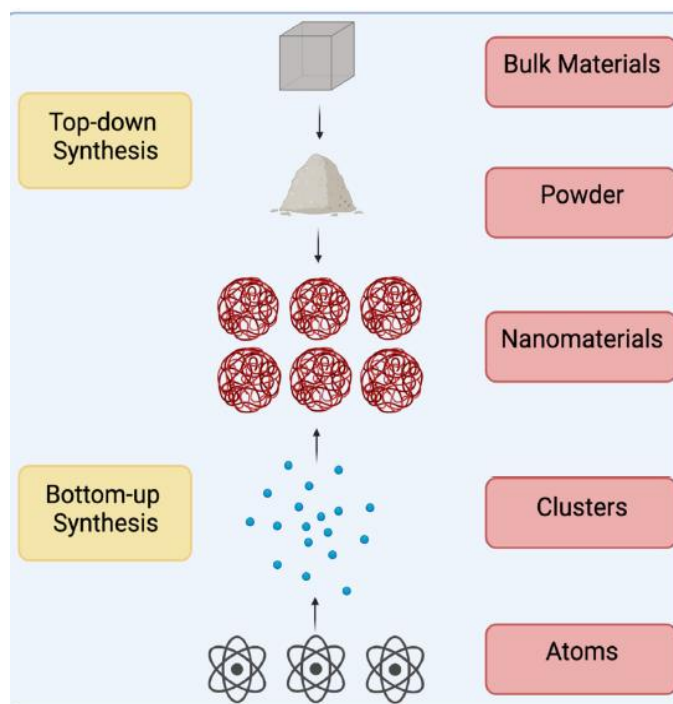
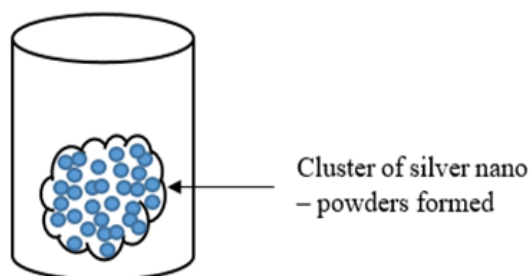


Figure 3.10 Figurative representation of the Top – Down and Bottom – Up methods of synthesis [111].

In this paper, ‘top – down process’ was used which means breaking down of the clustered and bulk of the material into smaller sized nano – particles. At first a stable colloidal dispersed solution of silver is obtained in water or other organic liquid solvents and which is further made to undergo the reduction step using a reducing agent such as; sodium borohydride or citrate. This step leads to the formation of the agglomeration of the nanoparticles, which are further broken down into desired sized nano structures by other means (**Figure 3.11**). The obtained sample powders with this process produces nanopowders with micro sized dimensions, no chemical purification is needed and also allows its easy deposition on the larger substrate surfaces. This process as well allows the production of the sample nanopowders on large scale [112][113][114] (**Figure 3.12**).



The formed agglomeration breaks down as the solution is heated and the H₂O molecules bonds breaks down and evaporates, leaving behind the residual of the desired nanopowders.

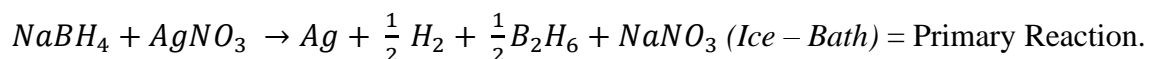
Figure 3.11 Figurative description of the cluster formation and breakdown of the solution.

There are specific experimental requirements that are a necessitate to implement prior to the synthesis process.

- Pre – Conditions for the Experimental Course of Action:

(I). Surplus volume for Sodium Borohydride (NaBH₄): the excessive amounts of NaBH₄ was required in the synthetisation procedure as it is an important constituent that stabilizes the Ag – nano – powders.

(II). Requirement of the Ice – Bath: now, NaBH₄ is an exceedingly strong reducing medium, so at room temperatures (or hot waters), NaBH₄ can very well interact with the nitrate – ions because with temperature rise the rate of reactivity also shows an ascent and this will lead to secondary reactions taking place that will in – turn reduce the Ag – ions. So, with purpose to obtain the desired sample products, cooling throughout the reaction is required to kept – up. The equations for the reactions; Primary (*Preferred Reaction*) and Secondary are shown below.



$\text{NaBH}_4 + \text{AgNO}_3 \rightarrow \text{Hydrogen and Borax}$, as Hydrogen will react with Ag – ion and reduce the Ag – ions instead of BH₄⁻ ions (*Room Temperature*) = Secondary Reaction.

Here, Hydrogen (H_2) and Diborane (B_2H_6) were the gases and therefore, during the stretch of the procedure, they evaporated. Sodium nitrate ($NaNO_3$, due to being salt, dissolved in the water only. Ag was the required product.

- Synthesis process of Silver nanopowders, Ag – nps.

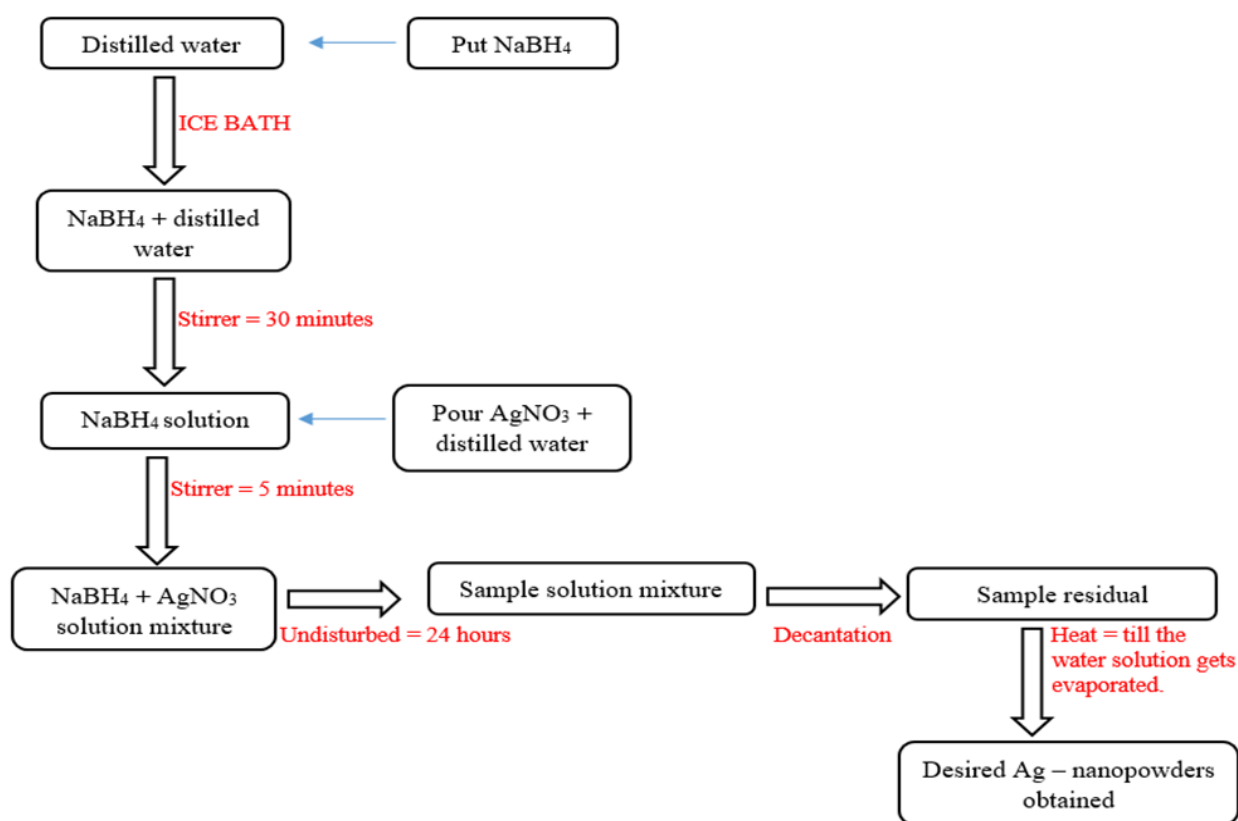


Figure 3.12 Diagrammatic representation of Top - Down method of synthesis for Ag – nanopowders.

3.4 Modified Hummer’s Method

Graphene Oxide (GO), the derivative of graphene is generally obtained from the graphitic powder using the Modified Hummer’s Method which is the most extensively method of synthesis. This process includes the usage of chemicals as: Sulphuric Acid (H_2SO_4), Potassium Permanganate ($KMnO_4$), Hydrogen Peroxide (H_2O_2) and Hydrochloric Acid (HCl) and also includes filtration process. H_2SO_4 acts as a catalyst that optimizes the graphite surface in order to have functional groups attached onto its surface in the presence of a reagent, whereas $KMnO_4$

is the oxidizing reagent. H_2O_2 is added in the concluding step of the said route in order to cease the oxidation reaction with the excess of KMnO_4 from happening i.e., by removing the $-\text{COOH}$ functional groups therefore, reducing the O – content. The resultant of filtration process is then heat – dried to obtain the powdered form of GO. The hummers method has been physically revised a lot through the years for the convince of the usage and to obtain a considerable amount **(Figure 3.13)**.

The advantages of the modified hummers method outweigh other methods: (1). The oxidant NaNO_3 is not used in this experimental work as NaNO_3 is highly toxic and when it is heated, it releases fumes of NO (Nitrogen Oxide) and Na_2O (Sodium Oxide), which are extremely harmful when inhaled. (2). This method as compared to the prior methods supplies an improved level of oxidation hence superior product quality is obtained. (3). The sample powders acquired as well have more amount of oxygen. (4). The quantity of GO powders obtained is also considerably more as compared to other methods.

<p>Brodie Method ^{12, 25}</p> <ul style="list-style-type: none"> • Oxidants: KClO₃, HNO₃ • Toxicity: Yes • Disadvantages: <ul style="list-style-type: none"> • Weak acidity. • Soft dispersability in basic solutions. • Small size, limiting thickness and providing an imperfect structure.
<p>Staudenmaier Method ^{13, 26}</p> <ul style="list-style-type: none"> • Oxidants: KClO₃ (NaClO₃), HNO₃, H₂SO₄ • Toxicity: Yes • Disadvantages: <ul style="list-style-type: none"> • Time-consuming and dangerous method. • Addition of KClO₃ generally takes longer than a week and CO₂ is evolved, thus making necessary to remove an inert gas. • The risk of explosions is a constant danger.
<p>Hummers Method ^{27, 14}</p> <ul style="list-style-type: none"> • Oxidants: KMnO₄, H₂SO₄, NaNO₃ • Toxicity: No (NO_x is released) • Advantages: <ul style="list-style-type: none"> • Higher oxidation degree than that obtained in Brodie or Staudenmaier Methods. • Disadvantages: <ul style="list-style-type: none"> • It is still considered that the oxidation is incomplete. • Separation and purification processes are tedious process. • Highly time-consuming process.
<p>Modified Hummers Method ^{27, 28}</p> <ul style="list-style-type: none"> • Oxidants: KMnO₄, H₂SO₄, NaNO₃, KMnO₄, H₂SO₄ • Toxicity: No (NO_x is released) • Advantages: <ul style="list-style-type: none"> • Improved level of oxidation and, therefore, product performance. • Disadvantages: <ul style="list-style-type: none"> • Separation and purification processes are tedious process. • Highly time-consuming process.
<p>Improved Hummers Method ²⁷</p> <ul style="list-style-type: none"> • Oxidants: KMnO₄, H₂SO₄, H₃PO₄ • Toxicity: No • Advantages: <ul style="list-style-type: none"> • Defects in the basal plane are reduced. • Larger amount of oxidized graphite is provided. • The degree of reduction provides an equivalent level of conductivity when compared to other methods. • Best process yield compared to Brodie, Staudenmaier and Hummers method. • Environmentally friendly, toxic gases are not generated during the preparation. • The product has a more organized structure compared to graphite oxide obtained by Brodie and Staudenmaier methods. • Disadvantages: <ul style="list-style-type: none"> • Separation and purification processes are tedious process. • Highly time-consuming process.

Figure 3.13 Tabular representation of improvisations done in Hummer's Method by time [115].

The resultant dried GO powders then underwent the reduction process using Hydrazine Hydrate (NH₂NH₂H₂O) as to acquire the conductive derivative of graphite which is rGO, reduced graphene oxide [116]. In this process, the functional groups constituting of oxygen or carboxyl groups are reduced or removed from surfaces and the rGO nanopowders procured

through the reduction of GO done by hydrazine has proved to exhibit exceptional electrically conductive capability [117] (**Figure 3.14**).

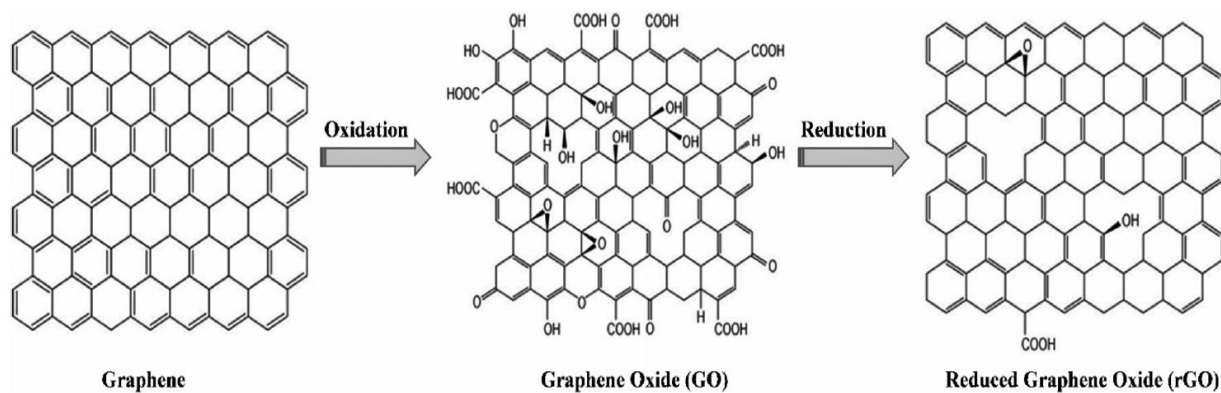
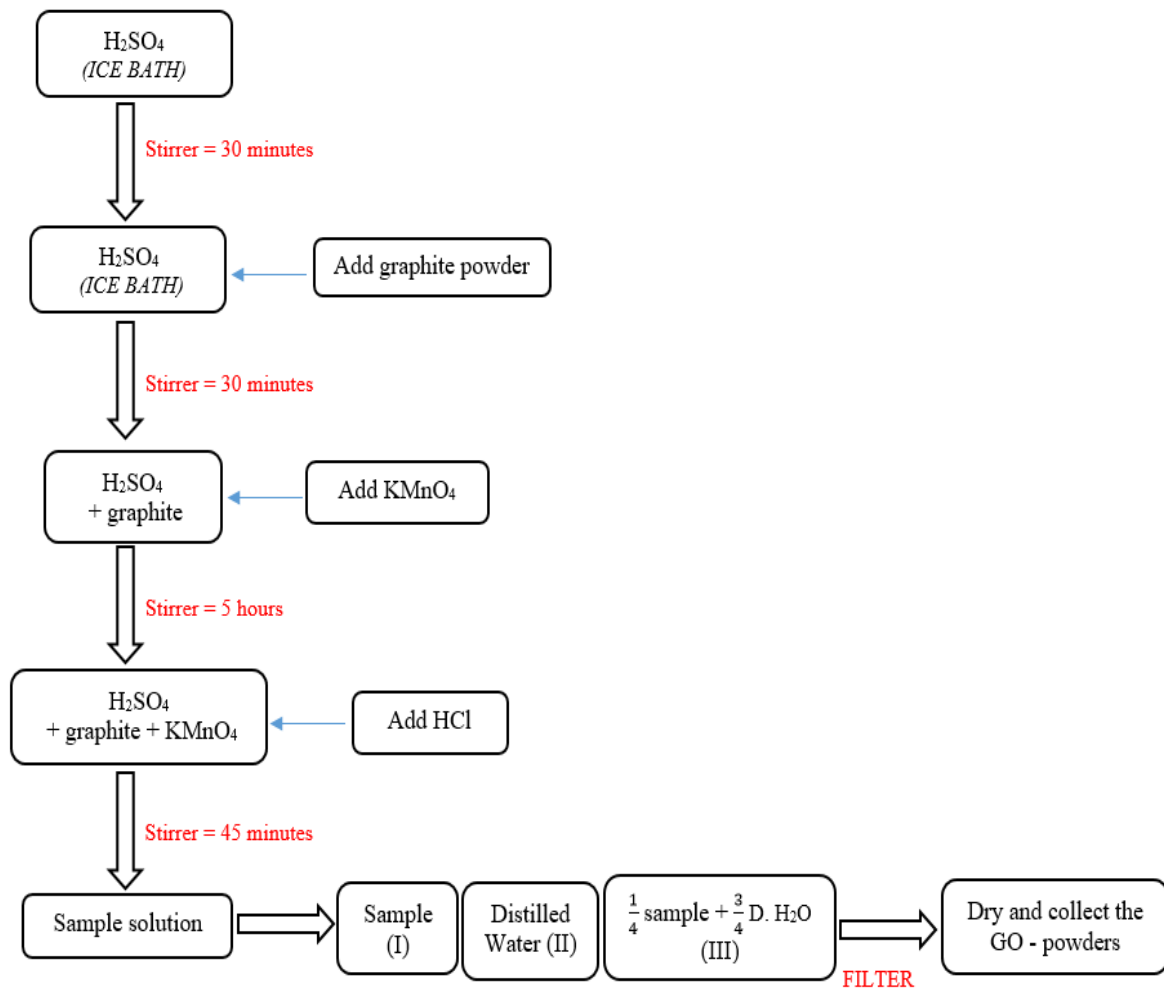


Figure 3.14 Figurative representation of conversion of Graphene into Graphene Oxide and final transformation into Reduced Graphene Oxide [118].

The upper hand with the reduction method for rGO done by hydrazine hydrate is: (1). The reduction process using $\text{NH}_2\text{NH}_2\text{H}_2\text{O}$ can be done under normal conditions with room temperature as it does not require very high temperature or any specific atmospheric conditions to operate in. (2). It provides with the better reduction of rGO because as the amount of $\text{NH}_2\text{NH}_2\text{H}_2\text{O}$ increases, the reduction degree of rGO also increases thus, a good quality of rGO is obtained. (3). The procured powders are of conducting form with less oxygen content, higher surface areas and finer rGO sheets (**Figure 3.15**).

- Synthesis process of Reduced Graphene Oxide, rGO.



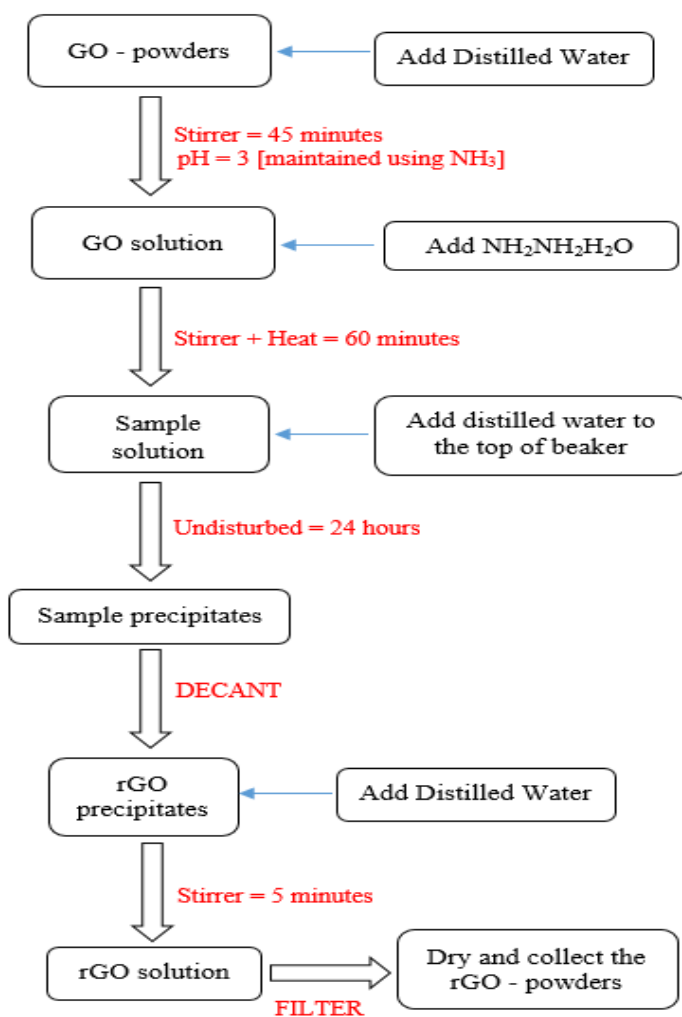


Figure 3.15 Diagrammatic representation of Modified Hummer's method of synthesis for rGO – nanopowders.

Chapter 4

4 CHARACTERISATION TECHNIQUES AND FORMULAE

4.1 Thermal Analysis

4.1.1 Thermo – Gravimetric Analysis (TGA)

TGA is an established approach to ascertain various factors that are inclusive of the physiology of the chemicals and substances such as; to discern the decompositions rates of explosions. Thermo – gravimetric analysis studies the mannerisms and properties of the materials by the means of the variation in mass of substance w.r.t the change in temperature. The sample undergoes thermal treatment in a provided environment, comprising of He, N₂, air, Ar or CO₂ etc at a supervised rate, where upon heat is used a tool to initiate the reactions and compel the materials to experience physical changes, to compute the oxidation reactions, the extent of an inorganic or / and organic constituents in a mixture, the absorbed humid section of substances, the have values for exotherms – endotherms and thermal stabilities, the decaying rate for the material and to study the properties of solvents residuals and polymers etc. The range scale of the materials is just not limited to the afore – mentioned, as the thermal analysis is also employed onto organic – inorganic substances, explosives, biological / chemical specimens, polymers – plastics, coatings and adhesives, petroleum, pharmaceuticals and composite samples.

The apparatus set – up incorporates of a sample pan and a balance that is exceedingly accurate. The pan is positioned in an oven or furnace which undergoes the heating and cooling procedures and is used to carry the sample throughout the whole analysis procedure. The temperature within the bounds of the furnace is controlled and measured using a thermocouple, furthermore a reactive or an inert gas may also be employed on to discharge or control the environment. The procedure is furthered by increasing the temperature values with moderation. The mass of the sample is under consistent supervision and the obtained weight values are plotted in comparison to temperature values. This obtained graphical plot acquired between varying weight of the materials w.r.t increasing temperature values is also known as thermogram or thermogravimetric curve. The output curves i.e., temperature versus weight plot

is acquired through a computer set – up which also manages the apparatus environment (**Figure 4.1**).

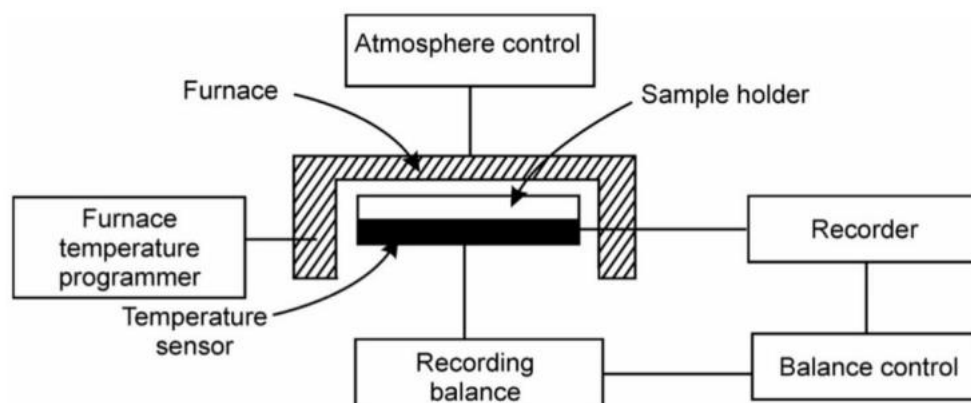


Figure 4.1 Figurative representation of the apparatus for thermo – gravimetric analysis.

TGA as well have its applicational purposes in the following; to determine the kinematics / dynamics for the rate of reaction constant, to understand the sublimation nature of substances, to compute thermal stability and purity factor for both primal and secondary reactions and to study the composition – decomposition of complex mixtures.

Thermo – gravimetric analysis (Thermogravimetric Analyzer (PERKIN ELMER TGA 4000)) was done to obtain the calcination temperature for CuO, CdO and TiO₂ (Anatase) and to understand the weight loss with respect to temperature for PANI, rGO and Ag nanopowders (**Table 4:1**).

Table 4:1: Tabular representation for the sample materials and drying and calcination temperatures.

Sample Name	Drying Temperature	Calcination Temperature
CuO	–	600 °C – 3 hours
CdO	–	400 °C – 7 hours
TiO ₂ (anatase)	110 °C – 3 hours	450 °C – 3 hours
PANI	60 °C – 7 hours	–
Ag	air dried at room temperature	–
GO, rGO	40 °C – 7 hours	–

4.2 Structural Analysis

4.2.1 X – Ray Diffraction (XRD)

X – Ray Diffraction technique plays a vital role in describing the physical and structural nature of the chemicals; powdered or thin films, gives details regarding chemical constituents and compositions, crystallographic nature / phases and orientations, state of purity, imperfection formations, phase composition, thickness of the thin films, magnitude of the particles, amorphous arrangement and crystallite size on an anatomical range, it also computes lattice parameters, grain stress and strain values, detects atomic arrangements, determines epitaxial structures and unit cell dimensions.

The device of this characterisation tool consists of a source that initiates and provides the radiations, the wavelength of the device is set using a mono – chromator, the outline of the incident beam is supervised and adjusted by the usage of slits, the sample holder in which sample is placed and a locator or detector to detect the values. The nature of the provided powdered type sample should be very fine and it should evenly spread out in the glass well so as to have values from all the corners when rotation is done. The role of goniometer is to determine the position of the detector and also adjustment required for the placement of sample, as the construction upholds both the detector and the sample which helps with detailed and specific motions. The originator for the X – Rays incorporates various modules; K_{α} and K_{β} , certain wavelengths are the primal attributes to the target substance such as; Fe, Cr, Cu, Mo. The filters and mono – chromator are fundamentally utilized to permit the passage of K_{β} wavelength, whilst absorbing the unnecessary K_{α} wavelength emissions. The umpteen consideration for the source of X – Ray radiations in this procedure is Copper, with wavelength $Cu K_{\alpha} = 1.5406 \text{ \AA}$. The sorted X – Rays are centralized and accumulated upon the sample material. The probability of orientation angle for the diffraction to take place is 2θ , when the striking of the incident beam takes place on the sample. Geiger counter is connected to the chart recorder and it is used as the moveable detector to discover the diffracted beams. The consideration for the pattern is done with the Geiger counter pre – determined over the range scale of 2θ values with an invariable angular velocity and scanning speed = 2θ for $2^{\circ} \text{ min}^{-1}$. The scale of $5^{\circ} - 70^{\circ}$ is considered for the spectrum values of 2θ for the readings of the sample material, as the required values and bonds tend to show within the said range. The obtained X

– Rays signals are then recorded and processed by a detector which further transforms these input signals to a count rate. These values are then put onto a computer monitor or a printer (Figure 4.2).

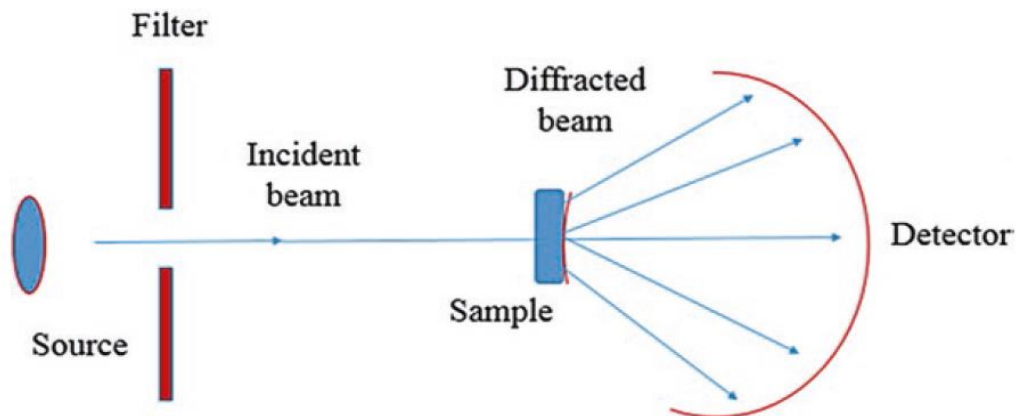


Figure 4.2 Figurative representation of the working for x – ray diffraction analysis [119].

The working principle of XRD tool is simply based on the formation of constructive interference of the mono – chromatic x – rays obtained from the crystalline ordered structure of the sample material. The x – rays are produced from the cathode – ray tube and are further sorted out to form mono – chromatic radiations which are then collected and concentrated in the direction where the sample is placed. The primal interaction happens between the x – rays and electrons existing in the atoms. They strike and a certain number of photons of the incoming ray get deviated from the intended path. This constructive and destructive interference of the x – rays form the diffraction pattern onto the detector. If the mirror image of the incident x – ray beam interferes constructively within the several planes, then it leads to the formation of Bragg’s Peak. The interference is considered constructive only when the phase shift is obtained as the multiple of 2λ . This requirement is known as Bragg’s Law and is given as:

$$n \lambda = 2 d \sin \theta$$

here; n = integer, λ = incident wavelength, d = spacing of the lattice planes and $\sin \theta$ = angle formed between the incident beam and the scattering planes [119] (Figure 4.3).

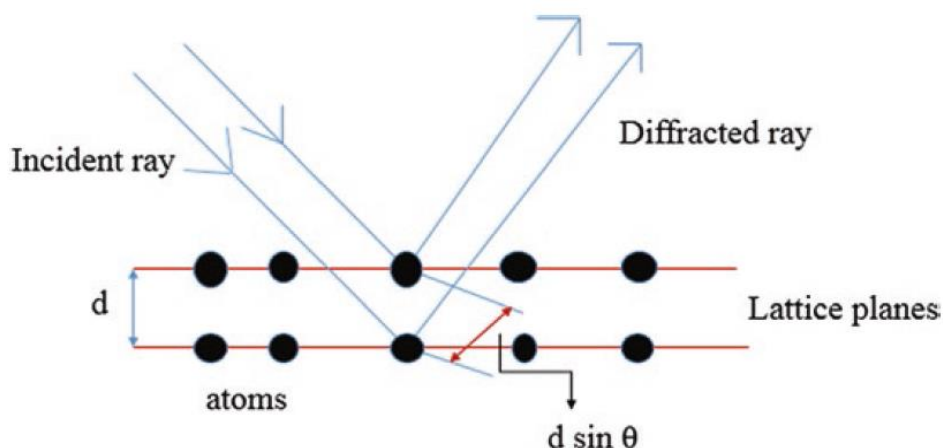


Figure 4.3 Figurative representation of the Bragg's Law [119].

X-Ray powder diffraction (XRD) (Bruker D8 Advance, $\text{CuK}\alpha$ 1.54\AA) was used for purity analysis as well as to acquire data regarding crystal structure and phase analysis for the sample powders.

- The crystallite size, D is defined as the smallest and theoretically, the single crystal present in the powdered form and is computed by Debye Scherrer's Equation.

$$D = \frac{k\lambda}{\beta^* \cos\theta}$$

Where, $\cos \theta$ = Bragg angle

β^* = full width at half maximum (*FWHM*) of the peak

λ = wavelength

k (*space factor*) = 0.94

- Lattice parameters are given by unit lengths; a , b , c which represents a unit cell or the unit defining the periodicity for an atomic arrangement. They are computed by the respective structural formulae (**Table 4:2**).

Table 4:2: Tabular representation for the Crystal Structure, Lattice Parameters and Formulae, Space Group, JCPDS for the sample materials of the present work.

Sample Name	Structure	Space Group	JCPDS	Lattice Parameter	Lattice Formula
CuO	Monoclinic [tenorite]	C_{2h}^6 C2/c	48-1548	$a \neq b \neq c,$ $\alpha = \gamma = 90^\circ \neq \beta$	$\frac{1}{d_{hkl}^2} = \frac{1}{\sin^2 \beta} \left[\frac{h^2}{a^2} + \frac{k^2 \sin^2 \beta}{b^2} + \frac{l^2}{c^2} - \frac{2hl \cos \beta}{ac} \right]$
CdO	Cubic [monteponite]	O_h^5 Fm3m	05-0640	$a = b = c,$ $\alpha = \beta = \gamma = 90^\circ$	$\frac{1}{d_{hkl}^2} = \frac{h^2 + k^2 + l^2}{a^2}$
TiO ₂	Anatase [Slender tetragonal]	D_{4h}^{19} I4 ₁ /amd	21-1272	$a = b \neq c,$ $\alpha = \beta = \gamma = 90^\circ$	$\frac{1}{d_{hkl}^2} = \frac{h^2 + k^2}{a^2} + \frac{l^2}{c^2}$
PANI	Amorphous	C _s	–	–	–
Ag	Cubic	O_h^5 Fm3m	04-0783	$a = b = c,$ $\alpha = \beta = \gamma = 90^\circ$	$\frac{1}{d_{hkl}^2} = \frac{h^2 + k^2 + l^2}{a^2}$
rGO	Amorphous	P6 ₃ /mmc	–	–	–

- Volume is represented by V which represents the amount of a three – dimensional space that is enclosed within a closed surface and is given by cubic meter. It is calculated using the given formula.

$$V = a \times b \times c$$

XRD Refinement was also done for the further confirmation of the sample purity.

4.2.2 Fourier Transform Infra – red Spectroscopy (FTIR)

FTIR is used to determine the organic and inorganic materials by identifying the occurrence of the peaks and the values and also to study the nature of the chemical groups pre-existing in the sample materials. The readings are taken over a large spectrum from 50 cm⁻¹ to 12500 cm⁻¹. The region that specifies the characteristics peaks of the material is called “Finger – print

region” and is usually considered between the scale from 400 cm^{-1} to 1500 cm^{-1} . This tool uses the infrared radiations absorptions against the wavelength values. These absorbed infrared bands recognize the structures and components of a molecule.

When the infrared radiations are made incident onto the materials surface, certain frequencies get transmitted without any absorption while, some frequencies get absorbed and these absorbed IR – frequencies provoke the molecules to enter into higher vibrational states. The wavelength of the light that is absorbed by a specific molecule occurs as the function of the energy difference between the stationary and excited states of vibrations. The occurrence of these vibrational bands in a molecule are used to identify and differentiate the various bonds and functional groups that have particular wavelength for the absorption. The apparatus consists of an interferometer which is used to regulate the wavelengths coming from the infrared source. The intensity of the transmitted and reflected rays is studied as the function of its wavelength and it is detected using a detector. The acquired signal is produced in the form of an interferogram, which is further examined by a computer that uses the Fourier – transform for the obtaining of infrared as single – beam spectrum. This FTIR spectra is graphically plotted between transmittance and wavelength (**Figure 4.4**).

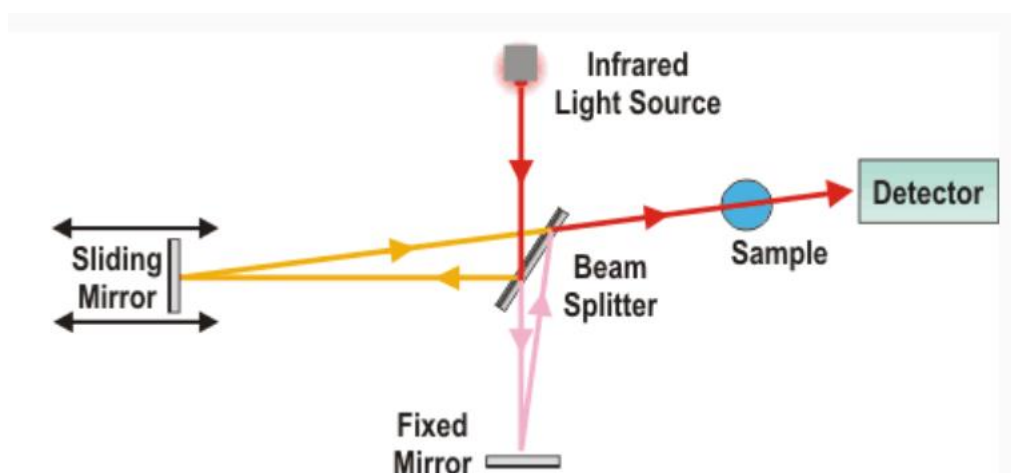


Figure 4.4 Figurative representation of the working for Fourier transform infrared spectroscopy analysis.

This tool is extremely helpful in identifying, determining and distinguishing the organic compounds and structures for various inorganic materials as well, unknown substances, fibres. To determine constituents of the bulk materials, components of multi – layered substances etc.

To get the peak values and to determine the nature for the chemical groups existing in sample powders, Fourier Transform Infrared Spectroscopy (FTIR), (Nicolet FTIR interferometer IR prestige-21 (model-8400S)) was utilized.

4.3 Molecular Analysis

4.3.1 Raman Spectroscopy

Raman analysis uses the spectroscopic approach to the molecular level using the data derived from the reaction between the incident light and the sample matter. This characterisation helps with determination of the material constituents by studying the light scattering processes occurring and giving details regarding the inter – and intra – molecular vibrations. Alike FTIR, Raman analysis also provides with a specific region for each vibration that determines the component, this particular region is called “Molecular Finger – print region”. This tool also helps with providing data for lower frequency modes, crystal lattice vibrations and molecular backbone structure. The applications of Raman spectroscopy also extend in determining the inorganic compounds, polymerization reactions and identification of polymorphism, chemical synthesis. They are employed on in various fields as well; solid – state and analytical chemistry, applied material, environmental and biomedical etc.

When the sample material interacts with the incident mono – chromatic beam of light then this light undergoes either absorption, reflection or scattering to some degree. Now the scattering route of the light plays the vital role in Raman analysis because the statistics concerning the molecular structure are obtained from the scattered light (**Figure 4.5**).

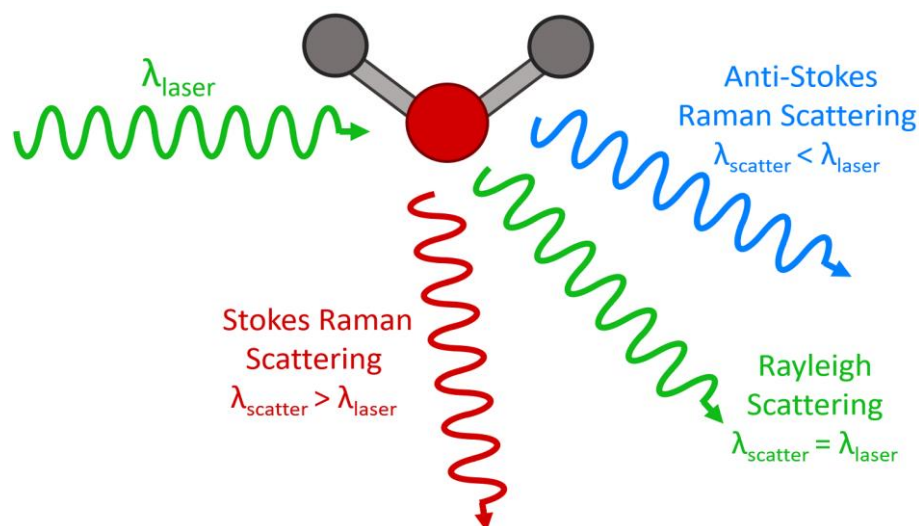


Figure 4.5 Figurative representation of the working for Raman and Rayleigh scattering.

The working mechanism includes the illumination of the material with the laser source and the interactivity between the light and the chemical bonds of the sample material. Majority of the light scattered has the wavelength equal to that of the laser wavelength and is not useful as it does not supply with functional details, this elastic scattering of light is known as Rayleigh scattering. Whereas, a certain quantity of the light gets scattered at varying wavelengths that has its dependence on the chemical structure and this type of inelastic scattering is known as Raman scattering. This is further sub – divided into two parts; Stokes and Anti – Stokes Raman scattering (**Figure 4.6**).

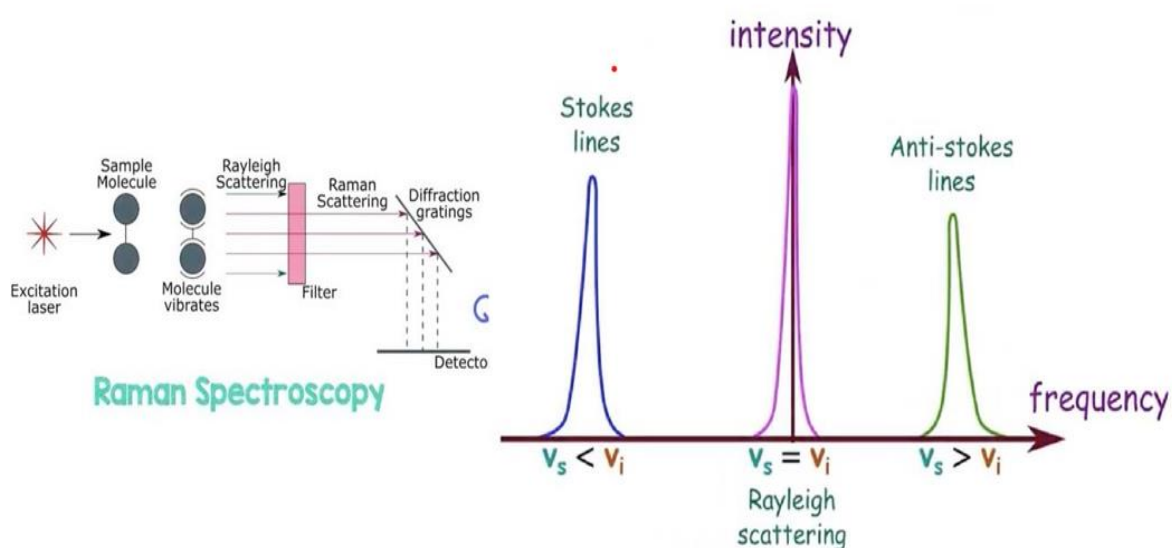


Figure 4.6 Figurative representation of the working for Raman spectroscopy analysis.

Raman Analysis via (Confocal Micro-Raman spectrometer (STR 500) AIRIS Japan using the solid-state laser with the excitation wavelength 532 nm) was done to obtain the molecular vibrations and the states of existence for the specific components.

4.4 Surface Analysis

4.4.1 Field Emission Scanning Electron Microscopy (FESEM)

FESEM utilizes the employment of electrons as compared to light used in structural and molecular spectroscopies. The electron is used to generate the electron beams at the pinnacle of the microscope. This beam of electron passes through the microscope in a perpendicular pathway that is supported in the vacuum. This electron beam then proceeds across the electro – magnetic fields and lenses which furthermore, centralize this beam into the sample's direction. As the beam comes in connection with the sample, certain electrons and x – rays get ejected out of the sample. These ejected electrons are obtained by the detectors in the form of secondary electrons and back – scattered electrons, which then transformed in the signals that are acquired on the screen in the form of a concluded resultant image. Back – scattered electrons are procured when they get reflected back from the elastic collision between the incident beam and the sample material, whereas the Secondary electrons stem from the within the atoms of the sample material and arise after inelastic collision of the incident light and sample (**Figure 4.7**).

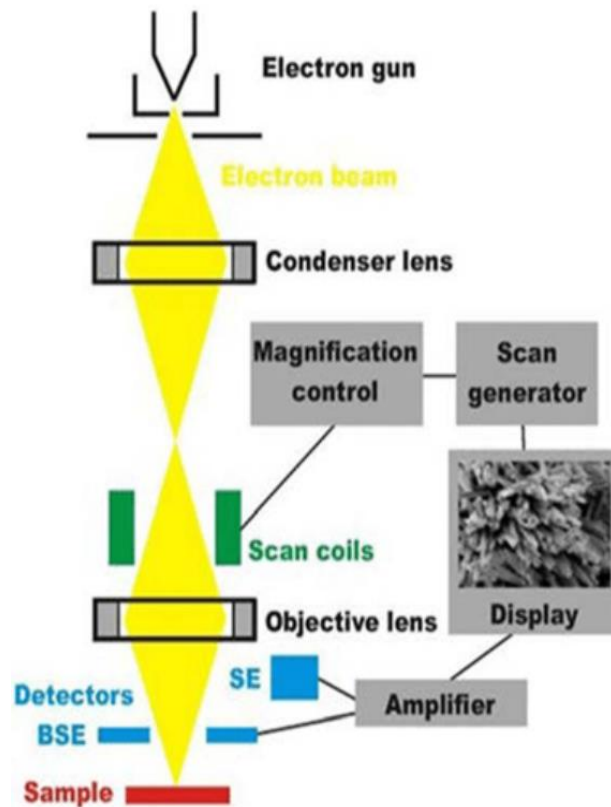


Figure 4.7 Figurative representation of the working for Field Emission Scanning Electron Microscopy analysis.

The tool is applied to analyse the semiconductor device cross – sectional values regarding the details concerning gate widths, construction and thickness of the films. It is also used in the studying the thickness for the modified coatings and to determine the structure homogeneity. It also provides information for the minuscule impurities that occur within the sample and the elemental compositions.

4.4.2 Energy Dispersive X – Ray (EDX)

EDX or EDAX is used to obtain information regarding the compositions of the elements existing in a sample material. It is a non – destructive tool that gives qualitative and quantitative information, it supplies the details for constituents in the form of elemental ratio and gives particulars for the spatial distribution in the form of elemental mapping. EDX mapping permits the exceedingly instantaneous accumulation of the elemental concentrations to be collected from either along the lines or points and can be obtained as maps as well. EDX provides the

ratio details by creating an analysis spectrum that exhibits the peaks adjacent to the elements that are constructing the material composition.

The working principle of EDX follows Moseley's Law i.e., the core electrons that are not present in the outer most shell of the atoms gets ejected by the high energy electro – magnetic x – rays. This determines and confirms the occurrence of the first – hand connection between the light frequency and atomic number of an atom. When the electron gets removed from the network, it results into the formation of a hole which c be filled with a high energy electron. This also causes in the discharging of the energy as the electron relaxes. This released energy whilst the relaxation reaction has specific values w.r.t each element of the periodic table. Through this way, the pre – existing elements and their percentage can be determined by incident x – rays attack on the sample material (**Figure 4.8**).

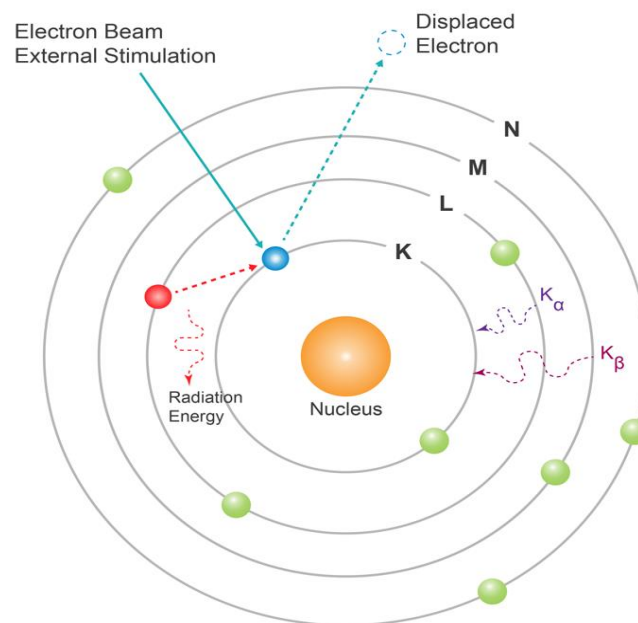


Figure 4.8 Figurative representation of the working for Energy Dispersive X - Ray analysis.

EDX is often used for the fastened determination for the impurities and their sources, to find out the origin of the problem in a process chain, it provides complete command over the emissions and environmental facets, it provides higher values for the output generated, this tool as well aids with the functionalise of the process and supports authority for the advancement in the quality section.

4.4.3 Particle Size Analysis (PSA)

Particle size distribution analysis is done to study the particle size distribution of the provided sample material and they can be employed on suspensions, aerosols, emulsions and solid-state substances. This characterization tool plays a vital role in various industries and firms where precisely fine particles are the requirements such as pharmaceuticals and medical industries, food – beverages, raw materials used for construction and building, paints, coatings etc.

It is utilized where grinding, milling and such techniques are worked on where the finer quality of the demanded substance need supervision. Due to fact that, it regulates and decides the productivity and working capability of the processing techniques as well their rate of performance.

The details regarding the topographical morphology were provided by Field Emission Scanning Electron Microscopy (FESEM) ((FEI Nova Nano SEM 450 FE-SEM), operated at 15 kV voltage). The particle size plot was also obtained using the softwares ImageJ and Origin. The elemental ratio was obtained using EDX.

4.5 Varistor

Varistors are the electrical tools, having variations in its voltage values with respect to the device's resistance. They are levelled up in parallel to the said circuits and are availed as the protection appliances against the high voltage outpouring. In the standard circumstances, a certain quantity of current is allowed to pass through the device, but when the voltage surpasses a definite value, the varistors shuns down the circuit activity by subduing the voltage and drastically decreasing the resistance within the circuit and thus protecting from short circuiting or causing fires. Varistors can operate with both low voltage and high voltage values, as per the requirement of the sector involved, such as; they are used in smart devices for households, where lower voltages are required and are used as protective measurements in electrical sectors in large scale sectors where higher voltages are necessity [64][66].

Current versus voltage trace was analysed for the in – depth understanding of the electrical performance of the samples and their functioning in terms of varistor usage. In order to see the

effect of the doped material in the working capability of the host material, the sample material content was also put against non – linear coefficient values (α) for the compositions where the said values were obtained. Pellets, each of thickness = 0.5 cm and diameter = 1.20 cm, were prepared and furthermore, a layer of silver paste which acted as an electrode was over – layered on them.

Chapter 5

5 RESULTS AND DISCUSSIONS

5.1 CuO mixed with Ag

5.1.1 TGA Studies

- TGA analysis – CuO nanopowders.

TGA is substantially availed to outline the thermal nature of the materials by evaluating the variations in the mass of sample powders w.r.t to increasing temperature. This tool provides details regarding the fluctuations in mass concerning with the quantity of water molecules present in the powders and due to process of evaporation, degradation or oxidation of the volatile compounds.

TGA was used onto the uncalcinated sample powders of copper oxide, CuO which were obtained through the auto – combustion sol – gel synthesis procedure. This characterisation was done in order to acquire the calcination temperature for the thermal treatment to procure the pure nano – structured powders. The variation in the mass of the CuO powders w.r.t temperature was studied over the temperature scale range from 40 °C to 800 °C at the rate of 10 °C per / minute, with a hold on the specimen for about 1 minute at 800 °C. In total 3 phases were obtained for the declining percentage in the mass that were as follows:

(I). Phase I: 41 °C – 619 °C, $\Delta Y =$ Major weight loss. The first stage sustained a massive loss in the mass percentile with regards to the temperature because of the thermal degradation of all the volatile and organic compounds that were coupled on the surface of the sample nano – powders during synthesis process. This step as well entailed the decomposition of the water molecules that were pre – existing within the sample structure and also the CO₂ molecules present in the atmosphere that were physiosorbed when the material was subjected to atmospheric conditions.

(II). Phase II: 619 °C – 754 °C, This step did not observed a significant weight loss amounting to a considerable value. It was obtained to be less than 10%. Which further implies that no thermal declining takes place due to the loss of any molecule during this heat scale and thus confirming that the crystallization of CuO nano – powders has taken place.

(III). Phase III: 754 °C – 800 °C, This last phase exhibited a drop in its nature after the 754 °C. This dip might be the indication of the probable appearance of the another intermediate of CuO i.e., Cuprous Oxide Cu₂O.

To obtain the needed pure metal – oxide phase for the sample material, CuO nano – powders were calcinated for 3 hours at 600 °C in the furnace [120][121][122][123][124] (**Figure 5.1**).

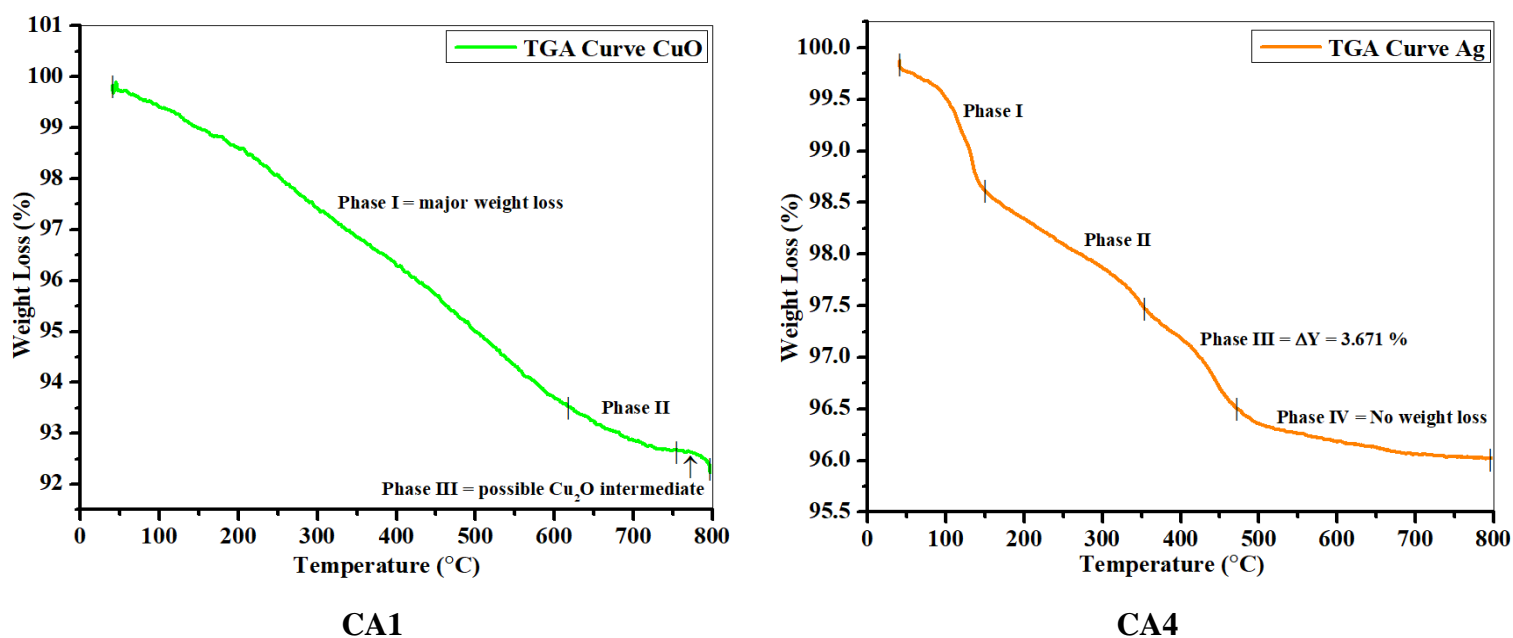


Figure 5.1 TGA Analysis of CA1 [CuO, 1:0] and CA4 [Ag, 0:1].

- TGA analysis – Ag nanopowders.

The Ag nano – powders were obtained by utilizing top – down method, in this process the procured sample nano – powders were dried in the atmospheric conditions by open air heat through the process of evaporation, till the water content of the solution was vaporized. Ag sample nano – powders underwent the heat treatment over the temperature range of 40 °C – 800 °C with the rate of 10 °C per minute. The temperature was held for 1.0 minute at 800 °C.

The TGA tool was employed on the Ag nanoparticles to observe the weight fluctuations with varying temperatures. The said plot exhibited 4 phases which were as follows:

(I). Phase I: 40 °C – 149 °C. This step was the result of the evaporation or release of the water molecules that were linked to the surface of the metallic nano – powders whilst the synthesis procedure.

(II). Phase II: 149 °C – 353 °C. In this phase, the degradation process of the volatile and organic – capping constituents that were prevailing in the sample Ag nano – structure takes place.

(III). Phase III: 353 °C – 472 °C; $\Delta Y = 3.671 \%$. During this phase, the initiation for the crystallization process of Ag nano – powders was observed.

(IV). Phase IV: 472 °C – 800 °C; $\Delta Y = >10\%$ weigh loss. In last stage not much of a decline in the mass percentile was obtained w.r.t temperature changes. This observation assured no further release of any molecules and thus confirmed the completion of the silver nano – structures.

The acquired TGA plot affirmed the process of desorption on the surface of metallic nano – powders regarding the bio – organic compounds [5][125][126][127][128][129][130] (**Figure 5.1**).

5.1.2 XRD Pattern

The tool of XRD was employed on to the sample nano – structured compositions for the analysis of the degree of the specimen purity, for the specifications w.r.t to unit dimensions, volume and crystallite size and crystalline phase.

Both CuO and Ag has highly ordered crystalline structure and therefore, XRD peaks for all the sample codes were procured which were further compared with the existing data for the confirmation of the formation of the desired crystal arrangement. For CA1, the attendance of CuO construction was observed with the appearance of the peaks at $2\theta^\circ$ values = 32.46°, 35.45°, 38.68°, 48.74°, 53.45°, 61.54°, 65.82°, 66.23°, 68.04°, 72.42°, 75.16° with the

corresponding (hkl) values at = (110), (11-1), (200), (20-2), (020), (11-3), (022), (310), (220), (311), (22-2) respectively. These values were obtained following the JCPDS card: 48 – 1548 [86][131][132][133][134][135][136][137][138][139][140][141][142][143][144]. For CA2, the characterized peaks were acquired for the $2\theta^\circ$ values at = 35.49°, 38.69°, 48.75°, 58.27°, 61.54°, 65.80°, 66.20°, 68.01° and the adjacent (hkl) values were indexed at = (11-1), (200), (20-2), (020), (11-3), (022), (310), (220) for CuO. In this case, the advent of Ag peaks was also observed for the values of $2\theta^\circ$ = 38.10°, 44.26°, 64.43°, 77.89° with the respective (hkl) values at = (111), (200), (220), (311). For CA3, the $2\theta^\circ$ values for CuO arrangement were = 35.48°, 38.67°, 48.75°, 61.52°, 66.21°, 68.01° and the (hkl) planes were observed for the said values at = (11-1), (200), (20-2), (11-3), (310), (220). The Ag peaks were obtained at $2\theta^\circ$ values = 38.09°, 38.18°, 44.27°, 64.43°, 77.38° and these values had (hkl) plane values recorded at = (111), (111), (200), (220), (311) respectively. For CA4, the peak values that were ascribed to Ag nature were procured at the $2\theta^\circ$ values = 38.09°, 44.27°, 64.45°, 77.40° with the values for (hkl) planes catalogued at = (111), (200), (220), (311). The afore – mentioned values were observed to be in assent with JCPDS card: 04 – 0783 [145][146][147][148][149][150][151][152][153][154] (**Figure 5.2**).

The outcomes of the sample codes CA1, CA2, CA3, CA4 were put in comparison to each other. CA1 (1:0) and CA4 (0:1) were containing of undoped sample powders therefore, they constituted purely of CuO and Ag nano – powders respectively. On the other hand, it was observed that the number of the peaks for CuO nano - powders showed a decline in the samples CA2 (1:1), CA3 (1:2) and the reason behind this was that the content of silver was increasing for the mentioned specimen codes. Thus, as the amount of Ag was increasing, the quantity of CuO was decreasing and hence the corresponding peaks were also lessening. This in furtherance assured the formation for silver crystal by exhibiting the corresponding peaks and **Table 5:1** provides the XRD peaks and (hkl) plane values in tabular form.

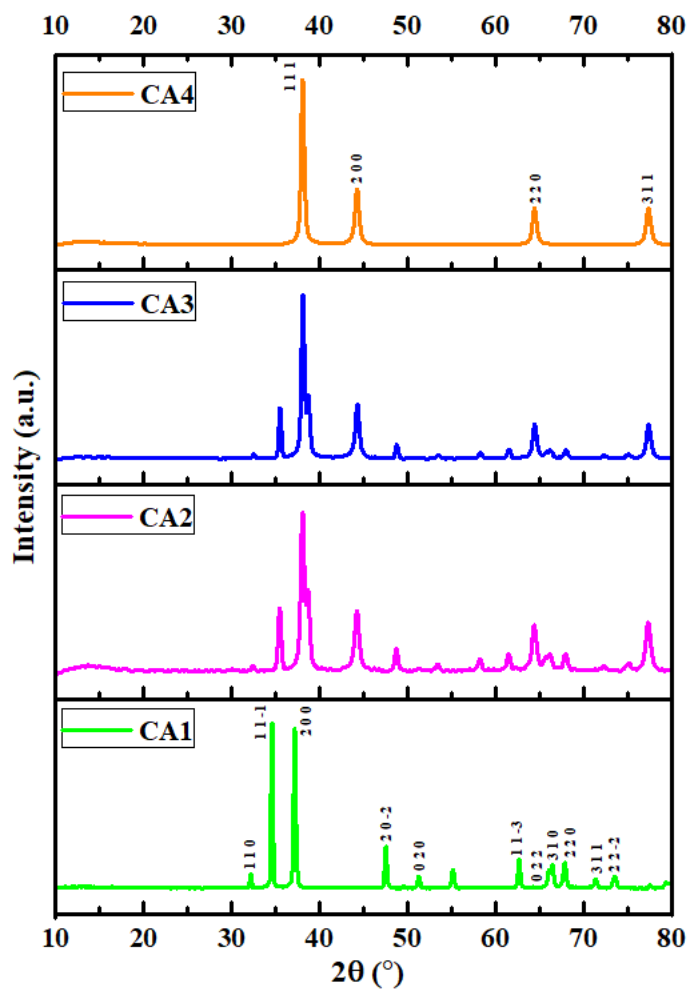


Figure 5.2 XRD Analysis of CA1 [CuO, 1:0], CA2 [CuO + Ag, 1:1], CA3 [CuO + Ag, 1:2] and CA4 [Ag, 0:1].

Table 5:1: Values for the XRD peaks and (hkl) index planes of CA1 [CuO, 1:0], CA2 [CuO + Ag, 1:1], CA3 [CuO + Ag, 1:2] and CA4 [Ag, 0:1].

Sample code	CuO		Ag	
	$2\theta^\circ$	<i>hkl</i>	$2\theta^\circ$	<i>hkl</i>
CA1 (1:0)	32.46°	110	-	
	35.45°	11-1		
	38.68°	200		
	48.74°	20-2		
	53.45°	020		
	61.54°	11-3		
	65.82°	022		
	66.23°	310		
	68.04°	220		
	72.42°	311		
75.16°	22-2			
CA2 (1:1)	35.49°	11-1	38.10°	111
	38.69°	200	44.26°	200
	48.75°	20-2	64.43°	220
	58.27°	020	77.89°	311
	61.54°	11-3		
	65.80°	022		
	66.20°	310		
	68.01°	220		
CA3 (1:2)	35.48°	11-1	38.09°	111
	38.67°	200	38.18°	111
	48.75°	20-2	44.27°	200
	61.52°	11-3	64.43°	220
	66.21°	310	77.38°	311
	68.01°	220		
CA4 (0:1)	-		38.09°	111
			44.27°	200
			64.45°	220
			77.40°	311

The crystallite size (D), lattice parameters (a, b, c), volume (V) were also computed for both CuO and Ag nano – powders. In this case, both copper oxide and silver have ordered structures and therefore the afore – mentioned variables were evaluated for all the sample codes. CuO executes monoclinic structure in tenorite phase and henceforth, the lattice parameters satisfy the condition $a \neq b \neq c$. Whereas, Ag constitutes of cubic crystalline arrangement and thus have lattice parameters $a = b = c$. The values for the parameters were calculated using the respective structural formulae and **Table 5:2** lay – outs the tabular representation for the values.

$$D = \frac{k\lambda}{\beta^* \cos\theta}; \text{ (Debye Scherrer's Equation)}$$

$$\frac{1}{d_{hkl}^2} = \frac{1}{\sin^2\beta} \left[\frac{h^2}{a^2} + \frac{k^2 \sin^2\beta}{b^2} + \frac{l^2}{c^2} - \frac{2hlc\cos\beta}{ac} \right]; \text{ (monoclinic formula – tenorite phase for CuO nanoparticles)}$$

$$\frac{1}{d_{hkl}^2} = \frac{h^2 + k^2 + l^2}{a^2}; \text{ (Cubic formula for Ag nanoparticles)}$$

$$V = a \times b \times c; \text{ (Volume)}$$

Table 5:2: Lattice parameters (a, b, c), Crystallite Size (D), FWHM (β^*), Bragg's angle (2θ) and Volume (V) for CA1 [CuO, 1:0], CA2 [CuO + Ag, 1:1], CA3 [CuO + Ag, 1:2] and CA4 [Ag, 0:1].

		a (Å)	b (Å)	c (Å)	D (nm)	β^* (°)	2θ (°)	V (Å) ³
CA1 (1:0)	CuO	4.7167	3.4256	5.1242	30.0148	5.1112×10^{-3}	38.68	82.8031
CA2 (1:1)	CuO	4.7159	3.4189	5.1774	23.1444	6.6288×10^{-3}	38.69	83.4799
	Ag	4.0894	4.0894	4.0894	19.7754	7.9023×10^{-3}	44.26	68.3878
CA3 (1:2)	CuO	4.7181	3.4181	5.1992	24.9131	6.1578×10^{-3}	38.67	83.8492
	Ag	4.0884	4.0884	4.0884	26.6625	5.8613×10^{-3}	44.27	68.3376
CA4 (0:1)	Ag	4.0866	4.0866	4.0886	23.9534	6.5242×10^{-3}	44.27	68.3476

Rietveld refinement graphical plots were also obtained using 'Fullprof Suite' software for all 4 compositions CA1 [CuO, 1:0], CA2 [CuO + Ag, 1:1], CA3 [CuO + Ag, 1:2] and CA4 [Ag, 0:1] as the both CuO and Ag has structured crystalline nature (**Figure 5.3**). From the graphs, Y_{obs} = these were the already computed values, Y_{cal} = these were obtained values from the experimental work done. $Y_{obs} - Y_{cal}$ = this gave details regarding the difference between already calculated values and experimentally acquired values, Bragg's angle = this revealed data concerning the positions and numbers of the visible peaks that were obtained from the

experimental work. From **Figure 5.3**, it was observed that all the computed peaks for both CuO and Silver nanopowders were in accordance with the standardised peaks values. The absence of Cu_2O peaks and other unnecessary peaks were also noticed which furthermore, confirmed that the experimentally synthesised samples were single phased nanopowders.

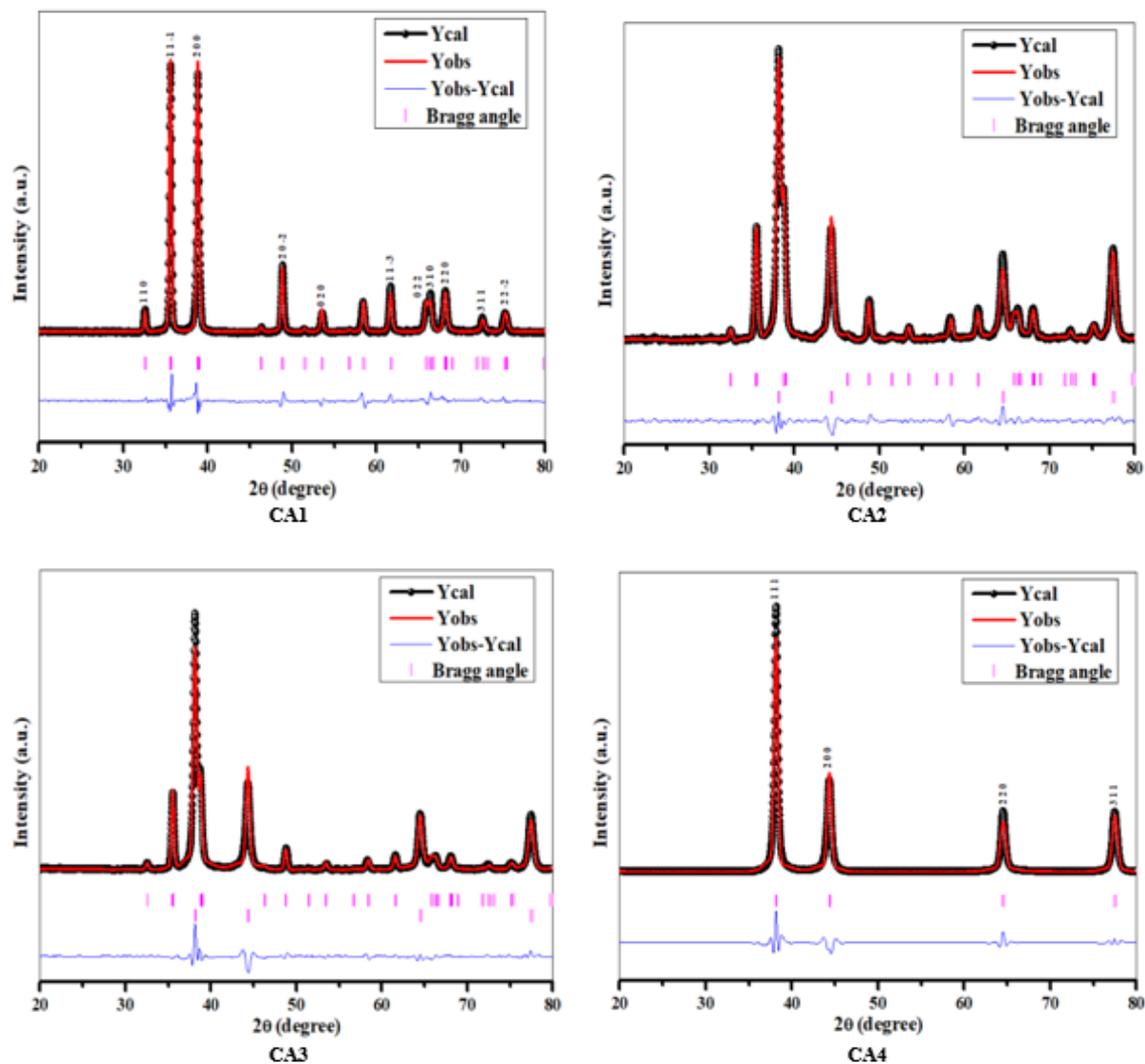


Figure 5.3 XRD-Refinement plot of CA1 [CuO, 1:0], CA2 [CuO + Ag, 1:1], CA3 [CuO + Ag, 1:2] and CA4 [Ag, 0:1].

5.1.3 FTIR Analysis

FTIR spectroscopy was put into play for the distinguishing the materials involved and thus confirming the formation of the desired nanopowders. This characterisation tool discloses the elemental constitutions for liquids, solids and gases. Furthermore, it helps with the identification of impurities and anatomization for the coatings and thin films. For CA1, the asymmetric stretching vibrations for the hydroxyl bonds of the water molecules that lead to the engender of – OH bonds were obtained within peak range from 3991.83 cm^{-1} to 3213.90 cm^{-1} . These were generated due to the H_2O molecules which were present in the atmosphere whilst synthesis process and the moistened CuO nanopowders that were adsorbed because of the ability of nanoparticles to exert higher surface volume ratio. The bond at 2977 cm^{-1} was for the – OH symmetric stretching for adsorbed water molecules. The O = C = O peak was observed at 2359 cm^{-1} . This peak was produced due the CO_2 molecules present in the aerosphere while making of the sample nano – powders. The peak obtained at 1647.56 cm^{-1} was for the symmetrical stretching for Cu – O bond. The 1535.39 cm^{-1} peak represented the development of the covalent bonding of the – OH molecule from H_2O on the surface of CuO nanopowders. The bond formation due to carboxylate ion acting up as bidentate ligand which led to C = O stretching was observed at procured at 1418.37 cm^{-1} . The peaks acquired at 1248.09 cm^{-1} , 1150.44 cm^{-1} , 1072.97 cm^{-1} were designated to stretching vibrations of the C – O bond correlating to the presence of metal cations. The characteristic peaks of for the CuO monoclinic structure that were adjacent to stretching vibrations for Cu – O bond were acquired at 687.22 cm^{-1} , 672.70 cm^{-1} , 663.01 cm^{-1} , 638.80 cm^{-1} , 629.12 cm^{-1} , 604.98 cm^{-1} , 595.22 cm^{-1} , 590.38 cm^{-1} , 575.05 cm^{-1} , 570.20 cm^{-1} , 536.31 cm^{-1} , 521.78 cm^{-1} , 507.26 cm^{-1} . There was no peak obtained at 615 cm^{-1} , which is related to the Cu_2O formation. This means that obtained sample nanopowders did not contained any impurities [155][156][157][158][159][160][161][162][163][164][165][166][167][168][169][170]. For CA2, the standardised peaks that were in accordance to the monoclinic arrangement of CuO were obtained as follows: a broad range of peaks in the scale range 3382.63 cm^{-1} – 3212.35 cm^{-1} (asymmetric – OH bond of H_2O molecules). 2973.48 cm^{-1} (symmetric – OH bond of H_2O molecules). 2354.50 cm^{-1} (O = C = O bond of atmospheric CO_2). 1647. 56 cm^{-1} (symmetric Cu – O bond). 1535.39 cm^{-1} (covalent bond between – OH and CuO surface). 1413.53 cm^{-1} (– C = O bond stretching). 1235.57 cm^{-1} , 1145.60 cm^{-1} , 1135.92 cm^{-1} , 1121.39 cm^{-1} , 1062.48 cm^{-1} (stretching vibrations of C – O bond). 696.91 cm^{-1} , 682.38 cm^{-1} , 672.72 cm^{-1} , 667.85 cm^{-1} , 575.05 cm^{-1} , 512.10 cm^{-1} (characteristic peaks for Cu – O bond). No peak was obtained for Cu_2O in this sample case. The emergence of Ag nanopowders was also observed. A widened curve in the plot from 3967.71 cm^{-1} –

3412.49 cm^{-1} (– OH bond of residual H_2O molecules). 1540.23 cm^{-1} , 1520.86 cm^{-1} , 1511.18 cm^{-1} (N – O bonds for nitro compounds). 1389.32 cm^{-1} (NO_3^- ion). 1360.27 cm^{-1} (N = O bond). For CA3, the characteristic bonds for CuO were; the peaks in the range from 3393.47 cm^{-1} – 3217.20 cm^{-1} (– OH asymmetric bond for H_2O molecules). 2973.48 cm^{-1} (– OH symmetric bond for H_2O molecules). 2354.50 cm^{-1} (O = C = O bond for atmospheric CO_2). 1647.56 cm^{-1} (Cu – O symmetric bond). 1535.39 cm^{-1} (covalent bonding of – OH and CuO surface). 1418.37 cm^{-1} (stretching bond for C = O). 1233.57 cm^{-1} , 1145.60 cm^{-1} , 1121.39 cm^{-1} , 1062.48 cm^{-1} (peaks for C – O stretching vibrations). 692.06 cm^{-1} , 687.22 cm^{-1} , 663.01 cm^{-1} , 638.80 cm^{-1} , 580.70 cm^{-1} , 571.20 cm^{-1} , 516.94 cm^{-1} , 502.42 cm^{-1} (Cu – O structural peaks). The Ag nanopowders also exhibited the structural peaks. The broad curve ranging from 3924.14 cm^{-1} – 3417.33 cm^{-1} (residual water molecule – OH bond). 1549.91 cm^{-1} , 1525.70 cm^{-1} , 1511.18 cm^{-1} (N – O bonds of nitro compounds). 1389.32 cm^{-1} (NO_3^- ion). 1360.27 cm^{-1} (N = O bond) and no peaks around 615 cm^{-1} for Cu_2O was observed in this case as well. For CA4, the Ag nanopowders displayed the desired peaks corresponding to its cubic structure. A broad – ranging curve was obtained which constituted of number of peaks from 3958.03 cm^{-1} to 3417.33 cm^{-1} . These peaks were the resultant of the unconsumed H_2O molecules because the silver solution was heated till dried to evaporate the water content of sample solution. The heating was done at room temperature as the synthesis procedure did not require any further chemical treatment. The peaks at 1545.07 cm^{-1} , 1525.39 cm^{-1} , 1516.02 cm^{-1} were designated as the peaks for the N – O bond concerning the nitro compounds. The peak for the NO_3^- ion bond was observed at 1384.48 cm^{-1} and 1365.11 cm^{-1} was recognised as the peak for the N = O bond [171][172][173][174][175][176] (**Figure 5.4**).

When the results for all the sample codes were compared against each other, it was noted that the intensity and quantity of CuO peaks were decreasing as the content for Ag nanopowders were increasing in the ratio for the composition sample codes CA2 (1:1) and CA3 (1:2). This also lessened the quality of peaks obtained for CuO nanopowders. Therefore, the peaks for Ag were observed to be more prominent and visible. This led to confirmation for the crystallisation of metallic nano – powders. The sample codes CA1 (1:0) and CA4 (0:1) consisted only of individual sample nanopowders and thus exhibited the bonds corresponding only for CuO and Ag respectively. **Table 5:3** lays – out the tabular representation for the obtained FTIR peaks for all the sample codes.

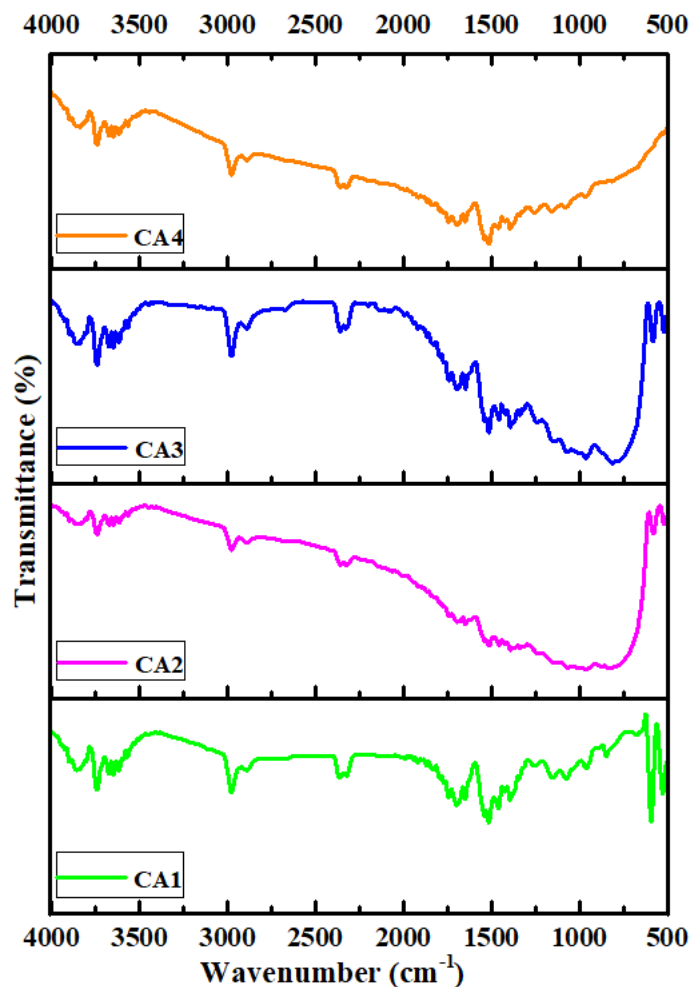


Figure 5.4 FTIR Analysis of CA1 [CuO, 1:0], CA2 [CuO + Ag, 1:1], CA3 [CuO + Ag, 1:2] and CA4 [Ag, 0:1].

Table 5:3: FTIR peaks and the corresponding bonds associations for CA1 [CuO, 1:0], CA2 [CuO + Ag, 1:1], CA3 [CuO + Ag, 1:2] and CA4 [Ag, 0:1].

	Peak Names	CA1 (CuO - 1:0)	CA2 (CuO + Ag - 1:1)	CA3 (CuO + Ag - 1:2)	CA4 (Ag - 0:1)
1.	- OH asymmetric bond of H ₂ O molecules	3991.83 cm ⁻¹ – 3213.90 cm ⁻¹	3382.63 cm ⁻¹ – 3212.35 cm ⁻¹	3393.47 cm ⁻¹ – 3217.20 cm ⁻¹	–

Chapter 5. Results and Discussions

2.	– OH symmetric bond of H ₂ O molecules	2977 cm ⁻¹	2973.48 cm ⁻¹	2973.48 cm ⁻¹	–
3.	– O = C = O bond due to atmospheric CO ₂ .	2359 cm ⁻¹	2354.50 cm ⁻¹	2354.50 cm ⁻¹	–
4.	Cu – O symmetric vibrations	1647.56 cm ⁻¹	1647.56 cm ⁻¹	1647.56 cm ⁻¹	–
5.	Covalent bonding of – OH and CuO surface	1535.39 cm ⁻¹	1535.39 cm ⁻¹	1535.39 cm ⁻¹	–
6	C = O stretching bond	1418.37 cm ⁻¹	1413.53 cm ⁻¹	1418.37 cm ⁻¹	–
7.	C – O stretching vibrations bond	1248.09 cm ⁻¹ , 1150.44 cm ⁻¹ , 1072.97 cm ⁻¹	1235.57 cm ⁻¹ , 1145.60 cm ⁻¹ , 1135.92 cm ⁻¹ , 1121.39 cm ⁻¹ , 1062.48 cm ⁻¹	1233.57 cm ⁻¹ , 1145.60 cm ⁻¹ , 1121.39 cm ⁻¹ , 1062.48 cm ⁻¹	–
8.	Characteristic peaks for Cu – O bond	687.22 cm ⁻¹ , 672.70 cm ⁻¹ , 663.01 cm ⁻¹ , 638.80 cm ⁻¹ , 629.12 cm ⁻¹ , 604.98 cm ⁻¹ , 595.22 cm ⁻¹ , 590.38 cm ⁻¹ , 575.05 cm ⁻¹ , 570.20 cm ⁻¹ , 536.31 cm ⁻¹ , 521.78 cm ⁻¹ , 507.26 cm ⁻¹	696.91 cm ⁻¹ , 682.38 cm ⁻¹ , 672.72 cm ⁻¹ , 667.85 cm ⁻¹ , 575.05 cm ⁻¹ , 512.10 cm ⁻¹	692.06 cm ⁻¹ , 687.22 cm ⁻¹ , 663.01 cm ⁻¹ , 638.80 cm ⁻¹ , 580.70 cm ⁻¹ , 571.20 cm ⁻¹ , 516.94 cm ⁻¹ , 502.42 cm ⁻¹	–
9.	– OH peaks due to the unevaporated water molecules left in sample solution	–	3967.71 cm ⁻¹ – 3412.49 cm ⁻¹	3924.14 cm ⁻¹ – 3417.33 cm ⁻¹	3958.03 cm ⁻¹ – 3417.33 cm ⁻¹

10.	N – O bond resultant of the presence of nitro compounds	–	1540.23 cm ⁻¹ , 1520.86 cm ⁻¹ , 1511.18 cm ⁻¹	1549.91 cm ⁻¹ , 152570 cm ⁻¹ , 1511.18 cm ⁻¹	1545.07 cm ⁻¹ , 1525.39 cm ⁻¹ , 1516.02 cm ⁻¹
11.	NO ₃ ⁻ ion bond	–	1389.32 cm ⁻¹	1389.32 cm ⁻¹	1384.48 cm ⁻¹
12.	N = O bond	–	1360.27 cm ⁻¹	1360.27 cm ⁻¹	1365.11 cm ⁻¹

5.1.4 Raman Spectroscopy

The employment of Raman spectra was done to analyse the inert structure of the sample powders. This tool helps with the identification of the attached functional groups, intra – molecular and chemical bonding. Furthermore, it gives details with respect to the crystal structure at molecular level by providing the respective structural finger – print concerning the vibrations of the molecules.

For CA1, CuO falls under the space group C_{2h}^6 i.e., each primitive cell is concerned with two primitive cells and therefore is associated with the monoclinic crystal structure. In this space group system, each primitive cell acquires 4 atoms within itself, thus the number of phonons branches existing are 12. The Zone – Centre Optical – Phonon modes are equated as: $r = A_g + 2 B_g + 4 A_u + 5 B_u$. Amid these, there are 9 optical modes and amongst them there persist 3 Raman active modes that are given by $(A_g + 2 B_g)$ and 6 Infra – red active modes that are represented as $(3 A_u + 3 B_u)$. In addition to this, there are 3 acoustic modes that is denoted by $(A_u + 2 B_u)$ symmetry. As only 3 effectual Raman modes exist therefore, the values for A_g , B_{1g} , B_{2g} – symmetry modes were obtained for CuO nanopowders. For the case of both A_g and B_g modes, O – atoms advance along the b – direction for A_g mode but moves in perpendicular direction to b – axis for B_g . The peak value procured at 286.37 cm⁻¹ was designated to A_g – mode. The B_{1g} – mode was observed at 332.71 cm⁻¹ and 616.32 cm⁻¹ peak was obtained for B_{2g} – mode [177][178][179][180][181][182]. For CA2, the Raman peaks for CuO were observed as follows: 286.69 cm⁻¹ (A_g – mode), 334.18 cm⁻¹ (B_{1g} – mode) and 616.48 cm⁻¹ (B_{2g} – mode). Proceeding from this sample case, silver content was introduced in varying rations and thus peaks for said nanopowders were as well obtained. 157.02 cm⁻¹ (Ag - lattice). 240.71 cm⁻¹, 257.32 cm⁻¹ (Ag – O bond). 687.57 cm⁻¹, 821.07 cm⁻¹, 896.47 cm⁻¹ (N – O bond for NO₃⁻ ion) 976.02 cm⁻¹, 988.47 cm⁻¹, 1059.71 cm⁻¹, 1293.52 cm⁻¹, 1365.51 cm⁻¹, 1519.02 cm⁻¹, 1615.71 cm⁻¹, 1660.82 cm⁻¹ (Ag – characteristic peaks). For CA3, 286.37 cm⁻¹ (A_g – mode), 336.32 cm⁻¹

$^1(B_{1g}$ – mode) and 616.32 cm^{-1} (B_{2g} – mode) were the designated CuO peaks for Raman spectra. In addition, 157.98 cm^{-1} (Ag - lattice). 241.93 cm^{-1} , 261.47 cm^{-1} (Ag – O bond). 687.20 cm^{-1} , 825.22 cm^{-1} , 896.21 cm^{-1} (N – O bond for NO_3^- ion). 971.86 cm^{-1} , 1055.68 cm^{-1} , 1084.62 cm^{-1} , 1293.08 cm^{-1} , 1318.42 cm^{-1} , 1364.76 cm^{-1} , 1519.02 cm^{-1} , 1623.47 cm^{-1} , 1660.54 cm^{-1} (Ag – characteristic peaks) were the corresponding Ag – Raman mode peaks. For CA4, silver has cubic structure and thus is concerned with respect to space group O_h^5Fm3m . The peak values for the desired Raman modes for silver nanopowders were acquired for this space system and were identified in such wise: the band at 157.82 cm^{-1} was obtained for the attendance for vibrational modes of silver lattice. The peaks at 244.86 cm^{-1} , 269.77 cm^{-1} were due to the formation of the Ag – O bond or silver – oxygen mode, which is the resultant of the ionic bracket being either undergoing absorption or adsorption when coming in contact with metal surface. The bonds that were recognised as doubly generated N – O in – plane vibrations were also observed at values 683.42 cm^{-1} , 825.41 cm^{-1} , 892.32 cm^{-1} . These are obtained because of the presence of NO_3^- ion in the silver system. The standard Ag peaks associated with its crystal cubic structure were also recognized at 967.71 cm^{-1} , 976.20 cm^{-1} , 1059.71 cm^{-1} , 1088.77 cm^{-1} , 1293.52 cm^{-1} , 1318.28 cm^{-1} , 1368.91 cm^{-1} , 1527.32 cm^{-1} , 1623.47 cm^{-1} , 1652.47 cm^{-1} . The attendance of such peaks was the confirmation of the formation of Ag nano – powders [183] [184][185] (**Figure 5.5**).

The results obtained for Raman studies were analysed against each other and it was observed that the sample systems CA1 (1:0) and CA4 (0:1) which constituted of individual nano – crystalline powders of CuO and Ag respectively, exhibited the peaks that were necessity in accordance to their crystal structure arrangement. For the sample cases of CA2 (1:1) and CA3 (1:2), these were comprised of composition of both the nano – powders in varying ratios and thus the peaks obtained were differentiated in both cases. As the content of Ag was increased, CuO peaks were lessened both in quality and quantity. The decreased intensity of the peaks for CuO led to the sharpness and visibility of silver peaks. The peaks values and corresponding bonds for the procured Raman modes are represented in tabular form in **Table 5:4**.

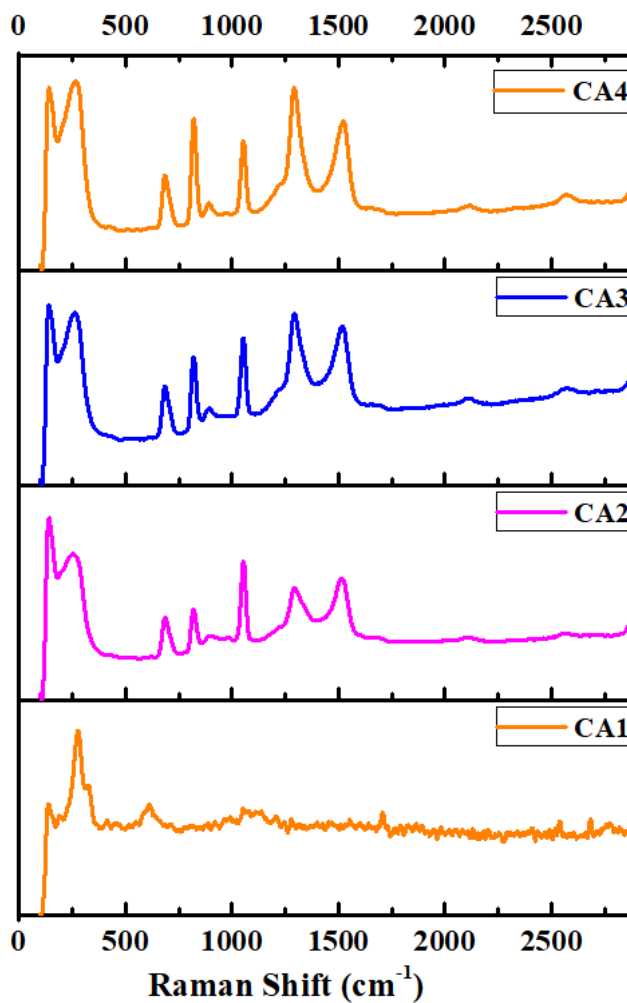


Figure 5.5 Raman Analysis of CA1 [CuO, 1:0], CA2 [CuO + Ag, 1:1], CA3 [CuO + Ag, 1:2] and CA4 [Ag, 0:1].

Table 5:4: Raman Spectra peaks and the adjacent bonds for CA1 [CuO, 1:0], CA2 [CuO + Ag, 1:1], CA3 [CuO + Ag, 1:2] and CA4 [Ag, 0:1].

	Peak Names	CA1 (CuO - 1:0)	CA2 (CuO + Ag - 1:1)	CA3 (CuO + Ag - 1:2)	CA4 (Ag - 0:1)
1.	A _g	286.37 cm ⁻¹	286.69 cm ⁻¹	286.37 cm ⁻¹	–
2.	B _{1g}	332.71 cm ⁻¹	334.18 cm ⁻¹	336.86 cm ⁻¹	–
3.	B _{2g}	616.32 cm ⁻¹	616.48 cm ⁻¹	616.32 cm ⁻¹	–
4.	Ag – lattice	–	157.02 cm ⁻¹	157.98 cm ⁻¹	157.82 cm ⁻¹
5.	Ag – O bond	–	240.71 cm ⁻¹ ,	241.93 cm ⁻¹ ,	244.86 cm ⁻¹ ,

			257.32 cm ⁻¹	261.47 cm ⁻¹	269.77 cm ⁻¹
6	N – O bond for NO_3^- ion	–	687.20 cm ⁻¹ , 825.22 cm ⁻¹ , 896.21 cm ⁻¹	687.20 cm ⁻¹ , 825.22 cm ⁻¹ , 896.21 cm ⁻¹	683.42 cm ⁻¹ , 825.41 cm ⁻¹ , 892.32 cm ⁻¹
7.	Characteristic peaks for Ag	–	976.02 cm ⁻¹ , 988.47 cm ⁻¹ , 1059.71 cm ⁻¹ , 1293.52 cm ⁻¹ , 1365.51 cm ⁻¹ , 1519.02 cm ⁻¹ , 1615.71 cm ⁻¹ , 1660.82 cm ⁻¹	971.86 cm ⁻¹ , 1055.68 cm ⁻¹ , 1084.62 cm ⁻¹ , 1293.08 cm ⁻¹ , 1318.42 cm ⁻¹ , 1364.76 cm ⁻¹ , 1519.02 cm ⁻¹ , 1623.47 cm ⁻¹ , 1660.54 cm ⁻¹	967.71 cm ⁻¹ , 976.20 cm ⁻¹ , 1059.71 cm ⁻¹ , 1088.77 cm ⁻¹ , 1293.52 cm ⁻¹ , 1318.28 cm ⁻¹ , 1368.91 cm ⁻¹ , 1527.32 cm ⁻¹ , 1623.47 cm ⁻¹ , 1652.47 cm ⁻¹

5.1.5 FESEM Analysis

FESEM studies were done in order to get the visual information of the topographical data for the crystalline sample nano – powders. This tool employs its ability to examine smaller areas with less distortions, confirming the presence of the desired samples and also revealing contaminations if present. For CA1, CuO demonstrated a pseudo – spherical shape concerning the structure of the nano – powders. They inhabited a consistent size allocation within itself which furthermore consisted of a closely – packed arrangement associated with some irregularities to a degree to its order. The analysis also displayed the presence of cluster formation which happened when the sample was exposed to higher values of thermal energy i.e., when the sample was calcinated at 600°C. This led to the increasing rate of nucleation which further resulted into the elevated rate of growth and hence agglomeration was obtained. This correlated to the ‘bulk’ nature of CuO nano – powders [186][187][188][189][190][191]. For the proceeding sample codes CA2 and CA3, the visual presence for Ag nano – powders were observed because the spherical shape of afore – mentioned was obtained and the accumulation of CuO nano – particles over the surface of the metallic sample system were also confirmed. The difference between CA2 (1:1) and CA3 (1:2) were the varying ratios of the Ag content for each case. As the Ag – ratio for latter case was more and thus the prominence of Ag structure was more defined for CA3. Nonetheless, the cluster formation of CuO was

exhibited in both cases but the attendance of CuO over Ag surface in case of CA2 was more in comparison to its presence in CA3 as the CuO content was lessened which effected its intensity of occurrence. For CA4, the attendance of Ag – crystalline nano – system was distinguished with the prevalence of spherical – like structure obtained for the nano – powders. The particles were identified to be existing with mono – dispersive nature which was associated with the exceedingly ordered arrangement due to silver following cubic system. One habitual innate trait of silver was the origination of the agglomeration of the particles which were confirmed to be acquired till some extent because of the appearance of the clump formation in certain areas [112][147][174][192][193] [194]. It was also observed that the type of porosity behaviour exhibited by the sample material was closed porosity i.e., isolated gaps with non – uniform occurrence were present within the sample material (**Figure 5.6**).

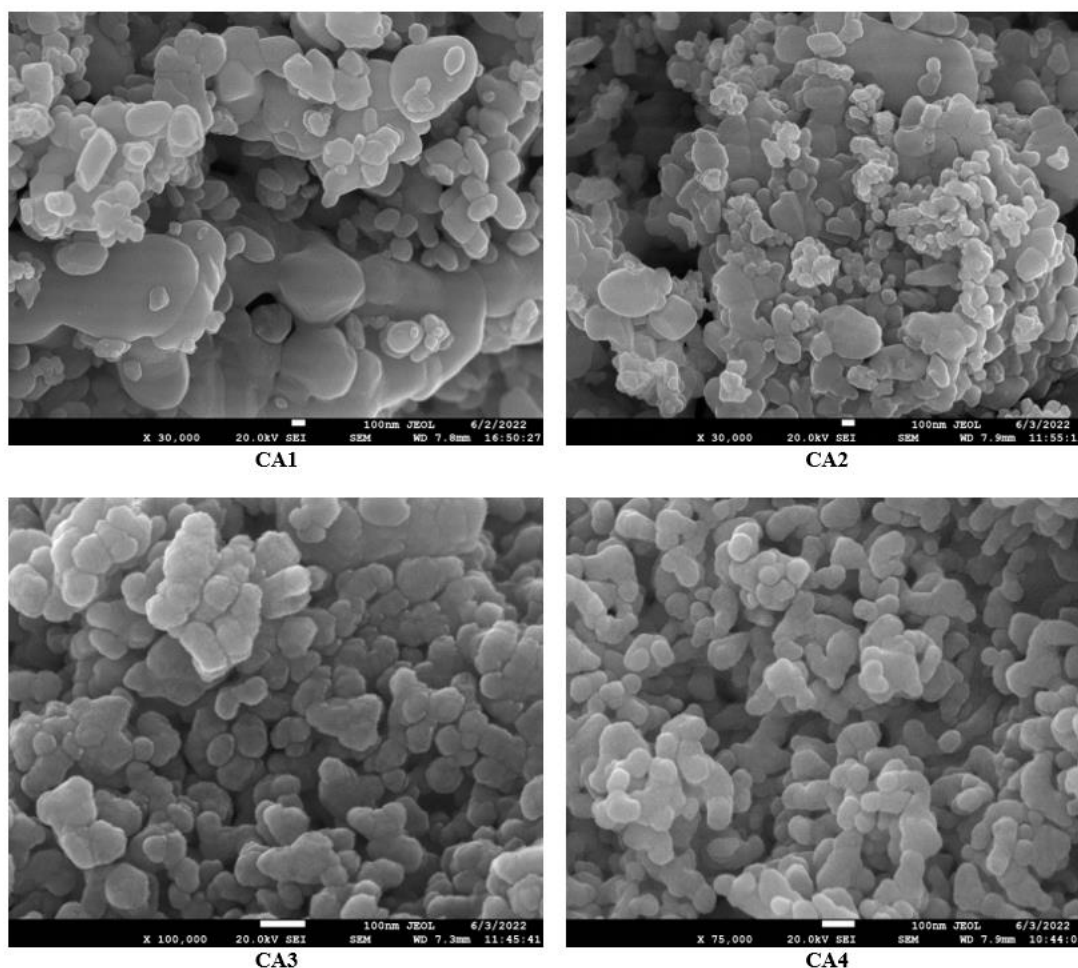


Figure 5.6 FESEM Analysis of CA1 [CuO, 1:0], CA2 [CuO + Ag, 1:1], CA3 [CuO + Ag, 1:2] and CA4 [Ag, 0:1].

5.1.6 EDX and Mapping Studies

Energy dispersive x – ray technique was used to attain the elemental ratio for each component present within the sample composition. A spectrum consisting of peaks was obtained as the result of the statistical figure which was produced due to the analysis tool. The procured peaks were observed to be adjacent to existing elements that were constructing the sample system. For CA1, the peaks for Cu and O corresponding to copper and oxygen – atoms respectively were observed. For CA2 and CA3, these sample systems were the composition mixture of CuO and Ag and therefore, the data revealed the peaks for Cu, O and Ag. For CA4, the peaks for Ag and O adjacent to silver and oxygen atoms (may be due to present in the atmosphere) were obtained (**Figure 5.7**).

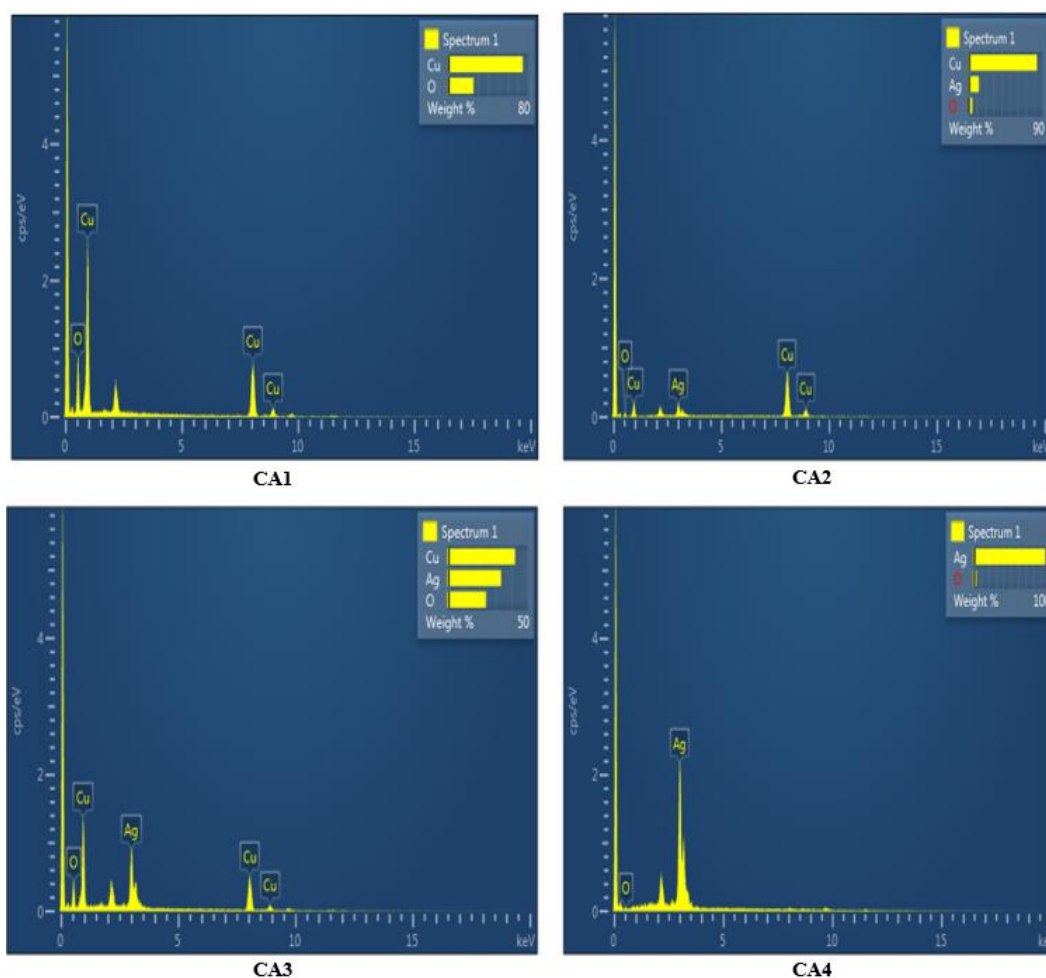
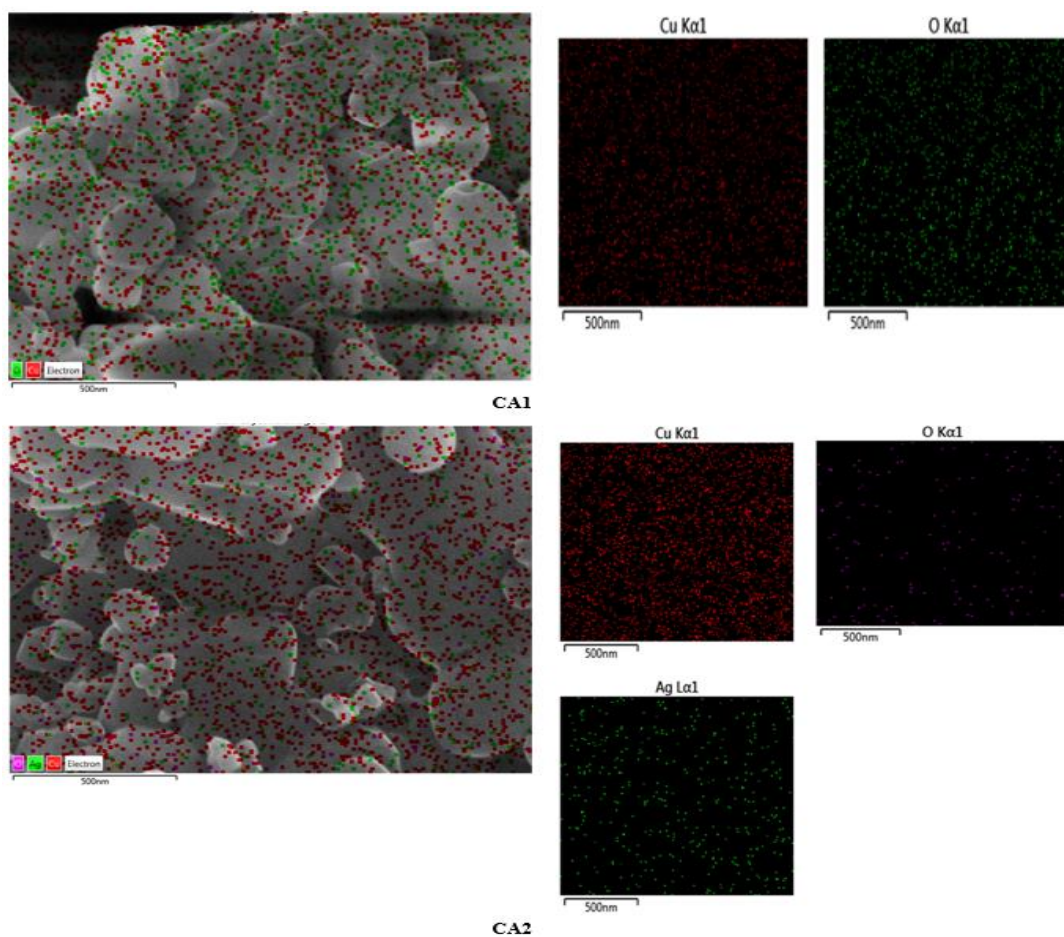


Figure 5.7 EDX Analysis of CA1 [CuO, 1:0], CA2 [CuO + Ag, 1:1], CA3 [CuO + Ag, 1:2] and CA4 [Ag, 0:1].

Elemental mapping for all the sample nano - powders were also done so as to obtain the data regarding the placements and the dispensation of the elements within the sample system (**Figure 5.8**).



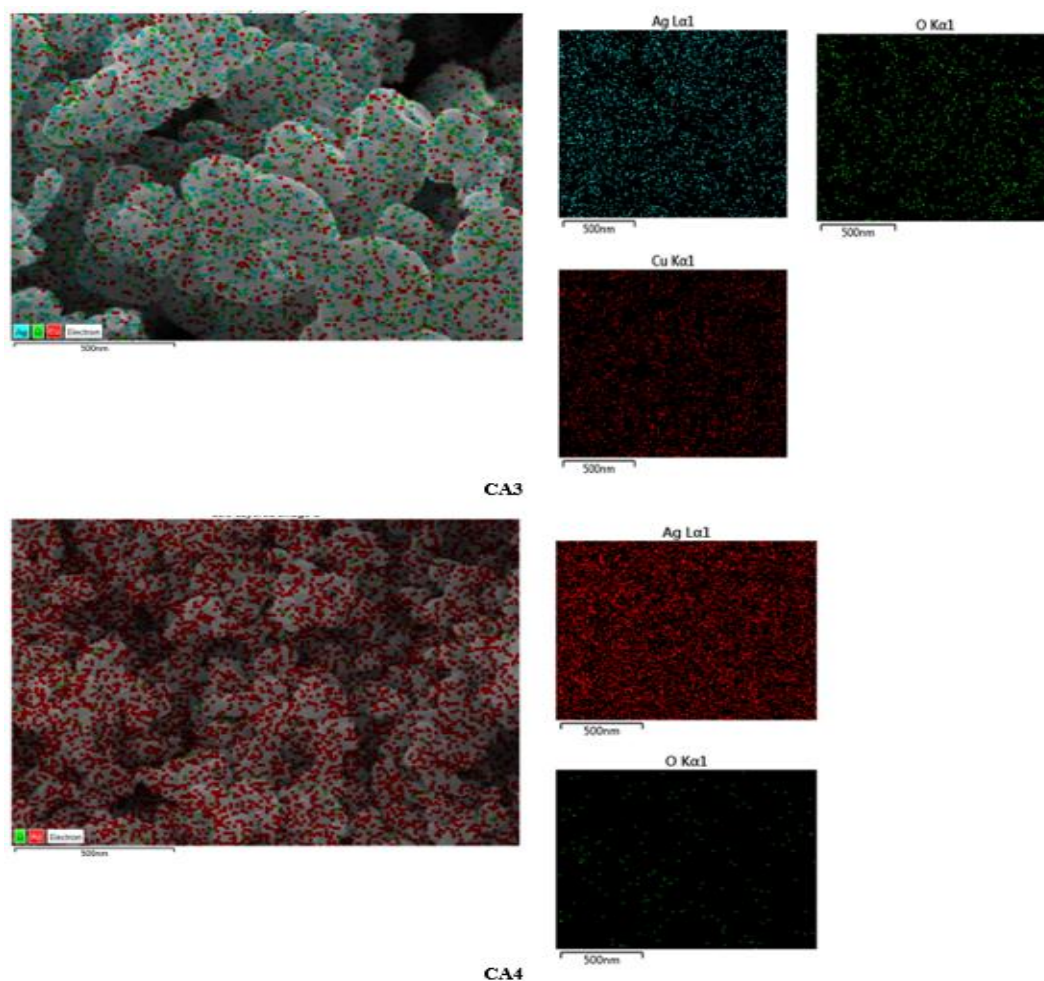


Figure 5.8 Elemental Mapping for CA1 [CuO, 1:0], CA2 [CuO + Ag, 1:1], CA3 [CuO + Ag, 1:2] and CA4 [Ag, 0:1].

5.1.7 PSA Analysis

Particle size analysis was done using the ImageJ software. The size distribution analysis was used to obtain the percentile data for the particles that were subjected to a specific size range. The particle size for CuO nano – powders was 6.5 nm with standard error = 0.419 % and particle size for Ag nano – particles was 7.75 nm having standard error = 0.073 %. The particle size value for Ag was slightly higher than CuO, that was because Ag nano – powders exist as colloidal particle phase and thus more likely to consist of larger shaped particles than CuO. When the results for the particle size and crystalline size obtained from PSA and XRD analysis were put in comparison to each other, it was noted the D – value from XRD was higher w.r.t

PSA analysis therefore, it was concluded that nature of the nano – system was crystalline (Figure 5.9).

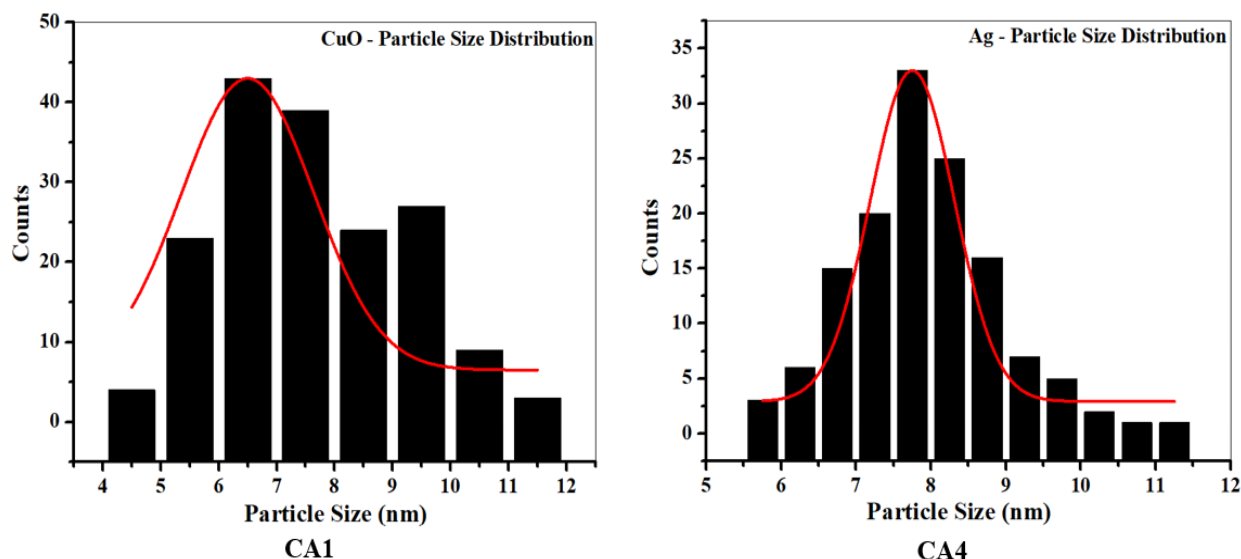


Figure 5.9 Particle Size Distribution Analysis of CA1 [CuO, 1:0] and CA4 [Ag, 0:1].

5.1.8 Varistor Studies

In this paper, the current and voltage nature was studied for a simpler two – constituent system which consisted of a semi – conducting metal oxide i.e., CuO as host material and metallic nano – powders i.e., Ag nanopowders were added into the sample composite using varying ratios. CuO has excellent electrical and thermal properties and silver exhibits exceptional electrical conduction capabilities due to the fact that silver has the lowest resistance value among all the metals. Now conductivity defined as the ease with which the charge carriers can move through the material. Even though silver consists of one free electron in its outer most shell per atom, the intrinsic nature of silver having lower resistivity compensates with higher rate of mobility of its free electrons and furthermore the anti-bacterial property of silver resists the growth of impurities thus aiding in the prolongation for the usage time – period of the devices.

Varistors by definition concerns with non – linear behaviour of resistance w.r.t the applied voltage. The role of varistors in an electrical circuit is to protect the circuit system from getting short – wired which can lead to further damage resulting in breaking of fires. These devices operate on the principle by giving the allowance for the passage of maximum amount of current

through the electrical device before it reaches its pinnacle limit. Once varistor reaches its maximal limit, it shuts down the system henceforth, preserving the integrated circuit board from short circuiting. The mechanism of materials studied in this case for varistors resembles the working mechanism of a Schottky device. Its diode in which a junction between semi-conducting material and metal is produced and it is used as a rectifier whereas in this case varistors are used as surge suppressors. The major difference between Schottky device and varistor is that, in the former device the necessary requirement is to have junction formed between a n-type semiconductor and a metal plate such as; Al and Pt instead of using p-type semiconductor. Whereas in the case of latter, the present work has been done to study the mobility capacity between a p-type semiconductor and metal. Therefore, the investigation of the sample powders has been studied through the understanding of formation of semi-conducting metal oxide and a metallic material using the basics of p-n junction charge carrier transportation mechanism.

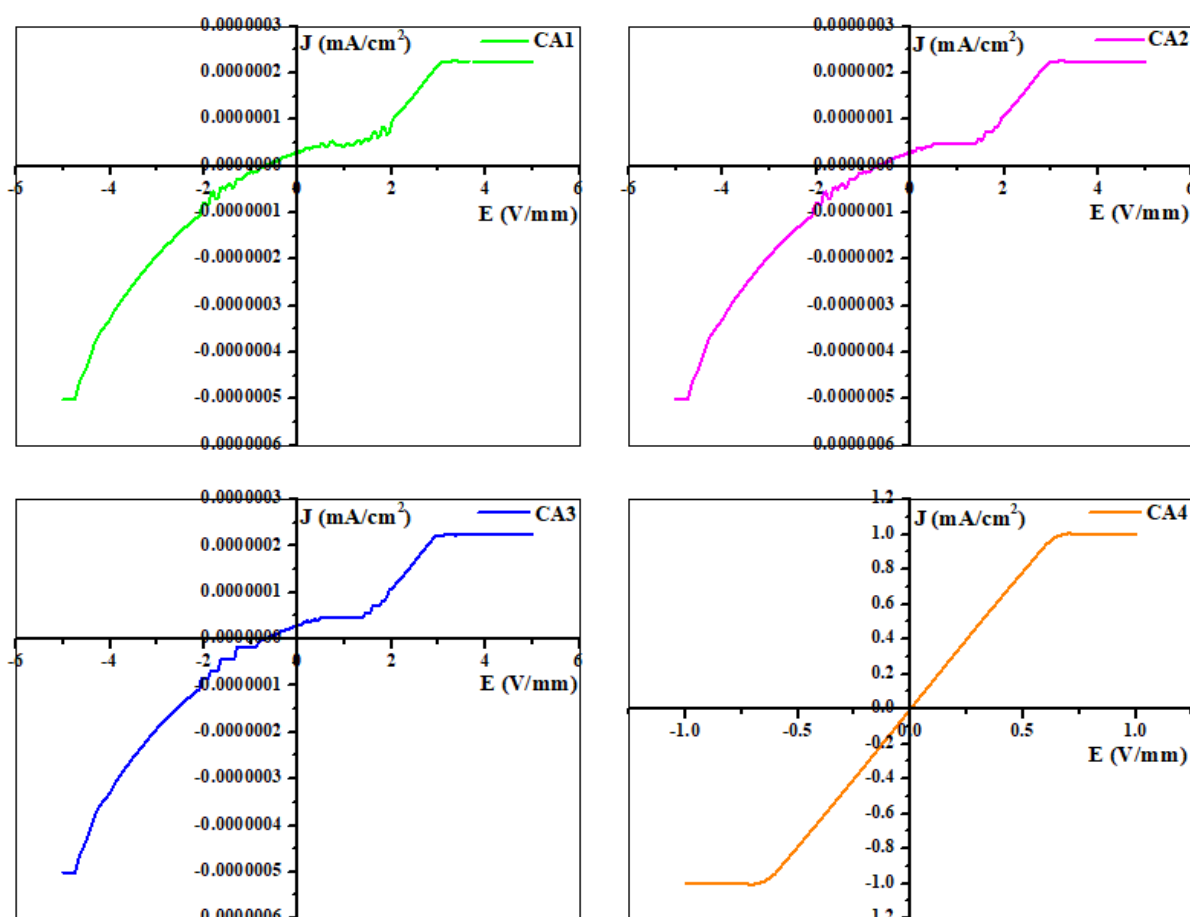


Figure 5.10 Current – Voltage Plot Analysis for CA1 [CuO, 1:0], CA2 [CuO + Ag, 1:1], CA3 [CuO + Ag, 1:2] and CA4 [Ag, 0:1].

For this case, the interpretation of the plots was done in order to study ‘for how much value of current and voltage, the sample composite mixture can exhibit its functioning effectiveness within the system. From **Figure 5.10**, it was noted that there were certain factors which effected the nature and operational values for the sample model. One of the prevalent factors was the existence of ‘current compliance’; which meant the utmost amount for the current values that the electro – chemical cell was capable to sustain. The maximum value for the current was obtained around 1.00 mA/cm^2 approximately, which was observed for the sample case of Ag, even though silver has an exceptional electron conduction value. This was the limitation relevant due to the device that was used to characterise the samples. Furthermore, the values for voltage were observed to be varying in the increasing order with minuscule differences.

Second factor was the occurrence of the ‘Knee Point’; which meant the point in the graph where the curve bent specifically from a higher slope values to lower slope i.e., when elevated slope of the graph changed and became the saturated horizontal line in the graph. With the attendance of the afore – mentioned point, the graph was then divided into two domains; liner region and non – linear region. Linear region was defined as the area which was obtained just before the development of the knee point in the graph where Ohm’s Law was applicable and the current values gave a direct proportional graph w.r.t to the voltage values. The conduction values were obtained in this area because of the forward bias connections, as in the circuit p – junction is made positive and n – junction is made negative. Therefore, the existing electrons and holes gets attracted towards the junction points which leads to decrease in potential barrier and thus flow of charges through the circuit. Moreover, from **Figure 5.6**, it was observed that sample consists of closed porosity i.e., sample structure consists of smaller and isolated gaps with the grain boundaries [less frequent occurrence]. This lessened the porosity values which further led to smaller amounts of entrapment of electrons within the grain boundaries while the conduction was proceeding. Therefore, majority of electron population was available for electrical conduction which further enhanced the conduction capability of the sample material. This also led to hardness of the material and increased the capacity of sample to absorb recognisable amounts of current for longer times [190]. Some smaller values of current were also observed in reverse region. In this circuit settings, the conditions on p – and n – junctions are reversed and the width of potential barrier is increased. Even with applicability of such terms, some minority charge carriers are still present which resulted in the electrical conduction.

Whereas, non – Linear region was the saturated area of the graph that was acquired after the existence of knee point. In this region, Ohm’s Law was not followed and constant values for current were obtained with small but varying values for voltage. This behaviour was exhibited by all four sample systems in both positive and negative planes [196].

Thirdly, there were irregular curves more like zig – zag pattern was noticed for sample cases CA1, CA2 and CA3. This could be possibly because of the polymorphism nature which tends to be an innate characteristic of CuO as it exists in two forms CuO and Cu₂O. Which moreover, could have also resulted into the occurrence of saturation level at smaller scale before regaining the linear region. A pre – mature non – linear plot was obtained momentarily at an inconsequential scale for both the cases of CA2 and CA3, from 4.6330×10^{-7} (I_{N1}), 0.5474 (V_{N1}) to 4.9508×10^{-7} (I_{N2}), 1.3941 (V_{N2}) for CA2 and from 4.4744×10^{-7} (I_{N1}), 0.5096 (V_{N1}) to 4.7914×10^{-7} (I_{N2}), 1.3506 (V_{N2}) for CA3 respectively. The values showed a decrease in values as the content for silver was increased for the proceeding sample cases.

Fourthly, as it was observed that the graphical plot did not pass through the origin. This was because there was still some value of current obtained voltage at zero value. This current value is called Black or Dark current which is defined as the amount of the current that flows within the detector when there is no photon flux. This happens due to the spontaneous and random production of hole – electron pairs in the depletion region which leads to the generation of current whilst in the absence of photon flux.

Lastly, as disclosed before, graphical plot between J (mA/cm²) and V (V/mm) values evinced the existence of two domains; the ‘before’ of the knee point i.e., direct proportional graph between current versus voltage values and ‘after’ of the knee point i.e., the saturated region. This led to another facet which was named ‘non – linear coefficient’. It was described as the ratio of the log values for differences of current densities to the log values for the differences of voltages. It was computed using the following equation and the values were chosen from initiating point and the end point of the saturated line [197].

$$\alpha = \frac{\log[J_2 - J_1]}{\log[V_2 - V_1]} ; J_2 > J_1, V_2 \text{ and } V_1 = \text{voltages at respective current density}$$

Where α = non – linear coefficient, I_N (mA/cm²) = current values across the device and V_N (V/mm) = voltage values across the device. The values obtained for non – linear coefficient, varistor current and voltage values were put in the tabular form in **Table 5:5**.

Table 5:5: Tabular form for the values of non – linear coefficient ' α ', voltage across the device ' V_N (V/mm)' and current across the device ' I_N (mA/cm²)' for CA1 [CuO, 1:0], CA2 [CuO + Ag, 1:1], CA3 [CuO + Ag, 1:2] and CA4 [Ag, 0:1].

Sample code	α - value	I_N [mA/cm ²]	V_N [V/mm]
CA1 (CuO - 1:0)	- 29.9706	2.1385×10^{-7}	2.8809
CA2 (CuO + Ag - 1:1)	- 27.7849	2.2495×10^{-7}	2.9905
CA3 (CuO + Ag - 1:2)	- 24.0964	2.3541×10^{-7}	3.0497
CA4 (Ag - 0:1)	- 1.5760	1.0392	0.6848

From the **Table 5:5**, it was recognised that when the values for all three sample cases were compared against each other, an increase in the values for all 3 variables were obtained even though, the changes were with considerably smaller value differences. For the varistor to have its functionality value counted, the higher values for α were a necessity because more were the value for α , further larger the linear arena in the graph will be obtained, henceforth more voltage values will be procured which will allow a substantial amount of current to be passed through the device. CA1, was the host material with only singular component i.e. CuO thus gave smaller amount of values for α , whereas CA2 and CA3 were the composite values and the amount of Ag was added in increasing ratio therefore, showed a steady increase within the plot.

Although, an elevated plot was obtained still the differences between the values were noted to be at smaller scale. The reasoning behind such conduct could be due to: (I). the subject composite materials were treated at only lower voltage – current values because of current compliance, (II). The selected specimen was constituting only of two components; CuO and Ag i.e., the composite mixture was of a much simpler and basic sphere as compared to a complex form with 3 or more chemicals [198]. The α – values were put against CuO weight

ratio as illustrated in **Figure 5.11**, it was seen that with the increase in the Ag – volume, an increase in the α – values were shown.

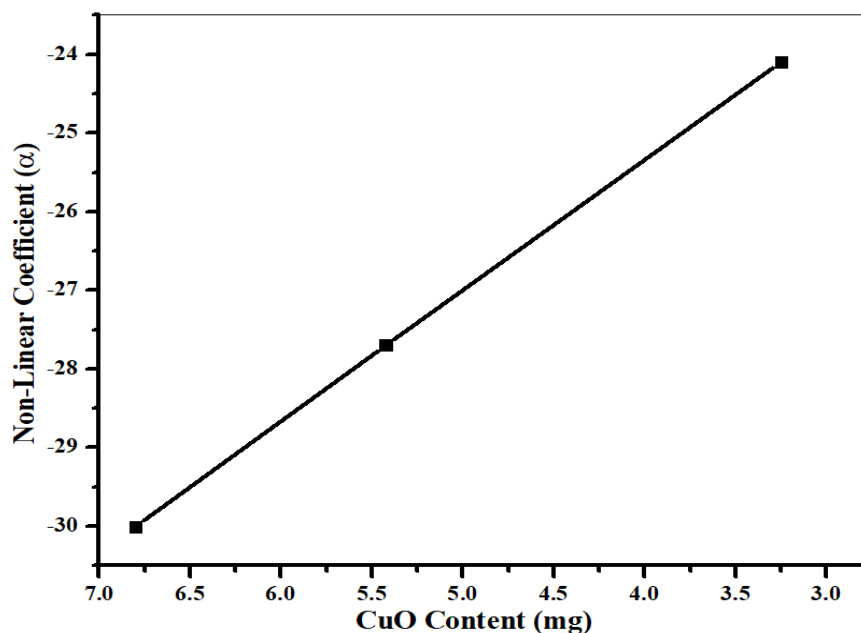


Figure 5.11 Graphical plot for α – value against the CuO content of CA1 [CuO, 1:0], CA2 [CuO + Ag, 1:1], CA3 [CuO + Ag, 1:2] and CA4 [Ag, 0:1].

Summarizing the afore – mentioned factors, an increase in the values for the non – linear coefficient, varistor current and varistor voltage were obtained even though, the values acquired exhibited a small-scale difference within the system. This was to a large extent because the matrix that was considered was of simpler form; CuO a semiconducting metal oxide was studied with the addition of metal oxide Ag with differing ratios. Yet, a steady growth was achieved which led to the conclusion that if the composite mixture was employed on with a stronger network, then a much more considerable set of values could be perceived which could have the device usage at larger scale such as in electrical circuits in industries etc. With the assortment of the values derived, the application areas for the intended sample codes were assessed to be at smaller scale where lower values of the voltages were required namely; smart door – bell systems, garage – door sensors, thermostats, resistors and several other smart - house equipments that require lower voltage potency for its operational efficiency.

5.2 PANI mixed with CdO

5.2.1 TGA Studies

- TGA analysis – PANI nanopowders.

The implementation of TGA characterisation technique overlays the statistical knowledge for the loss in the weight of sample by providing details regarding the decomposition of water, any organic and volatile compounds or sample's state of oxidation. The specimen undergoes thermal treatment over a consistent period of time and the fluctuations in the mass is plotted against temperature.

The said tool was applied on polyaniline nanopowders to procure the information regarding the variations in the weight with a constant increase in the temperature values. PANI was air – dried at room temperature and no calcination was done on the samples. TGA was applied on PANI powders to assess its thermal steadiness over the scale of 30 °C to 800 °C at the rate of 10 °C per minute. The temperature was held for 1.0 minute at 800 °C. In total, four phases of PANI were obtained and they are as follows:

(I). Phase I: was obtained in the temperature scale of 30 °C – 121 °C, this loss was ascribed to the release of the water in general that was present in the sample in the form of moisture or free water molecules and the water molecules that were adsorbed by sample surface.

PANI shows the thermal stability till this temperate, but proceeding this temperature, the conductive polymer commences to decay with a steady pace i.e., from the following stages the breaking – down of the existing organic substances begins.

(II). Phase II: was experienced within the range of 121 °C – 226 °C, this phase exhibited the degradation or evaporation of the unreacted aniline and any volatile compounds.

(III). Phase III: was observed in the plot from 226 °C – 450 °C, this phase was the result when the thermos – oxidative decomposition of polyaniline initiated.

(IV). Phase IV: the last phase was seen from the end section from 450 °C – 800 °C, in this phase the decomposition of the backbone of polymer takes place. The total weight loss experienced by the polymer sample was acquired to be $\Delta Y = 67.94\%$ for pure PANI nano – powders [199][200][201][202][203] (**Figure 5.12**).

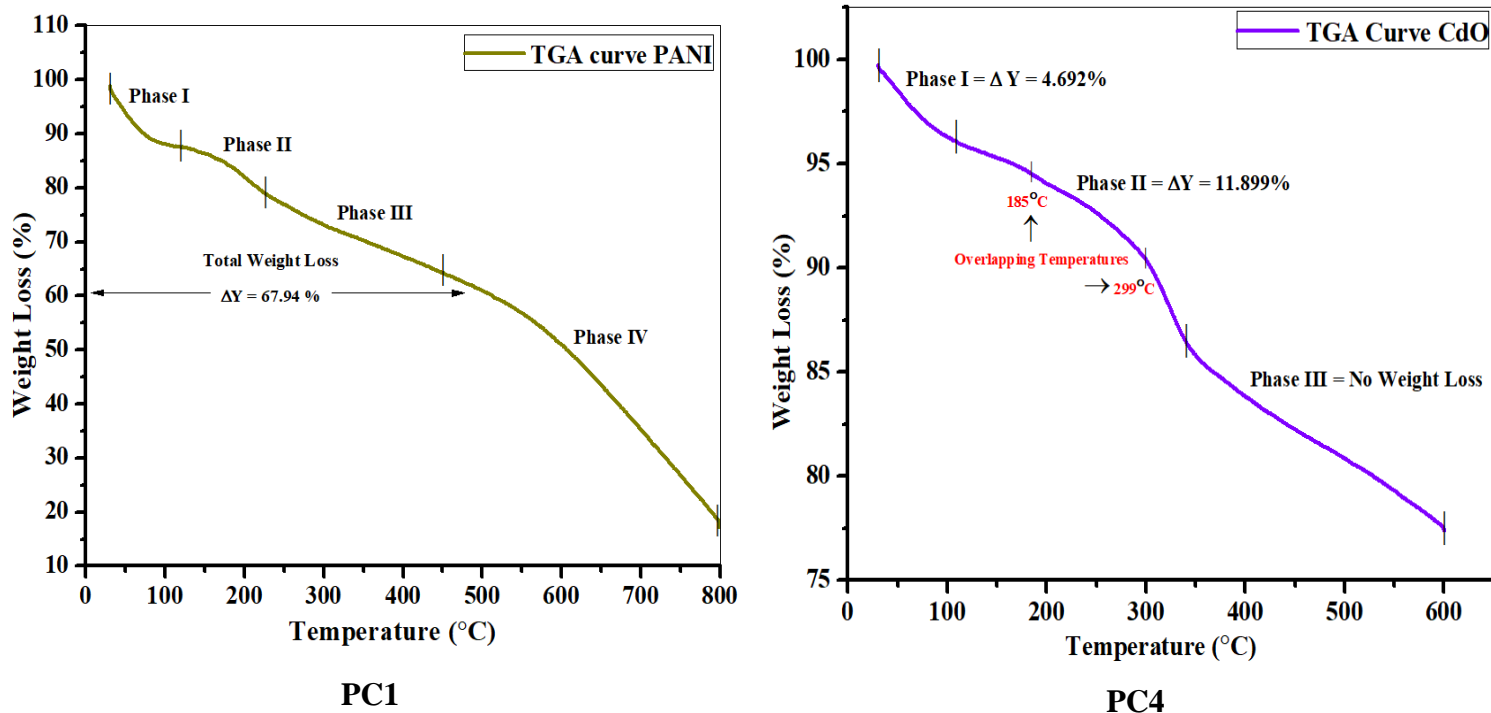


Figure 5.12 TGA Analysis of PC1 [PANI, 1:0] and PC4 [CdO, 0:1].

- TGA analysis – CdO nanopowders.

TGA, in case of CdO was employed on to the uncalcinated nano – powders that were procured after the completion of the auto – combustion process. This characterisation was done in the temperature range from 40 °C – 600 °C at 10 °C / minute so as to the obtain the calcination temperature for CdO sample powders. The heat on the specimen was held at 600 °C for about 1.0 minute. The sample underwent three major phases of weight loss w.r.t increase in temperature value.

(I). Phase I: 42 °C (room temperature) – 108 °C; total weight loss $\Delta Y = 4.692\%$ was acquired due to the discharge of the water contents or moisture. In addition, the freeing of the volatile compounds that were adsorbed and the surfactants molecules that got attached on the surface of the CdO sample powders whilst its preparation.

(II). Phase II: 108 °C – 350 °C, total weight loss $\Delta Y = 11.899 \%$. This phase took place as the thermal degradation of the organic compounds started in the precursor structure. This phase observed the occurrence two overlapping temperatures because the $Cd - NO_3^-$ ion bond takes time to wither out and thus exhibits two different temperatures for the breakage of the said bond.

1. 185.24 °C = weakening of the H – bonded nitrates of $Cd - NO_3^- + H_2O$ at the lower temperature.
2. 299.29 °C = breaking of the covalently bonded nitrates of $Cd - NO_3^-$ ion at the higher temperature. CdO being a semi – conductor metal conductor with ionic bonding constitutes of covalently bonded nitrates because of the nature of the $Cd - NO_3^-$ bond, as it falls under the definition of Polyatomic Ion. This term means the group of the atoms that are associated to one another through covalent bonds and in spite of that the atom in whole collection consists of a charge i.e., $Cd - NO_3^-$ has single N – atom and triple O – atoms.

(III). Phase III: 350 °C – 600 °C, less significant weight loss which did not interfered with the thermal plot w.r.t the temperature was seen in this temperature scale corresponding to any thermal decomposition, which means the CdO crystallization has taken place.

In the present work to obtain the metal oxide phase, the CdO powders were calcinated at 400 °C for 7 hours with the usage of an accelerated heating rate of 10 °C / minute. This was done as it facilitates the farther away movements of the base – line from the state of equilibrium due to the requirement of short – time response for apiece ascertainment [204][205][206][207][208][209] (**Figure 5.12**).

5.2.2 XRD Pattern

To understand the irregular – amorphous and ordered crystalline structure of both PANI and CdO nano – structured powders respectively, XRD was utilized. This technique also supplies with the information concerning the crystal phase and orientation. Furthermore, the details of

unit length and average crystal size can also be computed with the help of lattice parameters values obtained using the respective formulae.

Since, polyaniline has non – structured nature therefore its confirmation is secured through a broad curve constituting of certain peaks in the range of $10^\circ - 30^\circ$. For PC1, PANI exhibited its structural peaks at $2\theta^\circ$ values as = 14.47° , 19.56° , 20.42° , 25.33° , 25.40° , 26.41° , 27.10° and 29.54° and its corresponding d – spacing values were = 6.1178 \AA , 4.5341 \AA , 4.3451 \AA , 3.5127 \AA , 3.5043 \AA , 3.3722 \AA , 3.2878 \AA and 3.0214 \AA respectively. The peak obtained at 20.42° was attained parallel towards the direction of the polymer chain whereas, the peak values at 25.33° and 25.40° were attributed perpendicular to the polymer chain direction. The latter mentioned peaks have major influence in affirming the amorphous formation demonstrating the emeraldine salt disposition of the conductive polymer [210][211][212][213][214][215][216][217][218][219][220][221][222]. For PC2, the amorphous nature of polyaniline was revealed with the occurrence of peaks at $2\theta^\circ = 27.46^\circ$ and 29.36° with the respective d – spacing values at = 3.2455 \AA and 3.0393 \AA . The structure of CdO nano - powders was also dispositioned for $2\theta^\circ$ values = 32.96° , 38.25° , 55.24° , 65.88° , 69.21° having adjacent (hkl) – plane values = (111), (200), (220), (311), (222). For PC3, $2\theta^\circ$ values = 27.51° and 29.41° for d – spacing values = 3.2396 \AA and 3.0342 \AA for PANI nano – particles were acquired. The characteristic peaks for CdO were observed at $2\theta^\circ$ values = 32.99° , 38.29° , 55.29° , 65.92° , 69.26° with their corresponding reflection plane values = (111), (200), (220), (311), (222) respectively. For PC4, the ordered crystalline nature for CdO nano – granulates was evinced by the occurrence of $2\theta^\circ$ values at = 32.96° , 38.27° , 55.26° , 65.90° , 69.23° which were indexed in correspondence with (hkl) – reflection planes phases at = (111), (200), (220), (311), (222). These obtained values were in accordance with the JCPDS card no: 05 – 0640. Moreover, no other diffraction peak concerning to the formation of contaminations; CdCO_3 , Cd(OH)_2 and CdO_2 were obtained, thus concluding the synthesised CdO nano – powders as pure and spared of any kind of impurities [223][224][225][226][227][228][229][230][231][232][233][234][235][236][237][238] (**Figure 5.13**).

When the results for PC1, PC2, PC3 and PC4 were compared to one another, it was recognised that the intensity of the PANI curve was decreased and simultaneously the quantity of the peaks that were formed within the curve were also lessened. This was primarily due to the reason that sample code PC1 (1:0) and PC4 (0:1) constituted of undoped form of PANI and CdO nano –

powders, whereas PC2 (1:1) and PC3 (1:2) were the composition samples having both the said nanopowders. Now, as the quantity of CdO nano – powders were increasing, the PANI content was decreased and hence the occurrence of the said peaks was also reduced. The decreased in the PANI quantity means the more prevalent crystallisation of CdO peaks and **Table 5:6** provides the tabular representation for the XRD peaks.

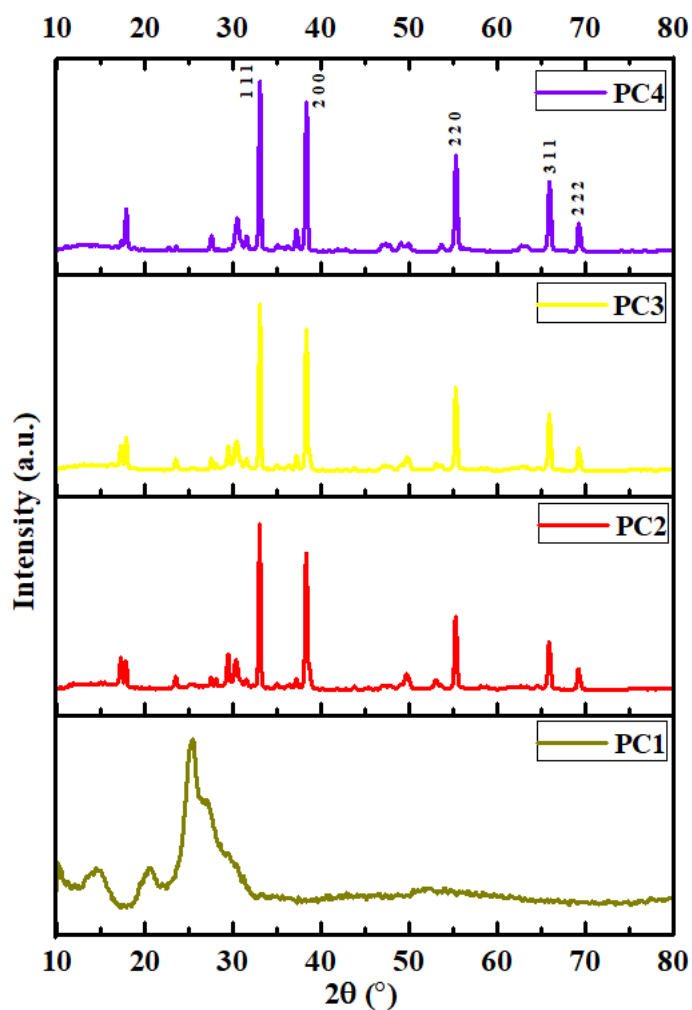


Figure 5.13 XRD Analysis of PC1 [PANI, 1:0], PC2 [PANI + CdO, 1:1], PC3 [PANI + CdO, 1:2] and PC4 [CdO, 0:1].

Table 5:6: XRD peak values for PC1 [PANI, 1:0], PC2 [PANI + CdO, 1:1], PC3 [PANI + CdO, 1:2] and PC4 [CdO, 0:1].

Sample code	PANI		CdO	
	2θ	d	2θ	hkl
PC1 (1:0)	14.47°	6.1178 Å	–	
	19.56°	4.5341 Å		
	20.42°	4.3451 Å		
	25.33°	3.5127 Å		
	25.40°	3.5043 Å		
	26.41°	3.3722 Å		
	27.10°	3.2878 Å		
	29.54°	3.0214 Å		
PC2 (1:1)	27.46°	3.2455 Å	32.96°	111
	29.36°	3.0393 Å	38.25°	200
	–		55.24°	220
			65.88°	311
			69.21°	222
PC3 (1:2)	27.51°	3.2396 Å	32.99°	111
	29.41°	3.0342 Å	38.29°	200
	–		55.29°	220
			65.92°	311
			69.26°	222
PC4 (0:1)	–		32.96°	111
			38.27°	200
			55.26°	220
			65.90°	311
			69.23°	222

The values for the crystallite size (D), lattice parameters (a, b, c) and volume (V) for the sample composites were also calculated. Since, PANI has amorphous nature therefore, its crystallite size, lattice and volume data weren't obtained. Whereas, CdO has cubic structure in monteponite phase and thus it has unit length $a = b = c$. The afore – mentioned values were evaluated utilizing the corresponding formula. **Table 5:7** provides with the computed values in tabular form.

$$D = \frac{k\lambda}{\beta \cos\theta}; \text{ (Debye Scherrer's Equation)}$$

$$\frac{1}{d_{hkl}^2} = \frac{h^2+k^2+l^2}{a^2}; \text{ (Cubic formula – monteponite phase for CdO nanoparticles)}$$

$$V = a \times b \times c; \text{ (Volume)}$$

Table 5:7: Lattice parameters (a, b, c), crystallite size (D), FWHM (β^*), Braggs angle (2θ) and volume (V) of PC2 [PANI + CdO, 1:1], PC3 [PANI + CdO, 1:2] and PC4 [CdO, 0:1].

		a (Å)	b (Å)	c (Å)	D (nm)	β^* (°)	2θ (°)	V (Å) ³
PC2 (1:1)	CdO	4.7022	4.7022	4.7022	46.9685	3.26218×10^{-3}	38.25	103.9688
PC3 (1:2)	CdO	4.698	4.698	4.698	49.3493	3.1051×10^{-3}	38.29	103.6905
PC4 (0:1)	CdO	4.7002	4.7002	4.7002	42.6390	3.5935×10^{-3}	38.27	103.8362

5.2.3 FTIR Analysis

FTIR analysis gives details regarding the elements present in the composition for gases, liquids and solids and organic compounds. It consists of a “Finger – print region” that exhibits the specific peaks for the particular molecule and henceforth confirming the formation of the desired structural bond.

For PC1, the structural peaks attributed to the amorphous nature of PANI were obtained as follows: the peak value for symmetric stretching vibration for secondary amines associated to the free N – H bond was observed at 3418.52 cm^{-1} , these bonds emerge from the polyaniline arrangement and thus the formation of PANI was assured. The value for the NH^{2+} bond equated in $-\text{C}_6\text{H}_4\text{NH}^{2+}\text{C}_6\text{H}_4-$ section of the polyaniline was around 2921.58 cm^{-1} . The peaks at 2900.68 cm^{-1} , 2826.03 cm^{-1} were assigned to C – H bond of CH_2 derived from the stretching vibrations of the aliphatic hydrocarbons. 1664.07 cm^{-1} , 1648.84 cm^{-1} were the vibrational peaks for C = N bond. The value for stretching vibration that was attributed to the quinonoid (Q) arrangement of polyaniline was procured at 1561.80 cm^{-1} whilst the stretching vibrational peak value for benzenoid (B) arrangement was obtained around 1471.30 cm^{-1} . The stretching vibrations for C – N bond was indexed at 1290.30 cm^{-1} , 1245.05 cm^{-1} . The capability of PANI to have electrical conduction is the consequence of the occurrence of protonation process in the polymer sample and its trademark peak was at 1137.26 cm^{-1} . The value observed at 1104.11 cm^{-1} was due to the in – plane bending whereas, the out – plane bending was obtained at 872.67

cm^{-1} . The C – C bond peak associated to aromatic ring was 568.03 cm^{-1} . The peak value seen at 513.84 cm^{-1} was given to the C – N – C bond for the aromatic ring structure [40][210][213][218][239][240][241][242][243][244][245][246][247][248][249][250][251]. For PC2, 3413.40 cm^{-1} (N – H), 2921.58 cm^{-1} (NH^{2+} bond of $-\text{C}_6\text{H}_4\text{NH}^{2+}\text{C}_6\text{H}_4-$). 2864.84 cm^{-1} , 2826.03 cm^{-1} (C – H bond of CH_2 of aliphatic hydrocarbons). 1666.63 cm^{-1} , 1648.72 cm^{-1} (C = N). 1574.19 cm^{-1} (Q – stretching vibration). 1487.15 cm^{-1} (B – stretching vibration). 1298.95 cm^{-1} (C – N). 1121.40 cm^{-1} (protonate PANI peak). 1114.49 cm^{-1} (C – H in plane). 879.59 cm^{-1} (C – H out plane). 569.76 cm^{-1} (C – C bond of aromatic ring). 506.92 cm^{-1} (C – N – C of aromatic structure). The presence of CdO was also observed as follows: the wide spectrum ranges from $3696.19 \text{ cm}^{-1} - 3104.15 \text{ cm}^{-1}$ (OH – molecules for H_2O content). 3580.81 cm^{-1} , 3521.21 cm^{-1} , 3516.07 cm^{-1} , 3495.73 cm^{-1} , 3475.25 cm^{-1} , 3457.34 cm^{-1} , 3441.98 cm^{-1} (OH – bonds of H_2O molecules on CdO surface). 2390.51 cm^{-1} , 2354.68 cm^{-1} (O = C = O of CO_2). 1725.92 cm^{-1} (C = O). 1647.11 cm^{-1} (O – H bond of H_2O because atmospheric water vapour). 1640.20 cm^{-1} (C = C). 1445.36 cm^{-1} , 1380.80 cm^{-1} (O – C – O). 1333.82 cm^{-1} (wagging CdO). 1251.97 cm^{-1} (M – O bond due to Cd (NO_3)₂). 1140.71 cm^{-1} (C – O bond due to crystallinity). 1077.88 cm^{-1} (C – O – C). 973.55 cm^{-1} , 959.71 cm^{-1} , 930.03 cm^{-1} , 907.26 cm^{-1} , 856.82 cm^{-1} , 822.23 cm^{-1} , 797.74 cm^{-1} , 726.26 cm^{-1} , 707.24 cm^{-1} , 451.30 cm^{-1} , 447.84 cm^{-1} , 439.19 cm^{-1} , 421.61 cm^{-1} , 412.96 cm^{-1} (characteristic peaks of CdO formation). 930.03 cm^{-1} (C – O – H of – COOH bond). 604.63 cm^{-1} (M – O bond of Cd – O). For PC3, 3426.20 cm^{-1} (N – H), 2926.70 cm^{-1} (NH^{2+} bond from $-\text{C}_6\text{H}_4\text{NH}^{2+}\text{C}_6\text{H}_4-$ polymer section). 2838.82 cm^{-1} , 2828.59 cm^{-1} (C – H peaks for the CH_2 bond of aliphatic hydrocarbons). 1664.07 cm^{-1} (C = N). 1577.65 cm^{-1} (Q – stretching vibration). 1487.15 cm^{-1} (B – stretching vibration). 1274.07 cm^{-1} (C – N). 1117.95 cm^{-1} (in plane C – H peak). 879.59 cm^{-1} (out of plane C – H peak). 568.03 cm^{-1} (aromatic ring bond peak for C – C). 506.92 cm^{-1} (aromatic orientation association C – N – C). The peak for protonated PANI was missing due to polyaniline content lessening in the sample code when compared to PC1 and PC2. The broad curve over the scale of $3681.25 \text{ cm}^{-1} - 3106.70 \text{ cm}^{-1}$ (OH – peaks associated to H_2O molecules). 3580.81 cm^{-1} , 3495.73 cm^{-1} , 3462.46 cm^{-1} , 3436.86 cm^{-1} (H_2O content bonds for the OH – molecules on CdO surface). 2352.12 cm^{-1} , 2328.66 cm^{-1} (O = C = O for CO_2 bond). 1728.48 cm^{-1} (C = O). 1651.27 cm^{-1} (O – H peaks for atmospheric water vapor content). 1645.38 cm^{-1} (C = C). 1447.09 cm^{-1} , 1407.03 cm^{-1} , 1389.73 cm^{-1} , 1384.26 cm^{-1} , 1379.07 cm^{-1} (O – C – O). 1335.55 cm^{-1} (CdO wagging). 1251.97 cm^{-1} (M – O peak because of Cd (NO_3)₂ bond). 1135.53 cm^{-1} (C – O bond because of crystallinity formation). 1083.07 cm^{-1} (C – O – C). 961.4 cm^{-1} , 855.09 cm^{-1} , 820.22 cm^{-1} , 799.46 cm^{-1} , 705.51 cm^{-1} ,

442.65 cm^{-1} , 400.86 cm^{-1} (characteristic peak values for CdO bond presence). 919.65 cm^{-1} (C – O – H peak for – COOH). 682.74 cm^{-1} , 611.55 cm^{-1} (M – O peak value for Cd – O bond). For PC4, the disposition of CdO was observed with the presence of its peaks that were attributed to its characteristic structural nature as follows: the widened spectrum of multitudinal peaks were obtained within the scale range of 3663.93 cm^{-1} – 3108.85 cm^{-1} . There were the OH – bonds of the molecules from the residual H₂O content when the sample was taken out from the thermal treatment apparatus. The peak values observed at 3582.54 cm^{-1} , 3553.95 cm^{-1} , 3526.05 cm^{-1} , 3461.95 cm^{-1} , 3416.76 cm^{-1} were the stretching vibrations for the – OH bond associated to the hydroxyl group from water molecules that got coupled onto the CdO surface. 2395.52 cm^{-1} , 2357.52 cm^{-1} were allocated to O = C = O bond formation due to the existence of CO₂ in the atmosphere whilst the synthesis process of CdO nano – powders. The C = O bond was procured at 1728.45 cm^{-1} . The – OH peak value observed at 1667.32 cm^{-1} was also from the presence of hydroxyl group. This bond was transpired due to the water vapor quantity that was in attendance while the fabrication process was on – going. The formation of C = C bond was assigned to peak value at 1642.72 cm^{-1} . The peaks at 1483.44 cm^{-1} , 1436.01 cm^{-1} , 1414.45 cm^{-1} , 1399.23 cm^{-1} were the resultant of the origination of O – C – O bond. The vibrational wagging CdO peak was exhibited at 1346.55 cm^{-1} . The emergence for the metal – oxygen (M – O) bond formed due to utilization of Cd (NO₃)₂ in the sol – gel method was secured at 1244.73 cm^{-1} . The peak values at 1171.13 cm^{-1} , 1131.01 cm^{-1} were designated to C – O bond formation which was because of the achievement of crystallinity of CdO nano – powders. This peak confirms the formation of crystal structure of the said metal – oxide sample. 1059.34 cm^{-1} was the C – O – C bond peak. The several peaks at 955.59 cm^{-1} , 858.25 cm^{-1} , 526.17 cm^{-1} , 496.01 cm^{-1} , 442.61 cm^{-1} , 400.83 cm^{-1} were the behavioural peaks w.r.t the characteristic aspect of CdO. 920.45 cm^{-1} was out of plane C – O – H bending peak for – COOH section of carboxyl group. The metal – oxygen bond between Cd – O were acquired at 681.66 cm^{-1} , 641.54 cm^{-1} . These bonds confirm the formation of CdO arrangement [233][234][252][253][254][255][256][257][258][259][260][261][262][263] (**Figure 5.14**).

By comparing the data obtained from PC1, PC2, PC3 and PC4, it was observed that the intensity of PANI peaks decreased with the increase in the quantity for CdO in sample composition PC2 (1:1), PC3 (1:2) and PC4 (0:1) and thus CdO peaks became sharper and visible. Furthermore, it confirmed the formation of crystallisation of CdO structure. **Table 5:8** furnishes the values for FTIR peaks and the associated bonds.

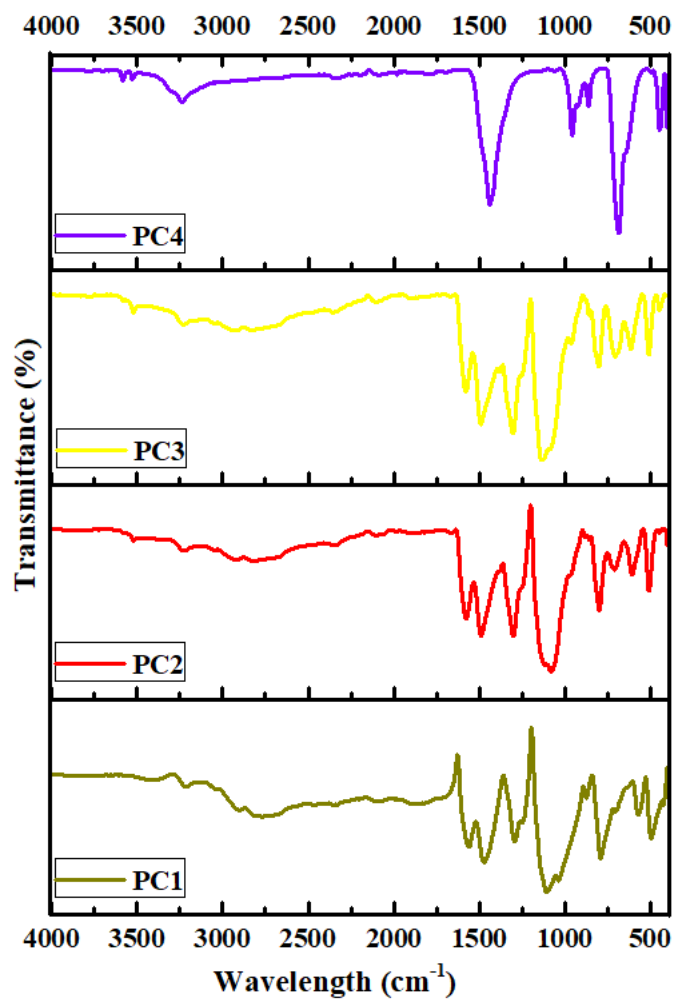


Figure 5.14 FTIR Analysis of PC1 [PANI, 1:0], PC2 [PANI + CdO, 1:1], PC3 [PANI + CdO, 1:2] and PC4 [CdO, 0:1].

Table 5:8: FTIR peaks and the associated bonds for PC1 [PANI, 1:0], PC2 [PANI + CdO, 1:1], PC3 [PANI + CdO, 1:2] and PC4 [CdO, 0:1].

	Peak Names	PC1 (PANI - 1:0)	PC2 (PANI + CdO - 1:1)	PC3 (PANI + CdO - 1:2)	PC4 (CdO - 0:1)
1.	N – H	3418.52 cm ⁻¹	3413.40 cm ⁻¹	3426.20 cm ⁻¹	–
2.	NH ²⁺ of – C ₆ H ₄ NH ²⁺ C ₆ H ₄ –	2921.58 cm ⁻¹	2921.58	2926.70 cm ⁻¹	–
3.	C – H of CH ₂	2900.68 cm ⁻¹ , 2826.03 cm ⁻¹	2864.84 cm ⁻¹ , 2826.03 cm ⁻¹	2838.82 cm ⁻¹ , 2828.59 cm ⁻¹	–

4.	C = N	1664.07 cm ⁻¹ , 1648.84 cm ⁻¹	1666.63 cm ⁻¹ , 1648.72 cm ⁻¹	1664.07 cm ⁻¹	–
5.	Quinonoid	1561.80 cm ⁻¹	1574.19 cm ⁻¹	1577.65 cm ⁻¹	–
6.	Benzenoid	1471.30 cm ⁻¹	1487.15 cm ⁻¹	1487.15 cm ⁻¹	–
7.	C – N	1290.30 cm ⁻¹ , 1245.05 cm ⁻¹	1298.95 cm ⁻¹	1274.07 cm ⁻¹	–
8.	Protonated PANI	1137.26 cm ⁻¹	1121.40 cm ⁻¹	–	–
9.	C – H in plane	1104.11 cm ⁻¹	1114.49 cm ⁻¹	1117.95 cm ⁻¹	–
10.	C – H out of plane	872.67 cm ⁻¹	879.59 cm ⁻¹	879.59 cm ⁻¹	–
11.	C – C	568.03 cm ⁻¹	569.76 cm ⁻¹	568.03 cm ⁻¹	–
12.	C – N – C	513.84 cm ⁻¹	506.92 cm ⁻¹	506.92 cm ⁻¹	–
13.	– OH bond of H ₂ O content	–	3696.19 cm ⁻¹ – 3104.15 cm ⁻¹	3681.25 cm ⁻¹ – 3106.70 cm ⁻¹	3663.93 cm ⁻¹ – 3108.85 cm ⁻¹
14.	– OH of H ₂ O – CdO	–	3580.81 cm ⁻¹ , 3521.21 cm ⁻¹ , 3516.07 cm ⁻¹ , 3495.73 cm ⁻¹ , 3475.25 cm ⁻¹ , 3457.34 cm ⁻¹ , 3441.98 cm ⁻¹	3580.81 cm ⁻¹ , 3495.73 cm ⁻¹ , 3462.46 cm ⁻¹ , 3436.86 cm ⁻¹	3582.54 cm ⁻¹ , 3553.95 cm ⁻¹ , 3526.05 cm ⁻¹ , 3461.95 cm ⁻¹ , 3416.76 cm ⁻¹
15.	O = C = O of CO ₂	–	2390.51 cm ⁻¹ , 2354.68 cm ⁻¹	2352.12 cm ⁻¹ , 2328.66 cm ⁻¹	2395.52 cm ⁻¹ , 2357.52 cm ⁻¹
16.	C = O	–	1725.92 cm ⁻¹	1728.48 cm ⁻¹	1728.45 cm ⁻¹
17.	– OH bond from atmospheric water vapor	–	1647.11 cm ⁻¹	1651.27 cm ⁻¹	1667.32 cm ⁻¹
18.	C = C	–	1640.20 cm ⁻¹	1645.38 cm ⁻¹	1642.72 cm ⁻¹
19.	O – C – O	–	1445.36 cm ⁻¹ , 1380.80 cm ⁻¹	1447.09 cm ⁻¹ , 1407.03 cm ⁻¹ , 1389.73 cm ⁻¹ , 1384.26 cm ⁻¹ , 1379.07 cm ⁻¹	1483.44 cm ⁻¹ , 1436.01 cm ⁻¹ , 1414.45 cm ⁻¹ , 1399.23 cm ⁻¹
20.	Wagging CdO	–	1333.82 cm ⁻¹	1335.55 cm ⁻¹	1346.55 cm ⁻¹
21.	M – O bond of Cd(NO ₃) ₂	–	1251.97 cm ⁻¹	1251.97 cm ⁻¹	1244.73 cm ⁻¹

22.	C – O of CdO crystallinity	–	1140.71 cm ⁻¹	1135.53 cm ⁻¹	1171.13 cm ⁻¹ , 1131.01 cm ⁻¹
23.	C – O – C	–	1077.88 cm ⁻¹	1083.07 cm ⁻¹	1059.34 cm ⁻¹
24.	Characteristic peaks of CdO	–	973.55 cm ⁻¹ , 959.71 cm ⁻¹ , 930.03 cm ⁻¹ , 907.26 cm ⁻¹ , 856.82 cm ⁻¹ , 822.23 cm ⁻¹ , 797.74 cm ⁻¹ , 726.26 cm ⁻¹ , 707.24 cm ⁻¹ , 451.30 cm ⁻¹ , 447.84 cm ⁻¹ , 439.19 cm ⁻¹ , 421.61 cm ⁻¹ , 412.96 cm ⁻¹	961.4 cm ⁻¹ , 855.09 cm ⁻¹ , 820.22 cm ⁻¹ , 799.46 cm ⁻¹ , 705.51 cm ⁻¹ , 442.65 cm ⁻¹ , 400.86 cm ⁻¹	955.59 cm ⁻¹ , 858.25 cm ⁻¹ , 526.17 cm ⁻¹ , 496.01 cm ⁻¹ , 442.61 cm ⁻¹ , 400.83 cm ⁻¹
25.	C – O – H of – COOH	–	930.03 cm ⁻¹	919.65 cm ⁻¹	920.45 cm ⁻¹
26.	M – O of Cd – O	–	604.63 cm ⁻¹	682.74 cm ⁻¹ , 611.55 cm ⁻¹	681.66 cm ⁻¹ , 641.54 cm ⁻¹

5.2.4 Raman Spectroscopy

Raman studies like IR – analysis also provides with “Molecular Finger – Print region” that is specific to each compound or element that exists in the sample or composition. This tool lays – down the details concerning both organic and inorganic compounds and as well provides with information regarding the vibrational level for the molecule. The accumulation and breakdown of such knowledge supplies the statics of the existing particle at micro level.

The aniline molecule is the construction of 26 atoms in total and it is affiliated to the C_s space group. This point group belongs in the inferior category and thus exhibits at the most two symmetries of elements i.e., S and E. Furthermore, this results in 42 representations that are counted as irreducible and as well exhibits 36 vibrational modes. These principal modes in whole comprises of Infra – red modes and Raman active modes. it is demonstrated by the

following expression: $\Gamma_{\text{vib}} = 20 A' + 16 A''$. The latter mentioned 36 vibrational modes incorporates of 6 (3 A' + 3 A'') modes for N – H bond vibrations, 15 (9 A' + 6 A'') modes for the C – H bond vibrations, 3 C – N bond vibrational modes and 12 (7 A' + 5 A'') modes for the ring vibrations. Polyaniline exists in the emeraldine structure for conductive polymer and constitutes of repetition of aniline monomer. It also belongs to the C_s space group. It has 138 vibrational modes which are both Infra – red active as well as Raman active modes. it is equated as: $\Gamma_{\text{vib}} = 93 A' + 45 A''$ [264]. For PC1, the peak obtained at 578.97 cm^{-1} was assigned to the out – of – plane deformation of C – H bond which was associated with quinonoid (Q) structure. The value for the amine site defect was observed at 746.36 cm^{-1} . The peak at 787.01 cm^{-1} was adjacent to the distortion in the quinone arrangement of polyaniline. The amine deformation was obtained at the peak of 812.77 cm^{-1} . The peak value 1176.61 cm^{-1} was due to vibrations obtained with the occurrence of the in – plane vibrations in C – H bond of quinonoid structure. The C – N bond of amine was acquired at 1238.87 cm^{-1} . The delocalised arrangement of the polarons $C \sim N^+$ resulted in vibrational stretching which were observed at 1347.52 cm^{-1} . The distorted form of vibrations for the stretched configuration of polymer was procured at 1385.51 cm^{-1} . The peak at 1489.97 cm^{-1} was the C = N bond of the imine. The value for N – H bending was obtained at 1567.81 cm^{-1} . The peak assigned to the C = C vibrational stretching formed of quinonoid structure was at 1598.57 cm^{-1} whereas, the C – C stretching vibrations of benzenoid arrangement was seen at 1611.02 cm^{-1} [265][266][267][268][269][270][271][272]. For PC2, the Raman peaks for PANI were obtained as follows: 577.25 cm^{-1} (C – H out plane of Q – structure). 749.36 cm^{-1} (imine site deformation). 785.34 cm^{-1} (Q – site distortion). 813.06 cm^{-1} (amine deformation). 1179.50 cm^{-1} (C – H in plane of Q – arrangement). 1233.45 cm^{-1} (amine C – N bond). 1346.10 cm^{-1} ($C \sim N^+$). 1387.82 cm^{-1} (delocalised vibrations of extended polymer). 1487.49 cm^{-1} (C = N of imine bonding). 1563.92 cm^{-1} (bending for N – H). 1591.65 cm^{-1} (C = C of Q - conformation). 1614.39 cm^{-1} (C – C of B - structure). The CdO Raman peaks were also obtained as such: 147.62 cm^{-1} (weak CdO peak). 287.65 cm^{-1} (2 TA (L) = TA + TO). 392.83 cm^{-1} (2 LA (L)). 957.68 cm^{-1} (pure CdO peak). For PC3, polyaniline exhibited values at peaks: 577.11 cm^{-1} (out of plane C – H of Q – arrangement). 744.86 cm^{-1} (distortion for imine). 785.33 cm^{-1} (deformation for Q – configuration). 813.06 cm^{-1} (deformation of amine). 1175.76 cm^{-1} (in – plane C – H of Q – structure). 1233.63 cm^{-1} (C – N of amine bond). 1346.61 cm^{-1} ($C \sim N^+$). 1383.92 cm^{-1} (delocalised vibrations in extended polymer backbone). 1482.95 cm^{-1} (imine C = N bond). 1568.42 cm^{-1} (N – H bending). 1591.65 cm^{-1} (C = C for Q - configuration). 1614.31 cm^{-1} (C – C of B – formation). The Raman values were procured for

CdO crystal as: 147.62 cm^{-1} (weaker CdO peak). 287.64 cm^{-1} (2 TA (L) = TA + TO). 391.97 cm^{-1} (2 LA (L)). 953.19 cm^{-1} (pure CdO peak). For PC4, the disposition of CdO was observed. As in accordance with the selection theory, there are two vibrational modes that are dipole forbidden; Transverse Optic (TO) mode and Longitudinal Optic (LO) mode for the crystal arrangement that has rock – salt conformation in nature. CdO has cubic configuration in monteponite phase which follows the afore – mentioned structure and thus, all the Raman peaks observed were assigned to second – order Raman scatterings. The space group of CdO is O_h^5Fm3m . A weaker CdO peak was obtained at 147.62 cm^{-1} . The band at 287.56 cm^{-1} was attributed to the amalgamation of 2 TA phonons at L – site i.e., TA + TO thus making up equation 2 TA (L) = TA + TO. The peak 391.87 cm^{-1} was the consequence of 2 LA (L) vibration. This stemmed within the domain that contained higher volume of phonon states in the two – phonon sum densities and was the resultant of overtone of 2 LA states at varying symmetry areas. The peak at 957.68 cm^{-1} was seen for pure CdO arrangement. As the LO and TO modes are dipole – forbidden therefore, no peaks were obtained concerning these modes [273][274][275][276][277][278][279] (**Figure 5.15**).

The results for PC1, PC2, PC3 and PC4 were put together for comparison purposes and it was discerned that the peaks for CdO became more distinguished for sample PC3 and PC4 as compared to PC2 because the CdO content was increased in latter sample code. Furthermore, the sharpness in the PANI peaks was declining with each proceeding sample with increasing acuteness in CdO peaks. Thus, that the visibility for the crystallinity of CdO was more prominent and henceforth, confirms the formation of said nano – powders **Table 5:9**.

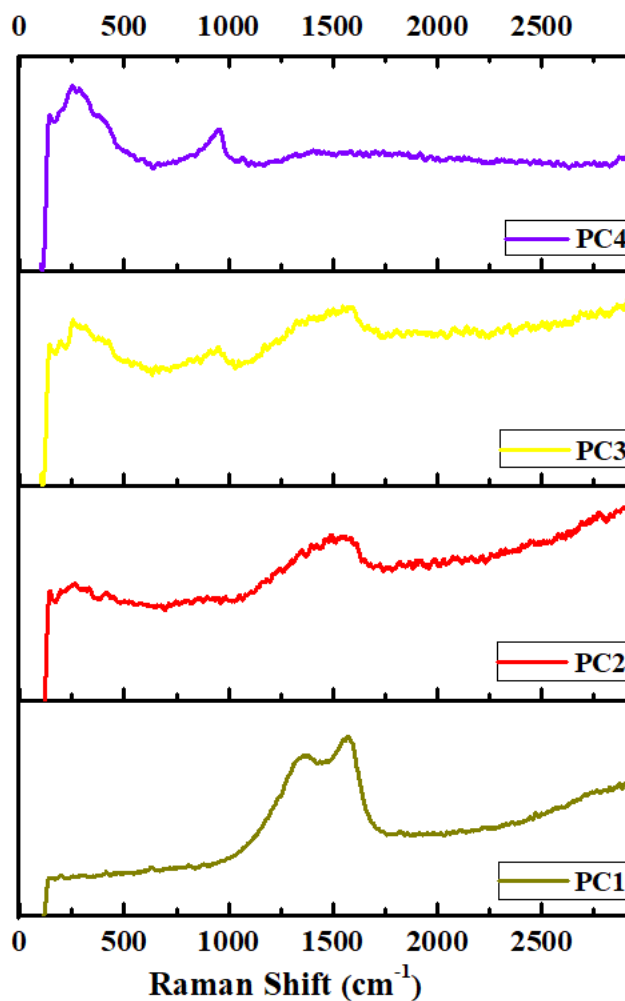


Figure 5.15 Raman Analysis of PC1 [PANI, 1:0], PC2 [PANI + CdO, 1:1], PC3 [PANI + CdO, 1:2] and PC4 [CdO, 0:1].

Table 5:9: Raman peak values and the bonds for PC1 [PANI, 1:0], PC2 [PANI + CdO, 1:1], PC3 [PANI + CdO, 1:2] and PC4 [CdO, 0:1].

	Peak Names	PC1 (PANI - 1:0)	PC2 (PANI + CdO - 1:1)	PC3 (PANI + CdO - 1:2)	PC4 (CdO - 0:1)
1.	C – H out plane of Q – structure	578.97 cm ⁻¹	577.25 cm ⁻¹	577.11 cm ⁻¹	–
2.	imine site deformation	746.36 cm ⁻¹	749.36 cm ⁻¹	744.86 cm ⁻¹	–
3.	Q – site distortion	787.01 cm ⁻¹	785.34 cm ⁻¹	785.33 cm ⁻¹	–
4.	amine deformation	812.77 cm ⁻¹	813.06 cm ⁻¹	813.06 cm ⁻¹	–

5.	C – H in plane of Q – arrangement	1176.61 cm ⁻¹	1179.50 cm ⁻¹	1175.76 cm ⁻¹	–
6	amine C – N bond	1238.87 cm ⁻¹	1233.45 cm ⁻¹	1233.63 cm ⁻¹	–
7.	C ~ N ⁺	1347.52 cm ⁻¹	1346.10 cm ⁻¹	1346.61 cm ⁻¹	–
8.	delocalised vibrations of extended polymer	1385.51 cm ⁻¹	1387.82 cm ⁻¹	1383.92 cm ⁻¹	–
9.	C = N of imine bonding	1489.97 cm ⁻¹	1487.49 cm ⁻¹	1482.95 cm ⁻¹	–
10.	N – H bending	1567.81 cm ⁻¹	1563.92 cm ⁻¹	1568.42 cm ⁻¹	–
11.	C = C of Q - conformation	1598.57 cm ⁻¹	1591.65 cm ⁻¹	1591.65 cm ⁻¹	–
12.	C – C of B - structure	1611.02 cm ⁻¹	1614.39 cm ⁻¹	1614.31 cm ⁻¹	–
13.	weak CdO peak	–	147.62 cm ⁻¹	147.62 cm ⁻¹	147.62 cm ⁻¹
14.	2 TA (L) = TA + TO	–	287.65 cm ⁻¹	287.64 cm ⁻¹	287.56 cm ⁻¹
15.	(2 LA (L))	–	392.83 cm ⁻¹	391.97 cm ⁻¹	391.87 cm ⁻¹
16.	pure CdO peak	–	957.68 cm ⁻¹	953.19 cm ⁻¹	957.68 cm ⁻¹

5.2.5 FESEM Analysis

The surface morphological information was obtained through the employment of FESEM tool as it lays – out the ocular analysis for the sample system by generating comprehensible and electro – statically images that were distorted to a lesser extent. It also helped with the understanding of purity for the samples by revealing the presence of contamination even at micro – level. For PC1, PANI outlaid the morphology that was similar to coral – like which has a higher degree of irregularity and asymmetry arrangement associated with its structure. The materialisation of cluster formation in abundance was observed for PANI molecules. The afore – mentioned traits were the common factors of occurrence that were generally analogous with the synthesis process applied i.e., chemical oxidation polymerisation process [247][280] [281][282]. For PC2 and PC3, the presence of CdO nano – powders were also visible because of the distinct structured shape morphology as compared to the irregular shape of PANI. CdO content was introduced into composition mixture at varying ratios for PC2 (1:1) and PC3 (1:2) i.e., the latter sample system has more percentage of CdO present in it, which was also confirmed. When the data obtained was studied against each other, the formation of CdO structures were observed for both PC2 and PC3 with the more prominent emergence of CdO

shape in the latter case whereas, the coral – like morphology of PANI becomes less visible in PC3 case. For PC4, the sample nano – powders obtained exhibited porous nature with the presence of clumped particles at certain areas. The agglomeration of the particles was due to fusion of many smaller particles because the sample was thermally treated for longer time period at 400 °C and hence further led to increased porosity. Even though clump – like arrangement was formed, a defined structure was pronounced for CdO nano – crystalline powders [283][284][285][286][287][288][289][290] (**Figure 5.16**).

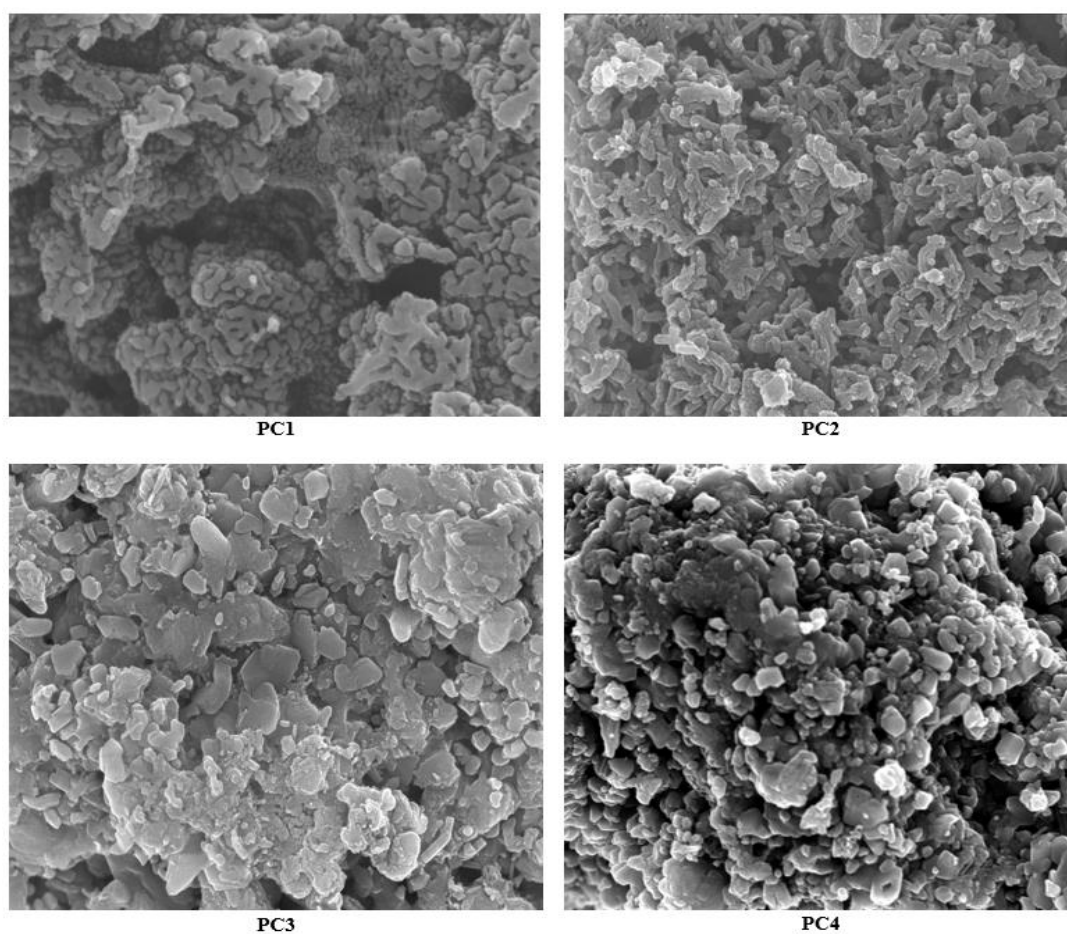


Figure 5.16 FESEM Analysis of PC1 [PANI, 1:0], PC2 [PANI + CdO, 1:1], PC3 [PANI + CdO, 1:2] and PC4 [CdO, 0:1].

5.2.6 EDX and Mapping Studies

The information concerning the elemental constituents was studied through EDX technique as this characterisation tool gave the analysis in the form of a spectra which consisted of peaks at

specific values which were studied to be adjacent to elements that formed the sample composition. For PC1, the formation of PANI was confirmed by acquiring the peaks corresponding to C (carbon), O (oxygen) and N (Nitrogen) – atoms. For PC2 and PC3, the peaks for C, O, N and Cd, O – atoms associated with both PANI and CdO nano - powders respectively were procured. For PC4, the spectra exhibited the attendance of peaks for Cd (cadmium) and O (oxygen) – atoms which solidified the fabrication of desired nano – powders. A small number of inconsequential but defined peaks were also observed. These were formed as the resultant of the compositions within the chemicals that were used as precursors in synthesis process (**Figure 5.17**).

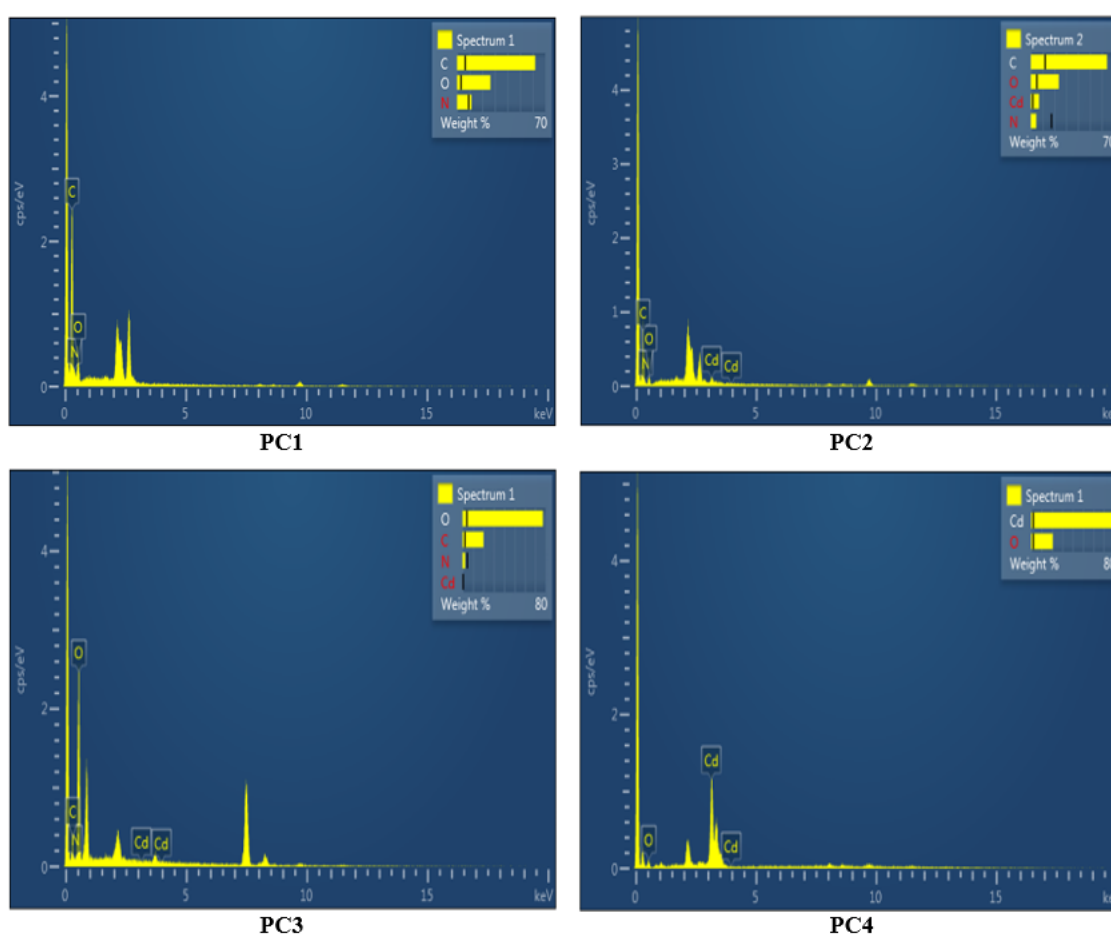


Figure 5.17 EDX Analysis of PC1 [PANI, 1:0], PC2 [PANI + CdO, 1:1], PC3 [PANI + CdO, 1:2] and PC4 [CdO, 0:1].

EDX mapping was also done so as to obtain the data concerning with the spatial distribution and the placements of the elements within sample domain (**Figure 5.18**).

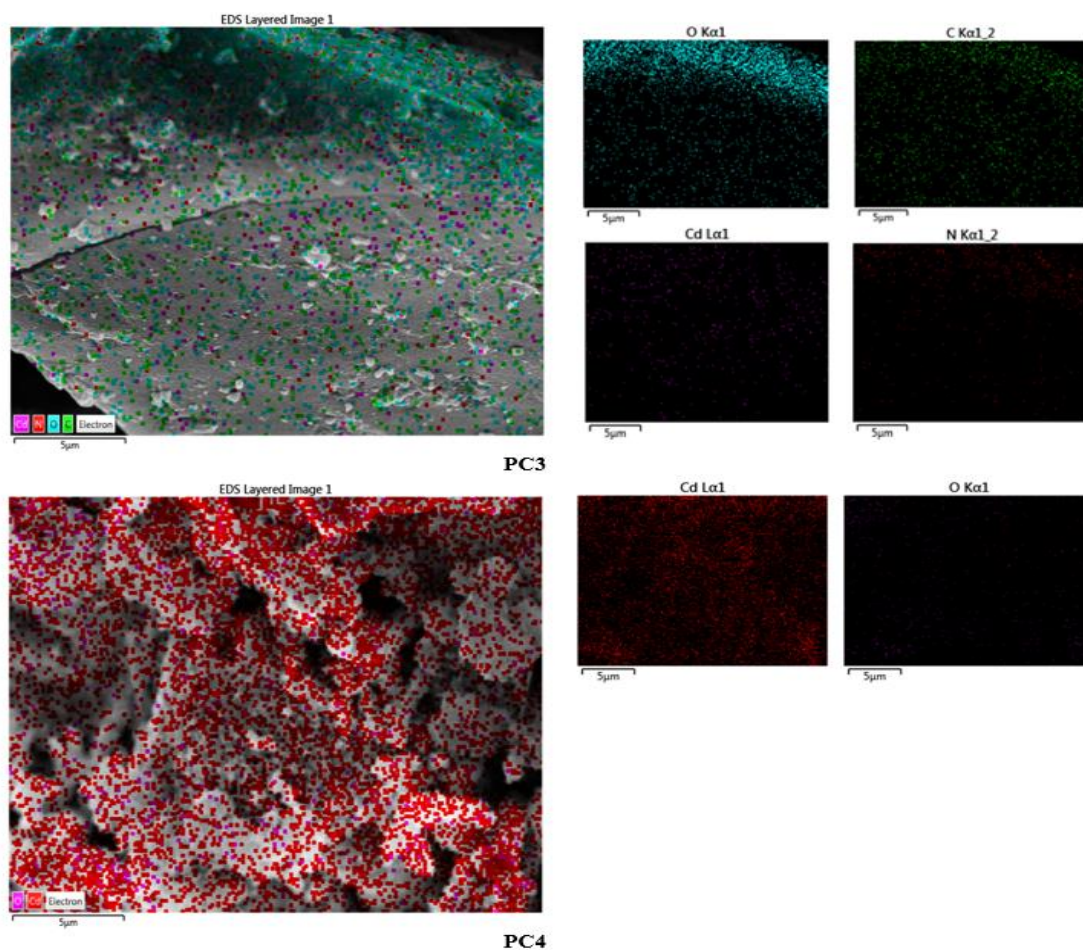


Figure 5.18 EDX - Mapping Analysis of PC1 [PANI, 1:0], PC2 [PANI + CdO, 1:1], PC3 [PANI + CdO, 1:2] and PC4 [CdO, 0:1].

5.2.7 PSA Analysis

Particle size distribution details were obtained in the form of bar graph regarding the size percentile details for the elements that were existing in the sample powders. The analysis was done only for CdO nano – powders as it falls under cubic crystalline arrangement whereas, PANI has an unordered structure and does not follow any specific crystalline arrangement. The particle size value was obtained to be 32.09243 nm with a standard error = 1.1823 %. These values were also studied against the crystallite values obtained by XRD spectra. It was observed that the size values computed through PSA were smaller as compared to XRD analysis which implied that the nano – powders synthesised has crystalline nature (**Figure 5.19**).

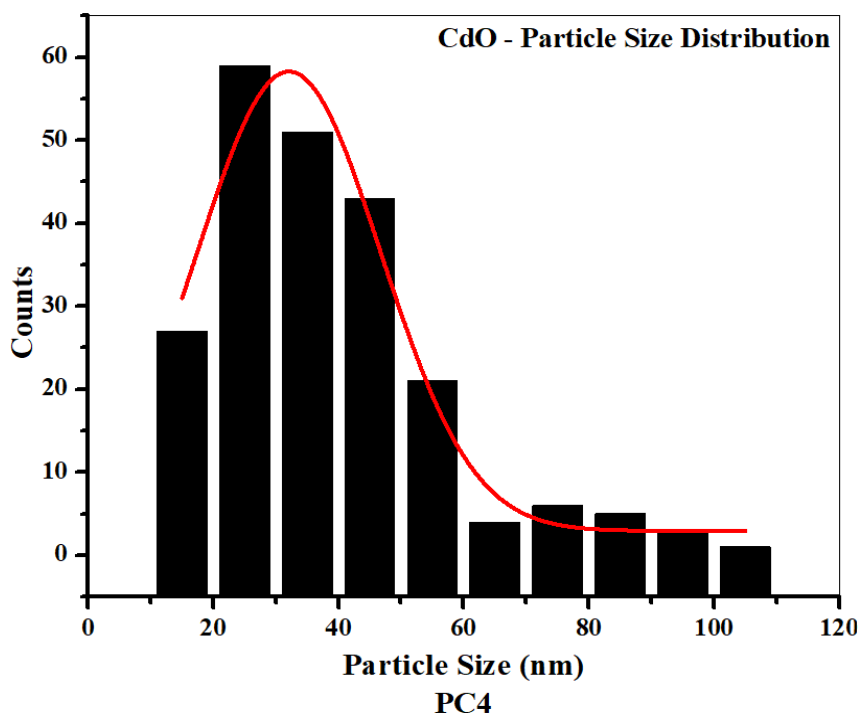


Figure 5.19 Particle Size Distribution Analysis of PC4 [CdO, 0:1].

5.2.8 Varistor Studies

Varistor studies were done by plotting the graph for current, J (mA/cm^2) and voltage, E (V/mm) values against each other and analysing the data obtained through it. The characterisation investigated the information concerning “the maximal capability of the device to accommodate the highest values for current and voltage, before the system reached its shut – down stage”. These devices see their employment in electrical circuits as circuit protectors because they prevent the occurrence of short – circuiting and fires by closing down the entire system before it gets damaged. Varistors work by permitting the surplus movement of current through them which results in averting of the impairment of integrated boards and circuits thus lengthening the operational aspect of the equipments.

The paper studies the carbon dominated polymer, PANI + transparent metal – oxide, CdO system for current – voltage graph. Polyaniline has been recognised as an excellent form of electrically conducting polymer due to the fact that it consists of majority of holes as charge carriers because it is a radical cation and as a result of this behaviour PANI has several advantages with its usage in sectors of electrical devices such as; sensors and photonic and opto

electronic devices. They can be easily synthesised, exhibit environmental stability and have the ability to be manipulated for betterment furthermore, they are emerging materials for anti – corrosion properties. CdO is a n – type semi conducting material and because it consists majorly of electrons as electrical conduction carriers, this metal oxide demonstrates exceptional potential for mobility of electrons across the system. It is also a robust material with higher melting temperature values which makes it thermally stable metal – oxide. In this case, the junction is obtained between cation rich polymer and n-type semiconducting metal-oxide.

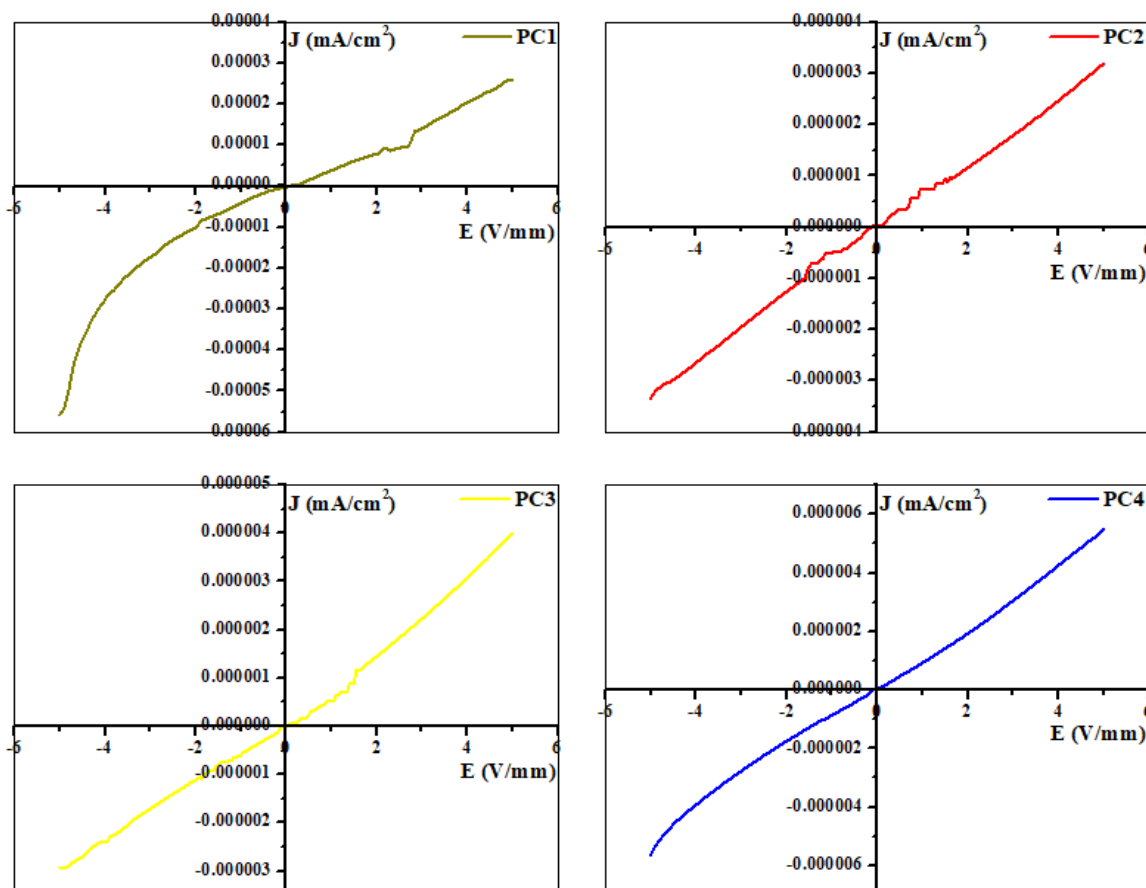


Figure 5.20 Current – Voltage Plot Analysis of PC1 [PANI, 1:0], PC2 [PANI + CdO, 1:1], PC3 [PANI + CdO, 1:2] and PC4 [CdO, 0:1].

When the graphs were plotted and studied in comparison to each other (**Figure 5.20**), it was observed that there were certain factors that governed the direction of the graphical analysis. Firstly, the attendance of current compliance was obtained within the system. Current compliance by definition meant, the highest value for current that an electro – chemical cell exhibited the capability to uphold within the system. In this case, the standardised current

compliance value for the cell w.r.t which the sample systems were studied for was 1.00 mA/cm^2 approximately. Therefore, the sample cases disclosed the working potential near and around the said value with varying voltage values. The lowest values were acquired for PANI samples when plotted individually and maximum values were observed for CdO nano – powders.

Secondly, a consistent and steady increase was noticed throughout the system domain which resulted in the formation of the linear region. This slope area of the graph exhibited the development of graph with current values being in direct proportional to the voltage values and leading to a continual elevation in the graphical plot before it reached its stopping point i.e., knee point. The knee point meant the point in the graph where the increasing slope exhibits a visible bend in the curve and reaches the saturation region i.e., non – linear region. This area before the knee point was named the ‘Linear Region’ which means that Ohm’s Law was applicable within this domain with little to no resistance present within the system [196]. In this area, the flow of current was due to the applied forward bias conditions where the p – and n – junctions are connected to the positive and negative terminals of the battery respectively. The holes and electrons flow towards the direction of the junction which leads to decrease in the potential barrier strength. This diminishing potential barrier provides no resistance to the current flow and thus conduction takes place within the system. Furthermore, the occurrence of closed porosity i.e., smaller gaps that are not interconnected within the grain boundaries were also observed which was further confirmed from **Figure 5.16**. The trapping of electrons within these isolated spaces in the grain boundaries were small and inconsequential and thus not effected the flow or values of conduction thus, the dominating population of electrons were available for current conduction process [190]. Some amounts of current conduction were also obtained in reverse biased graphs even with vice versa connections of the junctions and battery terminals respectively. Even though the width of potential barrier was increased in this case, there were still some minority amounts of electrons available for the conduction and thus led to the slope in the negative planes.

It was noted as the content of the CdO nano – powders were increased for the proceeding sample systems, the values for current and voltage were also increased, even though the values that were procured demonstrated a smaller scale difference among the values.

Thirdly, although a steady linear arena was acquired, an array of smaller and inconsequential curves was also observed for the cases of PC1, PC2 and PC3. This could be mainly due of the presence of PANI because it has carbon dominated structure. Since PANI categorises as a polymer, it does not consist of an ordered arrangement instead the amorphous nature of polyaniline resulted into the formation of zig – zag like pattern in the increasing slope of graphical curve. The curve revealed to get lessened in the intensity with the increase in the content of CdO nano – powders.

Lastly, the values for I_N and V_N were obtained from the ending points of linear slope for each sample case. I_N and V_N were described as the varistor current and varistor voltage values that were existing across the sample system. These values were represented in the tabular form as given by **Table 5:10**.

Table 5:10: V_N (V/mm) = Varistor Voltage and I_N (mA/cm²) = Varistor current for PC1 [PANI, 1:0], PC2 [PANI + CdO, 1:1], PC3 [PANI + CdO, 1:2] and PC4 [CdO, 0:1].

Sample code	I_N [mA/cm ²]	V_N [V/mm]
PC1 (PANI - 1:0)	2.6024×10^{-5}	4.9752
PC2 (PANI + CdO - 1:1)	3.2087×10^{-5}	5.0133
PC3 (PANI + CdO - 1:2)	4.0275×10^{-5}	5.0403
PC4 (CdO - 0:1)	5.4627×10^{-5}	5.1307

From the **Table 5:10**, it was noted that current and voltage values for all the sample systems exhibited an increase in the values, as the content of CdO nano – powders that was being added into the composite mixture was increased in terms of volume ratio. The differences among the values were noted to be minuscule w.r.t each other still the sample system showed an elevation in the scale. The cause for such small-scale differences could be due to: (I). the applicability of current compliance in the device which was used to obtain the analysis and therefore, the current – voltage exposure to the cells was limited to a lower region. (II). The composite sample

mixtures were constructed of only two materials which led to formation of a simpler matrix instead of a complicated 3 or more network system [198].

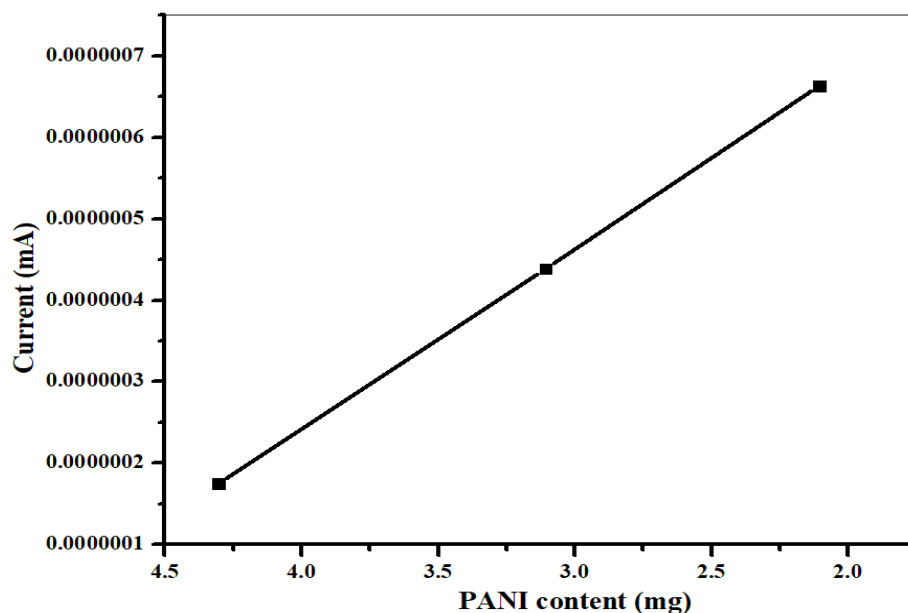


Figure 5.21 Graphical view of current values against the PANI content for PC1 [PANI, 1:0], PC2 [PANI + CdO, 1:1], PC3 [PANI + CdO, 1:2] and PC4 [CdO, 0:1].

For the understanding of how the behaviour of the sample were impacted when the quantity of CdO nano – powders was increased, PANI weight ratios were plotted w.r.t to current values as shown in **Figure 5.21**. It was recognised that as the volume for CdO nano – crystals were increased, the current values within the sample systems demonstrated a steady growth within the scale range. This meant, higher the current values were obtained, the voltage values were as well increased which will furthermore, lengthen the linear slope. This will result in elongated current – voltage direct proportional curve following Ohm’s Law. This implied that higher values for both current and voltages will be permitted to pass through the device before attaining the saturation region. This will prevent the pre – mature shut down of the system and hence, extending the employment time period of the system.

Concluding all the mentioned factors, the composite mixture of PANI and CdO nano – powders when studied with varying ratios, it exhibited a consistent growth for both varistor current and varistor voltage values within the applied system. Though the set of values that were obtained showed a smaller range difference, they still demonstrated the capability to enhance the

electrical properties which meant that if used with a complex material network, they could possibly exhibit much stronger conduction values. They can have its usage at larger scale where the higher values of voltages for the varistor were required. Now, with the assemblage of the values that were obtained for the studied sample system, it was noted that these have the employment opportunities in smaller scale industries where lower voltage varistor values are essential such as; smart – house gadgets, door bells, resistors, house alarms, thermostats etc.

5.3 TiO₂ (anatase) mixed with Ag

5.3.1 TGA Studies

- TGA analysis – TiO₂ (anatase) nanopowders.

TiO₂ prevails in three known phases; Rutile, Anatase and Brookite. Anatase form converts to rutile form at higher temperatures. And to obtain the specific value for the calcination of TiO₂ powders to have only the anatase form, TGA was employed on. Following the synthesis process (ultra – sonic assisted sol – gel method), TGA is basically employed on to the un – calcinated sample powders. This tool gives comprehensive knowledge regarding the changes in the mass w.r.t temperature when exposed to the heat treatments over a span of time. For this work, the sample underwent heat exposure from 40°C to 600°C at the rate of 10°C/min. The sample was also kept on hold for 1 min at 600°C. The TGA curve obtained exhibited three principal phases.

(I). Phase I: persisted in the temperature scale, 40.9°C – 150°C and in whole experienced weight loss of about 10.4%. This weight loss is accounted to the elimination of the ethanol, alcoholic contents attached on to the surface of the material and physically adsorbed water.

(II). Phase II: was observed in the temperature range from, 150°C – 350°C, with 18.9% of the weight loss, which was accredited to the decomposition of the organic functionalities.

(III). Phase III: was attained from 350°C – 600°C. This phase experienced > 10% weight loss, meaning the material weight was constant throughout this time span. It was as well seen that the amorphous structure of the nano – powder initiated its transformation to the anatase form i.e., its first crystalline phase. And no other conversions were observed till the temperature 600°C, thus confirming that no rutile phase was acquired.

Taking in the account of the details afore – mentioned, 450°C was taken as the acceptable temperature to calcinate the sample powders [291][292][293][294][295][296] (**Figure 5.22 a**).

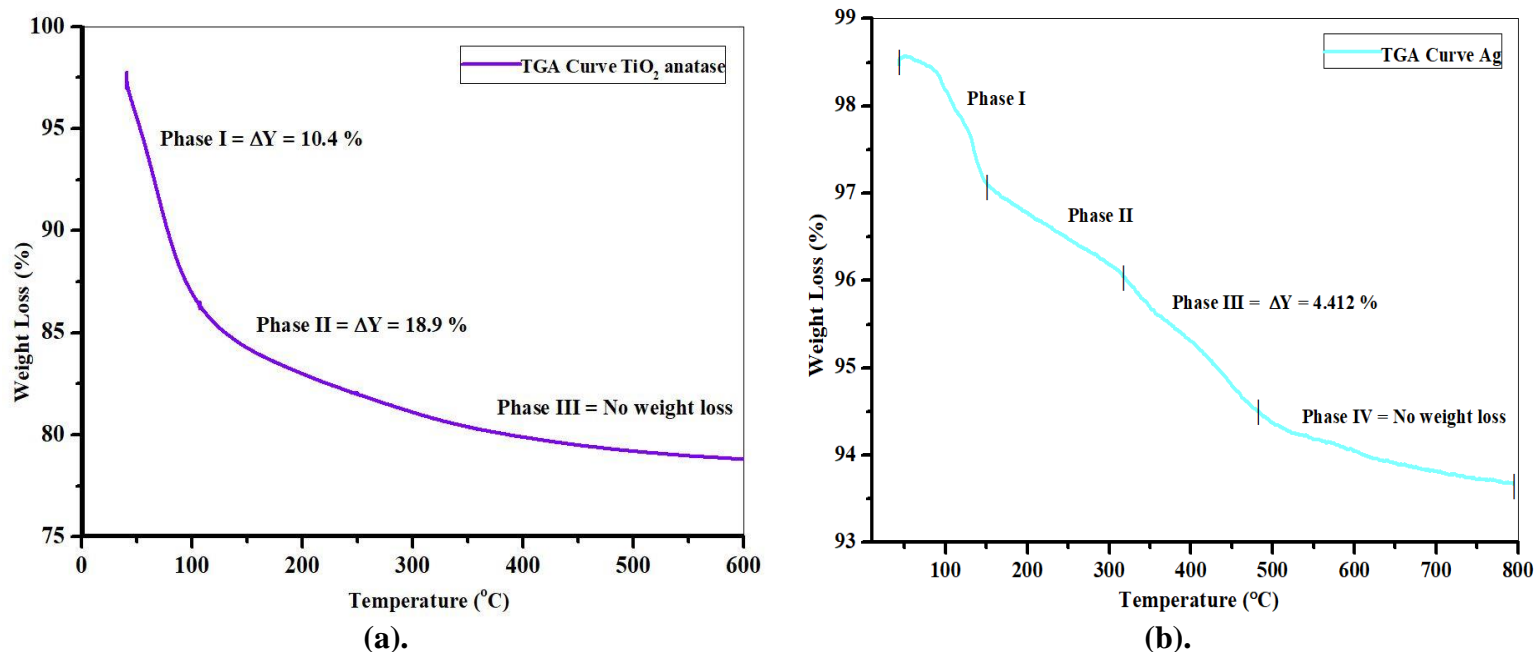


Figure 5.22 TGA Analysis of (a) TA1 [TiO₂, 1:0] and (b) TA4 [Ag, 0:1].

- TGA analysis – Ag nanopowders.

The synthesised silver nanopowders were air – dried by heating the sample solution with simultaneous evaporation of water molecules. This step was done at room temperature and to understand its weight loss with respect to the temperature, thermal analysis was done on the obtained nanopowders. The nano – structured samples experienced thermal treatment at 10°C/min in the temperature range of 40°C to 800°C. The sample was also put on hold for 1 min at 800°C. Four primary phases were obtained from the studied TGA graph.

(I). Phase I: was obtained in the temperature range from 43.6°C to 150°C. The occurrence of this phase is the resultant of the desorption process of the water molecules present in the sample composites nanopowders.

(II). Phase II: persisted from the temperature scale of 150°C to 317°C. This phase represents the decomposition of the organic or volatile compounds that gets attached to the surface of the powders during synthesis process.

(III). Phase III: was procured in the temperature stretch of 317°C to 482. This phase observed a weight loss of $\Delta Y = 4.412\%$, which is associated with the occurrence of the phenomenon of crystallisation of the silver nanoparticles.

(IV). Phase IV: the last phase was seen from 482°C to 800°C and considerably small amount of weight loss was attained. This means that the crystallisation of silver nanopowders was successfully done [5][125][130] [129][128][127][126] (**Figure 5.22 b**).

5.3.2 XRD Pattern

The structure of the crystalline materials prevailing in the composite mixture was examined through XRD. The obtained values exhibited the diffractogram for the characteristic Bragg reflections for both TiO₂ (anatase) and silver nanopowders, which were then compared to the already existing data for further confirmation [297].

For TA1, the characteristic peaks for TiO₂ (anatase) acquired at $2\theta^\circ$ values, were = 25.26°, 37.07°, 37.79°, 47.99°, 53.87°, 55.07°, and 62.62° having the corresponding crystal phase values at = (101), (103), (004), (200), (105), (211) and (204) respectively. The obtained values were in accordance with the JCPDS card no 21 – 1272 [298][299][300][301][302][303][304] [305][306][307][308][309]. For TA2, the anatase TiO₂ peak values were $2\theta^\circ = 25.26^\circ, 38.05^\circ, 47.98^\circ, 53.88^\circ, 54.98^\circ$ and 62.85° with the respective hkl – planes at (101), (004), (200), (105), (211) and (204). The metallic nature of Ag was also observed, with the $2\theta^\circ$ values = $38.05^\circ, 44.23^\circ, 64.38^\circ$ and 77.35° which were indexed to the simultaneous reflection planes at = (111), (200), (220) and (311) respectively. For TA3, the peak values at $2\theta^\circ = 25.26^\circ, 38.06^\circ, 47.96^\circ$ were procured for TiO₂, equating to the crystal planes = (101), (004) and (200) indicating the anatase form of the said sample. The structural peaks for Ag – nanopowders were observed at $2\theta^\circ$ values = $38.06^\circ, 44.23^\circ, 64.39^\circ$ and 77.34° having corresponding hkl planes values for (111), (200), (220) and (311). For TA4, the required characteristic peak values were as well obtained for the silver nanopowders. The procured values for $2\theta^\circ = 38.12^\circ, 44.29^\circ, 64.44^\circ$ and 77.39° gave the designated phase plane values at = (111), (200), (220) and (311). The observed values of sample were as per the JCPDS card no 04 – 0783 [154][153][152][151][150][149] [148][147][146][145] (**Figure 5.23**).

From comparisons of TA1, TA2, TA3 and TA4, it was observed that the number and the intensity of the peaks for TiO₂ were decreasing with each preceding sample, that is because the sample code TA1 (1:0) and TA4 (0:1) have pure TiO₂ and Ag nanopowders but the samples TA2 (3:1) and TA3 (1:1) consisted of composite of both aforementioned nanopowders. As the content of Ag was increasing with each sample composition, the amount of TiO₂ decreased and hence lesser peaks for the said were obtained which was expected. The lessening of TiO₂ peaks means the visible crystallisation of Ag peaks and the obtained XRD peak values are provided in **Table 5:11**.

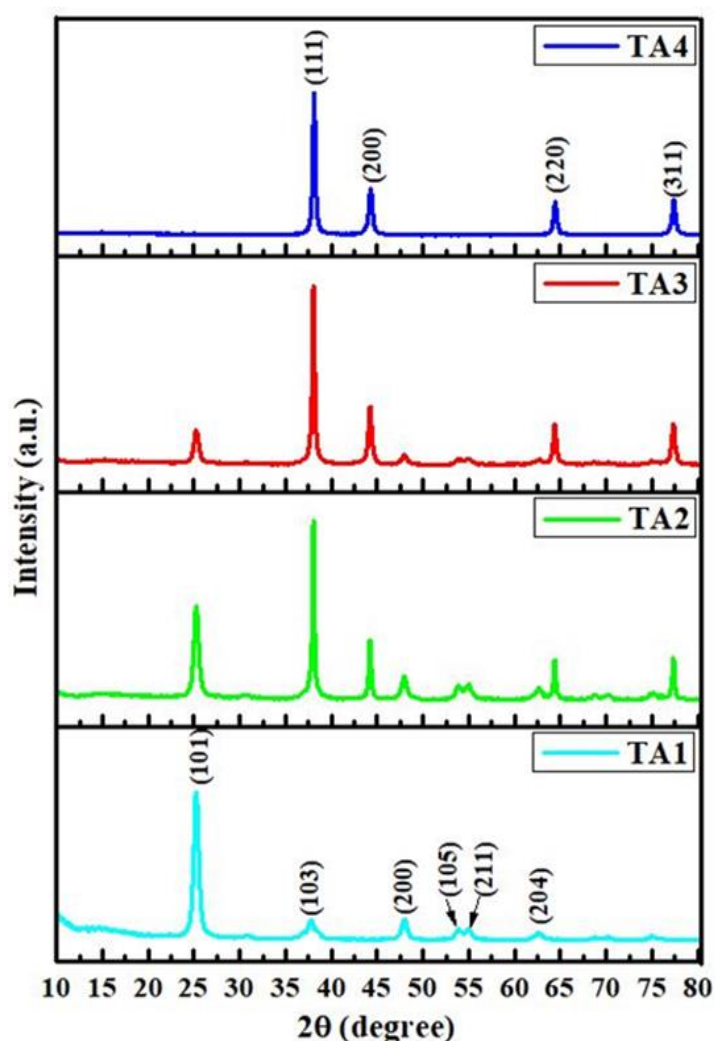


Figure 5.23 XRD Analysis of TA1 [TiO₂, 1:0], TA2 [TiO₂ + Ag, 3:1], TA3 [TiO₂ + Ag, 1:1] and TA4 [Ag, 0:1].

Table 5:11: XRD bonds and values for TA1 [TiO₂, 1:0], TA2 [TiO₂ + Ag, 3:1], TA3 [TiO₂ + Ag, 1:1] and TA4 [Ag, 0:1].

Sample code	TiO ₂		Ag	
	2θ	hkl	2θ	hkl
TA1 (1:0)	25.26°	101	–	
	37.07°	103		
	37.79°	004		
	47.99°	200		
	53.87°	105		
	55.00°	211		
	62.62°	204		
TA2 (3:1)	25.26°	101	38.05°	111
	38.05°	004	44.23°	200
	47.98°	200	64.38°	220
	53.88°	105	77.35°	311
	54.98°	211		
	62.85°	204		
TA3 (1:1)	25.26°	101	38.06°	111
	38.06°	004	44.23°	200
	47.96°	200	64.39°	220
			77.34°	311
TA4 (0:1)	–		38.12°	111
			44.29°	200
			64.44°	220
			77.39°	311

The crystallite size (D), lattice parameters values (a, b, c) and volume of sample (V) were as well obtained. TiO₂ anatase has slender tetragonal structure with unit lengths $a = b \neq c$ and silver follows cubic arrangement having unit lengths $a = b = c$; therefore, the said values were computed using the respective formulae and the calculated values were set in the tabular form as shown in **Table 5:12**.

$$D = \frac{k\lambda}{\beta \cos\theta}; \text{ (Debye Scherrer's Equation)}$$

$$\frac{1}{d_{hkl}^2} = \frac{h^2 + k^2}{a^2} + \frac{l^2}{c^2}; \text{ (Slender Tetragonal formula for anatase TiO}_2\text{)}$$

$$\frac{1}{d_{hkl}^2} = \frac{h^2 + k^2 + l^2}{a^2}; \text{ (Cubic formula for Ag nanoparticles)}$$

$$V = a \times b \times c; \text{ (Volume)}$$

Table 5:12: Lattice parameters (a, b, c), crystallite size (D), FWHM (β^*), Braggs Angle (2θ) and volume (V) of TA1 [TiO₂, 1:0], TA2 [TiO₂ + Ag, 3:1], TA3 [TiO₂ + Ag, 1:1] and TA4 [Ag, 0:1].

		a (Å)	b (Å)	c (Å)	D (nm)	β^* (°)	2θ (°)	V (Å) ³
TA1 (1:0)	TiO ₂	3.7884	3.7884	9.5144	14.4137	0.0129	25.26	136.5504
TA2 (3:1)	TiO ₂	3.7892	3.7892	9.4528	15.1318	9.8037×10^{-3}	25.26	135.7236
	Ag	4.092	4.092	4.092	24.0788	6.4893×10^{-3}	44.23	68.5183
TA3 (1:1)	TiO ₂	3.7908	3.7908	9.4584	14.5618	0.0101	25.26	135.9187
	Ag	4.128	4.128	4.128	24.0788	6.4893×10^{-3}	44.23	70.3427
TA4 (0:1)	Ag	4.0866	4.0866	4.0886	24.0839	6.4893×10^{-3}	44.29	68.2474

Rietveld refinement was also done for all the samples with the help of Fullprof suite software, the refined patterns were obtained for both the said sample materials because of their ordered crystalline nature (**Figure 5.24**). For the graphical plot, Y_{obs} were the already measured values, Y_{cal} were the experimentally obtained values, $Y_{obs} - Y_{cal}$ was the difference between the already calculated values and experimentally obtained values and Braggs angle = gave the details regarding the positions and number of the seen peaks which were obtained experimentally. From **Figure 5.24** it is learnt that all the peaks for the TiO₂ (anatase) and Ag – nanopowders matched the standardised peak values, with the absence of the any unexpected peaks, this evidenced that the experimentally synthesised samples were pure and had single phase nature. **Table 5:13** gives the tabular form of the refinement plot for the said sample compositions.

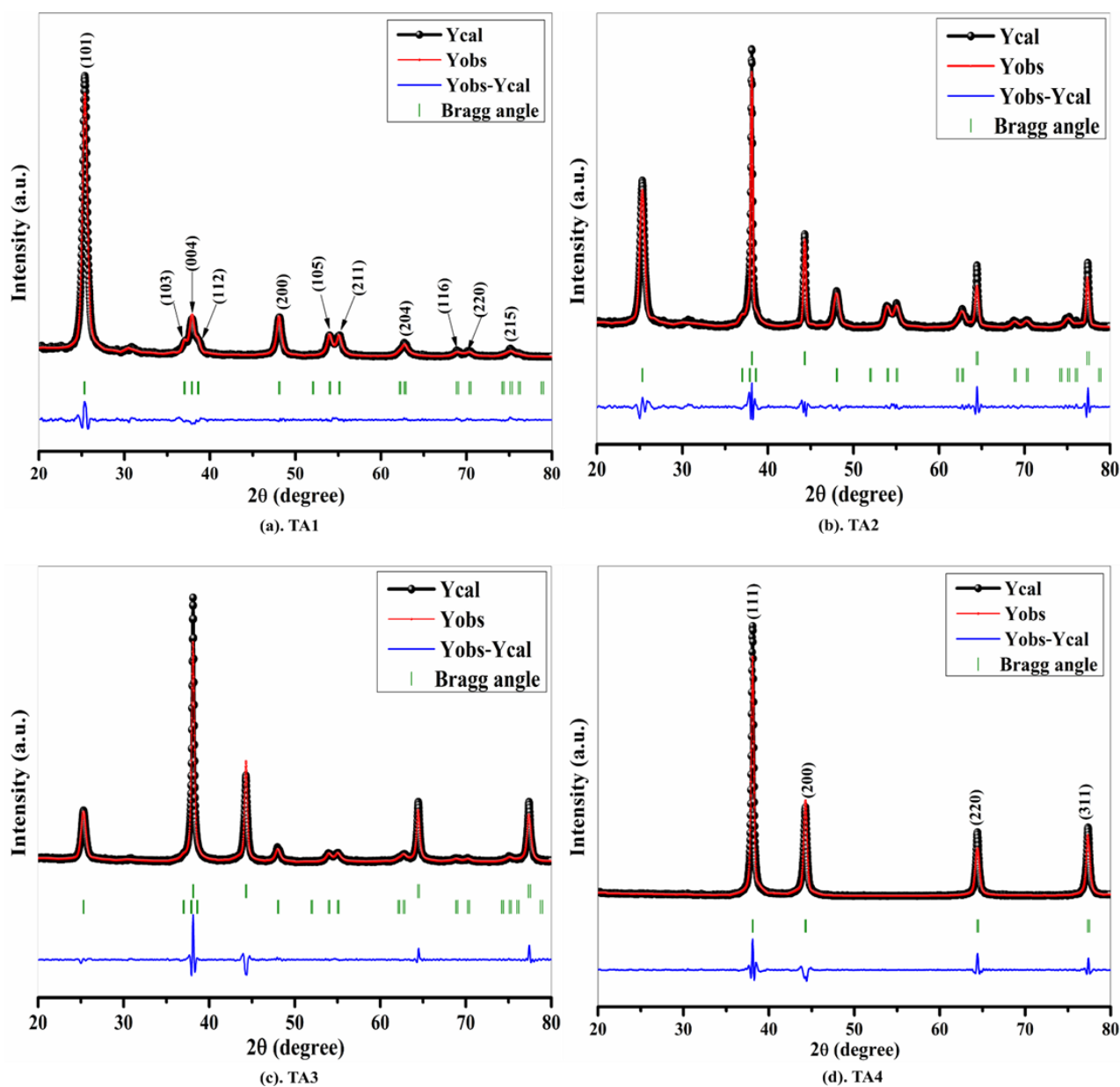


Figure 5.24 XRD Refinement Analysis of **(a)** TA1 [TiO_2 , 1:0], **(b)** TA2 [$\text{TiO}_2 + \text{Ag}$, 3:1], **(c)** TA3 [$\text{TiO}_2 + \text{Ag}$, 1:1] and **(d)** TA4 [Ag , 0:1].

Table 5:13: Conditions for refinement, reliability factor (R_p , R_{wp} , R_{exp}), chi-square (χ^2) and good of fit (GoF) of prepared samples

Sample composition	TA1 (1:0)	TA2 (3:1)		TA3 (1:1)		TA4 (0:1)
	TiO_2	TiO_2	Ag	TiO_2	Ag	Ag
$\lambda(\text{\AA})$	1.54056	1.54056		1.54056		1.54056

Cycles of refinement	30	30		30		30
Step (°)	0.020	0.020		0.020		0.020
Profile function	Pseudo-Voigt * Axial divergence asymmetry	Pseudo-Voigt * Axial divergence asymmetry		Pseudo-Voigt * Axial divergence asymmetry		Pseudo-Voigt * Axial divergence asymmetry
<i>a</i> (Å) (Rietveld)	3.797382	3.788213	4.089363	3.787725	4.089294	4.089480
<i>V</i> (Å ³) (Rietveld)	137.584 (0.052)	136.350 (0.016)	68.386 (0.003)	136.238 (0.028)	68.383 (0.004)	68.392 (0.004)
<i>R_p</i> (%)	28.8	17.2		13.0		15.5
<i>R_{wp}</i> (%)	43.0	18.5		14.9		16.6
<i>R_{exp}</i> (%)	8.78	23.8		23.7		17.1
χ^2	23.97	0.6063		0.3937		0.9329
GoF	4.8	0.77		0.62		0.94
Bragg R-factor (%)	24.9	3.62	3.42	3.44	4.43	4.78
Space group of phases	I 4 ₁ /amd	I 4 ₁ /amd	Fm-3m	I 4 ₁ /amd	Fm-3m	Fm-3m

5.3.3 FTIR Analysis

The chemical bonds present in the sample composite mixture were identified via FTIR. This characterisation tool produces a “Molecular Fingerprint Region” specifically within the range from 1500 cm⁻¹ to 400 cm⁻¹, unique to each material, providing the details regarding the bonds present in the sample mixture whether known or unknown.

For TA1, the characteristic peaks were obtained for TiO₂ (anatase), which were as follows: a broad curve was obtained from 3500 cm⁻¹ to 3000 cm⁻¹ which were the stretching vibrations for the adsorbed H₂O molecules present due to the intermolecular interactions of hydroxyl group (– OH). This broad spectrum represented the moisture existing within the sample. The stretching bond peaks for C – H were seen at 3349.60 cm⁻¹, 2976.84 cm⁻¹, these peaks were the

results of the remnants of the butyl group that were existing in the synthesised TiO₂ sample powder. 1642.85 cm⁻¹ was assigned to the stretching of the Ti – COOH bond, this peak was attained because of the precursors used in the synthesisation procedure which were titanium isopropoxide (Ti {OCH(CH₃)₂}₄) and isopropyl alcohol ((CH₃)₂CHOH). The bending vibrational mode for Ti – OH bond of the adsorbed H₂O molecules was obtained at 1634.04 cm⁻¹. The peak observed at 1385.86 cm⁻¹ was acquired due to TiO₂ (anatase) being thermally treated at 450°C. The vibrational mode for – C = O – Ti bond because of the adsorbed carbon dioxide (– CO₂) on the surface was seen at 1309.53 cm⁻¹. The wide spectrum of peaks at 1167.99 cm⁻¹, 1158.30 cm⁻¹, 1133.25 cm⁻¹, 1127.81 cm⁻¹, 1030.69 cm⁻¹ indicated the Ti – O – Ti vibrations. The Ti – O bond value observed at 952.95 cm⁻¹ was due to the homogeneity of the TiO₂ powder. The peak acquired at 832.20 cm⁻¹ was the characteristic peak for the TiO₂ synthesised using Sol – Gel method. The 775.25 cm⁻¹ peak was the stretching vibration of the Ti – O – C bond present. The characteristic peak values for O – Ti – O bond of TiO₂ were procured at 712.63 cm⁻¹, 668.20 cm⁻¹, 562.81 cm⁻¹, 523.82 cm⁻¹, 426.70 cm⁻¹, 421.26 cm⁻¹, 417.01 cm⁻¹, 412.99 cm⁻¹, 407.32 cm⁻¹ [298][294][301][310][311][312][313][314][315][316][317][318][319]. For TA2, 3948.76 cm⁻¹ (– OH bond of the adsorbed H₂O molecule). 3358.10 cm⁻¹, 2973.68 cm⁻¹ (C – H bond of TiO₂). 1634.80 cm⁻¹ (Ti – OH bond due to the adsorbed water molecules). 1623.20 cm⁻¹ (Ti – COOH bond because of the precursors used). 1382.81 cm⁻¹ (peak due to thermal treatment at 450°C). 1312.88 cm⁻¹ (– C = O – Ti vibrational bond because of CO₂). 1161.43 cm⁻¹, 1127.28 cm⁻¹, 1110.20 cm⁻¹, 1057.35 cm⁻¹, 1048.01 cm⁻¹, 1030.93 cm⁻¹, 1013.85 cm⁻¹, 1008.05 cm⁻¹ (Ti – O – Ti vibrational bonds). 948.44 cm⁻¹ (Ti – O bond due to the homogeneity of TiO₂). 837.85 cm⁻¹ (the characteristic peak for Sol – Gel method). 772.76 cm⁻¹ (Ti – O – C stretching vibrational bond). 712.95 cm⁻¹, 662.16 cm⁻¹, 563.05 cm⁻¹, 528.89 cm⁻¹, 427.45 cm⁻¹, 422.94 cm⁻¹, 417.65 cm⁻¹, 413.14 cm⁻¹, 407.73 cm⁻¹ (O – Ti – O bond peaks which were the characteristics of TiO₂) were procured. In this case, the emergence of the silver nanopowders was also observed as the peaks related to the metallic nature of silver were as well obtained. The peaks from 3977.12 cm⁻¹ to 3420.62 cm⁻¹ (were for the – OH group of the H₂O molecules). 1545.54 cm⁻¹, 1528.78 cm⁻¹, 1522.98 cm⁻¹, 1509.77 cm⁻¹, 1505.90 cm⁻¹ (N – O bonds of the nitro compound). 1399.89 cm⁻¹ (NO₃⁻ ion bond). 1367.66 cm⁻¹ (N = O bond). For TA3, the obtained TiO₂ peaks were: 3883.78 cm⁻¹ (– OH bond of the adsorbed H₂O molecule). 3343.39 cm⁻¹, 2973.68 cm⁻¹ (C – H bond of TiO₂). 1634.80 cm⁻¹ (Ti – OH bond because of the adsorbed H₂O molecules). 1623.00 cm⁻¹ (Ti – COOH bond due to the precursors). 1385.86 cm⁻¹ (peak value from the thermal treatment at 450°C). 1312.37

cm^{-1} ($-\text{C}=\text{O}-\text{Ti}$ vibrational bond because of CO_2). 1056.06 cm^{-1} , 1045.49 cm^{-1} , 1029.00 cm^{-1} , 1022.19 cm^{-1} , 1019.72 cm^{-1} , 1009.15 cm^{-1} (the vibrational bonds for $\text{Ti}-\text{O}-\text{Ti}$). 932.07 cm^{-1} ($\text{Ti}-\text{O}$ bond indicating the homogeneity of TiO_2). 830.78 cm^{-1} (the characteristic peak for Sol-Gel method). 772.92 cm^{-1} (stretching vibrational bond of $\text{Ti}-\text{O}-\text{C}$). 726.10 cm^{-1} , 653.40 cm^{-1} , 573.92 cm^{-1} , 525.24 cm^{-1} , 433.79 cm^{-1} , 432.22 cm^{-1} , 407.99 cm^{-1} , 398.96 cm^{-1} (the characteristics of TiO_2 for the $\text{O}-\text{Ti}-\text{O}$ bond). And the peak ranges from 3924.81 cm^{-1} to 3411.49 cm^{-1} (the H_2O molecules peaks for the $-\text{OH}$ group attachment) were obtained for Ag nanopowders. 1548.18 cm^{-1} , 1540.70 cm^{-1} , 1531.68 cm^{-1} , 1511.83 cm^{-1} ($\text{N}-\text{O}$ bonds for the nitro compound). 1387.84 cm^{-1} (NO_3^- ion bond). 1366.48 cm^{-1} ($\text{N}=\text{O}$ bond). For TA4, the structural peaks for the Ag-nanopowders were fully observant. The widened spectra of the peaks falling within the range from 3997.42 cm^{-1} to 3405.26 cm^{-1} were obtained, these peaks were the residual $-\text{OH}$ group of the H_2O molecules, left because the Ag-sample powders were heated / boiled to evaporate the water. The peaks specifying the $\text{N}-\text{O}$ for the nitro compounds were acquired at 1540.30 cm^{-1} , 1526.16 cm^{-1} , 1517.44 cm^{-1} , 1510.22 cm^{-1} . The characteristic peak for NO_3^- ion was seen at 1383.30 cm^{-1} . And 1367.36 cm^{-1} gave the peak value of the $\text{N}=\text{O}$ bond [176][175][174][173][172][171] (**Figure 5.25**).

The peaks for Ag were sharper in case of TA3 (1:1) than TA2 (3:1), that was due to the content of TiO_2 decreasing in TA3 sample which made the crystallization of Ag nanopowders more visible. The values of the FTIR peaks for all 4-sample composite mixture is furnished in the tabular arrangement in **Table 5:14**.

Table 5:14: FTIR bonds and the peak values for TA1 [TiO_2 , 1:0], TA2 [$\text{TiO}_2 + \text{Ag}$, 3:1], TA3 [$\text{TiO}_2 + \text{Ag}$, 1:1] and TA4 [Ag , 0:1].

	Peak Names	TA1 (TiO_2 - 1:0)	TA2 ($\text{TiO}_2 + \text{Ag}$ - 3:1)	TA3 ($\text{TiO}_2 + \text{Ag}$ - 1:1)	TA4 (Ag - 0:1)
1.	$-\text{OH}$, stretching vibrations of adsorbed H_2O molecules	$3500 \text{ cm}^{-1} - 3000 \text{ cm}^{-1}$	3948.76 cm^{-1}	3883.78 cm^{-1}	—

2.	C–H stretching of TiO ₂	3349.60 cm ⁻¹ 2976.84 cm ⁻¹	3358.10 cm ⁻¹ 2973.68 cm ⁻¹	3343.39 cm ⁻¹ 2973.68 cm ⁻¹	–
3.	Ti–OH bending vibration	1634.04 cm ⁻¹	1634.80 cm ⁻¹	1634.80 cm ⁻¹	–
4.	Ti–COOH stretching	1642.85 cm ⁻¹	1623.20 cm ⁻¹	1623.00 cm ⁻¹	–
5.	Thermally treated peak at 450°C	1385.86 cm ⁻¹	1382.81 cm ⁻¹	1385.86 cm ⁻¹	–
6	– C = O – Ti vibration	1309.53 cm ⁻¹	1312.88 cm ⁻¹	1312.37 cm ⁻¹	–
7.	Ti – O – Ti vibration	1167.99 cm ⁻¹ 1158.30 cm ⁻¹ 1133.25 cm ⁻¹ 1127.81 cm ⁻¹ 1030.69 cm ⁻¹	1161.43 cm ⁻¹ 1127.28 cm ⁻¹ 1110.20 cm ⁻¹ 1057.35 cm ⁻¹ 1048.01 cm ⁻¹ 1030.93 cm ⁻¹ 1013.85 cm ⁻¹ 1008.05 cm ⁻¹	1056.06 cm ⁻¹ 1045.49 cm ⁻¹ 1029.00 cm ⁻¹ 1022.19 cm ⁻¹ 1019.72 cm ⁻¹ 1009.15 cm ⁻¹	–
8.	Ti – O bond	952.95 cm ⁻¹	948.44 cm ⁻¹	932.07 cm ⁻¹	–
9.	Sol – gel synthesis peak	832.20 cm ⁻¹	837.85 cm ⁻¹	830.78 cm ⁻¹	–
10.	Ti – O – C stretching vibration	775.25 cm ⁻¹	772.76 cm ⁻¹	772.92 cm ⁻¹	–
11.	O – Ti – O characteristic peaks	712.63 cm ⁻¹ 668.20 cm ⁻¹ 562.81 cm ⁻¹ 523.82 cm ⁻¹ 426.70 cm ⁻¹ 421.26 cm ⁻¹ 417.01 cm ⁻¹ 412.99 cm ⁻¹ 407.32 cm ⁻¹	712.95 cm ⁻¹ 662.16 cm ⁻¹ 563.05 cm ⁻¹ 528.89 cm ⁻¹ 427.45 cm ⁻¹ 422.94 cm ⁻¹ 417.65 cm ⁻¹ 413.14 cm ⁻¹ 407.73 cm ⁻¹	726.10 cm ⁻¹ 653.40 cm ⁻¹ 573.92 cm ⁻¹ 525.24 cm ⁻¹ 433.79 cm ⁻¹ 432.22 cm ⁻¹ 407.99 cm ⁻¹ 398.96 cm ⁻¹	–
12.	– OH bonds due to the remaining H ₂ O molecules as the A solution was boiled	–	3977.12 cm ⁻¹ – 3420.62 cm ⁻¹	3924.81 cm ⁻¹ – 3411.49 cm ⁻¹	3997.42 cm ⁻¹ – 3405.26 cm ⁻¹

	for the evaporation of water				
13.	N – O of nitro compounds	–	1545.54 cm ⁻¹ 1528.78 cm ⁻¹ 1522.98 cm ⁻¹ 1509.77 cm ⁻¹ 1505.90 cm ⁻¹	1548.18 cm ⁻¹ 1540.70 cm ⁻¹ 1531.68 cm ⁻¹ 1511.83 cm ⁻¹	1540.30 cm ⁻¹ 1526.16 cm ⁻¹ 1517.44 cm ⁻¹ 1510.22 cm ⁻¹
14.	NO ₃ ⁻ ion	–	1399.89 cm ⁻¹	1387.84 cm ⁻¹	1383.30 cm ⁻¹
15.	N = O bond	–	1367.66 cm ⁻¹	1366.48 cm ⁻¹	1367.36 cm ⁻¹

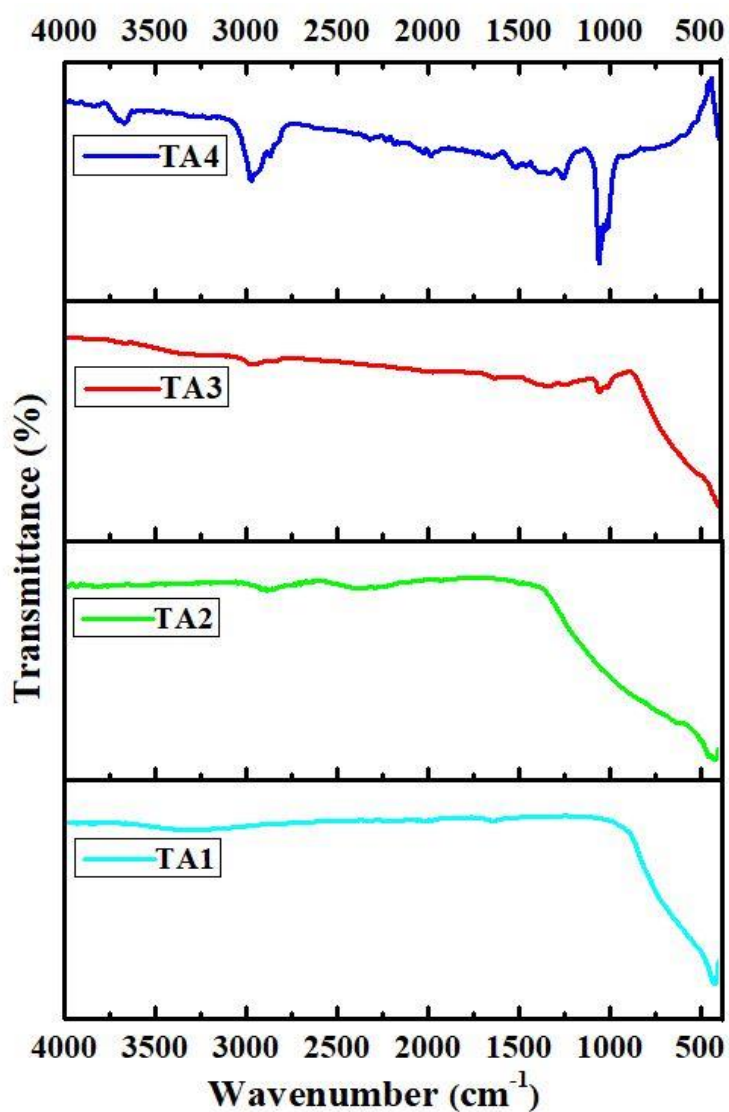


Figure 5.25 FTIR Analysis of TA1 [TiO₂, 1:0], TA2 [TiO₂ + Ag, 3:1], TA3 [TiO₂ + Ag, 1:1] and TA4 [Ag, 0:1].

5.3.4 Raman Spectroscopy

Raman spectroscopy as well provides with a “Finger – Print Region” which is specific to each material, the spectra obtained is due to the interactivity between the light and the chemical bonds that exist within the sample material. It determines the states that are in a molecular system by giving particulars concerning the rotational, vibrational or any other state. Titanium dioxide has three crystalline phases; Rutile, Anatase and Brookite. Both the anatase and brookite forms of TiO₂ exist at lower temperatures and when calcinated at higher temperatures, they irreversibly convert into the rutile form of TiO₂. The Anatase TiO₂ has Body Centred Cubic System (BCC), with its affiliation to the I₄₁/amd space group [320]. There are 15 – optical modes present: A_{1g} + A_{2g} + A_{2u} + B_{1g} + B_{2g} + 2B_{1u} + 3E_g + 2E_u; out of which only 6 – modes (A_{1g} + 2B_{1g} + 3E_g) are Raman Active Modes. The (A_{2u} + 2E_u) modes are the Active Infra – red Modes and the B_{2u} mode is the Inactive Mode for the both Infra – red and Raman region [321].

For TA1, the Raman spectra associated with the anatase TiO₂ single crystal were acquired as such; 144.23 cm⁻¹ (E_g), 197.93 cm⁻¹ (E_g), 399.90 cm⁻¹ (B_{1g}), 513.02 cm⁻¹ (A_{1g}), 519.01 cm⁻¹ (B_{1g}), 639.99 cm⁻¹ (E_g) [301][322][323][324][325][326]. For TA2, the characteristic TiO₂ peaks obtained were 144.04 cm⁻¹ (E_g), 197.65 cm⁻¹ (E_g), 399.48 cm⁻¹ (B_{1g}), 513.25 cm⁻¹ (A_{1g}), 519.76 cm⁻¹ (B_{1g}), 639.35 cm⁻¹ (E_g). In this sample case, the characteristic Raman peaks for Ag – nanopowders were as well obtained; 153.75 cm⁻¹ (peak value for the Ag - lattice). 236.01 cm⁻¹ (the peak for the Ag – O bond). 689.02 cm⁻¹ (the N – O bond of the NO₃⁻ ion). 1066.31 cm⁻¹, 1316.69 cm⁻¹, 1364.73 cm⁻¹, 1523.75 cm⁻¹ (the characteristic peaks for Ag). For TA3, 144.04 cm⁻¹ (E_g), 197.09 cm⁻¹ (E_g), 399.42 cm⁻¹ (B_{1g}), 513.19 cm⁻¹ (A_{1g}), 519.19 cm⁻¹ (B_{1g}), 639.35 cm⁻¹ (E_g) were the procured standard TiO₂ anatase peaks. And the standard Raman peaks for the silver nanoparticles were as follows; 153.91 cm⁻¹ (the Ag – lattice peak value). 227.89 cm⁻¹ (the Ag – O bond peak value). 681.27 cm⁻¹, 820.14 cm⁻¹ (were the N – O bonds for the NO₃⁻ ion). 959.39 cm⁻¹, 1050.75 cm⁻¹, 1082.55 cm⁻¹, 1316.69 cm⁻¹, 1364.73 cm⁻¹, 1527.81 cm⁻¹, 1638.05 cm⁻¹ (were the Ag characteristic peak values). For TA4, the standard peaks corresponding to the metallic nature of the silver were procured. The vibration modes of the Ag – lattice was observed at 153.98 cm⁻¹. The peak value at 240.26 cm⁻¹ was assigned to the Ag – O (silver – oxygen) bond. The presence of the NO₃⁻ ion was observed as well at the peaks 688.72 cm⁻¹, 824.06 cm⁻¹, these peaks were due to the vibrations resulted for doubly – generated

in – plane. The peak values obtained at 978.14 cm^{-1} , 1058.87 cm^{-1} , 1319.06 cm^{-1} , 1527.81 cm^{-1} , 1641.79 cm^{-1} were the indication of the characteristic nature for the Ag – nanopowders [185] [184][183] (**Figure 5.26**).

Now few differences were observed while comparing TA2 (3:1) and TA3 (1:1), the Ag – peaks in case for the latter sample composition were more prominent and has sharpness to them, and the number of silver peaks were as well more in this case, now that was because the quantity of TiO_2 in case of TA3 was less than TA2 and thus made the peaks of Ag more prominent. **Table 5:15** puts forward Raman bond classifications and peak values for the sample mixtures. **Figure 5.27** demonstrates the Raman fitting plot.

Table 5:15: Raman peak names and the values for TA1 [TiO_2 , 1:0], TA2 [$\text{TiO}_2 + \text{Ag}$, 3:1], TA3 [$\text{TiO}_2 + \text{Ag}$, 1:1] and TA4 [Ag , 0:1]

	Peak Names	TA1 (TiO_2 - 1:0)	TA2 ($\text{TiO}_2 + \text{Ag}$ - 3:1)	TA3 ($\text{TiO}_2 + \text{Ag}$ - 1:1)	TA4 (Ag - 0:1)
1.	E_g	144.23 cm^{-1}	144.04 cm^{-1}	144.04 cm^{-1}	–
2.	E_g	197.93 cm^{-1}	197.65 cm^{-1}	197.09 cm^{-1}	–
3.	B_{1g}	399.90 cm^{-1}	399.48 cm^{-1}	399.42 cm^{-1}	–
4.	A_{1g}	513.02 cm^{-1}	513.25 cm^{-1}	513.19 cm^{-1}	–
5.	B_{1g}	519.01 cm^{-1}	519.76 cm^{-1}	519.19 cm^{-1}	–
6.	E_g	639.99 cm^{-1}	639.35 cm^{-1}	639.35 cm^{-1}	–
7.	Ag - lattice	–	153.75 cm^{-1}	153.91 cm^{-1}	153.98 cm^{-1}
8.	Ag – O bond	–	236.01 cm^{-1}	227.89 cm^{-1}	240.26 cm^{-1}
9.	N – O bond of the NO_3^- ion	–	689.02 cm^{-1}	681.27 cm^{-1} 820.14 cm^{-1}	688.72 cm^{-1} 824.06 cm^{-1}
10.	Ag characteristic peaks	–	1066.31 cm^{-1} 1316.69 cm^{-1} 1364.73 cm^{-1} 1523.75 cm^{-1}	959.39 cm^{-1} 1050.75 cm^{-1} 1082.55 cm^{-1} 1316.69 cm^{-1} 1364.73 cm^{-1} 1527.81 cm^{-1} 1638.05 cm^{-1}	978.14 cm^{-1} 1058.87 cm^{-1} 1319.06 cm^{-1} 1527.81 cm^{-1} 1641.79 cm^{-1}

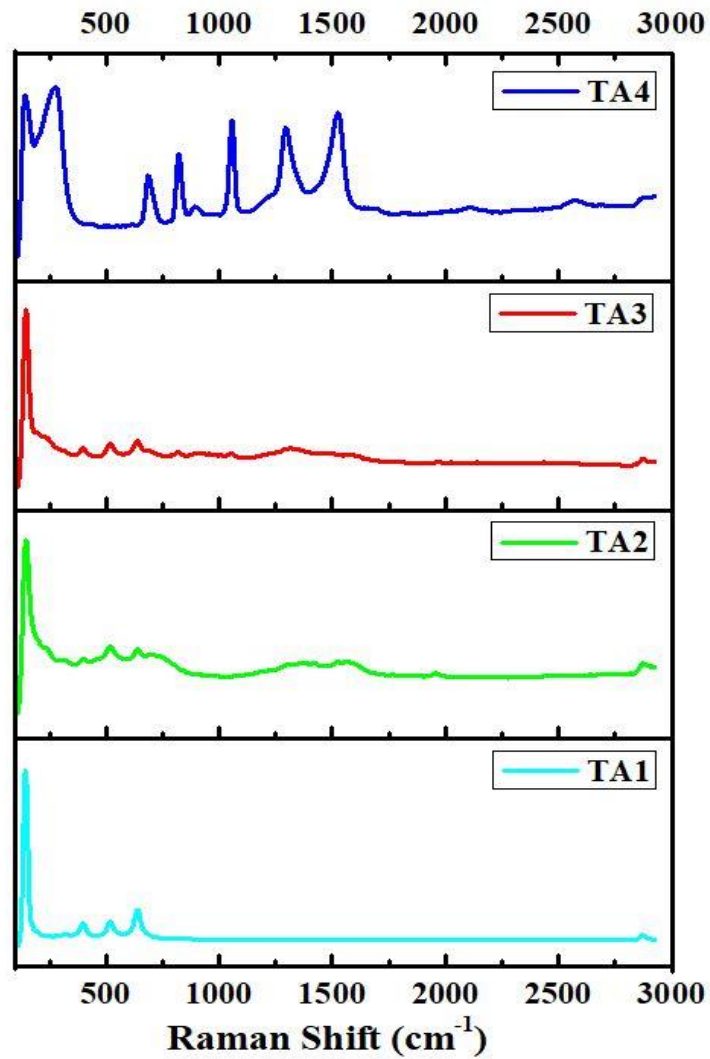


Figure 5.26 Raman Analysis of TA1 [TiO_2 , 1:0], TA2 [$\text{TiO}_2 + \text{Ag}$, 3:1], TA3 [$\text{TiO}_2 + \text{Ag}$, 1:1] and TA4 [Ag , 0:1].

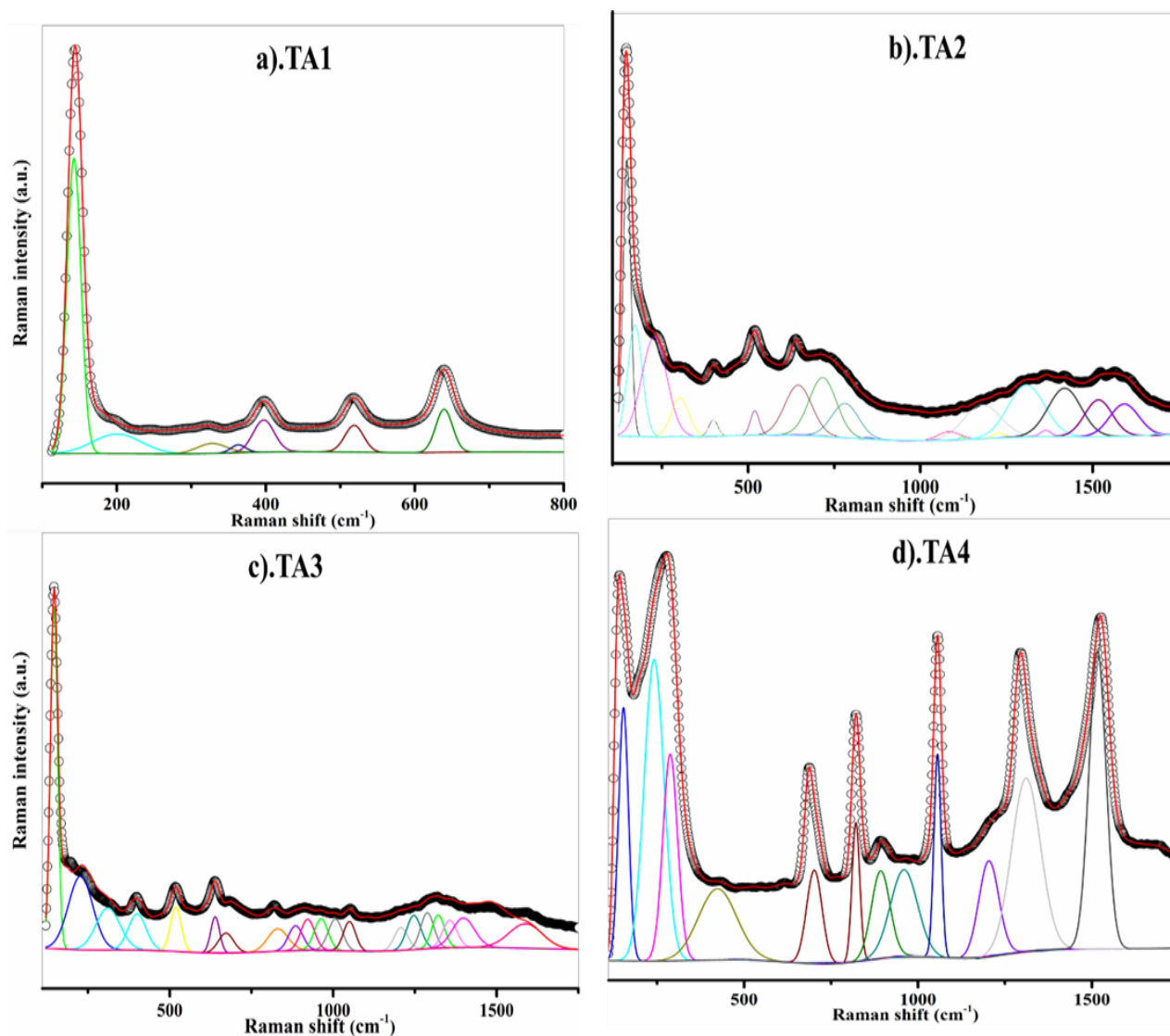


Figure 5.27 Raman fitting of TA1 [TiO₂, 1:0], TA2 [TiO₂ + Ag, 3:1], TA3 [TiO₂ + Ag, 1:1] and TA4 [Ag, 0:1].

5.3.5 FESEM Analysis

The FESEM characterization tool provides visualisation of the topographic aspects for the constituents of the sample material. FESEM for all the four sample compositions were done.

For TA1, the spherical shape of TiO₂ was seen. Now there were some factors that were observed as well; the agglomeration of the smaller particles was seen with the spherical aspects as well, and this clustering of the small – scaled molecules further resulted in the irregularity that was again attached to its shape [301][327][328][329][330]. For TA2 and TA3, the

clustering of particles was perceived. The mass collection of the larger particles of silver nanoparticles over the smaller units of TiO_2 was seen in both the cases. The difference being, for TA3, the clump over the surface of TiO_2 particles was more in volume as the content of silver was increased for this sample case as compared to the case of TA2. For TA4, the Ag – nanopowders have specifically orderly arranged crystalline structure with monodispersive nature. The spherical shaped particles were obtained for the synthesised particles. At some areas, the materialisation of the grouping of the sample particles were also noticed, which resulted in the occurrence of the larger – sized particles. This agglomeration of the Ag - nanoparticles over the surface are its habitual attribute and does not affect its properties [112] [147][174][194][193][192] (**Figure 5.28**).

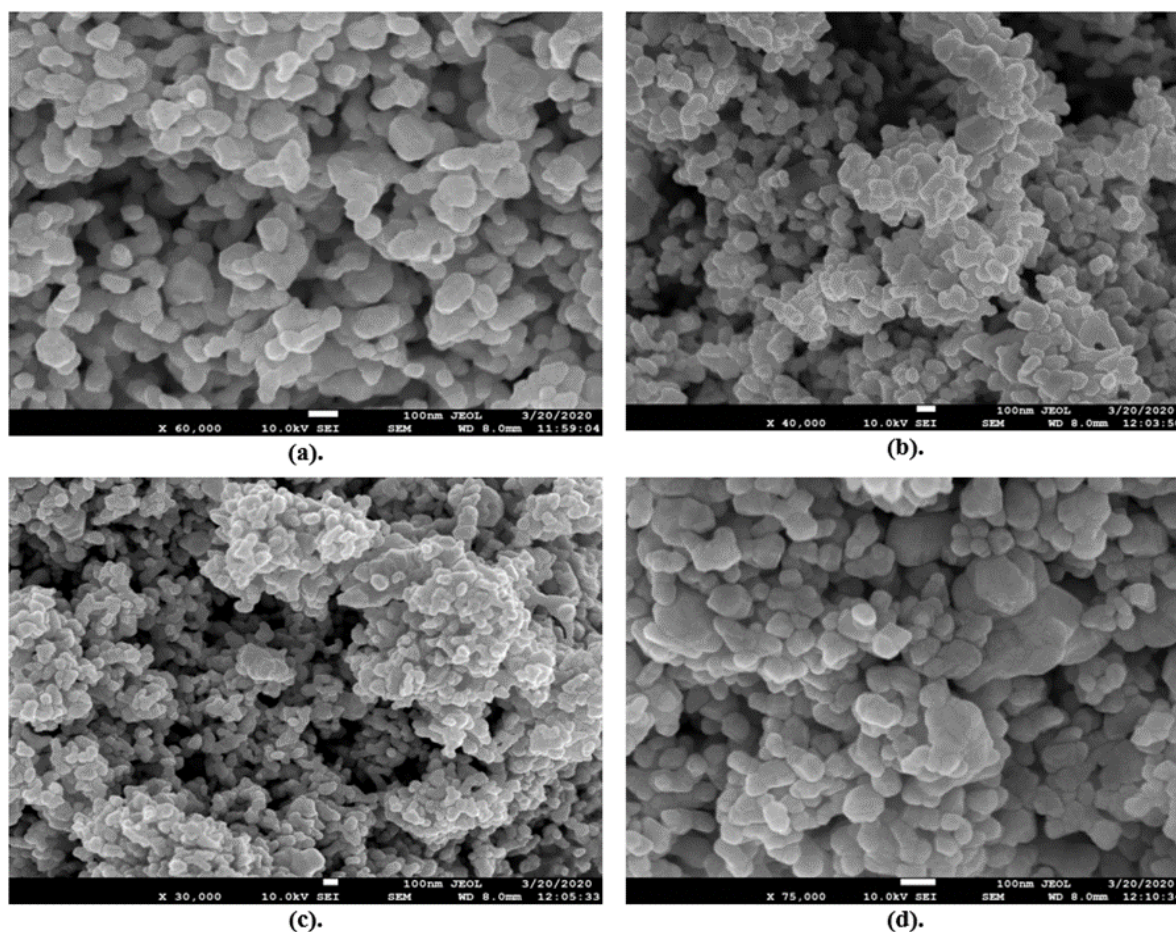


Figure 5.28 FESEM Images of (a) TA1 [TiO_2 , 1:0], (b) TA2 [TiO_2 + Ag, 3:1], (c) TA3 [TiO_2 + Ag, 1:1], (d) TA4 [Ag, 0:1].

5.3.6 PSA Pattern

Now the particle size and error % for both the TiO₂ (anatase) and Ag – nanopowders were also obtained both graphically and numerically; particle size for TiO₂ (anatase) was = 47.78 nm with an error of = 1.8 % and the particle size computed for Ag – nanoparticles was = 43.27 nm and error were = 0.65 %, which goes in accordance with the theoretical aspects for both to commonly have their sizes within the range of 10 – 100 nm. When compared with the crystallite size obtained from XRD analysis, the value of particle size calculated from PSA was more as compared to XRD. This was because D in XRD gives the value from the perspective of a single crystal whereas PSA provides the average value for the particle size, which also includes the agglomerated crystal units (**Figure 5.29**).

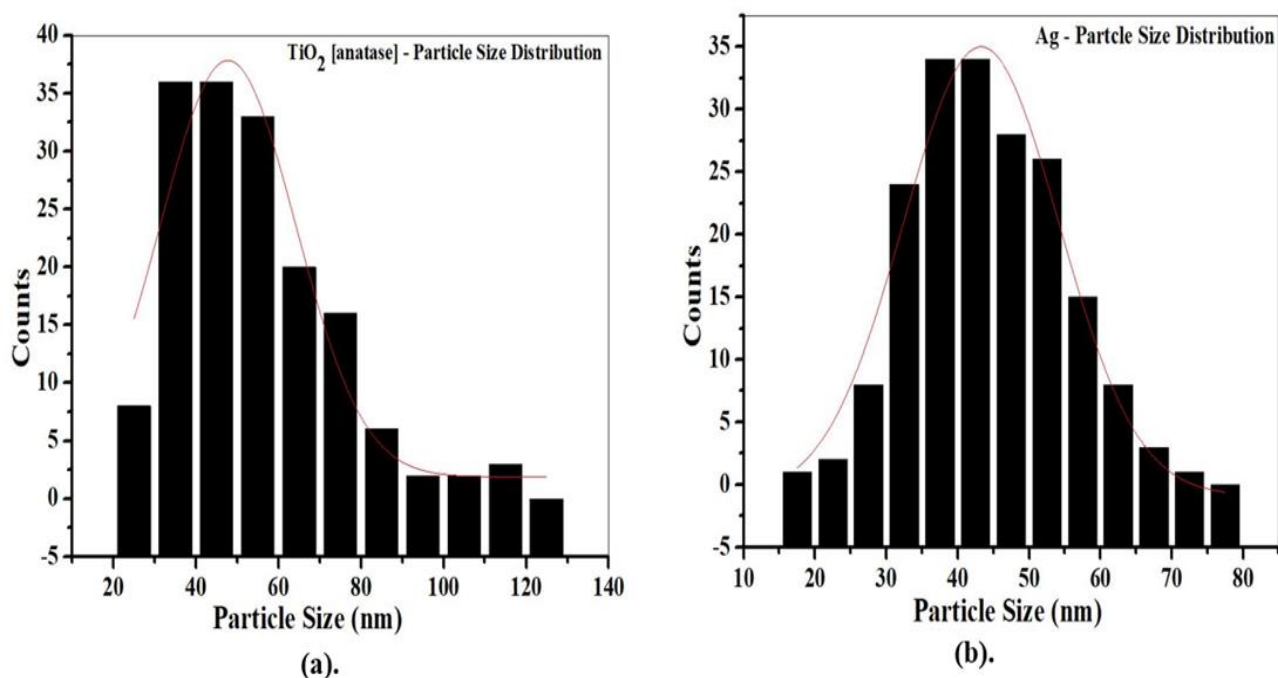


Figure 5.29 Particle Size Distribution images for (a) TA1 [TiO₂, 1:0] and (b) TA4 [Ag, 0:1].

5.3.7 Varistor Studies

Varistor property of the said composites was studied using the current (J (mA/cm²)) versus voltage (E (V/mm)) plot to understand the electrical inhibition of the sample powders, individually and when added together with variegated compositions so as to understand, how the increase in the content of Ag may have influenced the TiO₂ inert nature (**Figure 5.30**).

Varistors in general undergo a perpetual flow of voltage which with time results into the leakage of current in smaller values. As the time proceeds the device starts to deteriorate and therefore, the problem of gradual current leakage arises which furthermore, results in the thermal decay of the device [69]. The present work has been on done a simpler matrix system, in which the values for 'how much voltage and current the mentioned system can uphold' was conducted.

A recognisable amount of work has been done with the consideration of innumerable types of materials with the improvisations in their synthesis processes. The applicational factor of any composite mixture as well depends on the categories of the materials considered; many combinations as; Metal + Semiconducting Oxide, Polymer + Metal, Ferrites + Semiconducting Oxide or Polymer + Semiconducting Oxide etc. has been extensively researched on.

In this frame of work, the combination of the Semiconducting Oxide + Metallic nano – powders were considered, where TiO_2 played the host material whereas Ag was added with varying variations. The choice of the materials was done so as to have better thermal stability and strong defence against the atmospheric impurities. TiO_2 is a n – type semiconductor with the innate nature of having robust strength to withstand the harsher environments, which makes its application prospects spread out in various sectors. The operational factor of TiO_2 depends largely on its size and the shape of the particles obtained which in further are heavily influenced by the synthesis methods as they also impact the crystalline phase and the porosity. Theses structural aspects of the metal oxide impacts the operational characteristics as; number of the defects present, phase transition temperatures, specific surface area, the phase stability [331]. Now, studies with TiO_2 have also been conducted; it has been used as the dopant in ZnO varistor ceramic, to obtain the enhanced electrical properties of the host ceramic material [332]. Moreover, it has been used as the host material and doped with Bi_2O_3 and Nb_2O_5 , where its influence on the semi – conducting grains were noted to show an increase [333].

Silver is an indispensable by – product in the nanotechnology sphere because of its unrepeatable characteristics, specifically, anti – bacterial property which has now widely gained recognition in other arenas of the industrial sectors. Its high conductivity, strong anti – fungal, high catalytic and chemical stability has made silver the candidate for applications such as; raw materials for superconductors and water filters, composite fibres, textiles industry, food

and cosmetic industries and electric – electronic sectors. Its resistance towards the absorption of the environmental contamination has resulted the usage of silver nanopowders for the protection of the materials from its untimely degradation and thus lengthening the utilization time – period of the device in – use [334][335][336].

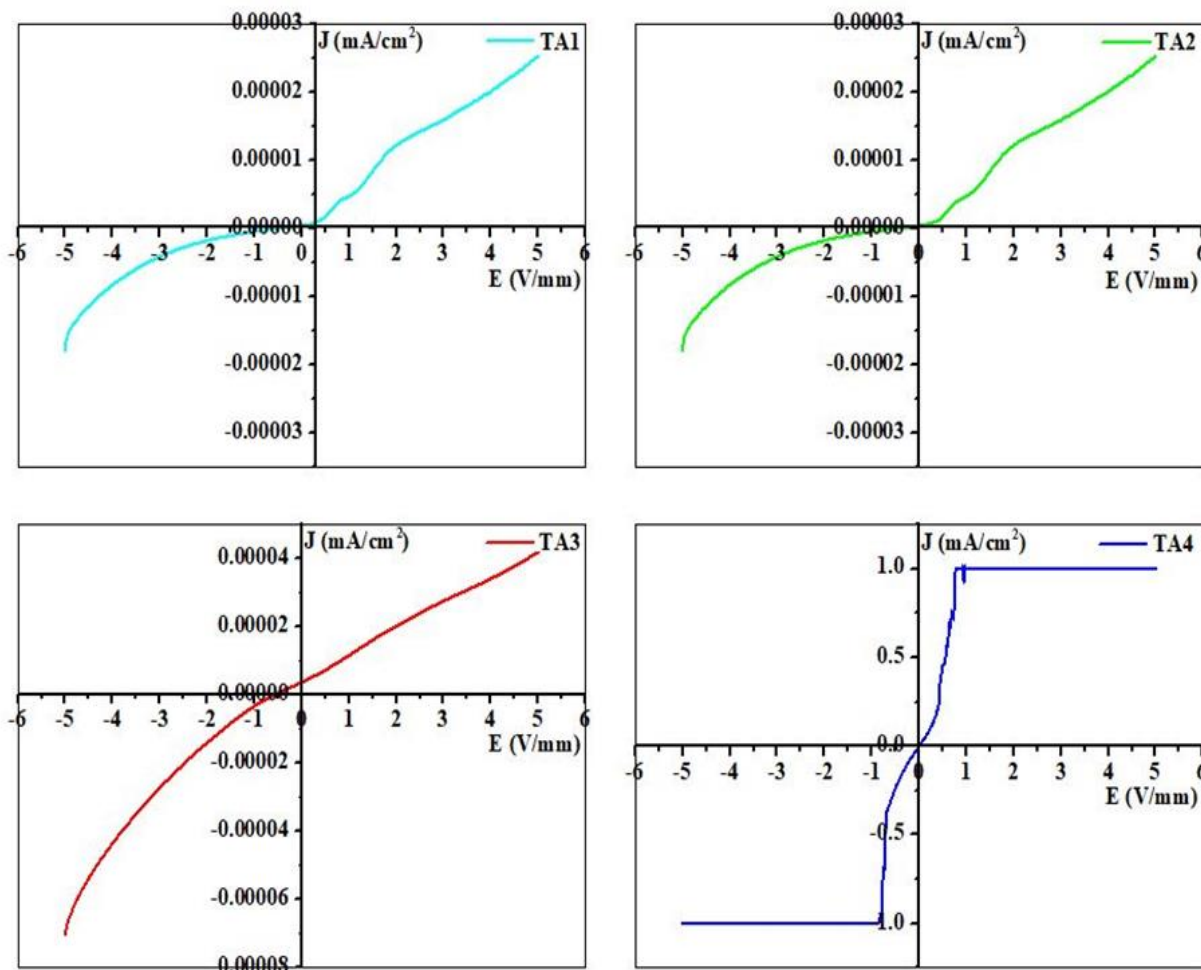


Figure 5.30 Current – Voltage Plot Analysis of TA1 [TiO_2 , 1:0], TA2 [$\text{TiO}_2 + \text{Ag}$, 3:1], TA3 [$\text{TiO}_2 + \text{Ag}$, 1:1] and TA4 [Ag , 0:1].

Now, from **Figure 5.30**, it was observed that there were certain prevailing factors that influenced the operational aspects of the considered domain. One of the major components was “Compliance Current”; by definition it is explained as the maximal limit of an electro – chemical cell for the current to be applied through it. Silver despite having the highest electrical conductivity, gave its maximum value for the current at 1.0 mA/cm^2 . So, this was the limitation applicable due to the device and hence the current values for each sample mixture were

acquired around 1.0 mA/cm^2 and less but the voltage values exhibited variations in their readings.

From the graphs of the samples TA1, TA2, TA3 and TA4, it was observed that, an almost straight line was obtained for each sample, indicating that the increase in the current – voltage values in linear ratios was acquired. The smaller zig – zag patterned curves that were prevalent in the sample with TiO_2 can be explained on the basis of its inert nature, as TiO_2 has polymorphism associated with its structure and therefore followed a curved and non - linear scheme. The straight line in TA2, TA3 and TA4 were obtained due to Ag because TA2 and TA3 were composite mixtures with silver added in them whereas, TA4 consists only Ag content. Silver is an excellent electrical conductor that meant it followed ohms' law and thus, exhibited a direct proportionality slope between current and voltage values. An almost linear behaviour was seen in TA1 because even though TiO_2 has polymorphism attached to its behaviour, it still falls under the group of semi – conducting oxide. Therefore, it showed concluded some form of conducting nature.

Nonetheless, the region of linearity i.e., the region of ohms' law, where the current and voltage exhibit a direct proportionality was obtained, for both the positive and the negative – planes. This can be explained due to effect of particle size of Ag grains in the composite mixtures. Both TiO_2 and Ag samples underwent thermal treatment at lower temperatures and therefore, exhibited higher particle sizes. This resulted in the lower porosity values for the sample systems because the porosity decreases in linearity against increasing grain size. The lesser values for porosity lead to smaller number of electron entrapments which meant that the dominating population of electrons were available for electrical conductivity. This also resulted in the hardness factor and enhanced the ability of sample system to absorb larger values of current without breaking down [195] This is the region that is observed before the knee point. The knee point is the point value where the higher slope curve bends to give a lower slope value. This was only seen in the case of TA4 i.e., Ag – nanopowders, where the linear region exhibited a very sharp bend to give a region of saturation. This region is the non – linear region in which ohms law is not applicable i.e., in this region, current became constant but the voltage gave varying values. There were some smaller values for the current observed specially in reverse regions for all the samples. In this area, the holes and electrons get distanced from junction due to the applicability of reverse bias condition, thus increasing the potential barrier. Still there

were some minority charge carriers present which resulted in the conduction of electrons within the system. The value of reverse current obtained was considerably lower and it appeared to be increasing at extremely small proportions w.r.t voltage values. Some values from the graph were accounted as well and thus put in the **Table 5:16** as: here V_N (V/mm) was the varistor voltage i.e., the total voltage that was across the device and I_N (mA/cm²) was the varistor current i.e., the total amount of current that flowed through the device.

Table 5:16: V_N (V/mm) = Varistor Voltage and I_N (mA/cm²) = Varistor current for TA1 [TiO₂, 1:0], TA2 [TiO₂ + Ag, 3:1], TA3 [TiO₂ + Ag, 1:1] and TA4 [Ag, 0:1].

Sample code	V_N [V/mm]	I_N [mA/cm ²]
TA1 (TiO ₂ - 1:0)	4.9849	2.5069×10^{-5}
TA2 (TiO ₂ + Ag - 3:1)	5.0011	2.5569×10^{-5}
TA3 (TiO ₂ + Ag - 1:1)	5.2152	4.2271×10^{-5}
TA4 (Ag - 0:1)	0.8941	1.0158

From the table, it was observed that the both the current and the voltage values for the sample compositions TA1, TA2 and TA3, showed an increase in their values, though the value differences were minuscule but they still showed the capability of widening their operational values. The causes for such minute variations could be because: (I). the matrix considered for the groundwork of the paper was of a simpler form, constituting only of two materials: metal oxide and metallic nanopowders, instead of an array of the materials. (II). and due to the applicability of the current compliance, the materials were inherently subjected to the lower systems of values for the comparison purposes.

To understand how the quantity of the considered sample materials, impacted on the current values, a graphical plot was done for the current values against the TiO₂ (anatase) content (**Figure 5.31**). Consequently, it was observed that as the content of the silver nano – powders were increased, the current values of the sample compositions also exhibited an elevation in the values. This was seen due to effect of presence of Ag content in the composite mixtures.

Silver itself being a great conductor enhanced the capability of electrical conductivity for the composites as well. That is, more the current values more could be the voltage values and hence more will be the area of the linear region obtained implying higher the current – voltage direct proportionality status, following the ohm's law. This means, more amount of voltage and current will be allowed to pass through the device before it reaches its saturation level leading to the shutdown of the system and therefore more will be working life of the device.

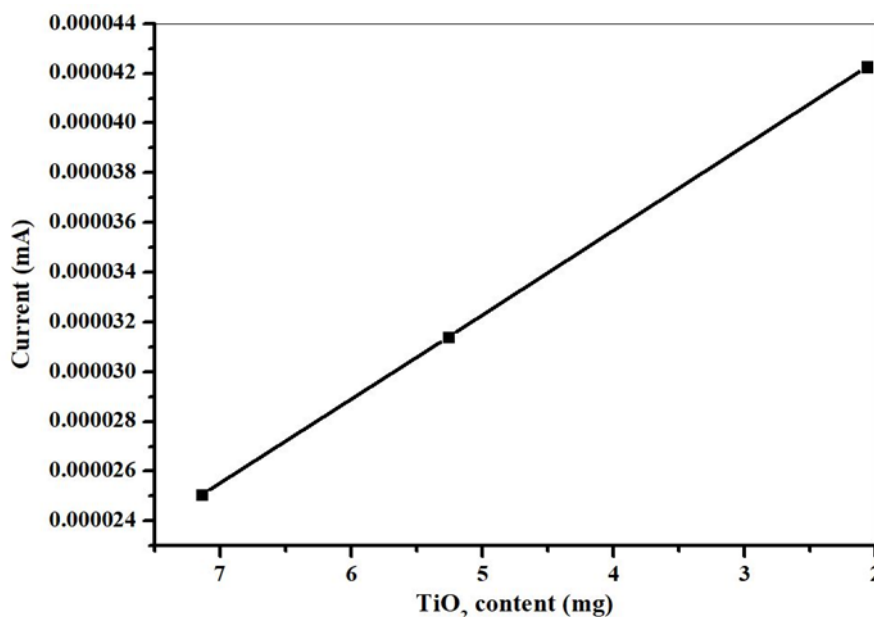


Figure 5.31 Graphical view of current values against the TiO₂ (anatase) content for TA1 [TiO₂, 1:0], TA2 [TiO₂ + Ag, 3:1], TA3 [TiO₂ + Ag, 1:1] and TA4 [Ag, 0:1].

- **Applicational Prospects**

The TiO₂ (anatase) sample composite mixtures, being only two – constituent system and when used with only one conductive material showed an increase in its operational values, though the increased variations were small. Now these obtained values have their applicability in the areas where smaller voltage values are required; like varistors with smaller voltage potency that are employed on in the smart house gadgets, smart door bells, as well thermostats and resistors and etc. Even though the values acquired were small, the TiO₂ samples exhibited its potency that if used with stronger matrix of the materials it can have its consideration for the larger measurement systems, complex domains where higher voltage varistors are used in the circuits for the safety purposes.

5.4 rGO mixed with Ag

5.4.1 XRD Pattern

To identify the purity factor of the sample, to get the information regarding the crystallite phases, X – Ray diffraction method was used. The peaks obtained were compared with the already existing data and thus were verified respectively. Both graphene oxide (GO) and reduced graphene oxide (rGO) has amorphous structures. The diffraction angle pattern attained, equates to the inter-layer distance among the graphitic layers.

For the case of GO, succeeding its oxidation, the inter-layer distance of the GO sheets grows because the intercalated oxygenated constituents establish on the basal planes at the edges. Alongside to them, the weaker Van der Waals bonds creates due to C=O (carbonyl group), COOH (carboxyl group), –COC– (epoxy group) and –OH (hydroxyl group). GO graph does not evince any specific peak but a curve in the range from 10° – 30° ; which goes apace with its amorphous nature [337][338][61].

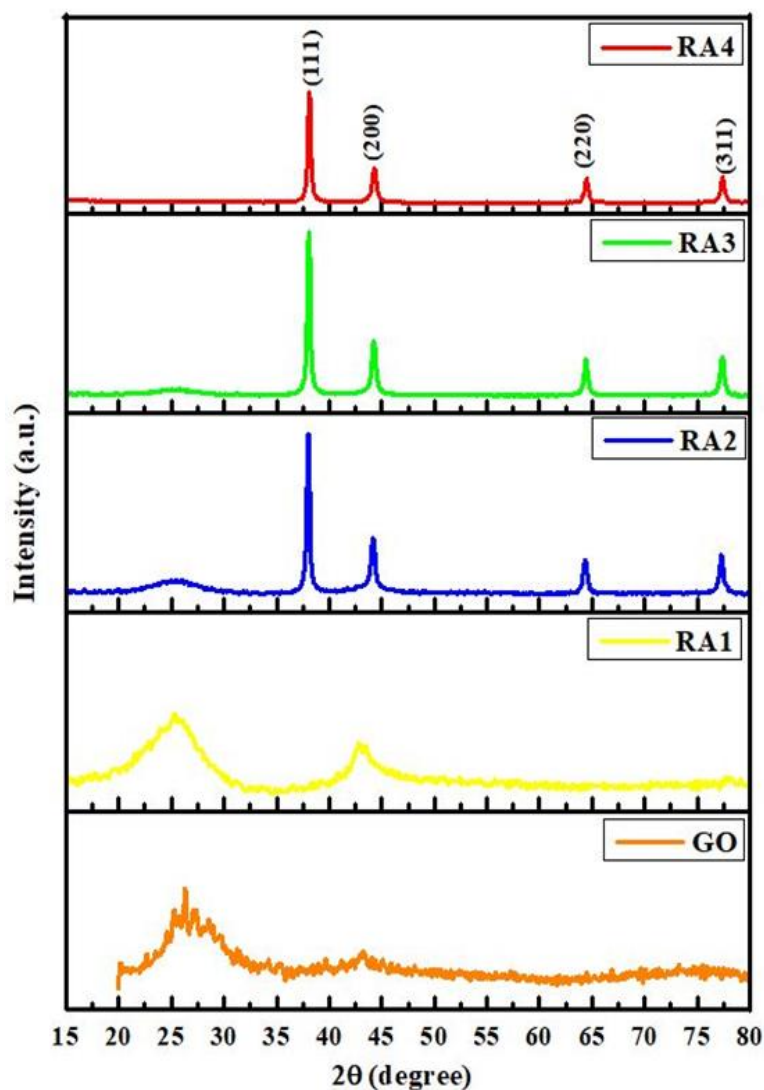


Figure 5.32 XRD Analysis of GO, RA1 [rGO, 1:0], RA2 [rGO + Ag, 3:1], RA3 [rGO + Ag, 1:1], RA4 [Ag, 0:1].

The rGO structural peaks were perceived at the higher diffraction peaks; $2\theta = 25^\circ$ (002 plane) and 43° (100 plane) for RA1, owing to the inter-layer spacing depletion obtained with the furthermore reduction of the GO sheets accompanied with the elimination of the oxygen related functional groups. In the case of RA2 and RA3, the second higher peak wasn't obtained rather a broad curve around 25° was seen and the increase in the flattening of the curve was the result of lessening of the rGO content and increase in the Ag quantity [337][339][340][341][342][343][344]. The metallic crystalline nature of silver nanopowders was affirmed by observing the characteristics peaks at the diffraction angles with their specific miller indices planes; $2\theta = 38.02^\circ$ (111), 44.18° (200), 64.33° (220) and 77.30° (311) for RA2. $2\theta = 38.08^\circ$ (111), 44.24°

(200), 64.39° (220) and 77.36° (311) for RA3 and $2\theta = 38.12^\circ$ (111), 44.30° (200), 64.46° (220) and 77.40° (311) for RA4 which refer to the peaks of Face Centred Cubic system. The procured values of the diffraction pattern are those of Ag and go in accordance with JCPDS card no. 04-0783 [152][145][62][63][149][154][148][147][146][153] (**Figure 5.32**).

The samples RA1 and RA4 consists of individual sample powders i.e., rGO (amorphous nature) and Ag – nanopowders (ordered structure) respectively and RA2 and RA3 were the composite mixtures of rGO and Ag – nanopowders, in which the Ag – powders were added in rGO powders at varying ratios. rGO is an amorphous sample therefore its high amount in RA1 and RA2 makes it more visible. It is observed that the intensity peak of rGO decreased from RA2 to RA3 sample. The reason behind this is the decrease in the amount of rGO in the prepared sample (ratio 3:1 RA2 to 1:1 for RA3) which was as expected. In fact, the decrease in rGO amount emphasizes the crystal structure of Ag-nanoparticles which becomes more visible in RA3 as compared to RA2. The peak around 25° denotes the presence of rGO and as its content was decreasing from RA1 to RA2 and RA3 with the increase of Ag, the peak around said value was also decreasing or more so exhibiting a flattened broad curve and the procured XRD peaks are put in tabular form in **Table 5:17**.

Table 5:17: XRD bonds and values for RA1 [rGO, 1:0], RA2 [rGO + Ag, 3:1], RA3 [rGO + Ag, 1:1] and RA4 [Ag, 0:1]

Sample code	Ag	
	2θ	hkl
RA1 (1:0)	–	
RA2 (3:1)	38.02°	111
	44.18°	200
	64.33°	220
	77.30°	311
RA3 (1:1)	38.08°	111
	44.24°	200
	64.39°	220
	77.36°	311
	38.12°	111

RA4 (0:1)	44.30°	200
	64.46°	220
	77.40°	311

The lattice parameter values (a, b, c), volume of the sample (V) and the crystallite size (D) were calculated for silver nanopowders through cubic formula: $\frac{1}{d_{hkl}^2} = \frac{h^2+k^2+l^2}{a^2}$, $V = a \times b \times c$ and $D = \frac{k\lambda}{\beta^* \cos\theta}$ (Debye Scherrer's Equation) respectively. Since Ag has cubic structure therefore, its unit lengths are a = b= c and thus have equal values. The values calculated are listed in **Table 5:18**.

Table 5:18: Lattice parameters (a, b, c), crystallite size (D), FWHM (β^*), Bragg's angle (2θ) and volume (V) of RA2 [rGO + Ag, 3:1], RA3 [rGO + Ag, 1:1] and RA4 [Ag, 0:1].

		a (Å)	b (Å)	c (Å)	D (nm)	β^* (°)	2θ (°)	V (Å) ³
RA2 (3:1)	Ag	4.0966	4.0966	4.0966	30.0528	5.198×10^{-3}	44.18	68.7497
RA3 (1:1)	Ag	4.0912	4.0912	4.0912	32.2217	4.849×10^{-3}	44.24	68.4782
RA4 (0:1)	Ag	4.0858	4.0858	4.0858	32.3450	4.832×10^{-3}	44.30	68.2073

From **Table 5:18** we can see that the value for the parameter “a” showed a decrease from 4.0966 Å to 4.0858 Å with the decrease in rGO content and this scenario was expected. Indeed, the high value of “a” observed for RA2 is related to the fact that the high amount of rGO that was present in the sample, stretched the crystal structure of Ag and by decreasing the amount, the lattice parameter values also exhibited decrease and tend to that of Ag (RA4). The Volume also decreased in accordance with the decrease in the value of the “a” parameter.

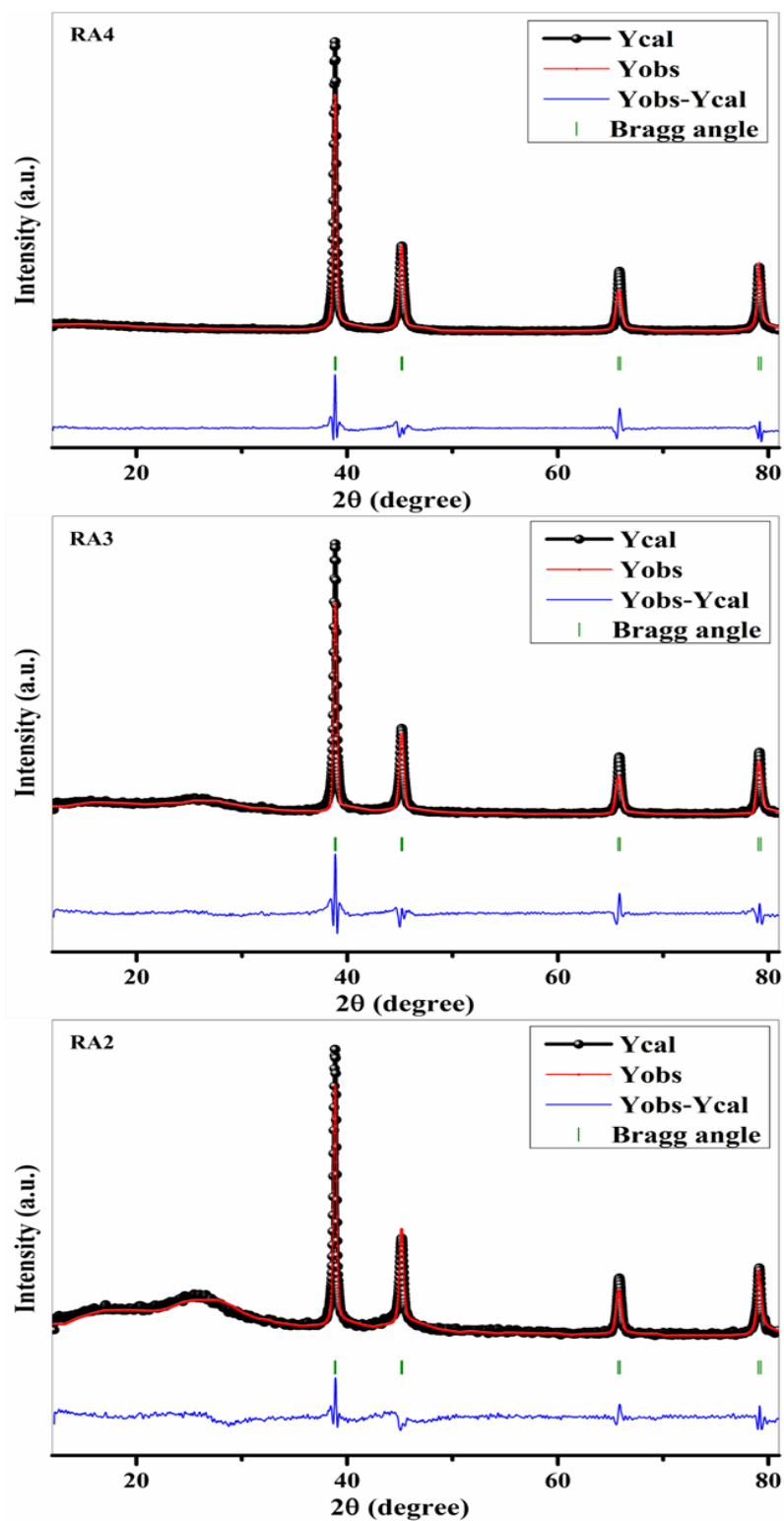


Figure 5.33 XRD Refinement Analysis of RA4 [Ag, 0:1], RA3 [rGO + Ag, 1:1] and RA2 [rGO + Ag, 3:1].

The observed XRD patterns of Ag were refined using Fullprof suite software (**Figure 5.33**). Only Ag – nanopowders showed a particular pattern because of its defined crystalline nature. In the given graph Y_{cal} are the experimentally obtained data, Y_{obs} are the already measured data, $Y_{obs}-Y_{cal}$ difference between the existing and experimental data and Bragg's angle gives the information concerning the number and position of the experimentally observed peaks. From **Figure 5.33** we can clearly observe that all the Ag peaks were matching with the standard peaks without any presence of the stranger peaks; this indicated the purity and the single phase of the prepared Ag sample. **Table 5:19** exhibits the values for the chi-square (χ^2), goodness of fit (*GoF*) and the reliability factors (R_{exp} , R_{wp} and R_p). Various other parameters that are upholding the accuracy of the fit are observed within the range of $0.70 \leq \text{GoF} \leq 0.87$, $19.80\% \leq R_{exp} \leq 21.30\%$, $14.00\% \leq R_{wp} \leq 17.70\%$ and $11.90\% \leq R_p \leq 16.00\%$; all these observed values are put in the tabular form **Table 5:19**.

Table 5:19: Conditions for refinement, reliability factor (R_p , R_{wp} , R_{exp}), refined half-width parameters (U, V, W) chi-square (χ^2) and good of fit (GoF) of prepared samples

Concentration (x)	RA2	RA3	RA4
$\lambda(\text{\AA})$	1.54056	1.54056	1.54056
Cycles of refinement	30	30	30
Step ($^\circ$)	0.021	0.021	0.021
Profile function	Pseudo-Voigt * Axial divergence asymmetry	Pseudo-Voigt * Axial divergence asymmetry	Pseudo-Voigt * Axial divergence asymmetry
R_p (%)	25.3	34.0	22.1
R_{wp} (%)	24.3	36.3	26.1
R_{exp} (%)	17.7	21.3	17.7
U	-2.537095	-3.425056	-3.491906
V	2.802554	4.225834	3.951043
W	-0.609907	-0.937486	-0.893150
χ^2	1.885	2.907	2.180
GoF	1.4	1.7	1.5
Bragg R-factor (%)	8.41	17.2	6.44
Space group of phases	F m -3 m	F m -3 m	F m -3 m

5.4.2 FTIR Analysis

The discerning of the chemical bonds, existing functional groups, sample's molecular structure was studied via Fourier Transform Infra-Red Spectroscopy. This tool provides a discrete pattern called "Molecular Finger Print Region" marking from 1500 cm^{-1} to 400 cm^{-1} , for the respective materials; secured through the interaction of the said sample with infrared rays. It produces both qualitative and quantitative databases determined with the amount of the IR light, the vibrating molecule's bonds can absorb.

For GO, the peaks determining its structural attributes were learned for as: 3403.54 cm^{-1} (–OH stretching of H_2O molecules), 2935.98 cm^{-1} (asymmetric C–H), 2833.83 cm^{-1} (symmetric C–H), 2320.62 cm^{-1} (CO_2 bond), 1721.59 cm^{-1} (C=O carbonyl stretching), 1645.68 cm^{-1} (C=C vibrational stretching of oxidised graphene domains), 1408.07 cm^{-1} (deformed –OH bending of C–OH), 1133.25 cm^{-1} (C–O–C epoxy) and 1022.19 cm^{-1} (C–O alkoxy). The above studied outcomes indicates that graphene was laboriously oxidized and had huge quantities of oxygenated functional groups [61][345][346][347][348][349][350][351][352][353]. The tabular form of the bond values of the GO sample has been provided in the **Table 5:20**.

Table 5:20: FTIR Bonds and the Peak values for the bonds obtained for the GO sample powders.

	Bond Names	Bond Peak Values
1.	– OH stretching of H_2O molecules	3403.54 cm^{-1}
2.	Asymmetric C – H bond	2935.98 cm^{-1}
3.	Symmetric C – H bond	2833.83 cm^{-1}
4.	CO_2 bond	2320.62 cm^{-1}
5.	C=O carbonyl stretching	1721.59 cm^{-1}
6.	C=C vibrational stretching of oxidised graphene domains	1645.68 cm^{-1}
7.	deformed –OH bending of C–OH	1408.07 cm^{-1}
8.	C–O–C epoxy	1133.25 cm^{-1}
9.	C–O alkoxy	1022.19 cm^{-1}

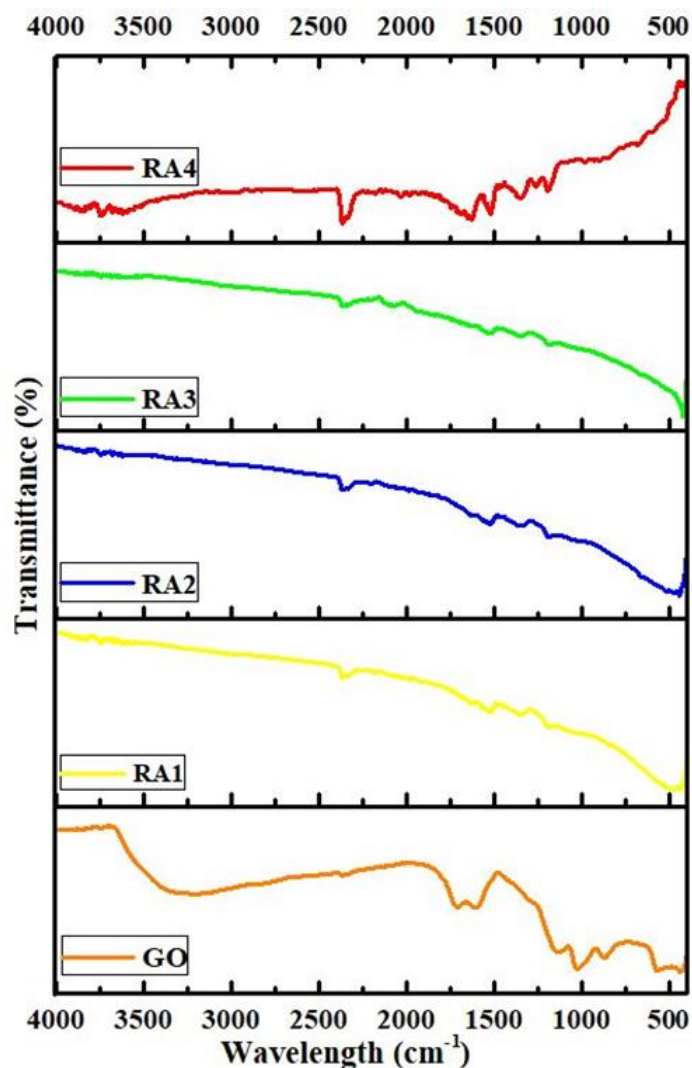


Figure 5.34 FTIR Analysis of GO, RA1 [rGO, 1:0], RA2 [rGO + Ag, 3:1], RA3 [rGO + Ag, 1:1], RA4 [Ag, 0:1].

For RA1, the formation of rGO was explained through the obtained peaks: 3418.04 cm⁻¹ (–OH stretching of H₂O molecule), 2925.57 cm⁻¹ (C–H symmetry), 2946.29 cm⁻¹ (symmetric CH₂), 2858.53 cm⁻¹ (asymmetric CH₂), 2364.75 cm⁻¹ (CO₂ bond), 1727.99 cm⁻¹ (C=O of –COOH stretching), 1630.87 cm⁻¹ (phenyl, unchanged sp² lattice), 1625.19 cm⁻¹ (alkene, unchanged sp² lattice), 1397.20 cm⁻¹ (C–C bond), 1261.85 cm⁻¹ (C–O–C epoxy), 1189.04 cm⁻¹ (C–OH bond), 1032.65 cm⁻¹ (C–O bond) [348][354][355][356][357][358][359][360][361][362][363][364][365][366]. The decrease and disappearance of some of the peaks can be explained as complete reduction of GO. For RA2, rGO gave peaks as: 3418.04 cm⁻¹ (–OH stretching of H₂O molecule), 2938.66 cm⁻¹ (symmetric CH₂), 2845.32 cm⁻¹ (asymmetric CH₂), 2925.47 cm⁻¹ (C–H symmetry), 2363.37 cm⁻¹ (CO₂ bond), 1727.28 cm⁻¹ (C=O of –COOH stretching), 1632.86

cm⁻¹ (phenyl, unchanged sp² lattice), 1625.13 cm⁻¹ (alkene, unchanged sp² lattice), 1396.02 cm⁻¹ (C–C bond), 1261.65 cm⁻¹ (C–O–C epoxy), 1183.99 cm⁻¹ (C–OH bond), 1038.34 cm⁻¹ (C–O bond). The formation of Ag nanopowders was also noted, as its characteristics peaks were also observed: 3980.88 cm⁻¹ – 3433.29 cm⁻¹ (–OH peaks of H₂O molecules, obtained because of boiling Ag solution). 1547.47 cm⁻¹, 1532.33 cm⁻¹, 1519.11 cm⁻¹ (N–O, nitro compounds), 1384.74 cm⁻¹ (NO₃⁻ ion) and 1362.19 cm⁻¹ (N=O bond). For RA3, 3419.33 cm⁻¹ (–OH stretching of H₂O molecule), 2928.57 cm⁻¹ (symmetric CH₂), 2833.94 cm⁻¹ (asymmetric CH₂), 2928.71 cm⁻¹ (C–H symmetry), 2365.30 cm⁻¹ (CO₂ bond), 1727.28 cm⁻¹ (C=O of –COOH stretching), 1630.93 cm⁻¹ (phenyl, unchanged sp² lattice), 1623.20 cm⁻¹ (alkene, unchanged sp² lattice), 1396.70 cm⁻¹ (C–C bond), 1261.65 cm⁻¹ (C–O–C epoxy), 1183.99 cm⁻¹ (C–OH bond), 1034.47 cm⁻¹ (C–O bond) are the procured rGO peaks. 3964.55 cm⁻¹ – 3449.62 cm⁻¹ (–OH peaks of H₂O molecules, boiling Ag solution peaks). 1547.47 cm⁻¹, 1532.33 cm⁻¹, 1519.11 cm⁻¹ (N–O, nitro compounds), 1386.68 cm⁻¹ (NO₃⁻ ion), 1362.19 cm⁻¹ (N=O bond) defines Ag nanopowders nature. The silver peaks for RA3 were more prominent than RA2, that could be because of the increase in Ag quantity in RA3 sample. For RA4, 3995.81 cm⁻¹ – 3422.23 cm⁻¹ (–OH peaks of H₂O molecules, residual water peaks existing because Ag solution was boiled / heated to evaporate the water). 1547.47 cm⁻¹, 1532.33 cm⁻¹, 1519.11 cm⁻¹ (N–O, nitro compounds), 1384.74 cm⁻¹ (NO₃⁻ ion), 1362.19 cm⁻¹ (N=O bond) were the attained the structural peaks for silver nanopowders [176][175][174][173][172][171] (**Figure 5.34**). **Table 5:21** is the table put together for the obtained FTIR values for the composite sample powders for comparable reasons.

Table 5:21: FTIR bonds and peaks values for the samples RA1 [rGO, 1:0], RA2 [rGO + Ag, 3:1], RA3 [rGO + Ag, 1:1], RA4 [Ag, 0:1].

	Bond Names	RA1 <i>[rGO, 1:0]</i>	RA2 <i>[rGO + Ag, 3:1]</i>	RA3 <i>[rGO + Ag, 1:1]</i>	RA4 <i>[Ag, 0:1]</i>
1.	–OH stretching of H ₂ O molecules	3418.04 cm ⁻¹	3418.04 cm ⁻¹	3419.33 cm ⁻¹	–
2.	C–H symmetry	2925.57 cm ⁻¹	2925.47 cm ⁻¹	2928.71 cm ⁻¹	
3.	Symmetric CH ₂	2946.29 cm ⁻¹	2938.66 cm ⁻¹	2928.57 cm ⁻¹	–
4..	Asymmetric CH ₂	2858.53 cm ⁻¹	2845.32 cm ⁻¹	2833.94 cm ⁻¹	–
5.	CO ₂ bond	2364.75 cm ⁻¹	2363.37 cm ⁻¹	2365.30 cm ⁻¹	–

6.	C=O of –COOH stretching	1727.99 cm ⁻¹	1727.28 cm ⁻¹	1727.28 cm ⁻¹	–
7.	Phenyl, unchanged sp ² lattice	1630.87 cm ⁻¹	1632.86 cm ⁻¹	1630.93 cm ⁻¹	–
8.	Alkene, unchanged sp ² lattice	1625.19 cm ⁻¹	1625.13 cm ⁻¹	1623.20 cm ⁻¹	–
9.	C–C bond	1397.20 cm ⁻¹	1396.02 cm ⁻¹	1396.70 cm ⁻¹	–
10.	C–O–C epoxy	1261.85 cm ⁻¹	1261.65 cm ⁻¹	1261.65 cm ⁻¹	–
11.	C–OH bond	1189.04 cm ⁻¹	1183.99 cm ⁻¹	1183.99 cm ⁻¹	–
12.	C–O Bond	1032.65 cm ⁻¹	1038.34 cm ⁻¹	1034.47 cm ⁻¹	–
13.	–OH peaks of H ₂ O molecules, residual water peaks existing because Ag solution was boiled / heated to evaporate the water	–	3980.88 cm ⁻¹ – 3433.29 cm ⁻¹	3964.55 cm ⁻¹ – 3449.62 cm ⁻¹	3995.81 cm ⁻¹ – 3422.23 cm ⁻¹
14.	N–O, nitro compounds	–	1547.47 cm ⁻¹ , 1532.33 cm ⁻¹ , 1519.11 cm ⁻¹	1547.47 cm ⁻¹ , 1532.33 cm ⁻¹ , 1519.11 cm ⁻¹	1547.47 cm ⁻¹ , 1532.33 cm ⁻¹ , 1519.11 cm ⁻¹
15.	NO ₃ ⁻ ion	–	1384.74 cm ⁻¹	1386.68 cm ⁻¹	1384.74 cm ⁻¹
16.	N=O bond	–	1362.19 cm ⁻¹	1362.19 cm ⁻¹	1362.19 cm ⁻¹

5.4.3 Raman Spectroscopy

Raman spectroscopy also, alike IR, lays out a fingerprint region specific to that material only resulted due to its vibrations. This tool provides more in-depth insight as it relays detailed information; values and peaks of crystal lattices, lower frequency modes, polymorphism, molecular interactions, structures and phases etc. Raman spectroscopy is particularly fancied when to deal with GO and rGO. In case of both GO and rGO, 4 peaks are predominantly observed; D- band, G- band, 2D- band and D+G- band. These obtained peaks values and certain shifts in their positions talk about the obtained graphitic nature; D- band (A_{1g} symmetry): this is the defect peak formed due to the disordered structure of graphene stemmed because of the attached functional groups deformities in the graphene basal plane sheets and is attributed to the out-plane vibrations. G- band (E_{2g} symmetry): this peak is formed due to the C–C bond

stretching in the graphitic materials. It is the first-order scattering, in-plane vibrations attained from the presence of defects of sp^2 hybridised carbon atom sheets. The D- band and G- band signify the disorder band and tangential band correspondingly. 2D- band: it is the second-order two phonon process. It is particularly perceptive towards the piling of graphene layers and thus informs about the present graphene layers as; monolayer, double layer, multilayer. D+G- band: it is the combination scattering peak.

For GO, all the characteristic peaks; D- band (1359.67 cm^{-1}), G- band (1604.51 cm^{-1}), 2D- band (2680.40 cm^{-1}) were secured, the obtained 2D peak value shows that monolayer graphene has been synthesised and D+G- band (2925.86 cm^{-1}) were procured as required. The ratio of the intensities of D- and G- band was also calculated, $\frac{I_D}{I_G} = 0.84$; it is influenced by the disorder level i.e., presence of sp^3 defects within the sp^2 hybridised graphene [345][349][367][368][369][370][371][372][373][374]. **Table 5:22** represents the Raman peaks obtained and the bond names as well.

Table 5:22: Raman bonds and values for GO sample powders.

	Peak Names	GO
1.	D – band (GO)	1359.67 cm^{-1}
2.	G – band (GO)	1604.51 cm^{-1}
3.	2D – band (GO)	2680.40 cm^{-1}
4.	D + G – band (GO)	2925.86 cm^{-1}

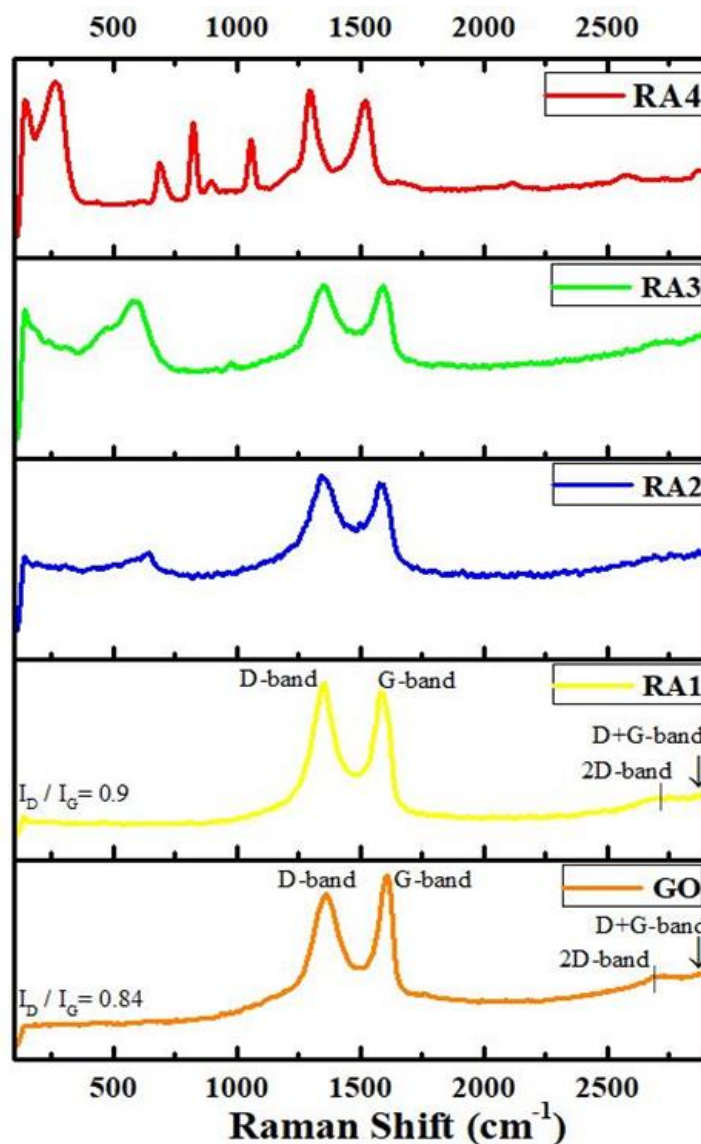


Figure 5.35 Raman Analysis of GO, RA1 [rGO, 1:0], RA2 [rGO + Ag, 3:1], RA3 [rGO + Ag, 1:1], RA4 [Ag, 0:1].

For RA1, the values of the D- and G- peaks slightly shifted towards the lower values. The peaks acquired were; 1352.55 cm^{-1} (D- band), 1583.30 cm^{-1} (G- band), 2747.89 cm^{-1} (2D- band) and 2915.03 cm^{-1} (D+G- band). The intensity ratio of D- and G- bands was; $\frac{I_D}{I_G} = 0.9$. The increase in the ratio of the band intensity as compared to GO, indicates the drop in the average sizes of the sp^2 carbon domain and also the reconditioning of the said domain, after the reduction process of GO [340][356][361][368][369][372][374][375][376][371][377]. For RA2, the secured rGO peaks were; 1345.11 cm^{-1} (D- band), 1583.30 cm^{-1} (G- band), 2756.01 cm^{-1} (2D-

band) and 2915.03 cm^{-1} (D+G- band) and the ratio $\frac{I_D}{I_G}$ was found to be 0.88 for the respective intensities. The Raman nature for silver nanopowders were observed as well. 143.98 cm^{-1} and 160.22 cm^{-1} were the peak values for Ag-lattice modes. 247.51 cm^{-1} Ag – O was the mode peak value. 732.70 cm^{-1} and 780.07 cm^{-1} were the peaks for NO_3^- ion presence. 966.84 cm^{-1} , 1066.31 cm^{-1} , 1539.32 cm^{-1} , 1690.90 cm^{-1} were deducted as the characteristic peaks. For this sample case, values around 695 cm^{-1} (NO_3^- ion) and 1320 cm^{-1} (characteristic peak) weren't seen, that could be because the Ag-ratio in this composite mixture was less. For RA3, the characteristic band values for rGO were; 1355.93 cm^{-1} (D- band), 1590.18 cm^{-1} (G- band), 2742.70 cm^{-1} (2D-band) and 2910.91 cm^{-1} (D+G- band). The intensity ratio; $\frac{I_D}{I_G} = 0.84$. And 144.23 cm^{-1} , 159.18 cm^{-1} (Ag- lattice peaks). 250.76 cm^{-1} (Ag – O), 693.70 cm^{-1} , 722.98 cm^{-1} , 780.92 cm^{-1} (NO_3^- ion). 989.62 cm^{-1} , 1066.87 cm^{-1} , 1319.18 cm^{-1} , 1535.35 cm^{-1} , 1696.09 cm^{-1} (characteristic peaks) were the Ag- peaks. For RA4, the structural peaks for Ag – nanopowders were acquired which confirmed the formation and purity of Ag nanopowders. 144.23 cm^{-1} , 159.18 cm^{-1} (Ag – lattice vibration modes). 247.02 cm^{-1} (Ag – O peak value). 691.96 cm^{-1} , 726.10 cm^{-1} , 799.61 cm^{-1} (NO_3^- ion occupancy, vibrations of the doubly generated N – O in-plane). 982.77 cm^{-1} , 1066.87 cm^{-1} , 1319.18 cm^{-1} , 1585.23 cm^{-1} , 1690.28 cm^{-1} (characteristic Ag – peak values) [185][184][183] (**Figure 5.35**).

The values of intensity peaks for RA1 and RA2, RA3 exhibited a significant difference, that could be because the RA2, RA3 were the composite mixture containing Ag nanopowders as well. Also, the silver peaks were sharp and prominent in RA3, that was because the Ag content in RA3 was more as compared to RA2. Whereas the intensity value difference between RA2 and RA3 was very less, only that of 0.04, meaning the addition of Ag did not cause any significant structural defect. The Raman analysis values obtained for the sample composite are presented in the tabular form in **Table 5:23**.

Table 5:23: Raman bonds and values for RA1 [rGO, 1:0], RA2 [rGO + Ag, 3:1], RA3 [rGO + Ag, 1:1] and RA4 [Ag, 0:1].

Peak Names	RA1 (rGO - 1:0)	RA2 (rGO + Ag - 3:1)	RA3 (rGO + Ag - 1:1)	RA4 (Ag - 0:1)

1.	D – band (rGO)	1352.55 cm ⁻¹	1345.11 cm ⁻¹	1355.93 cm ⁻¹	–
2	G – band (rGO)	1583.30 cm ⁻¹	1583.30 cm ⁻¹	1590.18 cm ⁻¹	–
3.	2D – band (rGO)	2747.89 cm ⁻¹	2756.01 cm ⁻¹	2742.70 cm ⁻¹	–
4.	D + G – band (rGO)	2915.03 cm ⁻¹	2915.03 cm ⁻¹	2910.91 cm ⁻¹	–
5.	Ag - lattice	–	143.98 cm ⁻¹ , 160.22 cm ⁻¹	144.23 cm ⁻¹ , 159.18 cm ⁻¹	144.23 cm ⁻¹ , 159.18 cm ⁻¹
6.	Ag – O bond	–	247.51 cm ⁻¹	250.76 cm ⁻¹	247.02 cm ⁻¹
7.	N – O bond of the NO ₃ ⁻ ion	–	732.70 cm ⁻¹ , 780.07 cm ⁻¹	693.70 cm ⁻¹ , 722.98 cm ⁻¹ , 780.92 cm ⁻¹	691.96 cm ⁻¹ , 726.10 cm ⁻¹ , 799.61 cm ⁻¹
8.	Ag characteristic peaks	–	966.84 cm ⁻¹ , 1066.31 cm ⁻¹ , 1539.32 cm ⁻¹ , 1690.90 cm ⁻¹	989.62 cm ⁻¹ , 1066.87 cm ⁻¹ , 1319.18 cm ⁻¹ , 1535.35 cm ⁻¹ , 1696.09 cm ⁻¹	982.77 cm ⁻¹ , 1066.87 cm ⁻¹ , 1319.18 cm ⁻¹ , 1585.23 cm ⁻¹ , 1690.28 cm ⁻¹

5.4.4 Surface Analysis

The surface morphology of the synthesised samples was studied through Field Emission Scanning Electron Microscopy (FESEM). This characterisation gives the optical specifications of the entire or fractioned surfaces as per needed. It lays down the topographical and elemental particulars with higher magnifications and provides with a much lucid picture of the samples.

For GO, the synthetisation process used, governs the micro surface level details. GO exhibited a much defined, flaky, layered, 3 – dimensional, fold-like microstructure with heavy wrinkled effect to it, which were present due to its amorphous nature. There are certain defects associated with the surfaces; partially due to sizeable numbers of functional groups; – OH, –COOH attached on to the edge and –C–O–C, –COOH groups in the internal areas. The interlayered length of the graphitic sheets swells due to these functional groups and thus dismantles the integrated layered microstructure leading to wrinkled surface appearance. The Electron Diffraction Spectra (EDX) was also conducted and thus gave the elemental distribution and the numbers of the elements present. Two peaks for carbon and oxygen atoms were procured, meaning them being the dominant elemental factors and the C: O-ratio of GO was 1.35, the

reason for such value was, because of GO considerably being the oxidised disposition of graphite, has higher oxygen content and thus lowered the ratio value [337][366][378][379][380][381] (**Figure 5.36**).

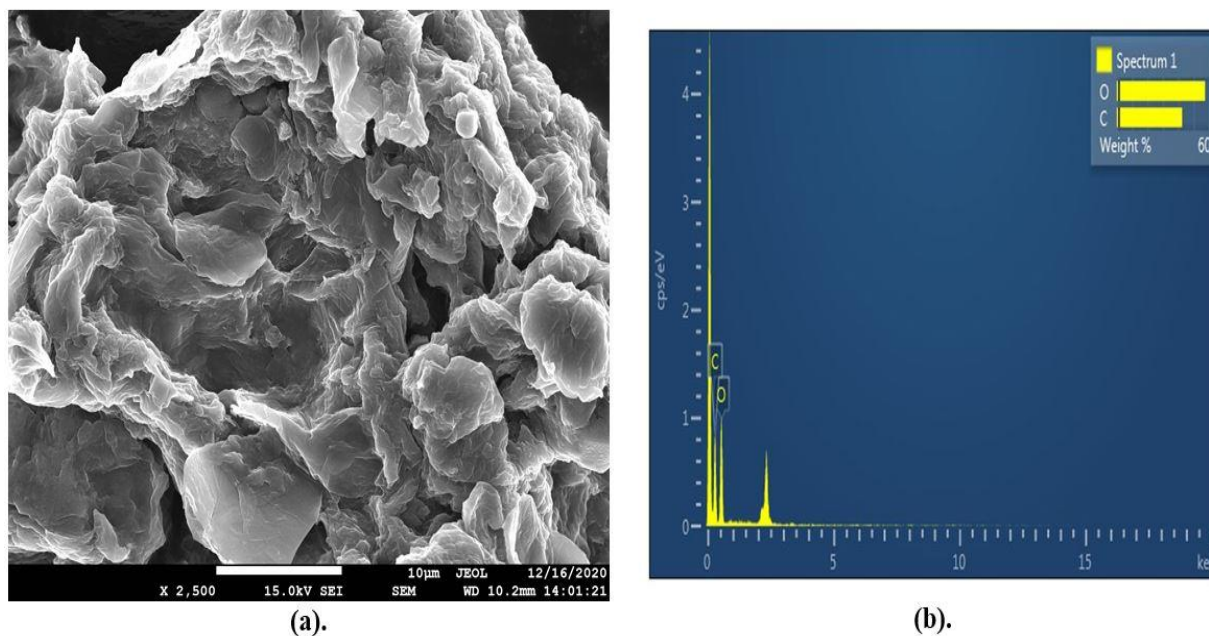


Figure 5.36 (a) FESEM Analysis and (b) EDX Analysis of GO.

For RA1, an apparent layered construction was being seen for rGO, giving out a wrinkly effect, alike GO. These paper-like wrinkled design of rGO sheets were individually identifiable and as well showed lower degrees of agglomeration in their system; because of erasure of oxygenated functional groups attached to the GO, meaning a successful reduction of the GO-system to rGO. This call of conduct was a necessitate, as the thermodynamic solidity of this carbon dominated network relies on the fluctuation morphology obtained. For both GO and rGO, their microstructures have disorders linked to them, thus communicating their polycrystalline or amorphous system [362][366][382][383][384][385]. For RA2 and RA3, the layered formation of rGO was still detectable, but now with the establishment of Ag-nanopowders over its surface. From Fig 8 (b) and (c), it was observable that RA2 has lesser density of Ag- system over its surface than RA3; since the amount of Ag- nanopowders added in rGO was less compared to RA3. For RA4, in some areas, larger sized particles were noticed as it is a habitual attribute of Ag- nanoparticles to have a clustered approach. These metal nanopowders exhibited ‘spherical-shaped’ particles; and are as well known to have

distinctively ordered arrangement and are mono dispersive in nature. The particle size distribution graph was also plotted and gave recommendable results. The particle size value procured was = 36.6 nm (with error = 1.14%), which goes in accordance with the theoretical aspects for silver to have particle size ranging from 20 nm – 110 nm [112][147][174][194][193][192] (Figure 5.37).

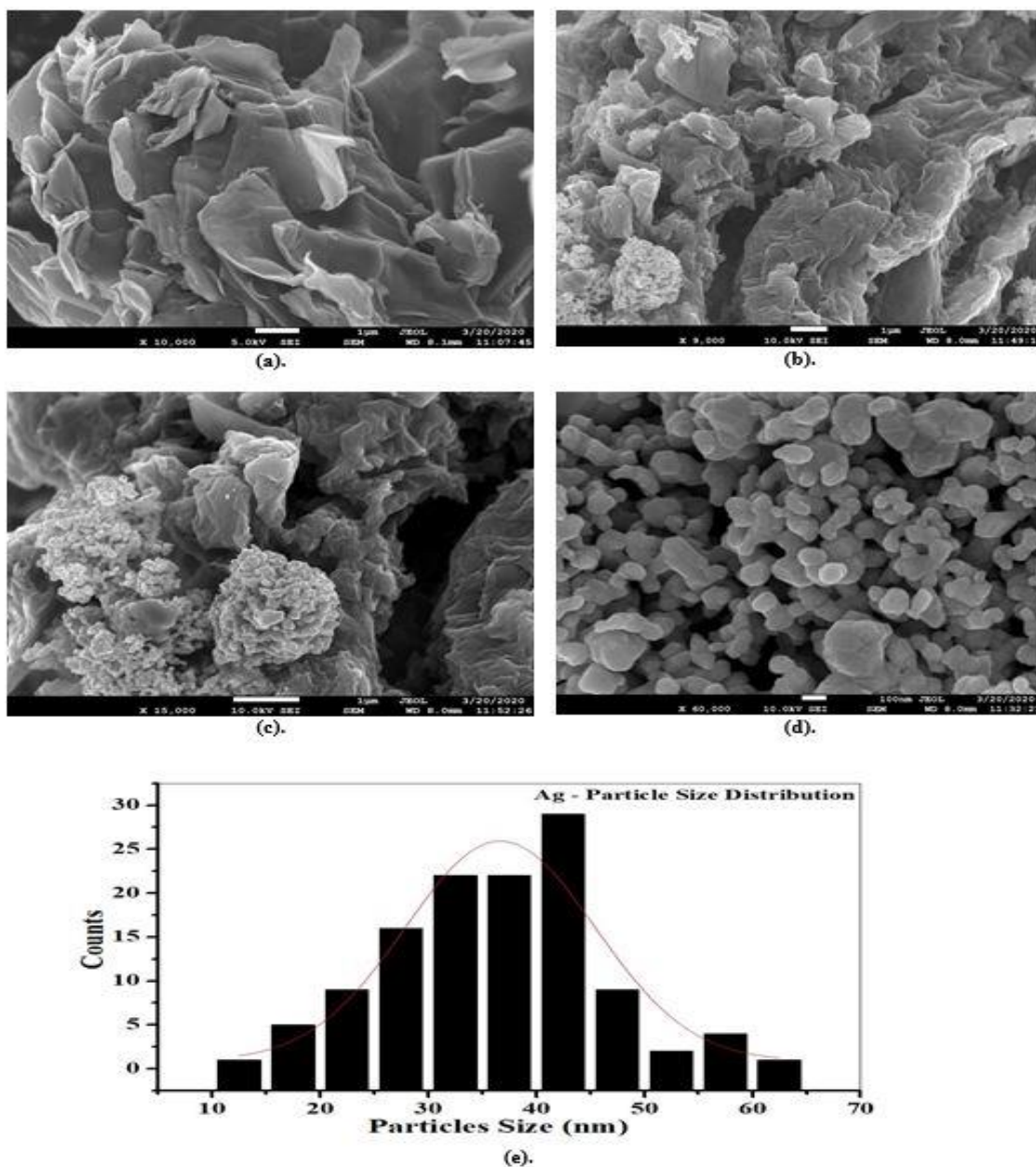


Figure 5.37 FESEM Analysis of (a) RA1 [rGO, 1:0], (b) RA2 [rGO + Ag, 3:1], (c) RA3 [rGO + Ag, 1:1], (d) RA4 [Ag, 0:1] and (e) Particle Size Distribution of RA4 [Ag, 0:1].

5.4.5 Varistor Studies

The varistor studies peruses ‘how much value of voltage and current, a device can acclimate within its working system, before it reaches the point of shut down’. In this paper, a ‘Carbon + Metal’ system was studied with rGO being a carbon dominated network and silver being an exceptionally electrically conductive metal. The analysis was done via current versus voltage graph and certain formula. **(Figure 5.38)** Communicates the IV- characteristics of the said composite mixture. The varistor studies were done in this case by investigating the mobility rate of charge carriers in junction formed between rGO and Ag. The lack of functional groups or lack of oxygen in rGO creates spaces for the charge carriers to conduce electrically and additionally, Ag has free electrons available for transportation process.

There are certain aspects governing the nature and direction of the graphical matrix. The Current – voltage curve plotted between J (mA/cm^2) and E (V/mm), evinced the two arenas of the graphs; linear region which followed the ohm’s law (before the knee point) and the non – linear region which does not followed the ohm’s law (after the knee point). The knee point of a curve, by definition, is the point where the curve of the graph visibly bends, in particular from a higher slope to a lower slope, in this case, the point value where the linear proportionality became the horizontal saturated line [196]. In the region of ohms law, forward bias was applied which was the connections of p and n – junctions to the positive and negative terminals of the battery respectively. As a result of this, holes and electrons present in the rGO and Ag flew towards the direction of the junction leading to the decrease in the width of potential barrier. This in return did not exhibit any resistance and thus charge carriers followed on with the transportation mechanism. Whereas, in the case of non-linear region, the reversal connections were done between junctions and terminals which led to the increasing width for potential barrier as the holes and electrons were now attracted towards the ends of terminals attached and thus moving in the opposite direction as opposed to junction. Even though charge conduction was not prevalent, there were some minority of charge carriers still existing and thus the process of conduction was still observed in the negative planes of the plot.

For the graphs of samples RA1, RA2 and RA3; though an ohmic region was acquired but it exhibited a very ‘zig – zag like pattern’ in both the positive and negative planes, that could be dominantly because of the amorphous disposition of rGO. Another facet that was prevailing in

this mechanism, was called ‘Compliance Current’ i.e., the maximal amount of current that an electrochemical cell can uphold to, which can be observed for the case of RA4. Silver despite being the highest electrically conductive metal, gave its highest value of current at around 1 mA/cm², which meant that it was the limitation applicable due to the device. So, for each sample graph, the maximum value of current across the device acquired was around and about 1 mA/cm² but the value of voltage had certain variations.

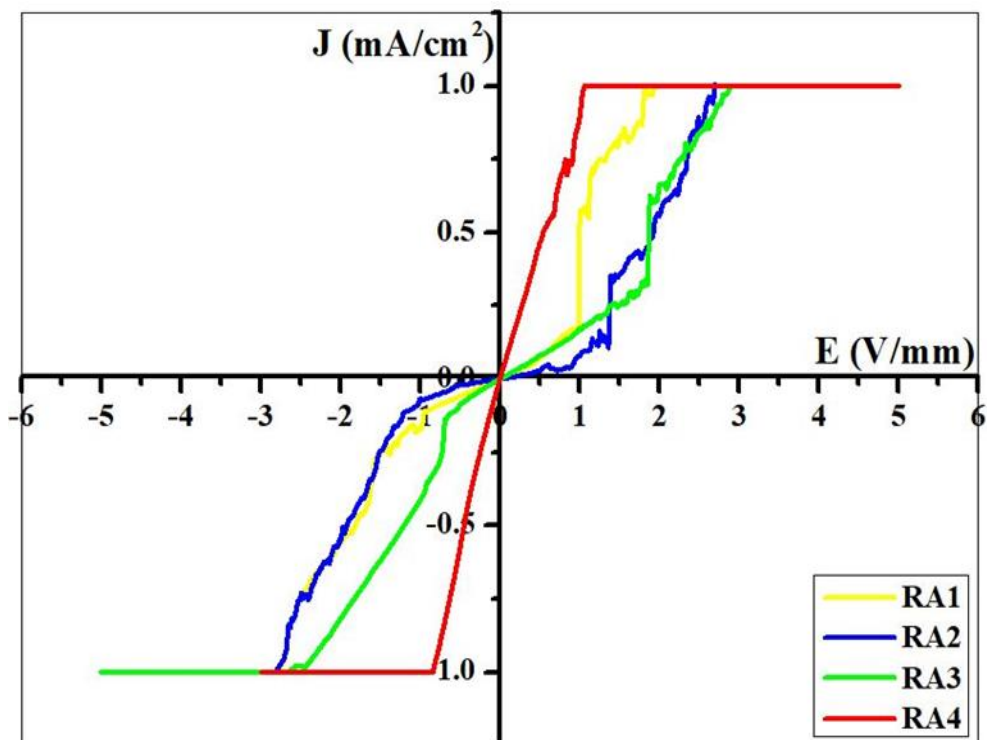


Figure 5.38 Current / Voltage Analysis of RA1 [rGO, 1:0], RA2 [rGO + Ag, 3:1], RA3 [rGO + Ag, 1:1], RA4 [Ag, 0:1].

As mentioned before, the graph displayed two areas ‘the before’ and ‘the after’ of the materialisation of the ‘the knee point’. The before of the knee point gave the maximum value of current and voltage in direct proportionality i.e., the extremity of the availability of the ohm’s law. But after the knee point, a saturation was obtained, where the values for current became constant but the voltage values were varying. Another salient peculiarity that arose due to this behaviour was ‘non – linear coefficient (α)’; it is defined as the ratio of the difference of the current densities to the log of the difference of the voltages [197]. The value taken were from the starting and the end point of the saturation line, expressed as:

$$\alpha = \frac{\log[J_2 - J_1]}{\log[V_2 - V_1]}; J_2 > J_1, V_2 \text{ and } V_1 = \text{voltages at respective current density}$$

Where α = non – linear coefficient, V_N (V/mm) = voltage values across the device and I_N (mA/cm²) = current values across the device. These α – values obtained then were set down in the tabular form w.r.t. to voltage and current values (**Table 5.24**).

Table 5.24: Tabular form for the values of non – linear coefficient ‘ α ’, voltage across the device ‘ V_N (V/mm)’ and current across the device ‘ I_N (mA/cm²)’ for RA1 [rGO, 1:0], RA2 [rGO + Ag, 3:1], RA3 [rGO + Ag, 1:1] and RA4 [Ag, 0:1].

Sample code	α	V_N [V/mm]	I_N [mA/cm ²]
RA1	- 7.2989	1.9849	0.9932
RA2	- 6.5734	2.7135	1.0021
RA3	- 4.9761	3.0012	1.1004
RA4	- 3.9761	1.0904	1.0158

For a varistor to have its usage, it is required to have a greater value of α . More is the value of α , means more is the linear part of the graph and more the voltage value, hence more it has the tolerance towards the current passing through it i.e., more it will be able to withstand the higher values of current and voltages. From the **Table 5.24**, RA1 being the host material and RA2 and RA3 the composite mixture samples; among them, both of the measurements; α – value and voltage exhibited an increase, though the difference being minute. The reasons behind the minuscule changes could be (I). The device inherently having the compliance voltage property, (II). The sample matrix considered was a simpler form, consisting only of two networks to work with, instead of 3 or more systems [198]. The α – values were also plotted against the rGO content, to individually understand the framework (**Figure 5.39**). It was observed that as the Ag – nanopowders content increased in the composite mixture, the α – value gave an increase.

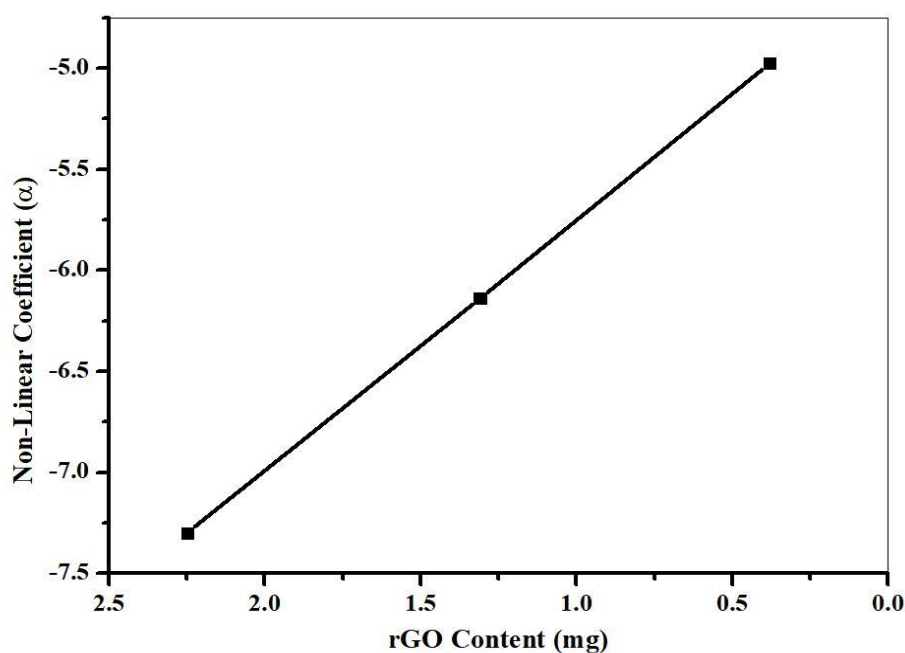


Figure 5.39 Graphical plot for α – value against the rGO content of RA1 [rGO, 1:0], RA2 [rGO + Ag, 3:1], RA3 [rGO + Ag, 1:1], RA4 [Ag, 0:1].

From all the above explanations, it was observed that, rGO when used with a single conductive material, demonstrated a rise in α – and voltage – values. Though, the differences were very small, and that could be because it was only a two-constituent system. Now the lower values obtained, make them candidate for the applicational sectors where low voltage varistors are considered. Such as; smart doorbell systems, garage door sensors, house alarms, heating cooling thermostats etc. But the samples as well exhibited the capability of increasing its values which means that this also has the possibility, if used with stronger matrix of networks, they can exhibit noticeable variations in larger system of measurements and thus can be employed on in the sectors where higher voltage varistors are utilised.

SUMMARY

In this research work, in total six chemicals and five synthesis processes for four objectives were studied. The composite mixture was studied using four varying weight compositions for each objective. CuO, CdO and TiO₂ were fabricated using sol – gel methods, silver was synthesis through top – down method and polyaniline was obtained by oxidative polymerisation method. Hummer's method was employed on for acquiring rGO nano – powders. Each objective was studied using the following ratios:

- CuO + Ag (0:1, 1:1, 1:2 and 0:1)
- PANI + CdO (0:1, 1:1, 1:2 and 0:1)
- TiO₂ (anatase) + Ag (0:1, 1:1, 3:1 and 0:1)
- rGO + Ag (0:1, 1:1, 3:1 and 0:1)

TGA was used for thermal analysis to obtain the values for calcination temperatures so as to acquire the desired phase and form for the nano – materials as CuO and TiO₂ has polymorphism attached to its nature i.e., they exist in more than one form and therefore, with certain temperature or pressure they could change into another form. XRD and FTIR was done to obtain the chemical peaks as it confirms the purity status for the composite mixtures. Raman spectroscopy gave the details concerning the molecular vibrations for the sample nano – systems and as well revealed the space group for each constituent. The surface knowledge was procured using FESEM as it discussed information regarding topographical morphology whereas, EDX was used for the elemental ratio of each constituent and EDX mapping gave the distribution and placement of the elements within the sample surface. PSA was used to obtain the particle size data. It was done only for metal – oxides and metallic nano – powders as they demonstrated an ordered network of atoms within its structure and follows a specific arrangement respective to its space group. The current and voltage values were investigated to study the varistor behaviour of sample powders. Each objective exhibited a consistent elevation in the slope adjacent to linear region before it attained its saturation region. Both linear region (ohms law) and non – linear region (non – ohms law) were observed in the graphical plot which further resulted for the values of non – linear coefficient. Each objective gave an increased value with the addition of dopants into the host materials, though the differences observed for small scale. These led to the applicational aspects for the objectives in small scale voltage

Summary

varistor industries where lower values of voltages are required such as; smart house gadgets, alarm or doorbell systems, small scale sensors, thermostats and likewise.

Monoclinic arrangement in tenorite phase was obtained for CuO nanopowders and cubic arrangement was observed for silver. Various structural analysis was done the composite mixtures consisting of variegated compositions; CA1 [CuO, 1:0], CA2 [CuO + Ag, 1:1], CA3 [CuO + Ag, 1:2] and CA4 [Ag, 0:1] including thermal studies and Raman spectroscopy. An increase in the linear region was obtained for the proceeding sample cases. This linear arena corresponded to slope of the graph that followed Ohm's Law which further implied an increase in the admittance for both current – voltage values within the system. This elevation was observed to be small scale and showed its employment range in lower scale voltage varistors.

Oxidative Polymerisation method and Sol – Gel auto combustion methods were found to be suited on for the synthesis of PANI and CdO nano – particles. FESEM revealed coral – like nature for polyaniline whereas, CdO exhibited more pronounced structure. Some agglomeration was obtained at certain areas which was a common trait for mentioned metal – oxide nano – particles. The varistor plot gave exceptional values as the current and voltage values showed a consistent increase in slope with noticeable differences between the obtained values. The sample system revealed its operational principle to be based on the small scale varistors where lower voltages were a necessity. The particle size analysis gave the size of the CdO nano – powders to be 32.09243 nm, which were in accordance with theoretical data.

The structural studies were done for the TiO₂ (anatase) sample mixtures with varying compositions; TA1 [TiO₂, 1:0], TA2 [TiO₂ + Ag, 3:1], TA3 [TiO₂ + Ag, 1:1] and TA4 [Ag, 0:1] and variegated characterisation tools. Ultra – Sonic assisted Sol – Gel Method was used to synthesise TiO₂ (anatase) nanopowders and Burst Method was done to obtain the Ag – nanopowders. FTIR and XRD gave the characteristic peaks which were confirmed by the Rietveld Refinement in which the experimentally obtained peak values matched the theoretical data. Raman analysis gave the details regarding the modes of the samples and FESEM was done to obtain the details concerning the topographical domain which were in accordance with the already existing data when compared. Its applicability for the varistors was studied through the analysis of the current – voltage graph. The plot, being a simpler grade, gave smaller values of increase which made less voltage needed varistors as it operational sectors.

Summary

In this paper, the applicational prospects of varistors for the composite mixture of rGO and Ag – nanopowders was studied via samples with varying compositions. Hummers modified method and burst method were employed on for the synthesis of GO, rGO and Ag – nanopowders respectively. The structural nature and electrical behaviour were understood by the means of variegated characterisations. The purity of GO and rGO were confirmed via Raman analysis. XRD and FTIR exhibited the attributed peak values for GO and rGO, Ag – nanopowders. The topographical and elemental details were acquired through FESEM and EDX studies, which talked about the wrinkled paper – like structure for GO and rGO and spherical structural nature of Ag. Current – voltage plot was studied for the better understanding of the electrical inhabitation. It was observed, rGO + Ag, being two constituent network gave small values but still showed an increase, means if used with complex arrangement, they have the possibility to be considered in the material fabrication for high voltage varistors domains.

When all the values were put together it was observed that in comparison to CuO, CdO and TiO₂ gave the best results which could be due to the fact that latter two metal – oxides are n – type semiconductors and therefore, have electrons as dominating electrical conduction carriers thus, they exhibited exceptional capability for the mobility of electrons. They also possess larger band – gaps and with the transparency in visible region which makes them transparent conducting oxides (TCO's). However, CuO falls under p – type semiconductor hence has majority hole carriers which effects its conduction potency. rGO and PANI also gave considerable results even for being carbon dominated species. Silver was used as an additional factor in each composition in order to boost the electrical property of the host material as Ag was the most conductive material.

BIBLIOGRAPHY

- [1] P. Biswas and C. Wu, "Nanoparticles and the Environment," *J Air Waste Manage Assoc*, vol. 55, no. 6, pp. 708–746, 2005.
- [2] F. H. Khan, "Chemical hazards of nanoparticles to human and environment (A review)," *Oriental Journal of Chemistry*, vol. 29, no. 4, p. 1399, 2013, doi: 10.13005/ojc/290415.
- [3] V. V. Kumar and S. P. Anthony, *Antimicrobial studies of metal and metal oxide nanoparticles*. Elsevier Inc., 2016. doi: 10.1016/B978-0-323-42861-3.00009-1.
- [4] M. De, P. S. Ghosh, and V. M. Rotello, "Applications of nanoparticles in biology," *Advanced Materials*, vol. 20, no. 22, pp. 4225–4241, 2008, doi: 10.1002/adma.200703183.
- [5] M. A. M. Khan, S. Kumar, M. Ahamed, S. A. Alrokayan, and M. S. AlSalhi, "Structural and thermal studies of silver nanoparticles and electrical transport study of their thin films," *Nanoscale Res Lett*, vol. 6, no. 1, pp. 1–8, 2011, doi: 10.1186/1556-276X-6-434.
- [6] R. Demir, S. Okur, and M. Şeker, "Electrical characterization of CdS nanoparticles for humidity sensing applications," *Ind Eng Chem Res*, vol. 51, no. 8, pp. 3309–3313, 2012, doi: 10.1021/ie201509a.
- [7] V. Harish *et al.*, "Review on Nanoparticles and Nanostructured Materials: Bioimaging, Biosensing, Drug Delivery, Tissue Engineering, Antimicrobial, and Agro-Food Applications," *Nanomaterials*, vol. 12, no. 3, p. 457, 2022, doi: 10.3390/nano12030457.
- [8] Y. Zhang, Y. Chen, P. Westerhoff, K. Hristovski, and J. C. Crittenden, "Stability of commercial metal oxide nanoparticles in water," *Water Res*, vol. 42, no. 8–9, pp. 2204–2212, 2008, doi: 10.1016/j.watres.2007.11.036.
- [9] I. Matsui, "Nanoparticles for electronic device applications: A brief review," *Journal of Chemical Engineering of Japan*, vol. 38, no. 8, pp. 535–546, 2005, doi: 10.1252/jcej.38.535.
- [10] A. A. Aslam, A. A. Aslam, M. S. Aslam, and S. Quazi, "An Overview on Green Synthesis of Nanomaterials and Their Advanced Applications in Sustainable Agriculture," 2022, doi: 10.20944/preprints202202.0315.v1.
- [11] M. Niederberger, "Nonaqueous sol-gel routes to metal oxide nanoparticles," *Acc Chem Res*, vol. 40, no. 9, pp. 793–800, 2007, doi: 10.1021/ar600035e.
- [12] M. D. Mauricio *et al.*, "Nanoparticles in medicine: A focus on vascular oxidative stress," *Oxid Med Cell Longev*, vol. 2018, 2018, doi: 10.1155/2018/6231482.

Bibliography

- [13] D. Zappa, E. Comini, R. Zamani, J. Arbiol, J. R. Morante, and G. Sberveglieri, "Preparation of copper oxide nanowire-based conductometric chemical sensors," *Sens Actuators B Chem*, vol. 182, pp. 7–15, 2013, doi: 10.1016/j.snb.2013.02.076.
- [14] T. Oku, R. Motoyoshi, K. Fujimoto, T. Akiyama, B. Jeyadevan, and J. Cuya, "Structures and photovoltaic properties of copper oxides/fullerene solar cells," *Journal of Physics and Chemistry of Solids*, vol. 72, no. 11, pp. 1206–1211, 2011, doi: 10.1016/j.jpcs.2011.06.014.
- [15] N. Verma and N. Kumar, "Synthesis and Biomedical Applications of Copper Oxide Nanoparticles: An Expanding Horizon," *ACS Biomater Sci Eng*, vol. 5, no. 3, pp. 1170–1188, 2019, doi: 10.1021/acsbiomaterials.8b01092.
- [16] A. A. Ziabari and F. E. Ghodsi, "Optoelectronic studies of sol-gel derived nanostructured CdO-ZnO composite films," *J Alloys Compd*, vol. 509, no. 35, pp. 8748–8755, 2011, doi: 10.1016/j.jallcom.2011.06.050.
- [17] K. Gurumurugan, D. Mangalaraj, and S. K. Narayandass, "Structural characterization of cadmium oxide thin films deposited by spray pyrolysis," *J Cryst Growth*, vol. 147, no. 3–4, pp. 355–360, 1995, doi: 10.1016/0022-0248(94)00634-2.
- [18] R. Kumaravel, S. Menaka, S. R. M. Snega, K. Ramamurthi, and K. Jeganathan, "Electrical, optical and structural properties of aluminum doped cadmium oxide thin films prepared by spray pyrolysis technique," *Mater Chem Phys*, vol. 122, no. 2–3, pp. 444–448, 2010, doi: 10.1016/j.matchemphys.2010.03.022.
- [19] R. R. Mahdi and S. A. Makki, "Synthesis and properties of cadmium oxide thin films prepared by simple chemical method," *Energy Procedia*, vol. 157, pp. 261–269, 2019, doi: 10.1016/j.egypro.2018.11.189.
- [20] E. A. Mwafy and A. M. Mostafa, "Multi walled carbon nanotube decorated cadmium oxide nanoparticles via pulsed laser ablation in liquid media," *Opt Laser Technol*, vol. 111, pp. 249–254, 2019, doi: 10.1016/j.optlastec.2018.09.055.
- [21] A. Tadjarodi and M. Imani, "A novel nanostructure of cadmium oxide synthesized by mechanochemical method," *Mater Res Bull*, vol. 46, no. 11, pp. 1949–1954, 2011, doi: 10.1016/j.materresbull.2011.07.016.
- [22] A. Nivetha, S. M. Devi, and I. Prabha, "Fascinating Physic-Chemical Properties and Resourceful Applications of Selected Cadmium Nanomaterials," *J Inorg Organomet Polym Mater*, vol. 29, no. 5, pp. 1423–1438, 2019, doi: 10.1007/s10904-019-01141-z.
- [23] A. M. Mostafa, S. A. Yousef, W. H. Eisa, M. A. Ewaida, and E. A. Al-Ashkar, "Synthesis of cadmium oxide nanoparticles by pulsed laser ablation in liquid environment," *Optik (Stuttg)*, vol. 144, pp. 679–684, 2017, doi: 10.1016/j.ijleo.2017.06.065.
- [24] A. B. Gaikwad, S. C. Navale, and V. Ravi, "TiO₂ ceramic varistor modified with tantalum and barium," *Materials Science and Engineering: B*, vol. 123, no. 1, pp. 50–52, 2005, doi: 10.1016/j.mseb.2005.06.015.

Bibliography

- [25] N. Ibrayev, A. Zhumabekov, S. Ghyngazov, and E. Lysenko, "Synthesis and study of the properties of nanocomposite materials TiO₂-GO and TiO₂-rGO," *Mater Res Express*, vol. 6, no. 12, p. 125036, 2019.
- [26] J. Y. Kim, D. W. Kim, H. S. Jung, and K. S. Hong, "Influence of anatase-rutile phase transformation on dielectric properties of sol-gel derived TiO₂ thin films," *Jpn J Appl Phys*, vol. 44, no. 8R, pp. 6148–6151, 2005, doi: 10.1143/JJAP.44.6148.
- [27] Y. V. Kolen'ko, A. A. Burukhin, B. R. Churagulov, and N. N. Oleynikov, "Synthesis of nanocrystalline TiO₂ powders from aqueous TiOSO₄ solutions under hydrothermal conditions," *Mater Lett*, vol. 57, no. 5–6, pp. 1124–1129, 2003, doi: 10.1016/S0167-577X(02)00943-6.
- [28] S. Singh and M. N. Tripathi, "Electronic structure and optical properties of prominent phases of TiO₂: First-principles study," *Pramana*, vol. 89, no. 1, pp. 1–6, 2017, doi: 10.1007/s12043-017-1400-5.
- [29] S. Boujday, F. Wünsch, P. Portes, J. F. Bocquet, and C. Colbeau-Justin, "Photocatalytic and electronic properties of TiO₂ powders elaborated by sol-gel route and supercritical drying," *Solar Energy Materials and Solar Cells*, vol. 83, no. 4, pp. 421–433, 2004, doi: 10.1016/j.solmat.2004.02.035.
- [30] T. C. Jagadale *et al.*, "N-doped TiO₂ nanoparticle based visible light photocatalyst by modified peroxide sol-gel method," *Journal of Physical Chemistry C*, vol. 112, no. 37, pp. 14595–14602, 2008, doi: 10.1021/jp803567f.
- [31] J. E. S. Haggerty *et al.*, "High-fraction brookite films from amorphous precursors," *Sci Rep*, vol. 7, no. 1, pp. 1–11, 2017, doi: 10.1038/s41598-017-15364-y.
- [32] U. Diebold, "Structure and properties of TiO₂ surfaces: A brief review," *Applied Physics A*, vol. 76, no. 5, pp. 681–687, 2003, doi: 10.1007/s00339-002-2004-5.
- [33] H. Jamil *et al.*, "Electrospun titanium dioxide nanofiber humidity sensors with high sensitivity," *Ceram Int*, vol. 38, no. 3, pp. 2437–2441, 2012, doi: 10.1016/j.ceramint.2011.11.010.
- [34] M. S. Waghmode, A. B. Gunjal, J. A. Mulla, N. N. Patil, and N. N. Nawani, "Studies on the titanium dioxide nanoparticles: biosynthesis, applications and remediation," *SN Appl Sci*, vol. 1, no. 4, pp. 1–9, 2019, doi: 10.1007/s42452-019-0337-3.
- [35] U. G. Akpan and B. H. Hameed, "The advancements in sol-gel method of doped-TiO₂ photocatalysts," *Appl Catal A Gen*, vol. 375, no. 1, pp. 1–11, 2010, doi: 10.1016/j.apcata.2009.12.023.
- [36] S. Z. Chu, S. Inoue, K. Wada, D. Li, H. Haneda, and S. Awatsu, "Highly porous (TiO₂-SiO₂-TeO₂)/Al₂O₃/TiO₂ composite nanostructures on glass with enhanced photocatalysis fabricated by anodization and sol-gel process," *J Phys Chem B*, vol. 107, no. 27, pp. 6586–6589, 2003, doi: 10.1021/jp0349684.
- [37] B. S. Misirlioğlu, M. Serin, F. Kuruoğlu, and D. S. Dasdan, "Optical properties of polyaniline synthesized by oxidative polymerization and electrical characterization of

- Ag/PANI/PEDOT:PSS/Ag structures,” *Journal of Nanoelectronics and Optoelectronics*, vol. 11, no. 2, pp. 219–224, 2016, doi: 10.1166/jno.2016.1886.
- [38] D. Zhang, D. Wang, P. Li, X. Zhou, X. Zong, and G. Dong, “Facile fabrication of high-performance QCM humidity sensor based on layer-by-layer self-assembled polyaniline/graphene oxide nanocomposite film,” *Sens Actuators B Chem*, vol. 255, pp. 1869–1877, 2018, doi: 10.1016/j.snb.2017.08.212.
- [39] A. Vijayan, M. Fuke, R. Hawaldar, M. Kulkarni, D. Amalnerkar, and R. C. Aiyer, “Optical fibre based humidity sensor using Co-polyaniline clad,” *Sens Actuators B Chem*, vol. 129, no. 1, pp. 106–112, 2008, doi: 10.1016/j.snb.2007.07.113.
- [40] H. Tai, Y. Jiang, G. Xie, J. Yu, X. Chen, and Z. Ying, “Influence of polymerization temperature on NH₃ response of PANI/TiO₂ thin film gas sensor,” *Sens Actuators B Chem*, vol. 129, no. 1, pp. 319–326, 2008, doi: 10.1016/j.snb.2007.08.013.
- [41] H. Tai, Y. Jiang, G. Xie, and J. Yu, “Preparation, Characterization and Comparative NH₃-sensing Characteristic Studies of PANI/inorganic Oxides Nanocomposite Thin Films,” *J Mater Sci Technol*, vol. 26, no. 7, pp. 605–613, 2010, doi: 10.1016/S1005-0302(10)60093-X.
- [42] M. L. Singla, S. Awasthi, and A. Srivastava, “Humidity sensing; using polyaniline/Mn₃O₄ composite doped with organic/inorganic acids,” *Sens Actuators B Chem*, vol. 127, no. 2, pp. 580–585, 2007, doi: 10.1016/j.snb.2007.05.018.
- [43] E. Llorens, E. Armelin, M. del M. Pérez-Madrugal, L. J. del Valle, C. Alemán, and J. Puiggali, *Nanomembranes and nanofibers from biodegradable conducting polymers*, vol. 5, no. 3. 2013. doi: 10.3390/polym5031115.
- [44] R. Nohria, R. K. Khillan, Y. Su, R. Dikshit, Y. Lvov, and K. Varahramyan, “Humidity sensor based on ultrathin polyaniline film deposited using layer-by-layer nano-assembly,” *Sens Actuators B Chem*, vol. 114, no. 1, pp. 218–222, 2006, doi: 10.1016/j.snb.2005.04.034.
- [45] L. Kumar, I. Rawal, A. Kaur, and S. Annapoorni, “Flexible room temperature ammonia sensor based on polyaniline,” *Sens Actuators B Chem*, vol. 240, pp. 408–416, 2017, doi: 10.1016/j.snb.2016.08.173.
- [46] P. Singh and S. K. Shukla, “Advances in polyaniline-based nanocomposites,” *J Mater Sci*, vol. 55, no. 4, pp. 1331–1365, 2020, doi: 10.1007/s10853-019-04141-z.
- [47] M. Beygisangchin, S. A. Rashid, S. Shafie, and A. R. Sadrolhosseini, “Preparations, properties, and applications of polyaniline and polyaniline thin films—A review,” *Polymers (Basel)*, vol. 13, no. 12, 2021.
- [48] M. Kanna and S. Wongnawa, “Mixed amorphous and nanocrystalline TiO₂ powders prepared by sol-gel method: Characterization and photocatalytic study,” *Mater Chem Phys*, vol. 110, no. 1, pp. 166–175, 2008, doi: 10.1016/j.matchemphys.2008.01.037.
- [49] K. Thamaphat, P. Limsuwan, and B. Ngotawornchai, “Phase characterization of TiO₂ powder by XRD and TEM,” *Agriculture and Natural Resources*, vol. 42, no. 5, pp. 357–361, 2008.

Bibliography

- [50] A. H. Alshehri *et al.*, “Enhanced electrical conductivity of silver nanoparticles for high frequency electronic applications,” *ACS Appl Mater Interfaces*, vol. 4, no. 12, pp. 7007–7010, 2012, doi: 10.1021/am3022569.
- [51] A. A. Yaqoob *et al.*, “Recent Advances in Metal Decorated Nanomaterials and Their Various Biological Applications: A Review,” *Front Chem*, vol. 8, p. 341, 2020, doi: 10.3389/fchem.2020.00341.
- [52] D. Chen, X. Qiao, X. Qiu, and J. Chen, “Synthesis and electrical properties of uniform silver nanoparticles for electronic applications,” *J Mater Sci*, vol. 44, no. 4, pp. 1076–1081, 2009, doi: 10.1007/s10853-008-3204-y.
- [53] M. Vivek, P. S. Kumar, S. Steffi, and S. Sudha, “Biogenic silver nanoparticles by gelidiella acerosa extract and their antifungal effects,” *Avicenna J Med Biotechnol*, vol. 3, no. 3, p. 143, 2011.
- [54] X. Zhang, Z. Liu, W. Shen, and S. Gurunathan, “Silver Nanoparticles : Synthesis , Characterization , Properties , Applications , and Therapeutic Approaches,” *Int J Mol Sci*, vol. 17, no. 9, p. 1534, 2016, doi: 10.3390/ijms17091534.
- [55] Q. H. Tran, V. Q. Nguyen, and A.-T. Le, “Silver nanoparticles : synthesis , properties , toxicology , applications and perspectives,” *Advnaces in Natural Sciences: Nanoscience and Nanotechnology*, vol. 4, no. 3, p. 033001, 2013, doi: 10.1088/2043-6262/4/3/033001.
- [56] T. M. Abdelghany *et al.*, “Recent Advances in Green Synthesis of Silver Nanoparticles and Their Applications: About Future Directions. A Review,” *Bionanoscience*, vol. 8, no. 1, pp. 5–16, 2018, doi: 10.1007/s12668-017-0413-3.
- [57] S. Borini *et al.*, “Ultrafast graphene oxide humidity sensors,” *ACS Nano*, vol. 7, no. 12, pp. 11166–11173, 2013, doi: 10.1021/nn404889b.
- [58] D. Li, T. Wang, Z. Li, X. Xu, C. Wang, and Y. Duan, “Application of graphene-based materials for detection of nitrate and nitrite in water—a review,” *Sensors*, vol. 20, no. 1, p. 54, 2019, doi: 10.3390/s20010054.
- [59] S. Y. Park *et al.*, “Room temperature humidity sensors based on rGO/MoS₂ hybrid composites synthesized by hydrothermal method,” *Sens Actuators B Chem*, vol. 258, pp. 775–782, 2018, doi: 10.1016/j.snb.2017.11.176.
- [60] W. De Lin, H. M. Chang, and R. J. Wu, “Applied novel sensing material graphene/polypyrrole for humidity sensor,” *Sens Actuators B Chem*, vol. 181, pp. 326–331, 2013, doi: 10.1016/j.snb.2013.02.017.
- [61] N. I. Zaaba, K. L. Foo, U. Hashim, S. J. Tan, W. W. Liu, and C. H. Voon, “Synthesis of Graphene Oxide using Modified Hummers Method: Solvent Influence,” *Procedia Eng*, vol. 184, pp. 469–477, 2017, doi: 10.1016/j.proeng.2017.04.118.
- [62] E. U. Park *et al.*, “Correlation between the sensitivity and the hysteresis of humidity sensors based on graphene oxides,” *Sens Actuators B Chem*, vol. 258, pp. 255–262, 2018, doi: 10.1016/j.snb.2017.11.104.

Bibliography

- [63] A. T. Dideikin and A. Y. Vul', "Graphene oxide and derivatives: The place in graphene family," *Front Phys*, vol. 6, p. 149, 2019, doi: 10.3389/fphy.2018.00149.
- [64] R. Danzer, B. Kaufmann, and P. Supancic, "Failure of high power varistor ceramic components," *J Eur Ceram Soc*, vol. 40, no. 11, pp. 3766–3770, 2020, doi: 10.1016/j.jeurceramsoc.2020.02.007.
- [65] S. Anas, K. V. Mahesh, M. Jeen Maria, and S. Ananthakumar, *Sol-Gel Materials for Varistor Devices*. 2017. doi: 10.1007/978-3-319-50144-4_2.
- [66] S. Mohammadi Aref, A. Olad, M. Parhizkar, M. Ghafouri, and H. Bidadi, "Effect of polyaniline content on electrophysical properties of gallium arsenide-polymer composite varistors," *Solid State Sci*, vol. 26, pp. 128–133, 2013, doi: 10.1016/j.solidstatesciences.2013.10.005.
- [67] A. Di Bartolomeo, "Graphene Schottky diodes: An experimental review of the rectifying graphene/semiconductor heterojunction," *Phys Rep*, vol. 606, pp. 1–58, 2016, doi: 10.1016/j.physrep.2015.10.003.
- [68] F. M. Frigura-Iliasa, S. Musuroi, C. Sorandaru, and D. Vatau, "New technical parameters and operational improvements of the Metal Oxide Varistors manufacturing process," *Processes*, vol. 7, no. 1, p. 18, 2019, doi: 10.3390/pr7010018.
- [69] J. Fan and R. Freer, "The electrical properties and d.c. degradation characteristics of silver doped ZnO varistors," *J Mater Sci*, vol. 28, no. 5, pp. 1391–1395, 1993, doi: 10.1007/BF01191983.
- [70] S. Singhal, J. Kaur, T. Namgyal, and R. Sharma, "Cu-doped ZnO nanoparticles: Synthesis, structural and electrical properties," *Physica B Condens Matter*, vol. 407, no. 8, pp. 1223–1226, 2012, doi: 10.1016/j.physb.2012.01.103.
- [71] M. S. Cho, S. Y. Park, J. Y. Hwang, and H. J. Choi, "Synthesis and electrical properties of polymer composites with polyaniline nanoparticles," *Materials Science and Engineering C*, vol. 24, no. 1–2, pp. 15–18, 2004, doi: 10.1016/j.msec.2003.09.003.
- [72] K. Karthik, S. K. Pandian, and N. V. Jaya, "Effect of nickel doping on structural, optical and electrical properties of TiO₂ nanoparticles by sol-gel method," *Appl Surf Sci*, vol. 256, no. 22, pp. 6829–6833, 2010, doi: 10.1016/j.apsusc.2010.04.096.
- [73] P. C. Ma, B. Z. Tang, and J. K. Kim, "Effect of CNT decoration with silver nanoparticles on electrical conductivity of CNT-polymer composites," *Carbon N Y*, vol. 46, no. 11, pp. 1497–1505, 2008, doi: 10.1016/j.carbon.2008.06.048.
- [74] C. C. Vidyasagar, Y. A. Naik, T. G. Venkatesh, and R. Viswanatha, "Solid-state synthesis and effect of temperature on optical properties of Cu-ZnO, Cu-CdO and CuO nanoparticles," *Powder Technol*, vol. 214, no. 3, pp. 337–343, 2011, doi: 10.1016/j.powtec.2011.08.025.
- [75] S. Pourbeyram, J. Abdollahpour, and M. Soltanpour, "Green synthesis of copper oxide nanoparticles decorated reduced graphene oxide for high sensitive detection of

Bibliography

- glucose,” *Materials Science and Engineering C*, vol. 94, pp. 850–857, 2019, doi: 10.1016/j.msec.2018.10.034.
- [76] Ş. Baturay, A. Tombak, D. Batibay, and Y. S. Ocak, “n-Type conductivity of CuO thin films by metal doping,” *Appl Surf Sci*, vol. 477, pp. 91–95, 2019, doi: 10.1016/j.apsusc.2017.12.004.
- [77] T. M. D. Dang, T. T. T. Le, E. Fribourg-Blanc, and M. C. Dang, “The influence of solvents and surfactants on the preparation of copper nanoparticles by a chemical reduction method,” *Advances in Natural Sciences: Nanoscience and Nanotechnology*, vol. 2, no. 2, p. 025004, 2011, doi: 10.1088/2043-6262/2/2/025004.
- [78] F. T. Thema, P. Beukes, A. Gurib-Fakim, and M. Maaza, “Green synthesis of Montepelite CdO nanoparticles by *Agathosma betulina* natural extract,” *J Alloys Compd*, vol. 646, pp. 1043–1048, 2015, doi: 10.1016/j.jallcom.2015.05.279.
- [79] R. Ranjithkumar, A. Albert Irudayaraj, G. Jayakumar, A. Dhayal Raj, S. Karthick, and R. Vinayagamorthy, “Synthesis and Properties of CdO and Fe doped CdO Nanoparticles,” *Mater Today Proc*, vol. 3, no. 6, pp. 1378–1382, 2016, doi: 10.1016/j.matpr.2016.04.018.
- [80] A. Askarinejad and A. Morsali, “Synthesis of cadmium(II) hydroxide, cadmium(II) carbonate and cadmium(II) oxide nanoparticles; investigation of intermediate products,” *Chemical Engineering Journal*, vol. 150, no. 2–3, pp. 569–571, 2009, doi: 10.1016/j.cej.2009.03.005.
- [81] B. Saha, R. Thapa, and K. K. Chattopadhyay, “Bandgap widening in highly conducting CdO thin film by Ti incorporation through radio frequency magnetron sputtering technique,” *Solid State Commun*, vol. 145, no. 1–2, pp. 33–37, 2008, doi: 10.1016/j.ssc.2007.10.001.
- [82] S. C. Navale, A. Vadivel Murugan, and V. Ravi, “Varistors based on Ta-doped TiO₂,” *Ceram Int*, vol. 33, no. 2, pp. 301–303, 2007, doi: 10.1016/j.ceramint.2005.07.026.
- [83] S. M. Oh and T. Ishigaki, “Preparation of pure rutile and anatase TiO₂ nanopowders using RF thermal plasma,” *Thin Solid Films*, vol. 457, no. 1, pp. 186–191, 2004, doi: 10.1016/j.tsf.2003.12.043.
- [84] Y. Zhang *et al.*, “Synthesis and characterization of TiO₂ nanotubes for humidity sensing,” *Appl Surf Sci*, vol. 254, no. 17, pp. 5545–5547, 2008, doi: 10.1016/j.apsusc.2008.02.106.
- [85] B. C. Yadav, R. Srivastava, and C. D. Dwivedi, “Synthesis and characterization of ZnO-TiO₂ nanocomposite and its application as a humidity sensor,” *Philosophical Magazine*, vol. 88, no. 7, pp. 1113–1124, 2008, doi: 10.1080/14786430802064642.
- [86] V. V. A. Thampi, S. Thanka Rajan, K. Anupriya, and B. Subramanian, “Functionalization of fabrics with PANI/CuO nanoparticles by precipitation route for anti-bacterial applications,” *Journal of Nanoparticle Research*, vol. 17, no. 1, pp. 1–12, 2015, doi: 10.1007/s11051-014-2853-9.

Bibliography

- [87] F. W. Zeng, X. X. Liu, D. Diamond, and K. T. Lau, "Humidity sensors based on polyaniline nanofibres," *Sens Actuators B Chem*, vol. 143, no. 2, pp. 530–534, 2010, doi: 10.1016/j.snb.2009.09.050.
- [88] M. Trchová, Z. Morávková, M. Bláha, and J. Stejskal, "Raman spectroscopy of polyaniline and oligoaniline thin films," *Electrochim Acta*, vol. 122, pp. 28–38, 2014, doi: 10.1016/j.electacta.2013.10.133.
- [89] M. Zong *et al.*, "Facile synthesis of RGO/Fe₃O₄/Ag composite with high microwave absorption capacity," *Mater Lett*, vol. 111, pp. 188–191, 2013, doi: 10.1016/j.matlet.2013.08.076.
- [90] M. Govarathanan *et al.*, "Biosynthesis and characterization of silver Nanoparticles using Panchakavya, an Indian traditional farming formulating agent," *Int J Nanomedicine*, vol. 9, p. 1593, 2014, doi: 10.2147/IJN.S58932.
- [91] A. C. Power, J. Betts, and J. F. Cassidy, "Silver nanoparticle polymer composite based humidity sensor," *Analyst*, vol. 135, no. 7, pp. 1645–1652, 2010, doi: 10.1039/c0an00133c.
- [92] G. Narasimha, Janardhan, M. Alzohairy, H. Khadri, and K. Mallikarjuna, "Extracellular synthesis, characterization and antibacterial activity of Silver nanoparticles by Actinomycetes isolative," pp. 77–83, 2013.
- [93] R. Guo, W. Tang, C. Shen, and X. Wang, "High sensitivity and fast response graphene oxide capacitive humidity sensor with computer-aided design," *Comput Mater Sci*, vol. 111, pp. 289–293, 2016, doi: 10.1016/j.commatsci.2015.09.032.
- [94] Y. Li, L. Tang, and J. Li, "Preparation and electrochemical performance for methanol oxidation of pt/graphene nanocomposites," *Electrochem commun*, vol. 11, no. 4, pp. 846–849, 2009, doi: 10.1016/j.elecom.2009.02.009.
- [95] M. Sohail *et al.*, "Modified and improved Hummer's synthesis of graphene oxide for capacitors applications," *Modern Electronic Materials*, vol. 3, no. 3, pp. 110–116, 2017, doi: 10.1016/j.moem.2017.07.002.
- [96] H. Ahmad, M. T. Rahman, S. N. A. Sakeh, M. Z. A. Razak, and M. Z. Zulkifli, "Humidity sensor based on microfiber resonator with reduced graphene oxide," *Optik (Stuttg)*, vol. 127, no. 5, pp. 3158–3161, 2016, doi: 10.1016/j.ijleo.2015.11.184.
- [97] V. B. Mohan, R. Brown, K. Jayaraman, and D. Bhattacharyya, "Characterisation of reduced graphene oxide: Effects of reduction variables on electrical conductivity," *Materials Science and Engineering: B*, vol. 193, pp. 49–60, 2015, doi: 10.1016/j.mseb.2014.11.002.
- [98] H. Bidadi, S. Mohammadi Aref, M. Ghafouri, M. Parhizkar, and A. Olad, "The effect of sintering temperature on varistor characteristics of gallium arsenide-polyaniline-polyethylene composite varistors," *Mater Sci Semicond Process*, vol. 16, no. 3, pp. 752–758, 2013, doi: 10.1016/j.mssp.2012.12.022.

Bibliography

- [99] F. H. Cristovan and E. C. Pereira, "Polymeric varistor based on PANI/ABS composite," *Synth Met*, vol. 161, no. 17–18, pp. 2041–2044, 2011, doi: 10.1016/j.synthmet.2011.06.030.
- [100] H. Lu, Y. Wang, and X. Lin, "Structures, varistor properties, and electrical stability of ZnO thin films," *Mater Lett*, vol. 63, no. 27, pp. 2321–2323, 2009, doi: 10.1016/j.matlet.2009.08.001.
- [101] A. V. Gaponov and A. B. Glot, "Electrical properties of SnO₂ based varistor ceramics with CuO addition," *Journal of Materials Science: Materials in Electronics*, vol. 21, no. 4, pp. 331–337, 2010, doi: 10.1007/s10854-009-9916-1.
- [102] D. M. Fernandes, R. Silva, A. A. W. Hechenleitner, E. Radovanovic, M. A. C. Melo, and E. A. G. Pineda, "Synthesis and characterization of ZnO, CuO and a mixed Zn and Cu oxide," *Mater Chem Phys*, vol. 115, no. 1, pp. 110–115, 2009, doi: 10.1016/j.matchemphys.2008.11.038.
- [103] F. Cui, Z. Xu, R. Chu, X. He, X. Guo, and G. Li, "Low temperature sintering ZnO - Bi₂O₃ based varistor ceramics with low electrical breakdown voltage and high nonlinear coefficient," *Ceram Int*, vol. 47, no. 3, pp. 4118–4126, Feb. 2021, doi: 10.1016/j.ceramint.2020.09.288.
- [104] L. Muremi, P. Bokoro, and W. Doorsamy, "Electrical degradation characteristics of Low Voltage Zinc Oxide Varistor subjected to AC Switching Surges," in *2021 IEEE 5th International Conference on Condition Assessment Techniques in Electrical Systems (CATCON)*. IEEE., Institute of Electrical and Electronics Engineers Inc., 2021, pp. 195–200. doi: 10.1109/CATCON52335.2021.9670532.
- [105] M. S. Shaifudin*, M. S. M. Ghazali*, W. R. W. Abdullah, S. Kassim, and W. M. I. W. M. Kamaruzzaman, "Microstructure and Electrical Properties of Low-Voltage Barium Titanate Doped Zinc Oxide Varistor Ceramics," *International Journal of Recent Technology and Engineering*, vol. 8, pp. 2713–2718, Nov. 2019, doi: 10.35940/ijrte.D7326.118419.
- [106] E. T. Staikos and T. E. Tsovilis, "Low-frequency response of low-voltage metal-oxide varistors used for telecommunication systems protection," in *2020 IEEE International Conference on High Voltage Engineering and Application (ICHVE)*. IEEE, 2020., Institute of Electrical and Electronics Engineers Inc., Sep. 2020. doi: 10.1109/ICHVE49031.2020.9280018.
- [107] S. M. Syaizwadi *et al.*, "Nonlinearity characteristics of low-voltage barium titanate based zinc oxide varistor ceramics modified by cobalt dopants," *Journal of Integrated Circuits and Systems*, vol. 16, no. 1, pp. 1–7, 2021, doi: 10.29292/jics.v16i1.220.
- [108] S. P. Goutam, G. Saxena, D. Roy, A. K. Yadav, and R. N. Bharagava, *Green Synthesis of Nanoparticles and Their Applications in Water and Wastewater Treatment*, no. Springer, Singapore. 2020. doi: 10.1007/978-981-13-1891-7_16.
- [109] D. Bokov *et al.*, "Nanomaterial by Sol-Gel Method: Synthesis and Application," *Advances in Materials Science and Engineering*, vol. 2021, 2021, doi: 10.1155/2021/5102014.

Bibliography

- [110] F. R. Rangel-Olivares, E. M. Arce-Estrada, and R. Cabrera-Sierra, "Synthesis and characterization of polyaniline-based polymer nanocomposites as anti-corrosion coatings," *Coatings*, vol. 11, no. 6, p. 653, 2021, doi: 10.3390/coatings11060653.
- [111] M. Huston, M. DeBella, M. DiBella, and A. Gupta, "Green Synthesis of Nanomaterials," *Nanomaterials*, vol. 11, p. 2130, 2021, doi: <https://doi.org/10.3390/nano11082130>.
- [112] S. V Banne, M. S. Patil, R. M. Kulkarni, and S. J. Patil, "Synthesis and Characterization of Silver Nano Particles for EDM Applications," in *Materials Today: Proceedings*, 2017, pp. 12054–12060. doi: 10.1016/j.matpr.2017.09.130.
- [113] K. M. M. A. El-nour, A. Al-warthan, and R. A. A. Ammar, "Synthesis and applications of silver nanoparticles," *Arabian Journal of Chemistry*, vol. 3, no. 3, pp. 135–140, 2010, doi: 10.1016/j.arabjc.2010.04.008.
- [114] E. M. MODAN and A. G. PLĂIAȘU, "Advantages and Disadvantages of Chemical Methods in the Elaboration of Nanomaterials," *The Annals of "Dunarea de Jos" University of Galati. Fascicle IX, Metallurgy and Materials Science*, vol. 43, no. 1, pp. 53–60, 2020, doi: 10.35219/mms.2020.1.08.
- [115] M. D. P. Lavin-Lopez, A. Romero, J. Garrido, L. Sanchez-Silva, and J. L. Valverde, "Influence of different improved hummers method modifications on the characteristics of graphite oxide in order to make a more easily scalable method," *Ind Eng Chem Res*, vol. 55, no. 50, pp. 12836–12847, 2016, doi: 10.1021/acs.iecr.6b03533.
- [116] A. Saini, A. Kumar, V. K. Anand, and S. C. Sood, "Synthesis of Graphene Oxide using Modified Hummer's Method and its Reduction using Hydrazine Hydrate," *Int. J. Eng. Trends Technol*, vol. 40, pp. 67–71, 2016, doi: 10.14445/22315381/ijett-v40p211.
- [117] M. C. Ramakrishnan and R. R. Thangavelu, "Synthesis and characterization of reduced graphene oxide," *Adv Mat Res*, vol. 678, no. Trans Tech Publications Ltd., pp. 56–60, 2013, doi: 10.4028/www.scientific.net/AMR.678.56.
- [118] S. Bhattacharjee, R. Joshi, A. A. Chughtai, and C. R. Macintyre, "Graphene Modified Multifunctional Personal Protective Clothing," *Adv Mater Interfaces*, vol. 6, no. 21, p. 1900622, 2019, doi: 10.1002/admi.201900622.
- [119] G. Hitkari, S. Singh, and G. Pandey, *Nanoparticles: An emerging weapon for mitigation/removal of various environmental pollutants for environmental safety*. 2019. doi: 10.1007/978-981-10-8669-4_16.
- [120] W. N. R. W. Isahak, Z. A. C. Ramli, W. Z. Samad, and M. A. Yarmo, "CAPTURING GREENHOUSE GAS CARBON DIOXIDE TO FORM CARBONATE COMPOUNDS," *J Teknol*, vol. 75, no. 33, 2015.
- [121] G. Manjari, S. Saran, T. Arun, A. Vijaya Bhaskara Rao, and S. P. Devipriya, "Catalytic and recyclability properties of phytogenic copper oxide nanoparticles derived from *Aglaia elaeagnoides* flower extract," *Journal of Saudi Chemical Society*, vol. 21, no. 5, pp. 610–618, 2017, doi: 10.1016/j.jscs.2017.02.004.

Bibliography

- [122] M. M. Peng, P. Hemalatha, M. Ganesh, R. Vinodh, and H. T. Jang, "Synthesis and characterization of novel mesoporous CuO and its application to CO₂ capture," *Asian Journal of Chemistry*, vol. 25, no. 17, p. 9941, 2013, doi: 10.14233/ajchem.2013.15666.
- [123] H. Veisi, B. Karmakar, T. Tamoradi, S. Hemmati, M. Hekmati, and M. Hamelian, "Biosynthesis of CuO nanoparticles using aqueous extract of herbal tea (*Stachys Lavandulifolia*) flowers and evaluation of its catalytic activity," *Sci Rep*, vol. 11, no. 1, pp. 1–13, 2021, doi: 10.1038/s41598-021-81320-6.
- [124] J. M. Rami, C. D. Patel, C. M. Patel, and M. V. Patel, "Thermogravimetric analysis (TGA) of some synthesized metal oxide nanoparticles," *Mater Today Proc*, vol. 43, pp. 655–659, 2020, doi: 10.1016/j.matpr.2020.12.554.
- [125] H. Zhang *et al.*, "Synthesis of silver nanoparticles using large-area arc discharge and its application in electronic packaging," *J Mater Sci*, vol. 52, no. 6, pp. 3375–3387, 2017, doi: 10.1007/s10853-016-0626-9.
- [126] A. C. Schneid *et al.*, "Silver nanoparticle thin films deposited on glass surface using an ionic silsesquioxane as stabilizer and as crosslinking agent," *J Braz Chem Soc*, vol. 26, pp. 1004–1012, 2015, doi: 10.5935/0103-5053.20150066.
- [127] N. Supraja, T. N. V. K. V. Prasad, E. David, and T. Giridhara Krishna, "Antimicrobial kinetics of *Alstonia scholaris* bark extract-mediated AgNPs," *Appl Nanosci*, vol. 6, no. 5, pp. 779–787, 2016, doi: 10.1007/s13204-015-0483-x.
- [128] M. R. H. Siddiqui, S. F. Adil, M. E. Assal, R. Ali, and A. Al-Warthan, "Synthesis and characterization of silver oxide and silver chloride nanoparticles with high thermal stability," *Asian J. Chem*, vol. 25, no. 6, pp. 3405–3409, 2013, doi: 10.14233/ajchem.2013.13874.
- [129] S. Kota, P. Dumpala, R. K. Anantha, M. K. Verma, and S. Kandepu, "Evaluation of therapeutic potential of the silver/silver chloride nanoparticles synthesized with the aqueous leaf extract of *Rumex acetosa*," *Sci Rep*, vol. 7, no. 1, pp. 1–11, 2017, doi: 10.1038/s41598-017-11853-2.
- [130] B. Adebayo-Tayo, A. Salaam, and A. Ajibade, "Green synthesis of silver nanoparticle using *Oscillatoria* sp. extract, its antibacterial, antibiofilm potential and cytotoxicity activity," *Heliyon*, vol. 5, no. 10, p. e02502, 2019, doi: 10.1016/j.heliyon.2019.e02502.
- [131] S. Ponmudi, R. Sivakumar, C. Sanjeeviraja, and C. Gopalakrishnan, "Influences of sputtering power and annealing temperature on the structural and optical properties of Al₂O₃:CuO thin films fabricated by radio frequency magnetron sputtering technique," *Journal of Materials Science: Materials in Electronics*, vol. 30, no. 20, pp. 18315–18327, 2019, doi: 10.1007/s10854-019-02185-0.
- [132] O. Diachenko *et al.*, "Structural and optical properties of cuo thin films synthesized using spray pyrolysis method," *Coatings*, vol. 11, no. 11, p. 1392, 2021, doi: 10.3390/coatings11111392.

Bibliography

- [133] G. Zampardi *et al.*, “Electrochemical Behavior of Single CuO Nanoparticles: Implications for the Assessment of their Environmental Fate,” *Small*, vol. 14, no. 32, p. 1801765, 2018, doi: 10.1002/sml.201801765.
- [134] G. N. Rao, Y. D. Yao, and J. W. Chen, “Superparamagnetic behavior of antiferromagnetic CuO nanoparticles,” *IEEE Trans Magn*, vol. 41, no. 10, pp. 3409–3411, 2005, doi: 10.1109/TMAG.2005.855214.
- [135] S. Sun, X. Zhang, Y. Sun, S. Yang, X. Song, and Z. Yang, “Hierarchical CuO nanoflowers: Water-required synthesis and their application in a nonenzymatic glucose biosensor,” *Physical Chemistry Chemical Physics*, vol. 15, no. 26, pp. 10904–10913, 2013, doi: 10.1039/c3cp50922b.
- [136] D. Zhu, L. Wang, W. Yu, and H. Xie, “Intriguingly high thermal conductivity increment for CuO nanowires contained nanofluids with low viscosity,” *Sci Rep*, vol. 8, no. 1, pp. 1–12, 2018, doi: 10.1038/s41598-018-23174-z.
- [137] K. G. Chandrappa and T. V. Venkatesha, “Electrochemical bulk synthesis and characterisation of hexagonal-shaped CuO nanoparticles,” *J Exp Nanosci*, vol. 8, no. 4, pp. 516–532, 2013, doi: 10.1080/17458080.2011.597440.
- [138] X. Zhang *et al.*, “Nanoparticle-aggregated CuO nanoellipsoids for high-performance non-enzymatic glucose detection,” *J Mater Chem A Mater*, vol. 2, no. 26, pp. 10073–10080, 2014, doi: 10.1039/c4ta01005a.
- [139] X. Duan *et al.*, “3D hierarchical CuO mesocrystals from ionic liquid precursors: Towards better electrochemical performance for Li-ion batteries,” *J Mater Chem A Mater*, vol. 4, no. 21, pp. 8402–8411, 2016, doi: 10.1039/c5ta10173e.
- [140] H. Siddiqui, M. R. Parra, M. S. Qureshi, M. M. Malik, and F. Z. Haque, “Studies of structural, optical, and electrical properties associated with defects in sodium-doped copper oxide (CuO/Na) nanostructures,” *J Mater Sci*, vol. 53, no. 12, pp. 8826–8843, 2018, doi: 10.1007/s10853-018-2179-6.
- [141] Ç. Oruç and A. Altındal, “Structural and dielectric properties of CuO nanoparticles,” *Ceram Int*, vol. 43, no. 14, pp. 10708–10714, 2017, doi: 10.1016/j.ceramint.2017.05.006.
- [142] C. H. Tsai, P. H. Fei, C. M. Lin, and S. L. Shiu, “CuO and CuO/graphene nanostructured thin films as counter electrodes for Pt-free dye-sensitized solar cells,” *Coatings*, vol. 8, no. 1, p. 21, 2018, doi: 10.3390/coatings8010021.
- [143] M. Balık, V. Bulut, and I. Y. Erdogan, “Optical, structural and phase transition properties of Cu₂O, CuO and Cu₂O/CuO: Their photoelectrochemical sensor applications,” *Int J Hydrogen Energy*, vol. 44, no. 34, pp. 18744–18755, 2019, doi: 10.1016/j.ijhydene.2018.08.159.
- [144] J. Hong, J. Li, and Y. Ni, “Urchin-like CuO microspheres: Synthesis, characterization, and properties,” *J Alloys Compd*, vol. 481, no. 1–2, pp. 610–615, 2009, doi: 10.1016/j.jallcom.2009.03.043.

Bibliography

- [145] S. Bykkam, M. Ahmadipour, S. Narisngam, V. R. Kalagadda, and S. C. Chidurala, "Extensive Studies on X-Ray Diffraction of Green Synthesized Silver Nanoparticles," *Adv. Nanopart*, vol. 4, no. 1, pp. 1–10, 2015, doi: 10.4236/anp.2015.41001.
- [146] G. Sharma, J. S. Nam, A. R. Sharma, and S. S. Lee, "Antimicrobial potential of silver nanoparticles synthesized using medicinal herb coptidis rhizome," *Molecules*, vol. 23, no. 9, p. 2268, 2018, doi: 10.3390/molecules23092268.
- [147] M. Shahjahan, M. H. Rahman, S. M. Hossain, M. A. Khatun, A. Islam, and M. H. A. Begum, "Synthesis and Characterization of Silver Nanoparticles by Sol-Gel Technique," *Nanosci. Nanometrol*, vol. 3, no. 1, pp. 34–39, 2017, doi: 10.11648/j.nsnm.20170301.16.
- [148] A. Raj, R. Lawrence, K. Lawrence, N. Silas, M. Jaless, and R. Srivastava, "Green synthesis and characterization of Silver nanoparticles from leaf extracts of *Rosa indica* and its antibacterial activity against Human Pathogen Bacteria," *Oriental Journal of Chemistry*, vol. 34, no. 1, p. 326, 2018, doi: 10.31788/RJC.2018.1132009.
- [149] H. M. M. Ibrahim, "Green synthesis and characterization of silver nanoparticles using banana peel extract and their antimicrobial activity against representative microorganisms," *J Radiat Res Appl Sci*, vol. 8, no. 3, pp. 265–275, 2015, doi: 10.1016/j.jrras.2015.01.007.
- [150] M. Gomathi, P. V Rajkumar, A. Prakasam, and K. Ravichandran, "Green synthesis of silver nanoparticles using *Datura stramonium* leaf extract and assessment of their antibacterial activity," *Resource-Efficient Technologies*, vol. 3, no. 3, pp. 280–284, 2017, doi: 10.1016/j.refit.2016.12.005.
- [151] M. Diantoro *et al.*, "Modification of Electrical Properties of Silver Nanoparticle," *London: IntechOpen*, pp. 233–248, 2018.
- [152] K. Tahir *et al.*, "Visible light photo catalytic inactivation of bacteria and photo degradation of methylene blue with Ag / TiO₂ nanocomposite prepared by a novel method," *Journal of Photochemistry and Photobiology B: Biology*, vol. 162, pp. 189–198, 2016, doi: 10.1016/j.jphotobiol.2016.06.039.
- [153] M. Vanaja and G. Annadurai, "Coleus aromaticus leaf extract mediated synthesis of silver nanoparticles and its bactericidal activity," *Appl Nanosci*, vol. 3, no. 3, pp. 217–223, 2013, doi: 10.1007/s13204-012-0121-9.
- [154] K. Shameli *et al.*, "Green biosynthesis of silver nanoparticles using *Curcuma longa* tuber powder," *Int J Nanomedicine*, vol. 7, p. 5603, 2012, doi: 10.2147/IJN.S36786.
- [155] Y. X. Zhang, M. Huang, F. Li, and Z. Q. Wen, "Controlled Synthesis of Hierarchical CuO Nanostructures for Electrochemical Capacitor Electrodes," *Int. J. Electrochem. Sci*, vol. 8, no. 6, pp. 8645–8661, 2013.
- [156] M. Taran, M. Rad, and M. Alavi, "Antibacterial activity of copper oxide (CuO) nanoparticles biosynthesized by bacillus sp. FU4: Optimization of experiment design," *Pharmaceutical Sciences*, vol. 23, no. 3, pp. 198–206, 2017, doi: 10.15171/PS.2017.30.

Bibliography

- [157] P. K. Singh, P. Kumar, M. Hussain, A. K. Das, and G. C. Nayak, "Synthesis and characterization of CuO nanoparticles using strong base electrolyte through electrochemical discharge process," *Bulletin of Materials Science*, vol. 39, no. 2, pp. 469–478, 2016, doi: 10.1007/s12034-016-1159-1.
- [158] D. Saravanakumar *et al.*, "Synthesis and characterization of ZnO-CuO nanocomposites powder by modified perfume spray pyrolysis method and its antimicrobial investigation," *Journal of Semiconductors*, vol. 39, no. 3, p. 033001, 2018, doi: 10.1088/1674-4926/39/3/033001.
- [159] P. K. Raul *et al.*, "CuO nanorods: A potential and efficient adsorbent in water purification," *RSC Adv*, vol. 4, no. 76, pp. 40580–40587, 2014, doi: 10.1039/c4ra04619f.
- [160] B. B. B. A. Asha Radhakrishnan*, "Structural and Optical Absorption Analysis of CuO Nanoparticles," *Indian J. Adv. Chem. Sci*, vol. 2, no. 2, pp. 158–161, 2014.
- [161] V. Prakash, R. K. Diwan, and U. K. Niyogi, "Characterization of synthesized copper oxide nanopowders and their use in nanofluids for enhancement of thermal conductivity," *Indian Journal of Pure and Applied Physics (IJPAP)*, vol. 53, no. 11, pp. 753–758, 2015.
- [162] K. Phiwdang, S. Suphankij, W. Mekprasart, and W. Pecharapa, "Synthesis of CuO nanoparticles by precipitation method using different precursors," *Energy Procedia*, vol. 34, pp. 740–745, 2013, doi: 10.1016/j.egypro.2013.06.808.
- [163] A. Manjunath, M. Irfan, K. P. Anushree, K. M. Vinutha, and N. Yamunarani, "Synthesis and Characterization of CuO Nanoparticles and CuO Doped PVA Nanocomposites," *Advances in Materials Physics and Chemistry*, vol. 06, no. 10, p. 263, 2016, doi: 10.4236/ampc.2016.610026.
- [164] I. Z. Luna, L. N. Hilary, A. M. S. Chowdhury, M. A. Gafur, N. Khan, and R. A. Khan, "Preparation and Characterization of Copper Oxide Nanoparticles Synthesized via Chemical Precipitation Method," *Open Access Library Journal*, vol. 02, no. 03, p. 1, 2015, doi: 10.4236/oalib.1101409.
- [165] A. S. Ethiraj and D. J. Kang, "Synthesis and characterization of CuO nanowires by a simple wet chemical method," *Nanoscale Res Lett*, vol. 7, no. 1, pp. 1–5, 2012, doi: 10.1186/1556-276X-7-70.
- [166] I. Y. Erdoğan and Ö. Güllü, "Optical and structural properties of CuO nanofilm: Its diode application," *J Alloys Compd*, vol. 492, no. 1–2, pp. 378–383, 2010, doi: 10.1016/j.jallcom.2009.11.109.
- [167] A. El-Trass, H. Elshamy, I. El-Mehasseb, and M. El-Kemary, "CuO nanoparticles: Synthesis, characterization, optical properties and interaction with amino acids," *Appl Surf Sci*, vol. 258, no. 7, pp. 2997–3001, 2012, doi: 10.1016/j.apsusc.2011.11.025.
- [168] M. Elango, M. Deepa, R. Subramanian, and A. Mohamed Musthafa, "Synthesis, Characterization, and Antibacterial Activity of Polyindole/Ag-Cuo Nanocomposites

Bibliography

- by Reflux Condensation Method,” *Polymer - Plastics Technology and Engineering*, vol. 57, no. 14, pp. 1440–1451, 2018, doi: 10.1080/03602559.2017.1410832.
- [169] M. A. Dar, Y. S. Kim, W. B. Kim, J. M. Sohn, and H. S. Shin, “Structural and magnetic properties of CuO nanoneedles synthesized by hydrothermal method,” *Appl Surf Sci*, vol. 254, no. 22, pp. 7477–7481, 2008, doi: 10.1016/j.apsusc.2008.06.004.
- [170] D. Manyasree, K. M. Peddi, and R. Ravikumar, “CuO nanoparticles: Synthesis, characterization and their bactericidal efficacy,” *Int J Appl Pharmaceut*, vol. 9, no. 6, pp. 71–74, 2017, doi: 10.22159/ijap.2017v9i6.71757.
- [171] K. Murugan, B. Senthilkumar, D. Senbagam, and S. Al-Sohaibani, “Biosynthesis of silver nanoparticles using *Acacia leucophloea* extract and their antibacterial activity,” *Int J Nanomedicine*, vol. 9, p. 2431, 2014, doi: 10.2147/IJN.S61779.
- [172] W. W. Drzewiecka, D. Gaikwad, Swapnil Laskowski, H. Dahm, J. Niedojadło, A. Gade, and M. Rai, “Novel approach towards synthesis of silver nanoparticles from *Myxococcus virescens* and their lethality on pathogenic bacterial cells,” *Austin J Biotechnol Bioeng*, vol. 1, no. 1, p. 7, 2014.
- [173] M. A. Huq, “Green synthesis of silver nanoparticles using *pseudoduganella eburnea* MAHUQ-39 and their antimicrobial mechanisms investigation against drug resistant human pathogens,” *Int J Mol Sci*, vol. 21, no. 4, p. 1510, 2020, doi: 10.3390/ijms21041510.
- [174] K. Paulkumar, G. Gnanajobitha, M. Vanaja, M. Pavunraj, and G. Annadurai, “Green synthesis of silver nanoparticle and silver based chitosan bionanocomposite using stem extract of *Saccharum officinarum* and assessment of its antibacterial activity,” *Advances in Natural Sciences: Nanoscience and Nanotechnology*, vol. 8, no. 3, p. 035019, 2017, doi: 10.1088/2043-6254/aa7232.
- [175] K. Jyoti, M. Baunthiyal, and A. Singh, “Characterization of silver nanoparticles synthesized using *Urtica dioica* Linn. leaves and their synergistic effects with antibiotics,” *J Radiat Res Appl Sci*, vol. 9, no. 3, pp. 217–227, 2016, doi: 10.1016/j.jrras.2015.10.002.
- [176] X. H. Vu, T. T. T. Duong, T. T. H. Pham, D. K. Trinh, X. H. Nguyen, and V. S. Dang, “Synthesis and study of silver nanoparticles for antibacterial activity against *Escherichia coli* and *Staphylococcus aureus*,” *Advances in Natural Sciences: Nanoscience and Nanotechnology*, vol. 9, no. 2, p. 025019, 2018, doi: 10.1088/2043-6254/aac58f.
- [177] J. F. Xu *et al.*, “Raman spectra of CuO nanocrystals,” *Journal of Raman Spectroscopy*, vol. 30, no. 5, pp. 413–415, 1999, doi: 10.1002/(SICI)1097-4555(199905)30:5<413::AID-JRS387>3.0.CO;2-N.
- [178] T. H. Tran and V. T. Nguyen, “Copper Oxide Nanomaterials Prepared by Solution Methods, Some Properties, and Potential Applications: A Brief Review,” *Int Sch Res Notices*, vol. 2014, pp. 1–14, 2014, doi: 10.1155/2014/856592.

Bibliography

- [179] M. Rashad, M. Rüsing, G. Berth, K. Lischka, and A. Pawlis, “CuO and Co₃O₄ Nanoparticles: Synthesis, Characterizations, and Raman Spectroscopy,” vol. 2013, 2013, [Online]. Available: <http://journals.cambridge.org>
- [180] S. Dolai, S. N. Sarangi, S. Hussain, R. Bhar, and A. K. Pal, “Magnetic properties of nanocrystalline nickel incorporated CuO thin films,” *J Magn Magn Mater*, vol. 479, pp. 59–66, 2019, doi: 10.1016/j.jmmm.2019.02.005.
- [181] V. Cretu *et al.*, “Synthesis, characterization and DFT studies of zinc-doped copper oxide nanocrystals for gas sensing applications,” *J Mater Chem A Mater*, vol. 4, no. 17, pp. 6527–6539, 2016, doi: 10.1039/c6ta01355d.
- [182] K. Anandaraj, R. Ilakkiya, and N. Natarajan, “Synthesis of Zinc Oxide (ZnO), Silver (Ag), Copper Oxide (CuO) and Titanium Oxide (TiO₂) Nanoparticles,” *Int. J. Curr. Microbiol. App. Sci*, vol. 7, no. 11, pp. 1514–1521, 2018, doi: 10.20546/ijcmas.2018.711.174.
- [183] Á. de Jesús Ruíz-Baltazar, S. Y. Reyes-López, D. Larrañaga, M. Estévez, and R. Pérez, “Green synthesis of silver nanoparticles using a *Melissa officinalis* leaf extract with antibacterial properties,” *Results Phys*, vol. 7, pp. 2639–2643, 2017, doi: 10.1016/j.rinp.2017.07.044.
- [184] A. J. Kora and J. Arunachalam, “Green fabrication of silver nanoparticles by gum tragacanth (*astragalus gummifer*): A dual functional reductant and stabilizer,” *J Nanomater*, vol. 2012, 2012, doi: 10.1155/2012/869765.
- [185] G. Naja, P. Bouvrette, S. Hrapovic, and J. H. T. Luong, “Raman-based detection of bacteria using silver nanoparticles conjugated with antibodies,” *Analyst*, vol. 132, no. 7, pp. 679–686, 2007, doi: 10.1039/b701160a.
- [186] S. Singh, G. Singh, and A. Singla, “Experimental studies on heat transfer performance of double pipe heat exchanger with using baffles and nanofluids,” *Indian J Sci Technol*, vol. 9, no. 40, pp. 1–7, 2016, doi: 10.17485/ijst/2016/v9i40/101486.
- [187] P. S. Murthy and V. P. Venugopalan, “Antibiofilm Activity of Nano sized CuO,” *International conference on nanoscience, engineering and technology (ICONSET 2011)*, no. IEEE, pp. 580–583, 2011.
- [188] M. R. Joya, J. Barba-Ortega, and A. M. Raba, “Vibrational Raman modes and particle size analysis of cupric oxide with calcination temperature,” *Indian Journal of Pure and Applied Physics (IJPAP)*, vol. 57, no. 4, pp. 268–271, 2019.
- [189] R. Javed, A. Mohamed, B. Yücesan, E. Gürel, R. Kausar, and M. Zia, “CuO nanoparticles significantly influence in vitro culture, steviol glycosides, and antioxidant activities of *Stevia rebaudiana* Bertoni,” *Plant Cell, Tissue and Organ Culture (PCTOC)*, vol. 131, no. 3, pp. 611–620, 2017, doi: 10.1007/s11240-017-1312-6.
- [190] J. Fang and Y. Xuan, “Investigation of optical absorption and photothermal conversion characteristics of binary CuO/ZnO nanofluids,” *RSC Adv*, vol. 7, no. 88, pp. 56023–56033, 2017, doi: 10.1039/c7ra12022b.

Bibliography

- [191] A. A. Baqer *et al.*, “Copper oxide nanoparticles synthesized by a heat treatment approach with structural, morphological and optical characteristics,” *Journal of Materials Science: Materials in Electronics*, vol. 29, no. 2, pp. 1025–1033, 2018, doi: 10.1007/s10854-017-8002-3.
- [192] F. Benakashani, A. R. Allafchian, and S. A. H. Jalali, “Biosynthesis of silver nanoparticles using Capparis spinosa L. leaf extract and their antibacterial activity,” *Karbala International Journal of Modern Science*, vol. 2, no. 4, pp. 251–258, 2016, doi: 10.1016/j.kijoms.2016.08.004.
- [193] O. V Mikhailov and E. O. Mikhailova, “Elemental silver nanoparticles: Biosynthesis and bio applications,” *Materials*, vol. 12, no. 19, p. 3177, 2019. doi: 10.3390/ma12193177.
- [194] S. F. A. Z. Yusoff, C. S. Lim, S. R. Azzuhri, H. Ahmad, and R. Zakaria, “Studies of Ag/TiO₂ plasmonics structures integrated in side polished optical fiber used as humidity sensor,” *Results Phys*, vol. 10, pp. 308–316, 2018, doi: 10.1016/j.rinp.2018.06.008.
- [195] R. K. Sendi and S. Mahmud, “Particle size and annealing ambient effect on properties of ZnO-Bi₂O₃-Mn₂O₃ varistor derived from ZnO micro- and nanoparticle powders,” *Superlattices Microstruct*, vol. 69, pp. 212–225, 2014, doi: 10.1016/j.spmi.2014.02.012.
- [196] F. Kharchouche, S. Belkhiat, and D. E. C. Belkhiat, “Non-linear coefficient of BaTiO₃-doped ZnO varistor,” *IET Science, Measurement and Technology*, vol. 7, no. 6, pp. 326–333, 2013, doi: 10.1049/iet-smt.2012.0022.
- [197] C. W. Nahm, “Microstructure and varistor properties of ZnO-V₂O₅-MnO₂-based ceramics,” *J Mater Sci*, vol. 42, no. 19, pp. 8370–8373, 2007, doi: 10.1007/s10853-007-1955-5.
- [198] G. Z. Zang, J. F. Wang, H. C. Chen, W. B. Su, C. M. Wang, and P. Qi, “Nonlinear electrical behaviour of the WO₃-based system,” *J Mater Sci*, vol. 39, no. 13, pp. 4373–4374, 2004, doi: 10.1023/B:JMSC.0000033430.73951.68.
- [199] V. Bansal, H. Bhandari, M. C. Bansal, and S. K. Dhawan, “Electrical and optical properties of poly(aniline-co-8-anilino-1-naphthalene sulphonic acid) -A material for ESD applications,” *Indian Journal of Pure & Applied Physics*, vol. 47, pp. 667–675, 2009.
- [200] C. Basavaraja, R. Pierson, D. S. Huh, A. Venkataraman, and S. Basavaraja, “Studies on properties of polyaniline-dodecylbenzene sulfonic acid composite films synthesized using different oxidants,” *Macromol Res*, vol. 17, no. 8, pp. 609–615, 2009, doi: 10.1007/BF03218917.
- [201] S. Gahlot, H. Gupta, P. K. Jha, and V. Kulshrestha, “Enhanced Electrochemical Performance of Stable SPES/SPANI Composite Polymer Electrolyte Membranes by Enriched Ionic Nanochannels,” *ACS Omega*, vol. 2, no. 9, pp. 5831–5839, 2017, doi: 10.1021/acsomega.7b00687.

Bibliography

- [202] H. Gholami, A. Shakeri, and V. Saadattalab, "Investigation of physical and mechanical properties of polyaniline/MMT nanocomposites," *Current Chemistry Letters*, vol. 6, no. 4, pp. 151–158, 2017, doi: 10.5267/j.ccl.2017.6.004.
- [203] V. Saadattalab, A. Shakeri, and H. Gholami, "Effect of CNTs and nano ZnO on physical and mechanical properties of polyaniline composites applicable in energy devices," *Progress in Natural Science: Materials International*, vol. 26, no. 6, pp. 517–522, 2016, doi: 10.1016/j.pnsc.2016.09.005.
- [204] T. S. Aldeen, H. E. A. Mohamed, and M. Maaza, "Bio-inspired Single Phase Monteponite CdO Nanoparticles via Natural Extract of Phoenix roebelenii Palm Leaves," *J Inorg Organomet Polym Mater*, vol. 30, no. 11, pp. 4691–4701, 2020, doi: 10.1007/s10904-020-01600-y.
- [205] S. Gowri, K. Gopinath, and A. Arumugam, "Experimental and computational assessment of mycosynthesized CdO nanoparticles towards biomedical applications," *J Photochem Photobiol B*, vol. 180, pp. 166–174, 2018, doi: 10.1016/j.jphotobiol.2018.02.009.
- [206] D. J. Jeejamol, A. M. E. Raj, K. Jayakumari, and C. Ravidhas, "CdO Nanoparticles : Facile Synthesis and Influence of Particle Size on Photocatalytic Degradation of Methylene Blue," *IOSR J. Appl. Phys.*, vol. 9, no. 5, pp. 66–73, 2017, doi: 10.9790/4861-0905016673.
- [207] D. Pathania, Sarita, P. Singh, and S. Pathania, "Preparation and characterization of nanoscale cadmium oxide using bovine serum albumin as green capping agent and its photocatalytic activity," *Desalination Water Treat*, vol. 52, no. 19–21, pp. 3497–3503, 2014, doi: 10.1080/19443994.2013.803342.
- [208] A. Tadjarodi, M. Imani, and H. Kerdari, "Application of a facile solid-state process to synthesize the CdO spherical nanoparticles," *Int Nano Lett*, vol. 3, no. 1, pp. 1–6, 2013, doi: 10.1186/2228-5326-3-43.
- [209] D. M. Yufanyi, J. F. Tendo, A. M. Ondoh, and J. K. Mbadcam, "CdO Nanoparticles by Thermal Decomposition of a Cadmium- Hexamethylenetetramine Complex," *Journal of Materials Science Research*, vol. 3, no. 3, p. 1, 2014, doi: 10.5539/jmsr.v3n3p1.
- [210] D. K. Bandgar, G. D. Khuspe, R. C. Pawar, C. S. Lee, and V. B. Patil, "Facile and novel route for preparation of nanostructured polyaniline (PANi) thin films," *Appl Nanosci*, vol. 4, no. 1, pp. 27–36, 2014, doi: 10.1007/s13204-012-0175-8.
- [211] S. M. Ambalagi, M. Devendrappa, S. Nagaraja, and B. Sannakki, "Dielectric Properties of PANI/CuO Nanocomposites," *IOP Conf Ser Mater Sci Eng*, vol. 310, no. 1. IOP Publishing, p. 012081, 2018, doi: 10.1088/1757-899X/310/1/012081.
- [212] A. Mehto, V. R. Mehto, J. Chauhan, S. IB, and P. RK, "Preparation and Characterization of Polyaniline/ZnO Composite Sensor," *J. Nanomed. Res*, vol. 5, p. 00104, 2017, doi: 10.15406/jnmr.2017.05.00104.
- [213] A. Mostafaei and A. Zolriasatein, "Synthesis and characterization of conducting polyaniline nanocomposites containing ZnO nanorods," *Progress in Natural Science:*

Bibliography

- Materials International*, vol. 22, no. 4, pp. 273–280, 2012, doi: 10.1016/j.pnsc.2012.07.002.
- [214] M. Fuseini, A. H. El-Shazly, and M. Elkady, “Effects of doping on zeta potential and pH of polyaniline colloidal suspension,” *Materials Science Forum*, vol. 1008, no. Trans Tech Publications Ltd, pp. 114–120, 2020, doi: 10.4028/www.scientific.net/MSF.1008.114.
- [215] K. C. Sajjan, M. Faisal, K. B. S, and S. Khasim, “Electrical Conductivity, Dielectric Behavior and Humidity Sensing Properties of Polyaniline-Graphite Oxide Composites,” *International Journal of Electrical and Electronics Engineering (IJEEE)*, vol. 2, pp. 67–76, 2013.
- [216] S. Bhadra and D. Khastgir, “Determination of crystal structure of polyaniline and substituted polyanilines through powder X-ray diffraction analysis,” *Polym Test*, vol. 27, no. 7, pp. 851–857, 2008, doi: 10.1016/j.polymertesting.2008.07.002.
- [217] Z. Hu *et al.*, “High specific capacitance of polyaniline/mesoporous manganese dioxide composite using KI-H₂SO₄ electrolyte,” *Polymers (Basel)*, vol. 7, no. 10, pp. 1939–1953, 2015, doi: 10.3390/polym7101491.
- [218] B. Sydulu Singu, P. Srinivasan, and S. Pabba, “Benzoyl peroxide oxidation route to nano form polyaniline salt containing dual dopants for pseudocapacitor,” *J Electrochem Soc*, vol. 159, no. 1, p. A6, 2011, doi: 10.1149/2.036201jes.
- [219] S. B. Kondawar, M. D. Deshpande, and S. P. Agrawal, “Transport Properties of Conductive Polyaniline Nanocomposites Based on Carbon Nanotubes,” *Int. J. Compos. Mater*, vol. 2, no. 3, pp. 32–36, 2012, doi: 10.5923/j.cmaterials.20120203.03.
- [220] M. Khan, T. Anwer, and F. Mohammad, “Sulphonated polyaniline/MWCNTs nanocomposite: preparation and promising thermoelectric performance,” *Int Nano Lett*, vol. 8, no. 3, pp. 213–220, 2018, doi: 10.1007/s40089-018-0246-2.
- [221] A. Kumar, L. K. Jangir, Y. Kumari, M. Kumar, V. Kumar, and K. Awasthi, “Optical and structural study of polyaniline/polystyrene composite films,” *Macromol Symp*, vol. 357, no. 1, pp. 229–234, 2015, doi: 10.1002/masy.201500039.
- [222] S. Padmapriya, S. Harinipriya, K. Jaidev, V. Sudha, D. Kumar, and S. Pal, “Storage and evolution of hydrogen in acidic medium by polyaniline,” *Int J Energy Res*, vol. 42, no. 3, pp. 1196–1209, 2018, doi: 10.1002/er.3920.
- [223] K. Anandhan and R. Thilak Kumar, “Synthesis, FTIR, UV-Vis and Photoluminescence characterizations of triethanolamine passivated CdO nanostructures,” *Spectrochim Acta A Mol Biomol Spectrosc*, vol. 149, pp. 476–480, 2015, doi: 10.1016/j.saa.2015.04.035.
- [224] C. Aydin, H. M. El-Nasser, F. Yakuphanoglu, I. S. Yahia, and M. Aksoy, “Nanopowder synthesis of aluminum doped cadmium oxide via sol-gel calcination processing,” *J Alloys Compd*, vol. 509, no. 3, pp. 854–858, 2011, doi: 10.1016/j.jallcom.2010.09.111.

Bibliography

- [225] M. Benhaliliba *et al.*, “Luminescence and physical properties of copper doped CdO derived nanostructures,” *J Lumin*, vol. 132, no. 10, pp. 2653–2658, 2012, doi: 10.1016/j.jlumin.2012.03.044.
- [226] P. Sakthivel *et al.*, “Radio frequency power induced changes of structural, morphological, optical and electrical properties of sputtered cadmium oxide thin films,” *Thin Solid Films*, vol. 654, pp. 85–92, 2018, doi: 10.1016/j.tsf.2018.04.004.
- [227] H. Chen, L. Sun, G. D. Li, and X. Zou, “Well-Tuned Surface Oxygen Chemistry of Cation Off-Stoichiometric Spinel Oxides for Highly Selective and Sensitive Formaldehyde Detection,” *Chemistry of Materials*, vol. 30, no. 6, pp. 2018–2027, 2018, doi: 10.1021/acs.chemmater.7b05251.
- [228] T. Prakash *et al.*, “Evaluation of structural, morphological and optical properties of CdO nanostructures,” *Ceram Int*, vol. 48, no. 1, pp. 1223–1229, 2022, doi: 10.1016/j.ceramint.2021.09.207.
- [229] B. Goswami and A. Choudhury, “Enhanced visible luminescence and modification in morphological properties of cadmium oxide nanoparticles induced by annealing,” *J Exp Nanosci*, vol. 10, no. 12, pp. 900–910, 2015, doi: 10.1080/17458080.2014.933492.
- [230] P. Sakthivel, S. Asaithambi, M. Karuppaiah, S. Sheikfareed, R. Yuvakkumar, and G. Ravi, “Different rare earth (Sm, La, Nd) doped magnetron sputtered CdO thin films for optoelectronic applications,” *Journal of Materials Science: Materials in Electronics*, vol. 30, no. 10, pp. 9999–10012, 2019, doi: 10.1007/s10854-019-01342-9.
- [231] K. Sankarasubramanian, P. Soundarrajan, T. Logu, K. Sethuraman, and K. Ramamurthi, “Enhancing resistive-type hydrogen gas sensing properties of cadmium oxide thin films by copper doping,” *New Journal of Chemistry*, vol. 42, no. 2, pp. 1457–1466, 2018, doi: 10.1039/c7nj03095a.
- [232] R. A. Ismail, A. M. E. Al-Samarai, S. J. Mohamed, and H. H. Ahmed, “Characteristics of nanostructured CdO/Si heterojunction photodetector synthesized by CBD,” *Solid State Electron*, vol. 82, pp. 115–121, 2013, doi: 10.1016/j.sse.2013.02.035.
- [233] K. Kaviyarasu, E. Manikandan, P. Paulraj, S. B. Mohamed, and J. Kennedy, “One dimensional well-aligned CdO nanocrystal by solvothermal method,” *J Alloys Compd*, vol. 593, pp. 67–70, 2014, doi: 10.1016/j.jallcom.2014.01.071.
- [234] G. Somasundaram, J. Rajan, P. Sangaiya, and R. Dilip, “Hydrothermal synthesis of CdO nanoparticles for photocatalytic and antimicrobial activities,” *Results in Materials*, vol. 4, p. 100044, 2019, doi: 10.1016/j.rinma.2019.100044.
- [235] S. Reddy, B. E. Kumara Swamy, U. Chandra, B. S. Sherigara, and H. Jayadevappa, “Synthesis of CdO nanoparticles and their modified carbon paste electrode for determination of dopamine and ascorbic acid by using cyclic voltammetry technique,” *Int. J. Electrochem. Sci*, vol. 5, pp. 10–17, 2010.
- [236] S. Kumar, B. Ahmed, A. K. Ojha, J. Das, and A. Kumar, “Facile synthesis of CdO nanorods and exploiting its properties towards supercapacitor electrode materials and

Bibliography

- low power UV irradiation driven photocatalysis against methylene blue dye,” *Mater Res Bull*, vol. 90, pp. 224–231, 2017, doi: 10.1016/j.materresbull.2017.02.044.
- [237] W. Xia, Y. Liu, J. Li, and C. Chen, “Investigation of CdO hexagonal nanoflakes synthesized by a hydrothermal method for liquefied petroleum gas detection,” *Analytical Methods*, vol. 8, no. 33, pp. 6265–6269, 2016, doi: 10.1039/c6ay01914e.
- [238] A. S. Aldwayyan *et al.*, “Synthesis and characterization of CdO nanoparticles starting from organometallic dmphen-CdI₂ complex,” *Int. J. Electrochem. Sci*, vol. 8, no. 8, pp. 10506–10514, 2013.
- [239] A. Yelil Arasi, J. Juliet Latha Jeyakumari, B. Sundaresan, V. Dhanalakshmi, and R. Anbarasan, “The structural properties of Poly(aniline)-Analysis via FTIR spectroscopy,” *Spectrochim Acta A Mol Biomol Spectrosc*, vol. 74, no. 5, pp. 1229–1234, 2009, doi: 10.1016/j.saa.2009.09.042.
- [240] M. B. Wasu and A. R. Raut, “Spectral and electrical investigation of polyaniline based conductive polymers,” *Int. J. Chem. Sci*, vol. 13, no. 3, pp. 1285–1294, 2015.
- [241] S. Senthilkumar and A. Rajendran, “Synthesis, Characterization and Electrical Properties of Nano Metal and Metal-Oxide Doped with Conducting Polymer Composites by in-Situ Chemical Polymerization,” *MOJ Poly. Sci.*, vol. 1, p. 31, 2017, doi: 10.15406/mojps.2017.01.00031.
- [242] M. M. Rahman Khan, Y. K. Wee, and W. A. K. Mahmood, “Effects of CuO on the morphology and conducting properties of PANI nanofibers,” *Synth Met*, vol. 162, no. 13–14, pp. 1065–1072, 2012, doi: 10.1016/j.synthmet.2012.05.009.
- [243] G. Rahman, M. U. Rahman, and Z. Najaf, “In situ Synthesis of PANI/CuO Nanocomposites for Non-Enzymatic Electrochemical Glucose Sensing,” *Applied Chemical Engineering*, vol. 3, no. 2, pp. 9–17, 2020, doi: 10.24294/ace.v2i2.645.
- [244] P. C. Maity and M. Khandelwal, “Synthesis time and temperature effect on polyaniline morphology and conductivity,” *Am. J. Mater. Synth. Process*, vol. 1, pp. 37–42, 2016, doi: 10.11648/j.ajmsp.20160104.11.
- [245] G. Liao, “Green Preparation of Sulfonated Polystyrene/Polyaniline/Silver Composites with Enhanced Anticorrosive Properties,” *Int J Chem*, vol. 10, no. 1, pp. 81–86, 2018, doi: 10.5539/ijc.v10n1p81.
- [246] A. John, S. K. Mahadeva, and J. Kim, “The preparation, characterization and actuation behavior of polyaniline and cellulose blended electro-active paper,” *Smart Mater Struct*, vol. 19, no. 4, p. 045011, 2010, doi: 10.1088/0964-1726/19/4/045011.
- [247] A. N. J. Al-Daghman, “Optical Characteristics of Conductive Polymer Polyaniline PANI-EB,” *Int. J. Res. Appl. Sci. Eng. Technol*, vol. 6, pp. 1555–1560, 2018, doi: 10.22214/ijraset.2018.6227.
- [248] U. M. Chougale, J. V. Thombare, V. J. Fulari, and A. B. Kadam, “Synthesis of polyaniline nanofibres by SILAR method for supercapacitor application,” *2013 International Conference on Energy Efficient Technologies for Sustainability*, no. IEEE, pp. 1078–1083, 2013, doi: 10.1109/ICEETS.2013.6533537.

Bibliography

- [249] I. Chakraborty, N. Chakrabarty, A. Senapati, and A. K. Chakraborty, "CuO@NiO/Polyaniline/MWCNT Nanocomposite as High-Performance Electrode for Supercapacitor," *Journal of Physical Chemistry C*, vol. 122, no. 48, pp. 27180–27190, 2018, doi: 10.1021/acs.jpcc.8b08091.
- [250] B. Butoi, A. Groza, P. Dinca, A. Balan, and V. Barna, "Morphological and structural analysis of polyaniline and poly(o-anisidine) layers generated in a DC glow discharge plasma by using an oblique angle electrode deposition configuration," *Polymers (Basel)*, vol. 9, no. 12, p. 732, 2017, doi: 10.3390/polym9120732.
- [251] A. N. Begum, N. Dhachanamoorthi, M. E. R. Saravanan, P. Jayamurugan, D. Manoharan, and V. Ponnuswamy, "Influence of annealing effects on polyaniline for good microstructural modification," *Optik (Stuttg)*, vol. 124, no. 3, pp. 238–242, 2013, doi: 10.1016/j.ijleo.2011.11.096.
- [252] R. Tripathi, A. Dutta, S. Das, A. Kumar, and T. P. Sinha, "Dielectric relaxation of CdO nanoparticles," *Appl Nanosci*, vol. 6, no. 2, pp. 175–181, 2016, doi: 10.1007/s13204-015-0427-5.
- [253] K. Sirohi, S. Kumar, V. Singh, and A. Vohra, "Synthesis and characterization of CdO-SnO₂ nanocomposites prepared by hydrothermal method," *Acta Metallurgica Sinica (English Letters)*, vol. 31, no. 3, pp. 254–262, 2018, doi: 10.1007/s40195-017-0659-3.
- [254] S. Sagadevan *et al.*, "Facile fabrication of Au-loaded CdO nanoconstructs with tuned properties for photocatalytic and biomedical applications," *J Nanostructure Chem*, vol. 11, no. 4, pp. 561–572, 2021, doi: 10.1007/s40097-020-00384-4.
- [255] T. Prakash, T. Arunkumar, D. S. Raj, and R. Jayaprakash, "Surfactant-aided variation in CdO nanocomposites morphology," *Phys Procedia*, vol. 49, pp. 36–43, 2013, doi: 10.1016/j.phpro.2013.10.008.
- [256] R. Nallendran, G. Selvan, and A. R. Balu, "CdO-Fe₃O₄ nanocomposite with enhanced magnetic and photocatalytic properties," *Mater. Sci. Poland*, vol. 37, pp. 100–107, 2019, doi: 10.2478/msp-2019-0012.
- [257] E. Mosquera, I. Del Pozo, and M. Morel, "Structure and red shift of optical band gap in CdO-ZnO nanocomposite synthesized by the sol gel method," *J Solid State Chem*, vol. 206, pp. 265–271, 2013, doi: 10.1016/j.jssc.2013.08.025.
- [258] C. Maria Magdalane, K. Kaviyarasu, J. Judith Vijaya, C. Jayakumar, M. Maaza, and B. Jeyaraj, "Photocatalytic degradation effect of malachite green and catalytic hydrogenation by UV-illuminated CeO₂/CdO multilayered nanoplatelet arrays: Investigation of antifungal and antimicrobial activities," *J Photochem Photobiol B*, vol. 169, pp. 110–123, 2017, doi: 10.1016/j.jphotobiol.2017.03.008.
- [259] R. P. Lefojane *et al.*, "CdO/CdCO₃ nanocomposite physical properties and cytotoxicity against selected breast cancer cell lines," *Sci Rep*, vol. 11, no. 1, pp. 1–11, 2021, doi: 10.1038/s41598-020-78720-5.

Bibliography

- [260] A. A. Kaya and K. Erturk, "Structural, spectral and optical properties of rocksalt Al,Mn-doped CdO: experimental and DFT studies," *Eur Phys J B*, vol. 92, no. 6, pp. 1–6, 2019, doi: 10.1140/epjb/e2019-90415-5.
- [261] K. Giribabu, R. Suresh, L. Vijayalakshmi, A. Stephen, and V. Narayanan, "Synthesis of cadmium oxide and its electrochemical detection of pollutants," *Adv Mat Res*, vol. 678, no. Trans Tech Publications Ltd, pp. 369–372, 2013, doi: 10.4028/www.scientific.net/AMR.678.369.
- [262] S. Balamurugan *et al.*, "Synthesis of CdO nanopowders by a simple soft chemical method and evaluation of their antimicrobial activities," *Pacific Science Review A: Natural Science and Engineering*, vol. 18, no. 3, pp. 228–232, 2016, doi: 10.1016/j.psra.2016.10.003.
- [263] K. J. Arun, A. K. Batra, A. Krishna, K. Bhat, M. D. Aggarwal, and P. J. Joseph Francis, "Surfactant Free Hydrothermal Synthesis of Copper Oxide Nanoparticles," *American Journal of Materials Science*, vol. 5, no. 3A, pp. 36–38, 2015, doi: 10.5923/s.materials.201502.06.
- [264] H. S. Abdullah, "Electrochemical polymerization and Raman study of polypyrrole and polyaniline thin films," *International Journal of Physical Sciences*, vol. 7, no. 38, pp. 5468–5476, 2012, doi: 10.5897/IJPS12.529.
- [265] D. Yoo, J. J. Lee, C. Park, H. H. Choi, and J. H. Kim, "N-type organic thermoelectric materials based on polyaniline doped with the aprotic ionic liquid 1-ethyl-3-methylimidazolium ethyl sulfate," *RSC Adv*, vol. 6, no. 43, pp. 37130–37135, 2016, doi: 10.1039/c6ra02334g.
- [266] L. Wang, Q. Yao, H. Bi, F. Huang, Q. Wang, and L. Chen, "PANI/graphene nanocomposite films with high thermoelectric properties by enhanced molecular ordering," *J Mater Chem A Mater*, vol. 3, no. 13, pp. 7086–7092, 2015, doi: 10.1039/c4ta06422d.
- [267] S. Tanwar and J. A. A. Ho, "Green synthesis of novel polyaniline nanofibers: Application in pH sensing," *Molecules*, vol. 20, no. 10, pp. 18585–18596, 2015, doi: 10.3390/molecules201018585.
- [268] N. M. Soudagar, V. K. Pandit, R. B. Pujari, K. B. Chorghade, C. D. Lokhande, and S. S. Joshi, "Chemically Synthesized Polyaniline Supercapacitor," *J. Eng. Res. Technol*, vol. 10, no. 1, 2017.
- [269] G. Shi, J. Chen, C. Ni, L. Zhang, D. Wang, and Y. Li, "Enhanced photoactivities of ternary composite coating by antireflection and double P–N heterojunctions," *J Mater Sci*, vol. 52, no. 4, pp. 1981–1987, 2017, doi: 10.1007/s10853-016-0486-3.
- [270] M. A. C. Mazzeu, L. K. Faria, A. de M. Cardoso, A. M. Gama, M. R. Baldan, and E. S. Gonçalves, "Structural and morphological characteristics of polyaniline synthesized in pilot scale," *Journal of Aerospace Technology and Management*, vol. 9, pp. 39–47, 2017, doi: 10.5028/jatm.v9i1.726.

Bibliography

- [271] E. Elanthamilan, A. Sathiyar, S. Rajkumar, E. J. Sheryl, and J. P. Merlin, “Polyaniline based charcoal/Ni nanocomposite material for high performance supercapacitors,” *Sustain Energy Fuels*, vol. 2, no. 4, pp. 811–819, 2018, doi: 10.1039/c7se00490g.
- [272] L. Dennany, P. C. Innis, S. T. McGovern, G. G. Wallace, and R. J. Forster, “Electronic interactions within composites of polyanilines formed under acidic and alkaline conditions. Conductivity, ESR, Raman, UV-vis and fluorescence studies,” *Physical Chemistry Chemical Physics*, vol. 13, no. 8, pp. 3303–3310, 2011, doi: 10.1039/c0cp00699h.
- [273] P. Velusamy *et al.*, “Characterization of spray pyrolytically deposited high mobility praseodymium doped CdO thin films,” *Ceram Int*, vol. 42, no. 11, pp. 12675–12685, 2016, doi: 10.1016/j.ceramint.2016.05.017.
- [274] V. Srihari *et al.*, “Raman scattering of cadmium oxide: In B1 phase,” *AIP Conf Proc*, vol. 1349, no. 1. American Institute of Physics, pp. 845–846, 2011, doi: 10.1063/1.3606122.
- [275] R. Oliva, J. Ibáñez, L. Artús, R. Cuscó, J. Zúñiga-Pérez, and V. Muñoz-Sanjosé, “High-pressure Raman scattering of CdO thin films grown by metal-organic vapor phase epitaxy,” *J Appl Phys*, vol. 113, no. 5, p. 053514, 2013, doi: 10.1063/1.4790383.
- [276] S. Kumar and A. K. Ojha, “Synthesis, characterizations and antimicrobial activities of well dispersed ultra-long CdO nanowires,” *AIP Adv*, vol. 3, no. 5, p. 052109, 2013, doi: 10.1063/1.4804930.
- [277] V. Ganesh *et al.*, “Detailed investigation of optical linearity and nonlinearity of nanostructured Ce-doped CdO thin films using Kramers–Kronig relations,” *Applied Physics A*, vol. 126, no. 7, pp. 1–9, 2020, doi: 10.1007/s00339-020-03727-8.
- [278] R. Cuscó, J. Ibáñez, N. Domenech-Amador, L. Artús, J. Zúñiga-Pérez, and V. Muñoz-Sanjosé, “Raman scattering of cadmium oxide epilayers grown by metal-organic vapor phase epitaxy,” *J Appl Phys*, vol. 107, no. 6, p. 063519, 2010, doi: 10.1063/1.3357377.
- [279] S. G. Choi *et al.*, “Temperature-dependent optical properties of epitaxial CdO thin films determined by spectroscopic ellipsometry and Raman scattering,” *J Appl Phys*, vol. 113, no. 18, p. 183515, 2013, doi: 10.1063/1.4803876.
- [280] Y. Mo, W. Meng, Y. Xia, and X. Du, “Redox-active gel electrolyte combined with branched polyaniline nanofibers doped with ferrous ions for ultra-high-performance flexible supercapacitors,” *Polymers (Basel)*, vol. 11, no. 8, p. 1357, 2019, doi: 10.3390/polym11081357.
- [281] V. K. Shukla, P. Yadav, R. S. Yadav, P. Mishra, and A. C. Pandey, “A new class of PANI-Ag core-shell nanorods with sensing dimensions,” *Nanoscale*, vol. 4, no. 13, pp. 3886–3893, 2012, doi: 10.1039/c2nr30963g.
- [282] A. Abdolahi, E. Hamzah, Z. Ibrahim, and S. Hashim, “Synthesis of uniform polyaniline nanofibers through interfacial polymerization,” *Materials*, vol. 5, no. 8, pp. 1487–1494, 2012, doi: 10.3390/ma5081487.

Bibliography

- [283] S. Sivakumar, A. Venkatesan, P. Soundhirarajan, and C. P. Khatiwada, "Synthesis, characterizations and anti-bacterial activities of pure and Ag doped CdO nanoparticles by chemical precipitation method," *Spectrochim Acta A Mol Biomol Spectrosc*, vol. 136, pp. 1751–1759, 2015, doi: 10.1016/j.saa.2014.10.078.
- [284] V. Revathi and K. Karthik, "Microwave assisted CdO–ZnO–MgO nanocomposite and its photocatalytic and antibacterial studies," *Journal of Materials Science: Materials in Electronics*, vol. 29, no. 21, pp. 18519–18530, 2018, doi: 10.1007/s10854-018-9968-1.
- [285] M. Z. A. Warshagha and M. Muneer, "Facile synthesis of CdO-ZnO heterojunction photocatalyst for rapid removal of organic contaminants from water using visible light," *Environ Nanotechnol Monit Manag*, vol. 18, p. 100728, 2022, doi: 10.1016/j.enmm.2022.100728.
- [286] N. Manjula, A. R. Balu, K. Usharani, N. Raja, and V. S. Nagarethinam, "Enhancement in some physical properties of spray deposited CdO:Mn thin films through Zn doping towards optoelectronic applications," *Optik (Stuttg)*, vol. 127, no. 16, pp. 6400–6406, 2016, doi: 10.1016/j.ijleo.2016.04.129.
- [287] K. Karthik, S. Dhanuskodi, C. Gobinath, S. Prabukumar, and S. Sivaramakrishnan, "Multifunctional properties of CdO nanostructures Synthesised through microwave assisted hydrothermal method," *Materials Research Innovations*, vol. 23, no. 5, pp. 310–318, 2019, doi: 10.1080/14328917.2018.1475443.
- [288] A. Din *et al.*, "Cadmium oxide based efficient electrocatalyst for hydrogen peroxide sensing and water oxidation," *Journal of Materials Science: Materials in Electronics*, vol. 28, no. 1, pp. 1092–1100, 2017, doi: 10.1007/s10854-016-5633-8.
- [289] J. Santos-Cruz, G. Torres-Delgado, R. Castanedo-Perez, C. I. Zúñiga-Romero, and O. Zelaya-Angel, "Optical and electrical characterization of fluorine doped cadmium oxide thin films prepared by the sol-gel method," *Thin Solid Films*, vol. 515, no. 13, pp. 5381–5385, 2007, doi: 10.1016/j.tsf.2007.01.036.
- [290] N. M. Al-Hada *et al.*, "A facile thermal-treatment route to synthesize the semiconductor CdO nanoparticles and effect of calcination," *Mater Sci Semicond Process*, vol. 26, pp. 460–466, 2014, doi: 10.1016/j.mssp.2014.05.032.
- [291] J. V. Marques Zoccal, F. de Oliveira Arouca, and J. A. Silveira Goncalves, "Synthesis and characterization of TiO₂ nanoparticles by the pechini method.," *Materials Science Forum*, vol. 660, no. Trans Tech Publications Ltd, pp. 385–390, 2010.
- [292] C. Marinescu *et al.*, "DSC investigation of nanocrystalline TiO₂ powder," *J Therm Anal Calorim*, vol. 103, no. 1, pp. 49–57, 2011, doi: 10.1007/s10973-010-1072-6.
- [293] G. Li, L. Li, J. Boerio-Goates, and B. F. Woodfield, "High purity anatase TiO₂ nanocrystals: Near room-temperature synthesis, grain growth kinetics, and surface hydration chemistry," *J Am Chem Soc*, vol. 127, no. 24, pp. 8659–8666, 2005, doi: 10.1021/ja050517g.
- [294] M. M. Ba-abbad, A. A. H. Kadhum, A. B. Mohamad, and M. S. Takriff, "Synthesis and Catalytic Activity of TiO₂ Nanoparticles for Photochemical Oxidation of

Bibliography

- Concentrated Chlorophenols under Direct Solar Radiation,” *Int. J. Electrochem. Sci*, vol. 7, no. 6, pp. 4871–4888, 2012.
- [295] Alamgir, W. Khan, S. Ahmad, N. Ahammed, and A. H. Naqvi, “Thermal analysis and temperature dependent dielectric responses of Co doped anatase TiO₂ nanoparticles,” *American Institute of Physics Conference Series*, vol. 1661, no. 1, p. 080001, 2015, doi: 10.1063/1.4915392.
- [296] R. Trejo-Tzab, L. Caballero-Espada, P. Quintana, A. Ávila-Ortega, and R. A. Medina-Esquivel, “Controlled Phase Changes of Titania Using Nitrogen Plasma,” *Nanoscale Res Lett*, vol. 12, no. 1, pp. 1–8, 2017, doi: 10.1186/s11671-016-1821-y.
- [297] P. K. Khanna, N. Singh, and S. Charan, “Synthesis of nano-particles of anatase-TiO₂ and preparation of its optically transparent film in PVA,” *Mater Lett*, vol. 61, no. 25, pp. 4725–4730, 2007, doi: 10.1016/j.matlet.2007.03.064.
- [298] S. S. Al-taweel and H. R. Saud, “New route for synthesis of pure anatase TiO₂ nanoparticles via ultrasound- assisted sol-gel method,” *J. Chem. Pharm. Res*, vol. 8, no. 2, pp. 620–626, 2016.
- [299] P. K. Khanna, N. Singh, and S. Charan, “Synthesis of nano-particles of anatase-TiO₂ and preparation of its optically transparent film in PVA,” *Mater Lett*, vol. 61, no. 25, pp. 4725–4730, 2007, doi: 10.1016/j.matlet.2007.03.064.
- [300] L. Zhou, R. C. Hoffmann, Z. Zhao, J. Bill, and F. Aldinger, “Chemical bath deposition of thin TiO₂-anatase films for dielectric applications,” *Thin Solid Films*, vol. 516, no. 21, pp. 7661–7666, 2008, doi: 10.1016/j.tsf.2008.02.042.
- [301] H. Y. Hafeez, S. k. Lakhera, P. Karthik, M. Anpo, and B. Neppolian, “Facile construction of ternary CuFe₂O₄-TiO₂ nanocomposite supported reduced graphene oxide (rGO) photocatalysts for the efficient hydrogen production,” *Appl Surf Sci*, vol. 449, pp. 772–779, 2018, doi: 10.1016/j.apsusc.2018.01.282.
- [302] C. H. Ashok and K. Venkateswara Rao, “Synthesis of Nanostructured Metal Oxide by Microwave-Assisted Method and its Humidity Sensor Application,” *Mater Today Proc*, vol. 4, no. 2, pp. 3816–3824, 2017, doi: 10.1016/j.matpr.2017.02.279.
- [303] Y. Choi, S. Yamamoto, T. Umebayashi, and M. Yoshikawa, “Fabrication and characterization of anatase TiO₂ thin film on glass substrate grown by pulsed laser deposition,” *Solid State Ion*, vol. 172, no. 1–4, pp. 105–108, 2004, doi: 10.1016/j.ssi.2004.03.014.
- [304] S. Dzwigaj *et al.*, “DFT makes the morphologies of anatase-TiO₂ nanoparticles visible to IR spectroscopy,” *J Catal*, vol. 236, no. 2, pp. 245–250, 2005, doi: 10.1016/j.jcat.2005.09.034.
- [305] A. V. Murugan, V. Samuel, and V. Ravi, “Synthesis of nanocrystalline anatase TiO₂ by microwave hydrothermal method,” *Mater Lett*, vol. 60, no. 4, pp. 479–480, 2006, doi: 10.1016/j.matlet.2005.09.017.
- [306] H. Y. Hafeez *et al.*, “Construction of ternary hybrid layered reduced graphene oxide supported g-C₃N₄-TiO₂ nanocomposite and its photocatalytic hydrogen production

Bibliography

- activity,” *Int J Hydrogen Energy*, vol. 43, no. 8, pp. 3892–3904, 2018, doi: 10.1016/j.ijhydene.2017.09.048.
- [307] H. G. Yang and H. C. Zeng, “Preparation of hollow anatase TiO₂ nanospheres via Ostwald ripening,” *Journal of Physical Chemistry B*, vol. 108, no. 11, pp. 3492–3495, 2004, doi: 10.1021/jp0377782.
- [308] S. R. Dhage, V. D. Choube, V. Samuel, and V. Ravi, “Synthesis of nanocrystalline TiO₂ at 100 °C,” *Mater Lett*, vol. 58, no. 17–18, pp. 2310–2313, 2004, doi: 10.1016/j.matlet.2004.02.021.
- [309] Y. J. He, J. F. Peng, W. Chu, Y. Z. Li, and D. G. Tong, “Retraction: Black mesoporous anatase TiO₂ nanoleaves: A high capacity and high rate anode for aqueous Al-ion batteries,” *J Mater Chem A Mater*, vol. 7, no. 35, pp. 1721–1731, 2019, doi: 10.1039/c3ta13906a.
- [310] J. C. Yu, L. Zhang, and J. Yu, “Rapid synthesis of mesoporous TiO₂ with high photocatalytic activity by ultrasound-induced agglomeration,” *New Journal of Chemistry*, vol. 26, no. 4, pp. 416–420, 2002, doi: 10.1039/b109173e.
- [311] R. Vinoth, P. Karthik, K. Devan, B. Neppolian, and M. Ashokkumar, “TiO₂–NiO p–n nanocomposite with enhanced sonophotocatalytic activity under diffused sunlight,” *Ultrason Sonochem*, vol. 35, pp. 655–663, 2017, doi: 10.1016/j.ultrsonch.2016.03.005.
- [312] A. K. Tripathi, M. K. Singh, M. C. Mathpal, S. K. Mishra, and A. Agarwal, “Study of structural transformation in TiO₂ nanoparticles and its optical properties,” *J Alloys Compd*, vol. 549, pp. 114–120, 2013, doi: 10.1016/j.jallcom.2012.09.012.
- [313] Y. Ren, L. Zhao, Y. Zou, L. Song, N. Dong, and J. Wang, “Effects of different TiO₂ particle sizes on the microstructure and optical limiting properties of TiO₂/reduced graphene oxide nanocomposites,” *Nanomaterials*, vol. 9, no. 5, p. 730, 2019, doi: 10.3390/nano9050730.
- [314] S. K. Kansal, S. Sood, A. Umar, and S. K. Mehta, “Photocatalytic degradation of Eriochrome Black T dye using well-crystalline anatase TiO₂ nanoparticles,” *J Alloys Compd*, vol. 581, pp. 392–397, 2013, doi: 10.1016/j.jallcom.2013.07.069.
- [315] T. Kalaivani and P. Anilkumar, “Role of Temperature on the Phase Modification of TiO₂ Nanoparticles Synthesized by the Precipitation Method,” *Silicon*, vol. 10, no. 4, pp. 1679–1686, 2018, doi: 10.1007/s12633-017-9652-8.
- [316] S. Bagheri, K. Shameli, and S. B. Abd Hamid, “Synthesis and characterization of anatase titanium dioxide nanoparticles using egg white solution via Sol-Gel method,” *J Chem*, vol. 2013, 2013, doi: 10.1155/2013/848205.
- [317] N. Arabi, A. Kianvash, A. Hajalilou, and E. Abouzari-lotf, “A facile and green synthetic approach toward fabrication of Alcea- and Thyme-stabilized TiO₂ nanoparticles for photocatalytic applications,” *Arabian Journal of Chemistry*, vol. 13, no. 1, pp. 2132–2141, 2020, doi: 10.1016/j.arabjc.2018.03.014.

Bibliography

- [318] A. León *et al.*, “FTIR and raman characterization of TiO₂ nanoparticles coated with polyethylene glycol as carrier for 2-methoxyestradiol,” *Applied Sciences*, vol. 7, no. 1, p. 49, 2017, doi: 10.3390/app7010049.
- [319] A. Amalraj and A. Pius, “Photocatalytic degradation of monocrotophos and chlorpyrifos in aqueous solution using TiO₂ under UV radiation,” *Journal of Water Process Engineering*, vol. 7, pp. 94–101, 2015, doi: 10.1016/j.jwpe.2015.06.002.
- [320] U. Balachandran and N. G. Eror, “Raman spectra of titanium dioxide,” *J Solid State Chem*, vol. 42, no. 3, pp. 276–282, 1982, doi: 10.1016/0022-4596(82)90006-8.
- [321] T. Ohsaka, F. Izumi, and Y. Fujiki, “Raman spectrum of anatase, TiO₂,” *Journal of Raman Spectroscopy*, vol. 7, no. 6, pp. 321–324, 1978, doi: 10.1002/jrs.1250070606.
- [322] W. F. Zhang, M. S. Zhang, Z. Yin, and Q. Chen, “Photoluminescence in anatase titanium dioxide nanocrystals,” *Applied Physics B*, vol. 70, no. 2, pp. 261–265, 2000, doi: 10.1007/s003400050043.
- [323] L. Stagi, C. M. Carbonaro, R. Corpino, D. Chiriu, and P. C. Ricci, “Light induced TiO₂ phase transformation: Correlation with luminescent surface defects,” *Physica Status Solidi (b)*, vol. 252, no. 1, pp. 124–129, 2015, doi: 10.1002/pssb.201400080.
- [324] Kothaplamoottil. S. Saranya *et al.*, “Green synthesis of high temperature stable anatase titanium dioxide nanoparticles using gum kondagogu: Characterization and solar driven photocatalytic degradation of organic dye,” *Nanomaterials*, vol. 8, no. 12, p. 1002, 2018, doi: 10.3390/nano8121002.
- [325] M. J. Šćepanović, M. Grujić-Brojčin, Z. D. Dohčević-Mitrović, and Z. V. Popović, “Characterization of anatase TiO₂ nanopowder by variable-temperature raman spectroscopy,” *Science of Sintering*, vol. 41, no. 1, pp. 67–73, 2009, doi: 10.2298/SOS0901067S.
- [326] M. Grujić-Brojčin *et al.*, “Infrared study of laser synthesized anatase TiO₂ nanopowders,” *J Phys D Appl Phys*, vol. 38, no. 9, p. 1415, 2005, doi: 10.1088/0022-3727/38/9/014.
- [327] and S. S. Abdullah. Lokman, Muhammad Quisar, Suhaidi Shafie, Suraya Shaban, Fauzan Ahmad, Haslina Jaafar, Rizuan Mohd Rosnan, Hafizal Yahaya, “Enhancing Photocurrent Performance Based on Photoanode Thickness and Surface Plasmon Resonance Using Ag-TiO₂ Nanocomposites in Dye-Sensitized Solar Cells,” *Materials*, vol. 12, no. 13, p. 2111, 2019.
- [328] A. Sharma, R. K. Karn, and S. K. Pandiyan, “Synthesis of TiO₂ nanoparticles by sol-gel method and their characterization,” *J Basic Appl Eng Res*, vol. 1, no. 9, pp. 1–5, 2014.
- [329] T. Santhoshkumar *et al.*, “Green synthesis of titanium dioxide nanoparticles using Psidium guajava extract and its antibacterial and antioxidant properties,” *Asian Pac J Trop Med*, vol. 7, no. 12, pp. 968–976, 2014, doi: 10.1016/S1995-7645(14)60171-1.

Bibliography

- [330] H. A. J. L. Mourão, A. R. Malagutti, and C. Ribeiro, “Synthesis of TiO₂-coated CoFe₂O₄ photocatalysts applied to the photodegradation of atrazine and rhodamine B in water,” *Appl Catal A Gen*, vol. 382, no. 2, pp. 284–292, 2010, doi: 10.1016/j.apcata.2010.05.007.
- [331] M. M. Viana, V. F. Soares, and N. D. S. Mohallem, “Synthesis and characterization of TiO₂ nanoparticles,” *Ceram Int*, vol. 36, no. 7, pp. 2047–2053, 2010, doi: 10.1016/j.ceramint.2010.04.006.
- [332] C. Zhang, Y. Hu, W. Lu, M. Cao, and D. Zhou, “Influence of TiO₂/Sb₂O₃ ratio on ZnO varistor ceramics,” *J Eur Ceram Soc*, vol. 22, no. 1, pp. 61–65, 2002, doi: 10.1016/S0955-2219(01)00232-1.
- [333] J. Zhao, C. Zhang, C. Hu, and K. Lu, “Effect of thermal treatment on TiO₂ varistor properties in different atmospheres,” *J Eur Ceram Soc*, vol. 37, no. 10, pp. 3353–3359, 2017, doi: 10.1016/j.jeurceramsoc.2017.04.021.
- [334] R. I. Lavrov, A. I. Ivon, and I. M. Chernenko, “Comparative characteristics of silver and copper electrodes on ZnO varistor ceramics,” *J Eur Ceram Soc*, vol. 24, no. 9, pp. 2591–2595, 2004, doi: 10.1016/j.jeurceramsoc.2003.09.003.
- [335] S. Ahmed, M. Ahmad, B. L. Swami, and S. Ikram, “A review on plants extract mediated synthesis of silver nanoparticles for antimicrobial applications : A green expertise,” *J Adv Res*, vol. 7, no. 1, pp. 17–28, 2016, doi: 10.1016/j.jare.2015.02.007.
- [336] P. Van Dong, C. H. Ha, L. T. Binh, and J. Kasbohm, “Chemical synthesis and antibacterial activity of novel-shaped silver nanoparticles,” *Int Nano Lett*, vol. 2, no. 1, pp. 1–9, 2012, doi: 10.1186/2228-5326-2-9.
- [337] B. A. Aragaw, “Reduced graphene oxide-intercalated graphene oxide nano-hybrid for enhanced photoelectrochemical water reduction,” *J Nanostructure Chem*, vol. 10, no. 1, pp. 9–18, 2020, doi: 10.1007/s40097-019-00324-x.
- [338] P. Subramanyam, T. Khan, G. Neeraja Sinha, D. Suryakala, and C. Subrahmanyam, “Plasmonic Bi nanoparticle decorated BiVO₄/rGO as an efficient photoanode for photoelectrochemical water splitting,” *Int J Hydrogen Energy*, vol. 45, no. 13, pp. 7779–7787, 2020, doi: 10.1016/j.ijhydene.2019.08.214.
- [339] G. Jayalakshmi, K. Saravanan, J. Pradhan, P. Magudapathy, and B. K. Panigrahi, “Facile synthesis and enhanced luminescence behavior of ZnO:Reduced graphene oxide(rGO) hybrid nanostructures,” *J Lumin*, vol. 203, pp. 1–6, 2018, doi: 10.1016/j.jlumin.2018.06.023.
- [340] K. Sa *et al.*, “Effect of reduced graphene oxide-carbon nanotubes hybrid nanofillers in mechanical properties of polymer nanocomposites,” *IOP Conf Ser Mater Sci Eng*, vol. 338, no. 1, p. 012055, 2018, doi: 10.1088/1757-899X/338/1/012055.
- [341] B. Vellaichamy and P. Periakaruppan, “A facile, one-pot and eco-friendly synthesis of gold/silver nanobimetallics smartened rGO for enhanced catalytic reduction of hexavalent chromium,” *RSC Adv*, vol. 6, no. 62, pp. 57380–57388, 2016, doi: 10.1039/c6ra10544k.

Bibliography

- [342] Z. Wang *et al.*, “Humidity-sensing properties of urchinlike CuO nanostructures modified by reduced graphene oxide,” *ACS Appl Mater Interfaces*, vol. 6, no. 6, pp. 3888–3895, 2014, doi: 10.1021/am404858z.
- [343] C. Zhao, S. L. Chou, Y. Wang, C. Zhou, H. K. Liu, and S. X. Dou, “A facile route to synthesize transition metal oxide/reduced graphene oxide composites and their lithium storage performance,” *RSC Adv*, vol. 3, no. 37, pp. 16597–16603, 2013, doi: 10.1039/c3ra42044b.
- [344] P. Zheng, T. Liu, Y. Su, L. Zhang, and S. Guo, “TiO₂ nanotubes wrapped with reduced graphene oxide as a high-performance anode material for lithium-ion batteries,” *Sci Rep*, vol. 6, no. 1, pp. 1–8, 2016, doi: 10.1038/srep36580.
- [345] Y. Zheng, A. Wang, Z. Wang, L. Fu, and F. Peng, “Facial synthesis of carrageenan/reduced graphene oxide/Ag composite as efficient SERS platform,” *Materials Research*, vol. 20, pp. 15–20, 2016, doi: 10.1590/1980-5373-MR-2016-0287.
- [346] Y. Zhang, J. Liu, Y. Zhang, J. Liu, and Y. Duan, “Facile synthesis of hierarchical nanocomposites of aligned polyaniline nanorods on reduced graphene oxide nanosheets for microwave absorbing materials,” *RSC Adv*, vol. 7, no. 85, pp. 54031–54038, 2017, doi: 10.1039/c7ra08794b.
- [347] H. Yu, B. Zhang, C. Bulin, R. Li, and R. Xing, “High-efficient Synthesis of Graphene Oxide Based on Improved Hummers Method,” *Sci Rep*, vol. 6, no. 1, pp. 1–7, 2016, doi: 10.1038/srep36143.
- [348] E. Andrijanto, S. Shoelarta, G. Subiyanto, and S. Rifki, “Facile synthesis of graphene from graphite using ascorbic acid as reducing agent,” *AIP Conf Proc*, vol. 1725, no. 1, p. 020003, 2016, doi: 10.1063/1.4945457.
- [349] K. M. Aujara, B. W. Chieng, N. A. Ibrahim, N. Zainuddin, and C. T. Ratnam, “Gamma-irradiation induced functionalization of graphene oxide with organosilanes,” *Int J Mol Sci*, vol. 20, no. 8, p. 1910, 2019, doi: 10.3390/ijms20081910.
- [350] M. Bera, Chandravati, P. Gupta, and P. K. Maji, “Facile One-Pot Synthesis of Graphene Oxide by Sonication Assisted Mechanochemical Approach and Its Surface Chemistry,” *J Nanosci Nanotechnol*, vol. 18, no. 2, pp. 902–912, 2018, doi: 10.1166/jnn.2018.14306.
- [351] X. Feng, W. Chen, and L. Yan, “Free-standing dried foam films of graphene oxide for humidity sensing,” *Sens Actuators B Chem*, vol. 215, pp. 316–322, 2015, doi: 10.1016/j.snb.2015.03.068.
- [352] K. Garg, R. Shanmugam, and P. C. Ramamurthy, “New covalent hybrids of graphene oxide with core modified and -expanded porphyrins: Synthesis, characterisation and their non linear optical properties,” *Carbon N Y*, vol. 122, pp. 307–318, 2017, doi: 10.1016/j.carbon.2017.06.052.

- [353] S. W. Lee *et al.*, “Sorption/desorption hysteresis of thin-film humidity sensors based on graphene oxide and its derivative,” *Sens Actuators B Chem*, vol. 237, pp. 575–580, 2016, doi: 10.1016/j.snb.2016.06.113.
- [354] B. D. Osseonon and D. Bélanger, “Synthesis and characterization of sulfophenyl-functionalized reduced graphene oxide sheets,” *RSC Adv*, vol. 7, no. 44, pp. 27224–27234, 2017, doi: 10.1039/c6ra28311j.
- [355] A. Rosy and G. Kalpana, “Influence of RGO/TiO₂ nanocomposite on photo-degrading rhodamine B and rose bengal dye pollutants,” *Bulletin of Materials Science*, vol. 41, no. 83, pp. 1–8, 2018, doi: 10.1007/s12034-018-1598-y.
- [356] M. Strankowski, D. Włodarczyk, Ł. Piszczyk, and J. Strankowska, “Polyurethane Nanocomposites Containing Reduced Graphene Oxide, FTIR, Raman, and XRD Studies,” *Journal of Spectroscopy*, vol. 2016, 2016, doi: 10.1155/2016/7520741.
- [357] T. F. Emiru and D. W. Ayele, “Controlled synthesis, characterization and reduction of graphene oxide: A convenient method for large scale production,” *Egyptian Journal of Basic and Applied Sciences*, vol. 4, no. 1, pp. 74–79, 2017, doi: 10.1016/j.ejbas.2016.11.002.
- [358] Y. Chen *et al.*, “Microbial reduction of graphene oxide by *Azotobacter chroococcum*,” *Chem Phys Lett*, vol. 677, pp. 143–147, 2017, doi: 10.1016/j.cplett.2017.04.002.
- [359] S. Kujur and D. D. Pathak, “Reduced graphene oxide-immobilized iron nanoparticles Fe(0)@rGO as heterogeneous catalyst for one-pot synthesis of series of propargylamines,” *Research on Chemical Intermediates*, vol. 46, no. 1, pp. 369–384, 2020, doi: 10.1007/s11164-019-03955-5.
- [360] R. Britto Hurtado, M. Cortez-Valadez, J. R. Aragon-Guajardo, J. J. Cruz-Rivera, F. Martínez-Suárez, and M. Flores-Acosta, “One-step synthesis of reduced graphene oxide/gold nanoparticles under ambient conditions,” *Arabian Journal of Chemistry*, vol. 13, no. 1, pp. 1633–1640, 2020, doi: 10.1016/j.arabjc.2017.12.021.
- [361] V. Sharma, Y. Jain, M. Kumari, R. Gupta, S. K. Sharma, and K. Sachdev, “Synthesis and Characterization of Graphene Oxide (GO) and Reduced Graphene Oxide (rGO) for Gas Sensing Application,” *Macromol Symp*, vol. 376, no. 1, p. 1700006, 2017, doi: 10.1002/masy.201700006.
- [362] G. Muruganandi, M. Saravanan, G. Vinitha, M. B. Jessie Raj, and T. C. Sabari Girisun, “Barium borate nanorod decorated reduced graphene oxide for optical power limiting applications,” *Opt Mater (Amst)*, vol. 75, pp. 612–618, 2018, doi: 10.1016/j.optmat.2017.11.017.
- [363] A. T. Habte, D. W. Ayele, and M. Hu, “Synthesis and Characterization of Reduced Graphene Oxide (rGO) Started from Graphene Oxide (GO) Using the Tour Method with Different Parameters,” *Advances in Materials Science and Engineering*, vol. 2019, 2019, doi: 10.1155/2019/5058163.

Bibliography

- [364] I. O. Faniyi *et al.*, “The comparative analyses of reduced graphene oxide (RGO) prepared via green, mild and chemical approaches,” *SN Appl Sci*, vol. 1, no. 10, pp. 1–7, 2019, doi: 10.1007/s42452-019-1188-7.
- [365] R. A. Rochman, S. Wahyuningsih, A. H. Ramelan, and Q. A. Hanif, “Preparation of nitrogen and sulphur Co-doped reduced graphene oxide (rGO-NS) using N and S heteroatom of thiourea,” *IOP Conf Ser Mater Sci Eng*, vol. 509, no. 1, p. 012119, 2019, doi: 10.1088/1757-899X/509/1/012119.
- [366] Y. Gong, D. Li, Q. Fu, and C. Pan, “Influence of graphene microstructures on electrochemical performance for supercapacitors,” *Progress in Natural Science: Materials International*, vol. 25, no. 5, pp. 379–385, 2015, doi: 10.1016/j.pnsc.2015.10.004.
- [367] P. Gangwar, S. Singh, and N. Khare, “Study of optical properties of graphene oxide and its derivatives using spectroscopic ellipsometry,” *Applied Physics A*, vol. 124, no. 9, pp. 1–8, 2018, doi: 10.1007/s00339-018-1999-1.
- [368] S. Yavuz and P. R. Bandaru, “Ag nanowire coated reduced graphene oxide/n-silicon Schottky junction based solar cell,” *2016 IEEE Conference on Technologies for Sustainability (SusTech)*, vol. IEEE, pp. 265–269, 2016, doi: 10.1109/SusTech.2016.7897178.
- [369] J. Mohammed *et al.*, “Lightweight SrM/CCTO/rGO nanocomposites for optoelectronics and K u band microwave absorption,” *Journal of Materials Science: Materials in Electronics*, vol. 30, no. 4, pp. 4026–4040, 2019, doi: 10.1007/s10854-019-00690-w.
- [370] A. Senatore, V. D’Agostino, V. Petrone, P. Ciambelli, and M. Sarno, “Graphene Oxide Nanosheets as Effective Friction Modifier for Oil Lubricant: Materials, Methods, and Tribological Results,” *Int Sch Res Notices*, vol. 2013, 2013, doi: 10.5402/2013/425809.
- [371] Kurniasari *et al.*, “Defect and Magnetic Properties of Reduced Graphene Oxide Prepared from Old Coconut Shell,” *IOP Conf Ser Mater Sci Eng*, vol. 196, p. 012021, 2017, doi: 10.1088/1757-899X/196/1/012021.
- [372] N. M. Nguyen Huynh, Z. A. Boeva, J. H. Smått, M. Pesonen, and T. Lindfors, “Reduced graphene oxide as a water, carbon dioxide and oxygen barrier in plasticized poly(vinyl chloride) films,” *RSC Adv*, vol. 8, no. 32, pp. 17645–17655, 2018, doi: 10.1039/c8ra03080d.
- [373] H. Qin, T. Gong, Y. Cho, C. Lee, and T. Kim, “A conductive copolymer of graphene oxide/poly(1-(3-aminopropyl)pyrrole) and the adsorption of metal ions,” *Polym Chem*, vol. 5, no. 15, pp. 4466–4473, 2014, doi: 10.1039/c4py00102h.
- [374] N. M. S. Hidayah *et al.*, “Comparison on graphite, graphene oxide and reduced graphene oxide: Synthesis and characterization,” *AIP Conf Proc*, vol. 1892, no. 1, p. 150002, 2017, doi: 10.1063/1.5005764.

Bibliography

- [375] Z. Wang *et al.*, “Comparative studies on single-layer reduced graphene oxide films obtained by electrochemical reduction and hydrazine vapor reduction,” *Nanoscale Res Lett*, vol. 7, no. 1, pp. 1–7, 2012, doi: 10.1186/1556-276X-7-161.
- [376] C. Fu, G. Zhao, H. Zhang, and S. Li, “Evaluation and characterization of reduced graphene oxide nanosheets as anode materials for lithium-ion batteries,” *Int. J. Electrochem. Sci*, vol. 8, no. 5, pp. 6269–6280, 2013.
- [377] W. E. Ghann *et al.*, “Synthesis and characterization of reduced graphene oxide and their application in dye-sensitized solar cells,” *ChemEngineering*, vol. 3, no. 1, p. 7, 2019, doi: 10.3390/chemengineering3010007.
- [378] R. Bhargava and S. Khan, “Effect of reduced graphene oxide (rGO) on structural, optical, and dielectric properties of Mg(OH)₂/rGO nanocomposites,” *Advanced Powder Technology*, vol. 28, no. 11, pp. 2812–2819, 2017, doi: 10.1016/j.appt.2017.08.008.
- [379] K. Rathi and K. Pal, “Impact of Doping on GO: Fast Response–Recovery Humidity Sensor,” *ACS Omega*, vol. 2, no. 3, pp. 842–851, 2017, doi: 10.1021/acsomega.6b00399.
- [380] C. Y. Ho, C. C. Liang, and H. W. Wang, “Investigation of low thermal reduction of graphene oxide for dye-sensitized solar cell counter electrode,” *Colloids Surf A Physicochem Eng Asp*, vol. 481, pp. 222–228, 2015, doi: 10.1016/j.colsurfa.2015.04.045.
- [381] N. H. N. Azman, H. N. Lim, M. S. Mamat, and Y. Sulaiman, “Synergistic enhancement of ternary poly(3,4-ethylenedioxythiophene)/graphene oxide/manganese oxide composite as a symmetrical electrode for supercapacitors,” *Energies (Basel)*, vol. 11, no. 6, p. 1510, 2018, doi: 10.3390/en11061510.
- [382] Q. A. Drmosh *et al.*, “A novel approach to fabricating a ternary rGO/ZnO/Pt system for high-performance hydrogen sensor at low operating temperatures,” *Appl Surf Sci*, vol. 464, pp. 616–626, 2019, doi: 10.1016/j.apsusc.2018.09.128.
- [383] W. N. A. Wan Khalit, M. N. Mustafa, and Y. Sulaiman, “Synergistic effect of poly(3,4-ethylenedioxythiophene), reduced graphene oxide and aluminium oxide) as counter electrode in dye-sensitized solar cell,” *Results Phys*, vol. 13, p. 102355, 2019, doi: 10.1016/j.rinp.2019.102355.
- [384] R. P. Antony, L. K. Preethi, B. Gupta, T. Mathews, S. Dash, and A. K. Tyagi, “Efficient electrocatalytic performance of thermally exfoliated reduced graphene oxide-Pt hybrid,” *Mater Res Bull*, vol. 70, pp. 60–67, 2015, doi: 10.1016/j.materresbull.2015.04.015.
- [385] F. T. Johra and W. G. Jung, “Hydrothermally reduced graphene oxide as a supercapacitor,” *Appl Surf Sci*, vol. 357, pp. 1911–1914, 2015, doi: 10.1016/j.apsusc.2015.09.128.

List of Publications

PUBLISHED

- **M. J. Panesar**, Tchouank Tekou Carol T, J. Mohammed, Pragati Kumar, Pushpendra Kumar and **A. K. Srivastava**, “IV– curve and Structural Studies of the Composite Mixture of Reduced Graphene Oxide and Silver – nanopowders” *J Mater Sci: Mater Electron.*, (2021). <https://doi.org/10.1007/s10854-021-07416-x>
- **M. J. Panesar**, J. Mohammed, Tchouank Tekou Carol T., Pushpendra Kumar and **A. K. Srivastava**, “Effect of titanium dioxide on the structural and electrical conductivity of cadmium oxide,” *Mater. Today Proc.*, vol. 26, pp. 1330–1335, 2020.
- **M. J. Panesar**, J. Mohammed, C. T. TchouanK Tekou, P. Kumar, Pushpendra Kumar and **A. K. Srivastava**, “Effect of Addition of Polyaniline (PANI) on the properties of copper (II) Oxide nanoparticles,” *J. Phys. Conf. Ser.*, vol. 1531, no. 1, p. 012036, 2020.

COMMUNICATED

- **M. J. Panesar**, C. T. TchouanK Tekou, J. Mohammed, P. Kumar, and **A. K. Srivastava**, “Investigation of Varistor Response and Structural Analysation of Silver mixed TiO₂ (anatase) Nanoparticles”.

TO BE COMMUNICATED

- **M. J. Panesar**, C. T. TchouanK Tekou, J. Mohammed, P. Kumar, and **A. K. Srivastava**, “Structural and Varistor Properties of CuO with Ag nano – structured powders”.
- **M. J. Panesar**, C. T. TchouanK Tekou, J. Mohammed, P. Kumar, and **A. K. Srivastava**, “Enhancement in Electrical Properties of Polyaniline with addition of Cadmium Oxide nanopowders”.

List of Conference Proceedings

- 10th International Conference on Materials Processing and Characterization [ICMPC – 2020] was organized at GLA university, Mathura (India) on February from 21st to 23rd, 2020.
- Recent Advances in Fundamental and Applied Sciences [RAFAS – 2019] was held in Lovely Professional University, Punjab (India) in November from 5th to 6th, 2019.

List of Workshops

- Advancements in Nano – materials with Futuristic Engineering Applications was held by Career Point University, Hamirpur, Himachal Pradesh (India) from January 18th to 22th, 2021.
- Scientific Writing Using Typesetting Software LaTeX was organized by Human Resource Development Centre, Lovely Professional University, Punjab (India) from March 13th to 14th, 2020.
- National Workshop on Electron Microscopy was arranged by Central Instrumentation Facility, DRP – LPU in Lovely Professional University, Punjab (India) in November 29th to 30th, 2019.
- X – Ray Diffraction: Theory and Practice was coordinated by the Central Instrumentation Facility, DRP – LPU at Lovely Professional University, Punjab (India) from November 9th to 10th, 2019.

List of Seminars

- Recent Advance in Material Characterization Techniques was administered by Vivekananda Institute of Technology, Jaipur (India) from February 15th to 19th, 2021.
- Spectroscopic Techniques for Materials Characterizations was conducted by Materials Research Centre, MNIT Jaipur (India) from January 4th to 8th, 2021.

STUDENT CURRICULUM VITAE

Mehar Jyoti Panesar

11, Raja Garden Colony,
Mithapur Chowk,
Near Ganpati Sweets Shop,
P.O. Model Town,
Jalandhar, Punjab (India)
Pin Code: 144003

Email: meharpanesar14@gmail.com

Phone No: 7087565605



CAREER OBJECTIVE

To pursue a challenging career in the arena of research and be a part of a progressive organization and a research environment that gives a scope to enhance my knowledge and help in developing new scientific skills and as well to work enthusiastically in a team where my skills can be utilized for the growth of the organization and self.

EDUCATIONAL QUALIFICATION

Degree	Institute	Year
Ph.D. Physics	Lovely Professional University, Phagwara	2022
M.Sc. Physics	Lovely Professional University, Phagwara	2016
B.Sc. Non-Med	Prem Chand Markanda SD College for Women, Jalandhar	2014
SSC (CBSE)	Guru Amar Dass Public School, Jalandhar	2011
HSC (CBSE)	Guru Amar Dass Public School, Jalandhar	2009

WORK EXPERIENCE

Assistant Professor [Physics, Contract Basis]

Lovely Professional University, Punjab
29, 2017

January 1, 2017 – April

- Prepared and delivered lectures to the first-year degree students and took their laboratory sessions as well.
- Assessed and graded the student work, including their tests, term project and lab work.

RESEARCH PROJECTS UNDERTAKEN

Project: Varistor Studies and Structural Analyzations. [Ph.D. Project]

Objective: Investigate the varistor properties of the composites of transition metal oxides, polymer, silver and reduced graphene oxide nanoparticles.

Description: Varistor properties have been studied for the individual and composite mixtures consisting of transition metals oxides [Copper Oxide, Cadmium Oxide, Titanium Dioxide (anatase)], reduced graphene oxide, polyaniline and silver nano – powders with varying ratios. The synthesis processes employed were: Sol – Gel Auto Combustion Method, ultra – Sonic assisted Sol – Gel Method, Modified Hummer’s Method, Oxidative Polymerization Method and Top - Down Method respectively, to acquire the aforementioned sample nanopowders. The structural nature was investigated through XRD and FTIR. RAMAN Spectroscopy was used for molecular analysis. Furthermore, the thermal relation was done using TGA and their topographical and elemental details have been obtained via FESEM, PSA and EDX. The varistor studies were done by plotting and studying the IV - graphs. The main objective of the work was to observe the pattern of the composite’s samples w.r.t an increase or decrease. The results exhibited a positive response i.e. the graphical plot showed an increase in the voltage values with current indicating the enhancement in the nature of the materials.

Project: Acoustic study of binary mixture. [M.Sc. Project]

Objective: To study the intermolecular interaction of binary mixture of Acetic Acid and Propan-2-ol.

Description: The ultrasonic study for the molecular interactions and to understand the thermodynamic and acoustic properties of the binary mixture constituting Acetic Acid and Propan-2-ol were analyzed by calculating certain parameters theoretically and experimentally. The experimental procedure was implied on at a constant frequency of 2MHz at three different temperatures (303K, 308 k and 313K) using eleven concentrations of the composite sample. Three parameters; Ultrasonic Velocity, Density and Viscosity were acquired experimentally with the usage of Ultrasonic Interferometer with water bath and these experimentally obtained values were further used to compute the theoretical values of the quantities; acoustic impedance, adiabatic compressibility, intermolecular free length, ultrasonic attenuation, relaxation time, molecular weight, free volume, Wada’s constant, Rao’s constant, molar volume, internal pressure, available volume and enthalpy. These procured values were then implemented on the graph for better understanding of the nature of interactions and for studying its applications for research and daily use basis

PUBLISHED RESEARCH ARTICLES

- M. J. Panesar, Tchouank Tekou Carol T, J. Mohammed, Pragati Kumar, Pushpendra, and A. K. Srivastava, “IV– curve and Structural Studies of the Composite Mixture of Reduced Graphene Oxide and Silver – nanopowders” *J Mater Sci: Mater Electron.*, (2021). <https://doi.org/10.1007/s10854-021-07416-x>

- M. J. Panesar, J. Mohammed, Tchouank Tekou Carol T., Pushpendra, and A. K. Srivastava, “Effect of titanium dioxide on the structural and electrical conductivity of cadmium oxide,” *Mater. Today Proc.*, vol. 26, pp. 1330–1335, 2020.
- M. J. Panesar, J. Mohammed, C. T. TchouanK Tekou, P. Kumar, and A. K. Srivastava, “Effect of Addition of Polyaniline (PANI) on the properties of copper (II) Oxide nanoparticles,” *J. Phys. Conf. Ser.*, vol. 1531, no. 1, p. 012036, 2020.

SKILL SET

Good oral and writing skills, Leadership, Teamwork and Collaboration skills, Critical thinking and problem solving, Good interpersonal skills.

Softwares:

MS office, Origin, Latex, Mendeley, X Powder, IRsolution, imagej.

Data Interpretation Strength:

Literature and Analytical, Thermo – Gravimetric Analysis (TGA), X – Ray Diffraction Analysis (XRD), Fourier Transform Infra – Red Spectroscopy (FTIR), Raman Spectroscopy, Field Emission Scanning Electron Microscopy (FESEM), Energy Dispersive X – Ray Analysis (EDX), Particle Size Analysis (PSA), Impedance Analysis and Varistor Studies.

CONFERENCE PROCEEDINGS

- 10th International Conference on Materials Processing and Characterization [ICMPC – 2020].
GLA university, Mathura February 21 – 23, 2020
- Recent Advances in Fundamental and Applied Sciences [RAFAS – 2019].
Lovely Professional University, Punjab November 5 – 6, 2019
- Recent Advances in Fundamental and Applied Sciences [RAFAS – 2016].
Lovely Professional University, Punjab November 25 – 26, 2016

WORKSHOPS

- Advancements in Nano – materials with Futuristic Engineering Applications
Career Point University, Hamirpur, Himachal Pradesh January 18 – 22, 2021
- Scientific Writing Using Typesetting Software LaTeX
Human Resource Development Centre, LPU Punjab March 13 – 14, 2020

- National Workshop on Electron Microscopy
Central Instrumentation Facility, DRP – LPU, Punjab November 29 – 30, 2019
- X – Ray Diffraction: Theory and Practice
Central Instrumentation Facility, DRP – LPU, Punjab November 9 – 10, 2019

SEMINARS / SHORT TERM COURSES

- Recent Advance in Material Characterization Techniques
Vivekananda Institute of Technology, Jaipur February 15 – 19, 2021
- Spectroscopic Techniques for Materials Characterizations
Materials Research Centre, MNIT Jaipur January 4 – 8, 2021
- LPU Project Expo
Lovely Professional University, Phagwara April 28 – 30, 2016

EXTRACURRICULAR ACTIVITIES

- Inter College Math Competition
Kanya Maha Vidyalaya, Jalandhar October 31, 2012
- National Cadet Corps
PCM SD College for Women, Jalandhar 2012 and 2011

AWARDS AND HONORS

- O grade:** Latex Workshop, Human Resource Development Center
Lovely Professional University, Punjab March 13 – 14, 2020
- First prize:** Choreography Skit in Inter College Math Competition
Kanya Maha Vidyalaya, Punjab October 31, 2012
- A grade:** NCC B- Certificate Paper
National Cadet Corps, Jalandhar June 30, 2012
- First Prize:** NCC Squad Drill
National Cadet Corps, Jalandhar July 29, 2012
- First Prize:** NCC Squad Drill
National Cadet Corps, Jalandhar October 11, 2011

LANGUAGES PROFICIENCY

English, Hindi, Punjabi

STRENGTHS

Hardworking, Loyal, Honest, Punctual, Willingness to learn.

HOBBIES

Reading and Gardening.

PERSONAL DETAILS

Mother's Name: Mrs. Parminder Kaur

Father's Name: Mr. Ranjit Singh Panesar

DOB: 14 – 07 – 1993

Gender: Female



IV-curve and structural studies of the composite mixture of reduced graphene oxide and silver nanopowders

Mehar J. Panesar¹, T. Tchouank Tekou Carol¹, J. Mohammed², Pragati Kumar³, Pushpendra Kumar⁴, and A. K. Srivastava^{1,*}

¹ Department of Physics, Lovely Professional University, Phagwara, Punjab 144411, India

² Department of Physics, Faculty of Science, Federal University Dutse, P. M. B. 7156, Dutse, Jigawa State, Nigeria

³ Department of Nano Sciences & Materials, Central University of Jammu, Rahya-Suchani (Bagla), Samba, Jammu 181143, India

⁴ Department of Chemistry, Lovely Professional University, Phagwara, Punjab 144411, India

Received: 9 September 2021

Accepted: 15 November 2021

© The Author(s), under exclusive licence to Springer Science+Business Media, LLC, part of Springer Nature 2021

ABSTRACT

Nanoparticles today have the upper hand in its manufacturing desirability in more or less every aspect of the working areas, from industrial and commercial to self-care products. In this paper, the applicational prospects of varistors for the composite mixture of rGO and Ag-nanopowders were studied via samples with varying compositions. Hummers modified method and burst method were employed for the synthetisation of GO, rGO, and Ag-nanopowders, respectively. The structural nature and electrical behaviour were understood by the means of variegated characterisations. The purity of GO and rGO were confirmed via Raman analysis. XRD and FTIR exhibited the attributed peak values for GO and rGO, Ag-nanopowders. The topographical and elemental details were acquired through FESEM and EDX studies, which talked about the wrinkled paper-like structure for GO and rGO and spherical structural nature of Ag. Current–voltage plot was studied for the better understanding of the electrical inhabitation. It was observed that rGO + Ag, being two constituent networks, gave small values but still showed an increase, which means if used with complex arrangement, they have the possibility to be considered in the material fabrication for high-voltage varistors domains.

1 Introduction

In today's world, comfort plays an indispensable part, be it in any domain: work, home, industrial sectors, and medical prospects and device

construction for that purpose and material synthetisation are the absolute factors. And one of the technologies involved in such is called nanotechnology. Nanotechnology is the province of research and development that concerns with the blueprint of

Address correspondence to E-mail: srivastava_phy@yahoo.co.in

<https://doi.org/10.1007/s10854-021-07416-x>

Published online: 25 November 2021



Contents lists available at ScienceDirect

Materials Today: Proceedings

journal homepage: www.elsevier.com/locate/matpr

Effect of titanium dioxide on the structural and electrical conductivity of cadmium oxide

Mehar J. Panesar^a, J. Mohammed^b, T. Tchouank Tekou Carol^a, Pushpendra Kumar^c, A.K. Srivastava^{a,*}

^a Department of Physics, Lovely Professional University, Phagwara 144411, Punjab, India

^b Department of Physics, Faculty of Science, Federal University Dutse, P. M. B. 7156, Dutse, Jigawa State, Nigeria

^c Department of Chemistry, Lovely Professional University, Phagwara 144411, Punjab, India

ARTICLE INFO

Article history:
Received 5 February 2020
Accepted 15 February 2020
Available online xxxxx

Keywords:
Cadmium oxide
Sol-gel auto combustion method
Titanium dioxide
Ultrasonic assisted sol-gel method
Dielectric properties
Paint-pigments

ABSTRACT

Paint pigments belong in the daily-uses classification which are required to have a certain set of substantial qualities, such as; it is needed to be corrosion proof, rust proof (which further leads to longer life), thermally stable, should not react with the environment etc. Sol-Gel Auto-combustion and Ultrasonic Assisted Sol-Gel method was employed on to obtain CdO and TiO₂ nanopowders respectively and their composite mixture was studied to understand the outcomes of incorporating TiO₂ in another metal oxide CdO. The structural and morphological studies of the pure and the blended composition were analysed with the help of XRD, FTIR, Raman Spectroscopy and FESEM while the conductive nature was investigated through Maxwell-Wagner model and Koop's phenomenological theory. The formation of CdO and anatase TiO₂ was confirmed through XRD with the emergence of standard peaks for both the mentioned metal oxides. The characteristic FTIR peaks were acquired for CdO (410.05–678.41 cm⁻¹) and TiO₂ (845.45–850.87 cm⁻¹ and 1391.45 cm⁻¹) and the standardised Raman peaks were also obtained for both CdO (144.66–954.01 cm⁻¹) and TiO₂ (147.49–634.52 cm⁻¹). The FESEM study showed the structural formation for CdO and TiO₂ while the EDX analysis showed the emergence of peaks of Cd, O & Ti for the studied sample cases. The Dielectric Analysis revealed the drop in the conductive graph. The fore-mentioned composite sample can have its consideration for the raw materials used in paints.

© 2020 Elsevier Ltd. All rights reserved.

Selection and of the scientific committee of the 10th International Conference of Materials Processing and Characterization.

1. Introduction

The microscopic matter with the diameter range from 1 nm to 100 nm is the definition for Nano-Particles. These nanopowders holds various physical, chemical and biological characteristics as; uniformity, good conductance, thermal stability and etc. all attributed to its nano-nature. It also has high surface to volume ratio which plays a huge role in its popularity. Nanopowders now a days are intensely studied on because of the wide radius it provides in terms of its usage in various domains/branches, physics, chemistry, biomedical, industrial areas. They are easily available, easy to fabricate and most of them being budget friendly as well. They are easy to work with as they can be moulded according to the desired needs, and can be used with other materials whilst improving the

abilities of the host material as well such as: obtaining materials that are durable, lighter, stronger.

The aspects of the metal oxide nano-crystallite powders bear a strong uphold when it comes to their applicational areas. Certain Metal-Oxide Nanopowders are also used in paints and ceramic industry as paint pigments. They should exhibit (I). Resistivity (II). Longevity (III). Should be Thermally stable (IV). Should not react with the surroundings, are few to mention. CdO is a degenerate, n-type semiconductor metal oxide having the rock-salt (FCC) lattice structure. It has direct band gap energy value of 2.2–2.7 eV and indirect band gap energy value 1.36–1.98 eV. This semiconductor possesses very articulate properties as; it has low electrical resistivity, large band gap, high transmission in the visible region which allows it to have applications in various optoelectrical industrial sectors. It baggage its requirements mainly in transparent electrodes, photodiodes, IR reflectors, liquid crystal displays, phototransistors, anti-reflection coatings, photovoltaic cells, paint pigments. Cadmium pigments has an excellent

* Corresponding author.

E-mail addresses: ak.srivastava@lpu.edu.in, srivastava_phy@yahoo.co.in (A.K. Srivastava).

<https://doi.org/10.1016/j.matpr.2020.02.270>

2214-7853/© 2020 Elsevier Ltd. All rights reserved.

Selection and of the scientific committee of the 10th International Conference of Materials Processing and Characterization.

Please cite this article as: M. J. Panesar, J. Mohammed, T. Tchouank Tekou Carol et al., Effect of titanium dioxide on the structural and electrical conductivity of cadmium oxide, Materials Today: Proceedings, <https://doi.org/10.1016/j.matpr.2020.02.270>

Effect of Addition of Polyaniline (PANI) on the properties of copper (II) Oxide nanoparticles

Mehar J. Panesar¹, J. Mohammed^{1,2}, Tchouank Tekou Carol T.¹, Pushpendra Kumar³, A. K. Srivastava^{1,*}

¹Department of Physics, Lovely Professional University, Phagwara-144411, Punjab, India

²Department of Physics, Faculty of Science, Federal University Dutse, P. M. B. 7156, Dutse, Jigawa State, Nigeria

³Department of Chemistry, Lovely Professional University, Phagwara-144411, Punjab, India

*Email: srivastava_phy@yahoo.co.in

Abstract

High resistivity (or low electrical conductance values) materials have found their applicational foot in those domains of electrical-electronical where resistors, heat filaments, space heaters, shunt resistors electric irons and etc. are broadly exercised on. This paper investigates the effect of addition of polyaniline (PANI) on the properties of copper (II) oxide (CuO) nanoparticles. Sol-Gel method was used to synthesize CuO nanoparticles while PANI was obtained by oxidative polymerization process. The structural characterizations of the composite material and the effect of PANI on the CuO nanoparticles are studied through FESEM, XRD, FTIR and Raman Spectroscopy. XRD confirmed the formation of CuO without the presence of Cu₂O. FESEM showed the clear formation monoclinic structure of CuO. EDX revealed that Cu and O- atoms are in stoichiometry, thus confirming the formation of CuO bond and peaks of C, N and O are also obtained depicting the PANI formation. The characteristic peaks are obtained for both CuO (402.99-678.74 cm⁻¹) and PANI (1109.94-1568.54 cm⁻¹ and 3058.81-3436.21 cm⁻¹) through FTIR. The Raman analysis of CuO sample showed 3 peaks (290.01 cm⁻¹, 333.51 cm⁻¹ and 624.81 cm⁻¹) and while PANI showed peaks in the range from 1166.48 cm⁻¹ – 1582.81 cm⁻¹. The dielectric properties were investigated using Maxwell-Wagner model and Koop's phenomenological theory. The fore-mentioned composite material can also be considered to be devised in a resistor.

Keywords: Copper Oxide, Sol-Gel Auto Combustion method, Oxidative polymerization method, Polyaniline, Dielectric Properties, Resistors.

1. Introduction

The sphere of nanomaterial science has been studied extensively. They have many structural and surface morphological merits as compared to their counterpart, Bulk Materials. The one standing out the most, being higher surface to volume ratio. The worth of the device is counted if the material used in the fabrication of the device exhibits superior surface & physical nature as it is one of the predominant point in determining the chemical, thermal, electrical and magnetic aspects. The primary reactions take place on the surface of the material which influences the mechanisms of the device and thus controls the applicational facet of it. More the surface/ volume ration, better will be the adsorption/ absorption process and thus more the preferable outputs.

The Transition Metal Oxides or commonly used with the acronym MO's, they belong to a peculiar bracket of nanomaterial domain. They have been garnishing ample recognitions all because of their outstanding structural nature. The physical/ chemical characteristics of MOs strongly rely on compositions, sizes, shapes and structures of the nanopowders. Also a notable change in the surface



Content from this work may be used under the terms of the [Creative Commons Attribution 3.0 licence](https://creativecommons.org/licenses/by/3.0/). Any further distribution of this work must maintain attribution to the author(s) and the title of the work, journal citation and DOI.

Published under licence by IOP Publishing Ltd

1